DEFENCE

RESEARCH

TELECOMMUNICATIONS

ESTABLISHMENT

ALOUETTE I
THE FIRST THREE YEARS IN ORBIT

by

I. Paghis, C.A. Franklin and J. Mar

OTTAWA CANADA

DRTE REPORT NO. 1159

MARCH 1967

DEFENCE RESEARCH BOARD

DEPARTMENT OF NATIONAL DEFENCE
CANADA

DEFENCE RESEARCH TELECOMMUNICATIONS ESTABLISHMENT

ALOUETTE I
THE FIRST THREE YEARS IN ORBIT

by

I. PAGHIS, C.A. FRANKLIN and J. MAR

DRTE REPORT NO. 1159

OTTAWA

Submitted July 1966
Published April 1967

66-372

ROGER DUHAMEL, F.R.S.C.
Queen's Printer and Controller of Stationery
Ottawa, Canada
1967

FOREWORD

As this three part report * is being written, (September, 1965), Alouette II † is being readied by DRTE for launch by NASA. The international character of Alouette I will be even more widely demonstrated when Alouette II and the subsequent satellites in this program are launched, and will extend the present list of cooperating laboratories in the United States, the United Kingdom, and Canada to include organizations in Australia, Japan, Norway and France.

A comprehensive report on the engineering and physics of the Alouette I program was successively postponed after the first and then the second year in orbit because everyone concerned was too busy—either in building Alouette II or in studying the data obtained from Alouette I. After three years in orbit the situation has not changed—everyone is still too busy! This time however drastic action has been taken and the story of the first three years of Alouette I is fairly completely told in these three sections of a single report.

Too many people have contributed in DRTE, in industry, in the RCAF, and in several cooperating laboratories in Canada, the USA and the UK, to allow of individual mention. To some extent, the increasing bibliography of published papers does achieve this, but there are very many more people whose contributions were and are essential who cannot be known except to their team-mates. During the Alouette program all of us have been impressed with the efficiency and friendly response of the many officials of NASA and its cooperating agencies.

In three years Alouette I has completed nearly 15000 orbits, answered over 39000 commands and yielded vast amounts of useful data over the earth, between 80°N and 80°S latitudes. The policy of conservative assessment of components and considerable redundancy in critical systems has been justified as there has as yet been no need to use the spare batteries, telemetry transmitters, and pulse transmitter. It is fair to expect continued useful data from Alouette I through a fourth year.

Frank T. Davies

Frank T. Davies
Chief Superintendent
DRTE

* The three parts of this report are:

ALOUETTE I: THE FIRST THREE YEARS IN ORBIT

Part 1, Ionospheric Studies. DRTE Report No. 1159-1.
Part 2, Electrical Design and Performance. DRTE Report No. 1159-2.
Part 3, Mechanical Design and Environment. DRTE Report No. 1159-3.

† On November 28, 1965, the Canadian Alouette II and the U.S. Explorer 31 were launched by a Thor-Agena B rocket into an elliptical polar orbit, with apogee and perigee of 3000 and 500 km respectively. The two satellites are drifting apart very slowly, at the rate of about 9 km per day and it should be possible to make direct comparisons of measurements in the two spacecraft. Such analysis is expected to have a major impact on the design of future upper atmospheric satellite experiments.

TABLE OF CONTENTS

(A detailed list of contents appears at the beginning of each of the three parts)

DEFENCE RESEARCH BOARD

DEPARTMENT OF NATIONAL DEFENCE
CANADA

DEFENCE RESEARCH TELECOMMUNICATIONS ESTABLISHMENT

ALOUETTE I: THE FIRST THREE YEARS IN ORBIT

PART I – IONOSPHERIC STUDIES

Compiled by

IRVINE PAGHIS

DRTE REPORT NO. 1159-1

PCC No. D48-95-11-36

Submitted September 1965
Published April 1967
OTTAWA

66-373

TABLE OF CONTENTS

PART I

ALOUETTE I: THE FIRST THREE YEARS IN ORBIT

PART I – IONOSPHERIC STUDIES

Compiled by

Irvine Paghis

1. INTRODUCTION

Since its formation in 1947 the Defence Research Telecommunications Establishment (DRTE) of the Defence Research Board (DRB) has specialized in the study of high-latitude ionospheric communication systems. Until quite recently most knowledge of the ionosphere was obtained through ground-based equipments. In the late 1950's earth satellites became practical possibilities, and it was realized that new and vital data could be obtained by the use of an ionospheric sounder in a satellite. This led to the design and construction by DRTE at Ottawa of the first Canadian earth satellite. Known as Alouette I (1962 Beta Alpha), this satellite was launched by the United States National Aeronautics and Space Administration (NASA) from California on September 29, 1962, as part of a long-term international program of studies in the ionized constituents of the earth's upper atmosphere.

The Alouette I experiments are designed to improve knowledge and understanding of the ionosphere, with special emphasis on the highly disturbed polar ionosphere. The project has proven to be entirely successful [1-5] and three years after launch all of the experiments continue to provide high-quality data. The present report is concerned primarily with results obtained by one group of workers, namely the staff of DRTE. The Alouette I data are also being analyzed by scientists in many other countries and, because of the close co-operation between the various research groups, it is difficult in some instances to make a clear distinction between DRTE work and that done elsewhere. The total number of resulting relevant scientific publications is now more than one hundred and intensive work is still continuing.

For convenience, in addition to a review of the DRTE work and directly related research, Part I of this report includes background information on the history and organization of the project, together with a brief discussion of the design and operation of the satellite. Parts II and III of the report provide detailed information on the satellite design and in-flight performance [6,7]

1.1 History and Organization

Even before Sputnik was launched into orbit in 1957, many scientists had proposed experiments for studying the ionized constituents of the upper atmosphere from an earth-satellite platform. In 1958, the Space Science Board of the U. S. National Academy of Sciences established a working group to consider topside sounding of the ionosphere. Representatives from the Defence Research Board of Canada were invited to participate in these discussions and, in late 1958, DRTE made a specific proposal for a topside sounder experiment. The DRTE proposal was accepted, and it was arranged that the project should be a joint undertaking of the newly formed NASA, and DRTE. The basic arrangement was that DRTE would design and construct the satellite, NASA would provide the rocket and associated facilities for rocket qualification tests and for launch into orbit, and each country would pay its own costs.

Continuous co-ordination between DRTE, NASA, and many of the other agencies that have participated in the program was essential both before and after launch. This applies not only to the specific Alouette project, but also to the related ionospheric satellite programs. (See Appendix I for a summary of the related programs.) Such co-ordination was achieved through a committee known as the Topside Sounder Working Group (TSWG). The Chairman of the TSWG was Mr. J.E. Jackson of the Goddard Space Flight Center; the senior Canadian representative was the Deputy Chief Superintendent of DRTE, Dr. John H. Chapman, who also was made responsible for co-ordination of all Canadian work on Alouette. Membership of the TSWG included representatives from the participating agencies: NASA; the Central Radio Propagation Laboratory (CRPL)*, Boulder, Colorado; the Radio Research Station (RRS) †, Slough, England; and DRTE. Included were representatives from the U.S. Department of Defense and from the contractors for the U.S. S48 satellite.

1.2 Ground Telemetry Stations

At an early stage in the project, it was decided that current techniques for data storage within a satellite were not sufficiently reliable, and therefore that the satellite should be operated on command from a number of ground telemetry stations. The main experimental requirements were for coverage of the northern auroral region, and along the 75°W meridian. Great Britain offered to assist and installed and manned a telemetry station at Singapore and on an island in the South Atlantic.

The initial coverage provided on the launch date by thirteen British, U.S., and Canadian stations is shown in Figure 1. Relatively minor alterations to these patterns have been made from time to time depending on experimental requirements and the availability of ground facilities.

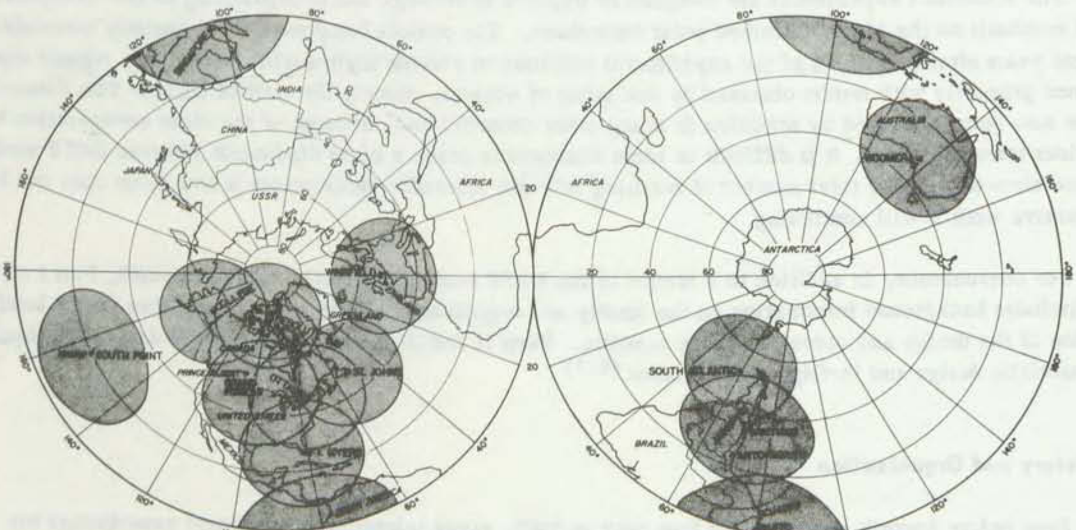

Fig. 1. Location of Monitoring Telemetry Stations at Alouette I Launch.
The shaded areas indicate the coverage for a 1000 km circular orbit, and a minimum telemetry antenna pattern elevation of 15° (after Chapman and Warren (8)).

* The name of CRPL was changed to 'Institute for Telecommunication Sciences and Aeronomy' in October, 1965.

† Effective 1 April, 1965, Radio Research Station (RRS), Slough, became known as the Radio and Space Research Station, (RSRS).

1.3 General Description of Alouette I and Its Operation

1.3.1 Configuration, Power Supply, Command, etc.

Alouette 1 is an oblate spheroid (Fig. 2), 42 inches in diameter, 34 inches high, and weighs 320 lbs. The orbit is nearly circular at an altitude of about 1000 km, and the orbital period is 105.5 minutes. The initial satellite spin of 1.4 rpm decreased to 0.9 and then to 0.2 rpm by the end of the first and second years in orbit; at present the satellite is not attitude-stabilized. (See reference 7 for further details.) This loss of attitude-stabilization increases data reduction problems, especially for the energetic particle detectors. The orbital plane rotates by about 2° per day relative to the sun-earth line. If the difference between northward and southward passes is ignored, a cycle of variation of the orbital plane with respect to solar illumination occurs once every three months.

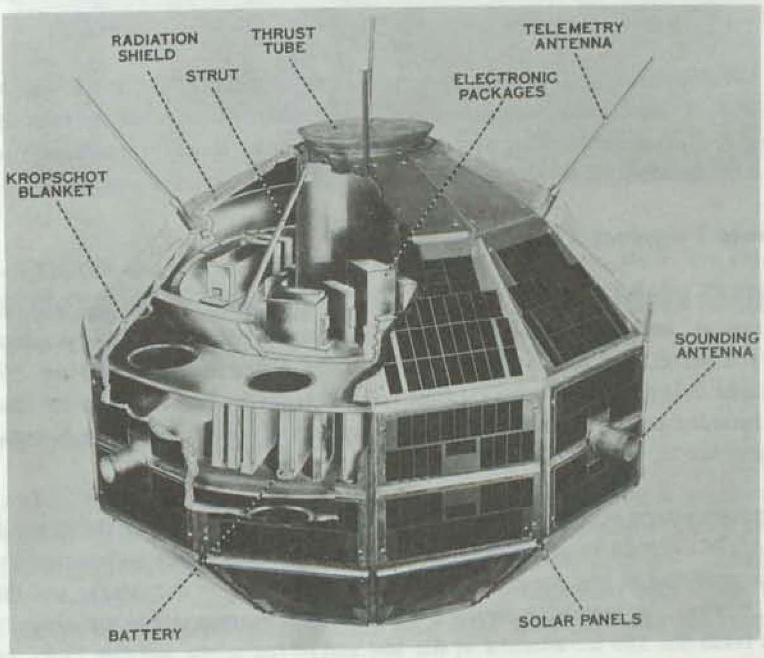

Fig. 2. The Alouette I Satellite with Sounding Antennas Retracted in Launch Position (after Chapman and Warren (8)).

The original DRTE proposal for Alouette I was based on a single experiment, a high frequency (HF) ionosonde, to sweep from 0.5 to 12 Mc/s. As the project progressed, three complementary and relatively small experiments were added: a very low frequency (VLF) receiver to record natural and man-made radio emissions from 0.4 to 10 kc/s, circuitry to measure the intensity of radio noise from extra-terrestrial sources, and a number of detectors for measuring the flux of energetic particles.

Three separate antenna systems protrude from the satellite skin:

(i) On the satellite equator there are two crossed dipoles, 75 ft. and 150 ft. tip-to-tip. These are designed primarily for the topside sounder, but they are also used for the VLF and extra-terrestrial radio noise experiments.

(ii) Four short antennas 90° apart and inclined at 45° to the satellite axis are connected to two telemetry transmitters and to a command receiver.

(iii) A single antenna is mounted at the top of the satellite to serve the tracking beacon transmitter.

Solar radiation is the prime source of power for these experiments. Solar cells mounted on most of the outer surface of the satellite provide power to charge a number of storage batteries. The charging power of the cells is substantially less than the 30 watts maximum power consumption required for the instrumentation; hence, the satellite operation must be carefully scheduled.

Normally the satellite is in a 'power-off' mode in which either there are no transmissions, or the only transmission is a tracking beacon at 136.980 Mc/s. An operation command schedule is determined at a control center at DRTE, in Ottawa, and this is passed to the telemetry ground stations. Forty different commands are available: e.g., one or more of the experiments may be turned on and connected to an appropriate telemetry system; spare units may be brought into use; spare batteries may be switched in for recharging from the solar cells, etc. About 30 commands are executed each day. Experiments are usually commanded on when the satellite has risen to 15^{o}, or somewhat less, above the horizon and then switched off by an automatic timer ten minutes later. The experimental data are broadcast, in real time, by two satellite telemetry systems[5].

As this report is being written all of the experiments are functioning normally, and there has been no requirement to command into operation any of the standby spare equipment. Some components (such as the solar cells) are deteriorating at a predictable rate, and in addition, minor, sporadic malfunctions are beginning to occur (see reference 6 for details).

1.3.2 The Sweep-Frequency Topside Sounder

The HF ionospheric sounder in Alouette I is essentially a conventional sweep-frequency pulsed radar system. There is, however, one important difference. In the usual radar case, the propagation velocity is very nearly identical with the velocity of light in a vacuum, and the distance of a reflecting object is readily determined from the measured delay time between transmitted and received pulses. The HF sounder pulses, however, may be significantly retarded by the ionosphere, and the amount of retardation must be established before distances can be determined.

The sounder transmissions consist of 100 microsecond pulses, repeated 62 times per second. The frequency range of 0.4 to 12 Mc/s is swept in approximately 12 seconds, and this sweep is repeated every 18 seconds. Frequency markers are provided at one megacycle intervals, beginning at 0.5 Mc/s, and there are additional markers at 2.0 and 7.0 Mc/s. A matching network between the transmitter and the antennas has a crossover point at 4.7 Mc/s; it feeds the 150 ft. antenna at the low end of the range and the 75 ft. antenna at the high end. The mean power in the radiated pulse over the range is 10 watts. The sounder transmissions are not beamed in any specific direction with respect to the earth, and there is no built-in discrimination against echoes that arrive from non-vertical directions. However, such echoes can usually be readily identified through a comparison with the normal vertical echoes.

In many circumstances it is convenient (temporarily) to ignore the effect of wave retardation. The measured time delay is converted to an equivalent (or 'virtual', or 'apparent') distance, and the ionosonde receiver output is displayed in the form of an *ionogram* : i.e., a graph of the variation of frequency versus apparent distance of a reflecting region. A representative low-latitude topside ionogram is shown in Figure 3. In addition to ionospheric reflections from the F region (appearing between 1 and 6.5 Mc/s), there may be reflections from a sporadic E layer (E_s), as well as reflections from the ground (see Appendix III for a more detailed discussion of ionosondes and ionograms).

The main continuous source of noise in the sounder receiver is galactic radio noise. An automatic gain control (AGC) loop maintains a constant receiver noise output, and therefore the AGC voltage is a measure of the relative galactic noise levels. Intermittent radio interference from ground-based transmitters is also a significant source of receiver noise[9]. Over most of the world, during the day, high-quality ionograms are usually recorded during 'quiet' ionospheric conditions. At night the ionogram quality tends to deteriorate because of man-made ground-based interference. In general, the strongest night-time interference is found over Europe and North America.

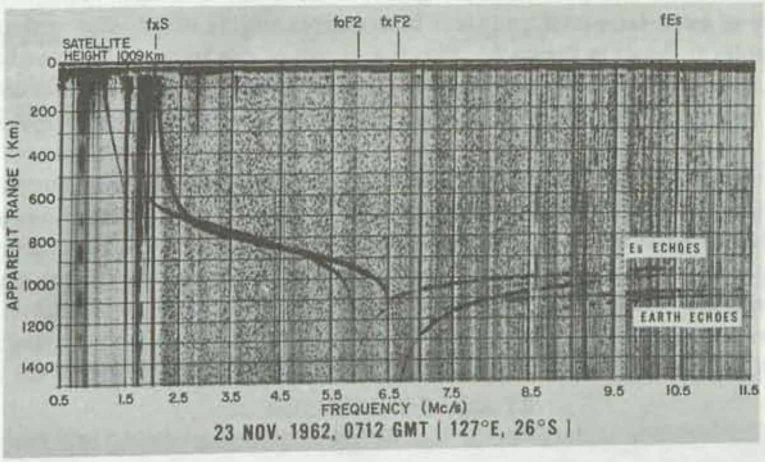

Fig. 3. Alouette I Topside Ionogram. The Vertical Lines at 0.5, 1.5..etc., Mc/s, are Frequency Markers.
The echoes shown here originate from regions vertically below the satellite, and the apparent height of the reflecting region is obtained by subtracting the apparent range from the satellite height.(The symbols at the top of the ionogram are discussed in Appendix II.)

1.3.3 The Very Low Frequency (VLF) Receiver

The VLF receiver in Alouette I has a pass band of 400 cps to 10 kc/s, and is connected to the 150 ft. sounder antenna. The receiver output is maintained constant by an AGC loop which may be monitored either by itself, or else when superimposed on the sounder receiver output. The output of the VLF receiver is normally displayed in the form of a *sonogram* : i.e., by a graph showing the frequency band of the received signals versus time. A great variety of VLF emissions have been recorded. Two examples of ionospheric noise bands at middle latitudes are shown in Figure 4.

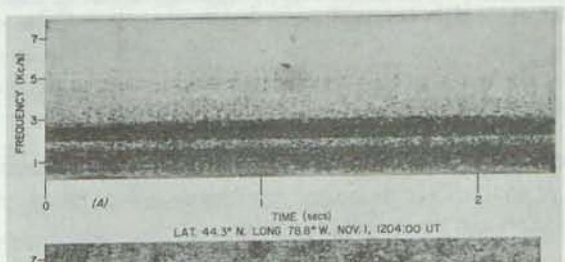

Fig. 4. Continuous and Sporadic VLF Noise Bands Recorded by Alouette I
(after Barrington and Belrose [10]).

1.3.4 Extra-Terrestrial Radio Noise Measurements

The AGC voltage in the sounder receiver can provide information on extra-terrestrial radio noise from about 1.5 to 12 Mc/s. (The low-frequency limit is determined by the sensitivity of the receiving system.) The strongest noise sources observed by Alouette I within this frequency range are sporadic noise emissions from the active sun and continuous noise emissions from the galaxy as a whole. The term 'cosmic noise' is frequently applied to the totality of extra-terrestrial emissions from sources outside of our solar system. A representative recording of cosmic noise is shown in Figure 5. This is a record of one frame of the sounder receiver AGC voltage, corresponding to one 12 second upward frequency sweep. Frequency (and time) advance from right to left. The vertical scale of this record covers about 50 db and the central portion of the range is approximately linear in db.

The sounder receiver is inactive during the transmission pulse, and the AGC circuit has an integration time of 20 ms to reduce possible contamination of the AGC voltage by echo pulses. This precaution is necessary because the vast majority of the cosmic-noise records are made with the sounder transmitter switched on, as in Figure 5. On some occasions, however, the transmitter was alternately commanded on and off for successive frames of the AGC voltage. Such records confirm that operation of the sounder transmitter during quiet ionospheric conditions does not significantly affect the AGC data. The smooth, slowly varying trace in Figure 5, labelled 'background noise level', is due to galactic noise. Other details of Figure 5 are discussed in section 2.5.

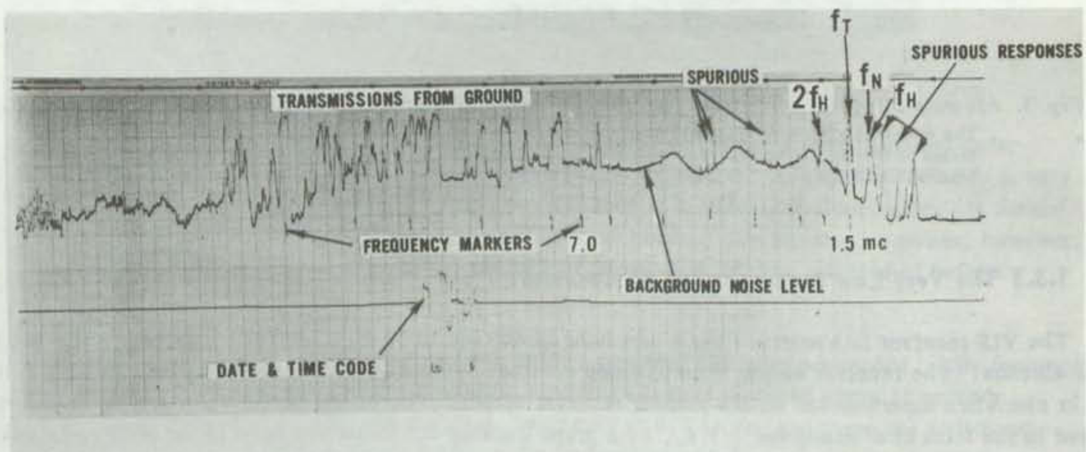

Fig. 5. Alouette I Cosmic-Noise Record, with Sounder Transmitter Switched On.
The vertical axis is the telemetered AGC voltage information from the sounder receiver; the horizontal axis is frequency, increasing from 0.5 Mc/s on the right to 12.0 Mc/s on the left (after Hartz (11)).

1.3.5 Energetic Particle Detectors

Six counters for energetic particles were provided by the National Research Council of Canada and both the experiment and the results of analysis are described elsewhere. (See, for example[12].) For convenience, the following table lists the counters and their characteristics.

TABLE 1

Particle Counter	Electrons	Protons	Alpha Particles
Anton 302 Geiger counter	> 4 MeV	> 40 MeV	
Anton 223 Geiger counter with collimator	> 40 keV	>500 keV	
Anton 223 Geiger counter with collimator and magnetic field	>250 keV	>500 keV	
RCA silicon junction particle detector with collimator		1-8 MeV in Channel 1	5-24 MeV in Channel 2
Geiger telescope		>100 MeV	
Plastic scintillator		100-700 MeV	400 MeV-2.8 GeV

2. SCIENTIFIC RESULTS

2.1 Introduction

The analysis and interpretation of Alouette I data has led to major advances in our knowledge of upper atmospheric ionization. Substantial progress has also been made in understanding the relevant physical processes. Nevertheless, there are several reasons why the present review should be regarded as preliminary and tentative. To begin with, analysis of the data is far from complete: indeed, it is highly probable that some of the significant phenomena that appear on the records have not yet been identified. Moreover, although most of the phenomena depend on solar activity, the precise nature of this solar dependence is highly speculative. During the three years of observation the sunspot activity was very low and there were relatively few ionospheric disturbances. (The first major ionospheric storm occurred about one year after launch, on 22 September, 1963.) This means that caution must be used in extrapolating the present results to other epochs of the solar cycle.

In the following discussion of the scientific results Section 2.2 is concerned with temporal and spatial variations in the electron number density of the topside ionosphere, and with the propagation of HF radio waves. As observed from above the ionosphere, the influence of the earth's magnetic field on both the background ionization and ionization irregularities is even more pronounced than in the bottomside ionosphere, and there are three latitude regions with distinctive properties: equatorial, mid-latitude, and high latitude. The measurements obtained by Alouette have enabled the characteristics of the quiet ionosphere and of various types of ionization irregularity to be examined, and new forms of irregularity to be identified. In addition, the guided propagation of HF waves over abnormally long distances has been studied, and properties of the guiding ionization irregularities have been inferred.

In Section 2.3, where observations of ionospheric resonances at VLF and HF are discussed, it is noted that several of these resonances, such as the lower-hybrid resonance (Sec. 2.3.3) and the 'resonance trace' (Sec. 2.3.2) have not been previously observed, either in laboratory or in space experiments. From the resonance observations various parameters of the upper atmosphere can be inferred. In particular, the data have been used to compute the magnitude of the earth's magnetic field and the ionic composition at the height of the satellite.

Observations of VLF and HF emissions, as distinct from ionospheric resonance phenomena, are treated in Sections 2.4 and 2.5. Although there is a wide variety of VLF emissions, detailed analysis has, so far, been concentrated on the relatively strong short fractional hop (SFH) whistlers, in order to obtain information on the mean ionic mass below the satellite. The HF emissions, unlike the VLF, are primarily extra-terrestrial in origin.

The flux density of galactic noise between 1.5 and 5 Mc/s has been measured over the celestial sphere, and a preliminary investigation of solar radio noise at these frequencies has been completed.

A number of miscellaneous investigations that do not fit into the preceding general subject categories are described briefly in Section 2.6.

2.2 Electron Number Density

The electron number density of the ionosphere, from 1000 km down to the height of the F-region maximum, may be computed from the reflection traces of the topside ionograms. (Wave propagation and reflection are discussed in Appendix III.) At these heights the relative concentration of negative ions or of multiply charged positive ions is probably very low, so that the electron number density may be taken to be equal to the number density of positive ions.

2.2.1 The Computation of N(h) Profiles

In the routine computation from topside ionograms of height profiles of electron number density, N(h), a number of assumptions are made. The routine analysis is usually restricted to ionograms on which the reflection traces can be identified unambiguously. It is then assumed that the ionosphere consists of horizontal layers, and that variations in the horizontal direction are smooth and regular. It is further assumed that total reflection of the sounder transmissions takes place in a region vertically below the satellite. Values for the dip angle of the earth's magnetic field are obtained from the Jensen and Cain (epoch 1960) 7th order Legendre expansion[12a]. A lamination method is used to compute N(h), and a linear change of plasma frequency with height is assumed within each lamination. The frequency interval at which the record is read, and consequently the laminar thickness, is adjusted in the course of reading each ionogram so that the significant features of the ionogram are adequately resolved. About 20 to 40 laminations are used for each ionogram. Most of the N(h) profiles are calculated from the extraordinary wave reflection trace, since the ordinary wave trace is not usually visible near the satellite.

Tabulated values of N(h) profiles computed for selected groups of ionograms have been published[78] and some details of the information available in these publications is included in Appendix II.

Ionization irregularities are observed very frequently in the topside ionosphere, even during magnetically quiet conditions. In these circumstances it may no longer be reasonable to assume that reflection occurs in a region vertically below the satellite; instead, it is necessary to give detailed consideration to the path (or paths) followed by the radio waves. On some ionograms, for example, instead of only one set of reflection traces, additional traces appear. Sometimes the multiple traces are caused by a very rapid variation of the electron number density at constant height (see Fig. 6); on other occasions they are due to guided propagation of the waves for long distances along the magnetic field direction (see Sec. 2.2-3.3).

At the present time the N(h) profiles obtained by the preceding lamination process are being examined critically[14] to check the accuracy of the routine computations, and to investigate the cause of occasional discrepancies between the height of the F2 maximum obtained from bottomside and topside data. The general procedure is to carry out the reverse computation, i.e., to assume that the N(h) profile is correct and then compute the vertical heights (or delay times) at selected frequencies. These vertical heights are then compared with the vertical heights recorded on the ionograms.

More specifically, ray paths for the ordinary and extraordinary waves at a specified frequency and direction of departure from the satellite are traced, by applying the Haselgrove equations[15] to N(h) profiles computed from topside ionograms. The present computations are restricted to a simple ionospheric model in which horizontal variations are neglected, i.e., a single ionogram is taken to represent the entire region traversed by the rays. To justify this simplification, individual ionograms are selected from sequences in which horizontal

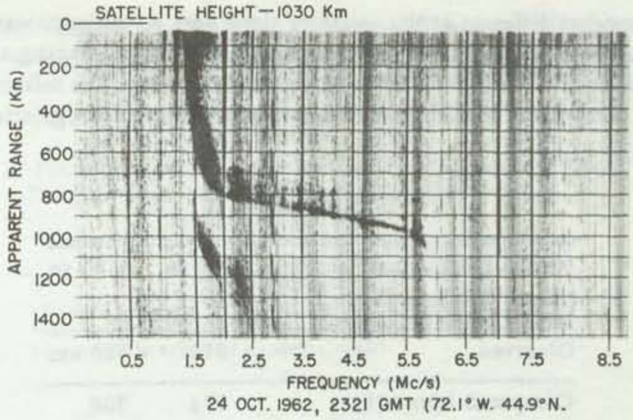

Fig. 6. Topside Ionogram Showing Oblique Reflections due to a Sharp Horizontal Gradient in the Electron Number Density (after Warren [13]).
The upper trace is due to reflections from one edge of a 'trough' in ionization density; the lower trace results from reflection inside the trough. The diffuseness of the traces is spread F (Sec. 2.2.3).

variations of the N(h) profiles are at a minimum. However, horizontal variations in magnetic field are taken into account. A fourth order Lagrange equation is used to interpolate electron densities in height, between the computed points on the N(h) profiles. Ray paths are traced until one of the following happens:

(i) The wave penetrates the F-layer maximum.
(ii) The wave travels above the height of the satellite.
(iii) The distance travelled by the wave exceeds a specified distance.

Preliminary results of the ray-tracing program confirm that a wave launched vertically does not deviate from the vertical by more than a few degrees, except for the last one or two kilometers before reflection. Detailed ray tracings have so far been done for only a few ionograms, selected as representative of ionograms for a 'smooth' ionosphere at equatorial, mid- and high latitudes. In these examples, there was negligible variation of electron density with latitude.

Results obtained for the extraordinary wave, using a mid-latitude topside profile are shown in Table 2.

TABLE 2

Virtual height of (X) wave reflections (km)	Frequency (Mc/s) 2.7	3.5	4.5	6.0	6.5
Observed	837	851	870	903	926
Computed from N(h)	832	842	864	900	927

There is excellent agreement between the observed and computed virtual heights. However, computations of the ray paths for an ordinary wave launched at -90° elevation angle, at these same frequencies, have produced discrepancies of greater than 50 km. This is due partly to the fact that the ordinary wave does not return to the satellite, but instead returns some kilometers to the north (in the northern hemisphere) of the satellite. When an appropriate initial elevation angle is chosen for the computation, to permit the wave to return to the satellite, the discrepancy between observed and computed virtual heights is greatly reduced.

The situation is somewhat different at the equator, since here an ordinary wave launched at -90° elevation angle can return to the satellite. Table 3 shows the results obtained by ray-tracing a vertical wave at 2.7 Mc/s, using an equatorial N(h) profile that contains a ledge (Fig. 2 of Ref. 16). The reflection traces were smooth and well defined, although the presence of the ledge is definite evidence of an irregularity in the horizontal distribution of ionization.

TABLE 3

Virtual height of reflection (km), at 2.7 Mc/s.	O Wave	X Wave
Observed	570	720 km
Computed from N(h)	574	708

Such results indicate that the accuracy of computation of N(h) profiles is comparable with the accuracy of ionogram scaling. The statistical sample checked to date, however, is very small and more analysis is required before firm conclusions can be reached.

2.2.2 Global Morphology

The orbital plane of Alouette I rotates 2° per day relative to the sun-earth line. Ionograms are recorded at intervals of about 120 km along the orbit and, except at polar latitudes, there is only a small change in local time during one ionogram. Accordingly, when there are only relatively slow temporal variations in the local ionosphere*, N(h) profiles computed from successive ionograms may be combined to provide continuous contours of electron density (or the equivalent plasma frequency)[17, 18, 18a]. Near 75°W longitude, in particular, the distribution of telemetry sites makes it possible to obtain continuous data over a wide range of latitudes.

Contours of plasma frequency are shown in Figures 7(a) to 7(d) as a function of latitude and height above the ground. The data are for the region near 75° W longitude and represent magnetically quiet conditions ($K_p \leq 3^{+}$), selected from a three month period centered on the vernal equinox, 8 February to 28 April, 1963. The following points should be noted:

(a) Figures 7(a) to 7(d) do *not* show the diurnal variation at vernal equinox. Data at any particular local time are available for a few successive days, but only once every three months. Accordingly, a rather complex form of seasonal variation is superimposed on the diurnal variation.

(b) Local times at the equator are given. Above about $\pm 50^{\circ}$ latitude, the differences from equatorial local times become significant, and this difference increases until at $\pm 80^{\circ}$ latitude it is about ± 6 hours.

(c) The small-scale structures shown in the night-time contours may not be significant. Night-time ionograms are relatively difficult to analyze, due to low signal-to-noise ratios and to an increased rate of occurrence of obliquely reflected echoes.

The quiet ionosphere appears to be divided naturally into three geomagnetic latitude regions: equatorial $\pm 20^{\circ}$, mid-latitude $\pm 20^{\circ}$ to $\pm 70^{\circ}$, and high latitude $\pm 70^{\circ}$ to $\pm 90^{\circ}$. During the day (Figs. 7(a),(b) the contours are generally smooth and uniform over the equatorial and mid-latitude regions, but large-scale irregularities occur in the high latitude region. The ionization builds up gradually as the day progresses, and a given plasma frequency contour rises higher in the summer than in the winter hemisphere. (The 'summer' hemisphere is the one with a higher ratio of sunlight to darkness.) The irregular contours in the high latitude region become less pronounced

* Temporal variations may be inferred, for example, from bottomside ionograms at appropriate fixed locations.

near noon, when the electron densities are high. In the equatorial region a marked 'dome' effect develops shortly after sunrise and the dome remains until about 20 hrs. LMT. (See Sec. 2.2.3.5 for details of this equatorial anomaly.)

Fig. 7. Plasma Frequency Variations during an Alouette 1 Pass(18)*.*
The local mean times at the geographic equator were:
(a) 0930, 1150, 1451
(b) 1615, 1858, 1956
(c) 2247, 0018, 0300
(d) 0420, 0615, 0651
(Dashed curves in the vicinity of the magnetic equator indicate the direction of the earth's magnetic field for an arbitrarily selected magnetic shell).

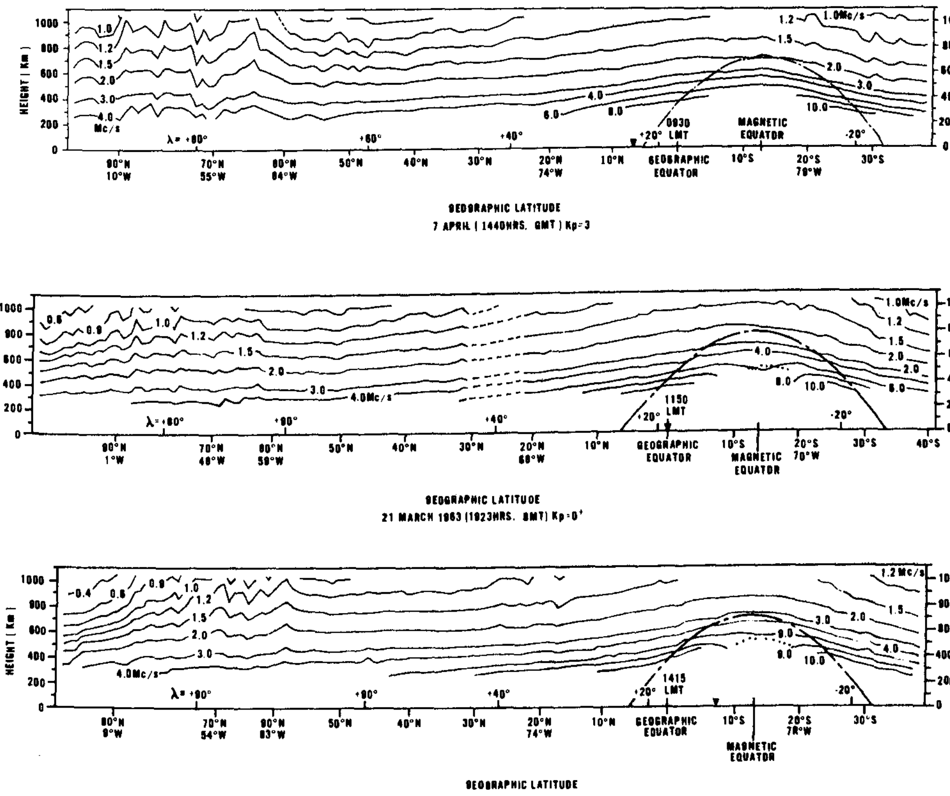

Fig. 7(a). The local mean times at the geographic equator were 0930, 1150, 1451.

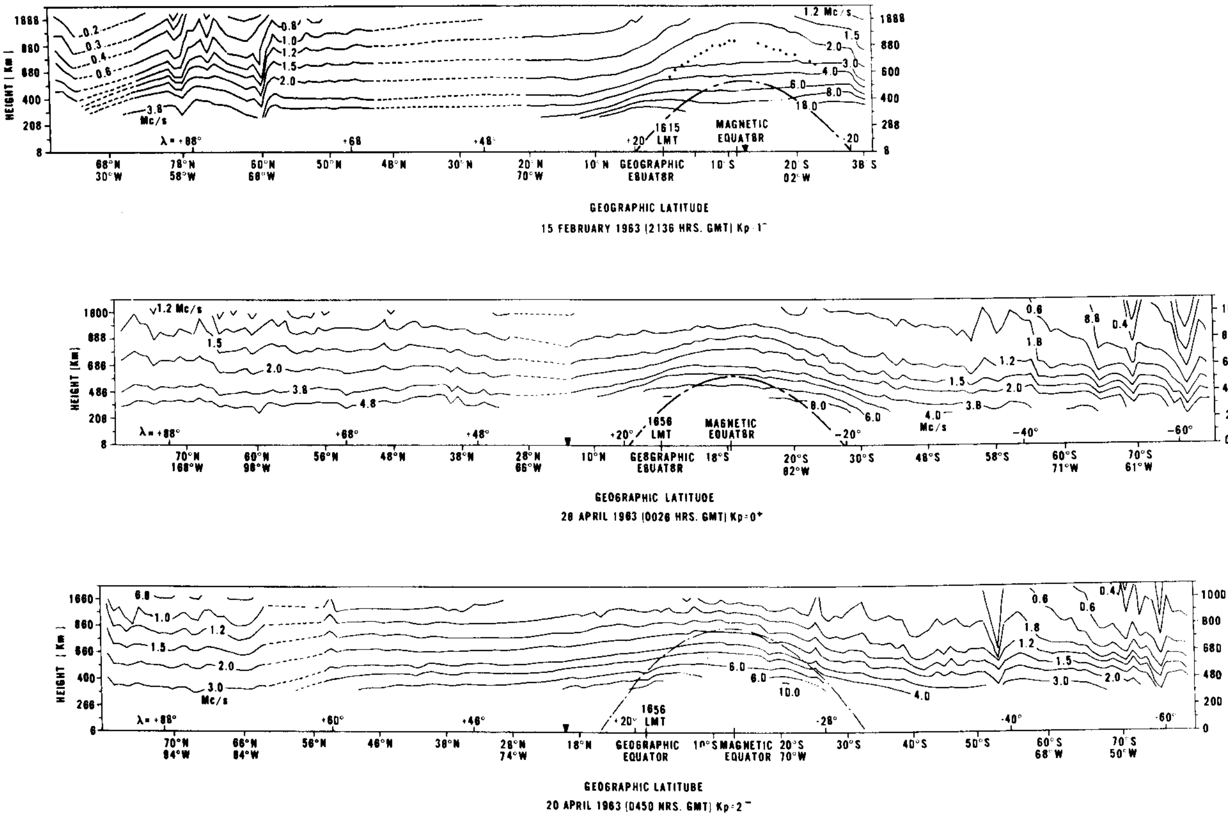

Fig. 7(b). 1615, 1858, 1956.

During the night (Figs. 7(c), 7(d)), the contours are irregular at all latitudes. The plasma frequency remains high between latitudes of 30° and 50° throughout the night in the winter hemisphere, but drops on either side of this zone. On the equatorial side the drop is gradual and contours are depressed, whereas the contours between 50° and 60° converge rather sharply. This region of converging contours is characteristic of the winter night-time ionosphere; a similar phenomenon occurs in the summer hemisphere but it is less well defined.

These phenomena probably arise from ionization movements. The ledge associated with the equatorial anomaly appears to have a consistent pattern of diurnal motion. Direct observation of the ledge becomes difficult near midnight, but the motions derived from early evening data suggest that the high electron density at about 50° latitude is a remnant of the daytime equatorial anomaly. After midnight, the region of high electron density remains centered on about 50°, but the ionization density tends to decrease continuously until sunrise. The converging contours between 50° and 60° are associated with a well-defined trough in the ionization over a wide range of heights. (See Sec. 2.2.3.4 for details.)

Magnetic disturbances have been relatively rare and mild since Alouette I was launched. Topside ionograms obtained during one major storm event, on 21-23 September, 1963, and during several smaller storms have been analyzed[18]. The data are as yet insufficient to permit a clear separation between storm-time variations, and diurnal or seasonal variations at times of moderate disturbances. During the one major storm event the electron number density at the peak of the F layer showed only minor fluctuations over the mid-latitude regions during the early milder phases of the storm. When K_p was larger than 5, however, the electron densities decreased over a wide range of latitudes. At high latitudes there was very little alteration in the F-layer electron densities, even when bottomside ionosondes were completely blacked out, until K_p reached a value of 9^-.

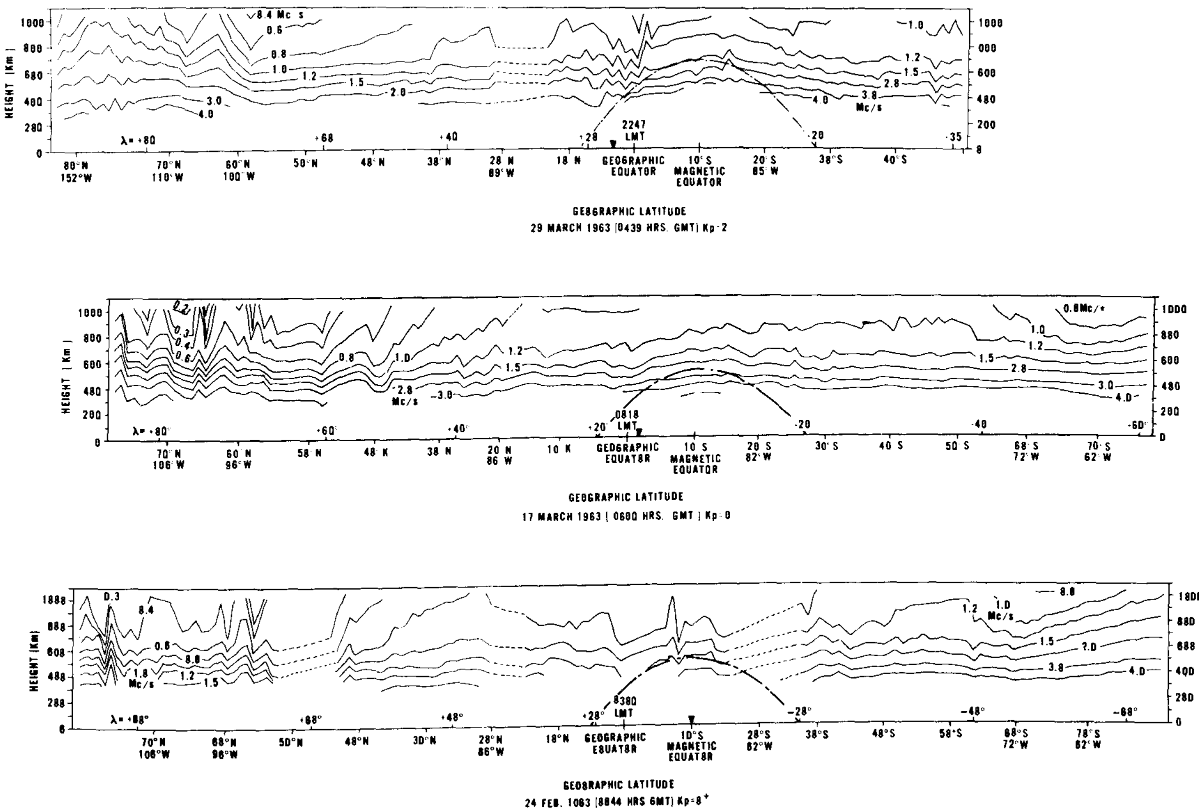

Fig. 7(c). 2247, 0018, 0300.

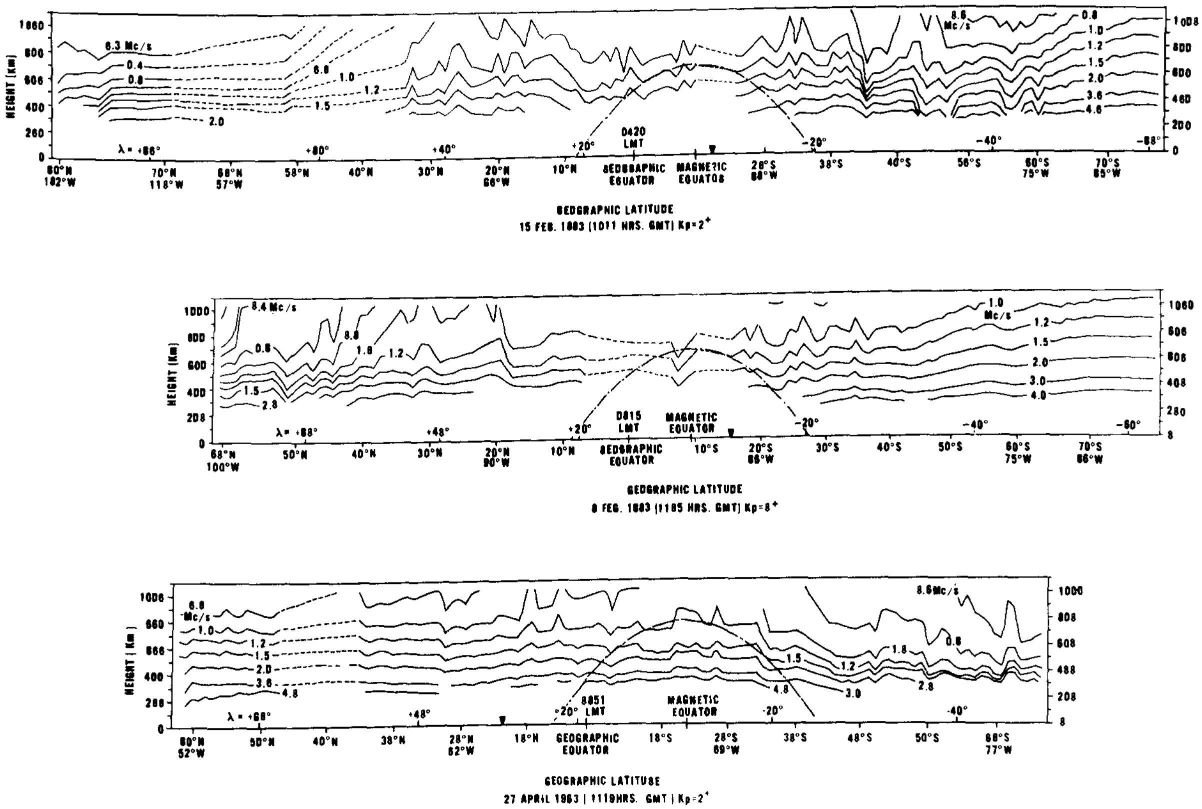

Fig. 7.(d). 0420, 0615, 0651.

2.2.3 Ionospheric Irregularities

2.2.3.1 Introduction

The identification and classification of ionospheric irregularities is highly dependent on the measurement techniques used. The present report is concerned primarily with irregularities found in the reflection traces of the Alouette I ionogram. In effect, this means that only irregularities in electron number density are considered herein, and that the horizontal resolution of the irregularities is limited by the 18 seconds required for one complete frequency sweep of the sounder. Moreover, because of the relatively rapid motion of the satellite, movements of the irregularities are neglected. (The Alouette VLF data can potentially provide better horizontal resolution of ionization irregularities at the height of the satellite; however, the data have not yet been analyzed for this purpose.) Usually, various types of irregularities are named according to their appearance on the ionograms and the assumed propagation geometry, such as frequency spread, height spread, clouds, field-aligned sheets, sporadic E, holes, troughs, ducts, ledges, etc.

The causes of these irregularities, and their diversity, are unknown. The influence of the earth's magnetic field is obvious. Most, if not all, of the irregularities are either field-aligned or form a continuous front along the field line direction, and the regions in which a particular type of irregularity occurs are located symmetrically with respect to the geomagnetic equator. The mechanism by which irregularities are formed, however, remains uncertain. (See, for example, a recent survey by Hines[19].) Therefore it is necessary to distinguish clearly between the observed reflection traces and deductions that may be drawn from the observations.

The following sub-sections consider electron density irregularities under several arbitrary classifications:

(a) *Spread F*

Spread F is identified by the relatively diffuse and broad appearance of the reflection traces, or of a part of the reflection trace.

Sometimes the only evidence of the presence of ionization irregularities is the occurrence of spread F, but more commonly there is additional evidence of irregularities on the ionograms.

(b) *Ionization 'sheets' or 'ducts'*

Reflection traces appear occasionally on the topside ionograms at exceptionally long ranges, and it can be deduced from such echoes that the HF sounder pulses were guided for long distances (north or south) along magnetic field-lines before they were reflected[20]. In principle, either an increase or decrease of ionization of appropriate configuration would guide HF waves. The actual guiding irregularities appear to have a thickness in the order of 1 km in a direction transverse to the magnetic shell. Their precise nature and configuration, (i.e., increase or decrease, sheets/or ducts, etc.) is still a matter of debate.

The sounder pulses may be launched within a guiding irregularity, or they may be refracted into one or more such irregularities. In the latter case, if the refraction occurs near the height of reflection for vertically incident waves, spread F appears on the resultant long-range reflection traces.

(c) *Anomalous Decreases in Ionization*

A sharp decrease in electron density, within a restricted latitude range, is frequently observed at high and polar latitudes. This decrease occurs simultaneously over a wide range of heights, and the so-called 'trough' is elongated in the magnetic east-west direction[21]. Very frequently, because of the latitudes at which troughs occur, the reflection traces in the vicinity of a trough are spread.

(d) *Anomalous Increases in Ionization*

Anomalous increases in electron density within a restricted height range are common both at high and equatorial latitudes. Most of these increases appear to fall into two classes: sporadic layers, and ledges.

Sporadic Layers- When the anomalous increase appears on the ionograms over a wide frequency range, but at a relatively constant height, the irregularities are called ' sporadic E' or ' sporadic F', depending on the specific heights (this designation is commonly used even at latitudes where sporadic E occurs regularly!). Sporadic layers are only infrequently visible on the Alouette I ionograms.

Ledges - When the anomalous increase is restricted to a narrow frequency and height range on each ionogram, it is usually called a ' ledge' . Ledges in the topside ionosphere occur quite regularly at equatorial latitudes, where they are found to lie along a magnetic shell. The thickness of this shell of ionization is of the order of tens of kilometers, rather than kilometers, and it is thought to be responsible for the well-known bottomside ' equatorial anomaly' . Topside spread F is associated with the occurrence of ledges, but only within a restricted range of local times(16).

2.2.3.2 Spread F

The occurrence of ionospheric irregularities in the F-region has been studied for many years, using ground-based equipment. The bulk of the data has been obtained by two methods, (a) the observation of spread F on the reflection traces of bottomside ionograms, and (b) the scintillation of HF and VHF radio waves that have passed through the E and F regions. It is difficult to obtain a direct comparison between spread F and scintillation data for the same volume of space, due to the quite different techniques used. Nevertheless, the observed correlations indicate that spread F and scintillations are different aspects of the same ionospheric phenomenon. Alouette data have not yet been used for extensive studies of scintillations; accordingly, the following discussion is limited to information obtained from ionograms.

Bottomside Spread F -- Bottomside spread F is on the whole a night-time phenomenon that occurs primarily at equatorial and high latitudes. Spread F is also observed occasionally at night in middle latitudes, or during the day at high latitudes, but such occurrences are usually associated with magnetic disturbances. At high latitudes the most frequent occurrence is between midnight and sunrise. Near the magnetic poles during the polar night (i.e., winter) spread F occurs 80 to 100 % of the time(22) . Both the frequency of occurrence and the intensity of high-latitude bottomside spread F increase with increasing magnetic disturbance.

At equatorial latitudes, the most frequent occurrence of bottomside spread F is between sunset and midnight. The occurrences are also more frequent during years of sunspot minimum than they are at sunspot maximum. On magnetically disturbed days, during active solar years, the occurrence of equatorial spread F is reduced (in direct contrast with high-latitude spread F). Analysis of radio scatter data indicates that the ionospheric irregularities associated with bottomside equatorial spread F are aligned along the geomagnetic field lines(23).

Topside Spread F -- Spread F, at least during 1963-1964, appears to be a permanent feature of the topside ionosphere(24,25) for magnetic dip angles greater than 72°. On occasion, high latitude spread F is observed up to the satellite height of 1000 km, and may well extend to greater heights. Although equatorial spread F is essentially a night-time phenomenon, during the last quarter of 1962 there was also a secondary maximum of occurrence three or four hours after sunrise(26).

Results of the analysis to date support the view that many of the irregularities responsible for the bottomside high-latitude spread F extend through the F-layer peak. The association between top- and bottomside equatorial spread F is, however, somewhat weaker; there is some evidence for a broad statistical association[26], but the detailed correlation is not particularly strong. This is not too surprising, since there are at least two distinct types of spread F. The first type seems to be due to scattering (direct or multiple) from field-aligned ionization irregularities; frequently these irregularities form sheets along the east-west direction. The second type arises from 'combination-mode' echoes[20]; the ionosonde radio pulse is refracted into a set of ionospheric irregularities and guided along the magnetic field line direction before undergoing reflection. The resultant echoes are spread in range.

At high latitudes, the magnetic field lines are nearly vertical. The irregularities that cause the scatter-type of spread F extend through the F-region peak and may well be observed at about the same geographic location on both top- and bottomside ionograms. At equatorial latitudes, the magnetic field lines are very nearly horizontal, and irregularities are frequently confined to a narrow range of heights. Equatorial spread F caused by topside guiding irregularities is frequently observed; there is no intrinsic reason why the geographic location of the topside sounder at such times should correspond closely with the locations at which bottomside spread F is observed. Of course, when spread F extends over a large region, the top- and bottomside regions may overlap.

High-latitude topside spread F is often so intense that separation into distinctive types becomes impossible. Accordingly, much of the high-latitude analysis does not subdivide the spread F occurrences.

During magnetically quiet conditions, high-latitude topside spread F occurs in both hemispheres whenever the magnetic dip is greater than about 72°; during disturbances the spread F extends to lower latitudes. The spread of the reflection traces tends to increase with increasing latitude, as shown in Figure 8. The height range over which spread F occurs reaches its maximum near the auroral zone maximum and here the field-aligned irregularities appear to occur in sheets that are frequently several hundred kilometers thick. The irregularities spread along the entire reflection trace, and in all probability, extend to well above 1000 km. During quiet conditions, at higher and lower latitudes, the maximum height of high-latitude spread F is gradually decreased until it is seen only in a narrow range of heights just above the F2 peak. During storms, details of the height range of spread F are still uncertain, because such details tend to be obscured by temporal variations during one frequency sweep.

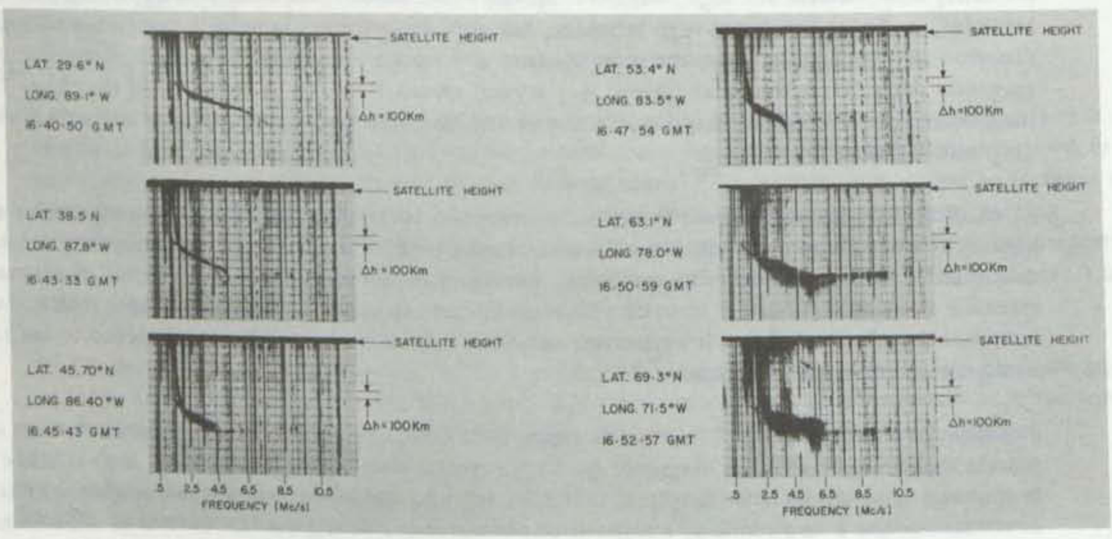

Fig. 8. Latitude Dependence of High-Latitude Spread F
(after Petrie [24]).

Since spread F appears to be a permanent feature of the high-latitude topside ionosphere, it is necessary to define a spread-F index in order to study the spread-F variations. In the only study that has been reported to date[24], the frequency range of the spread at 1000 km was measured from April 15 to August 15, 1963, when Kp ≤ 2, and ' intense spread F' was defined as spread in which the frequency range is ≥ 1.5 Mc/s. Results of this investigation are plotted in Figure 9. (No data were available for 2000-2200 hours local time and only limited data for 1400 hrs.) The intense spread F occurred within a latitude region, or belt, about 10° wide, and the location of this belt varied with local time. Near noon, intense spread F at 1000 km was confined to geomagnetic latitudes greater than about 75°. The belt of intense spread gradually shifted to lower latitudes until at midnight, it extended from about 65° to 75°; the belt then returned to higher latitudes. Near 0600 and 1800 LT, the intense spread F appeared confined to latitudes between 70° and 80°.

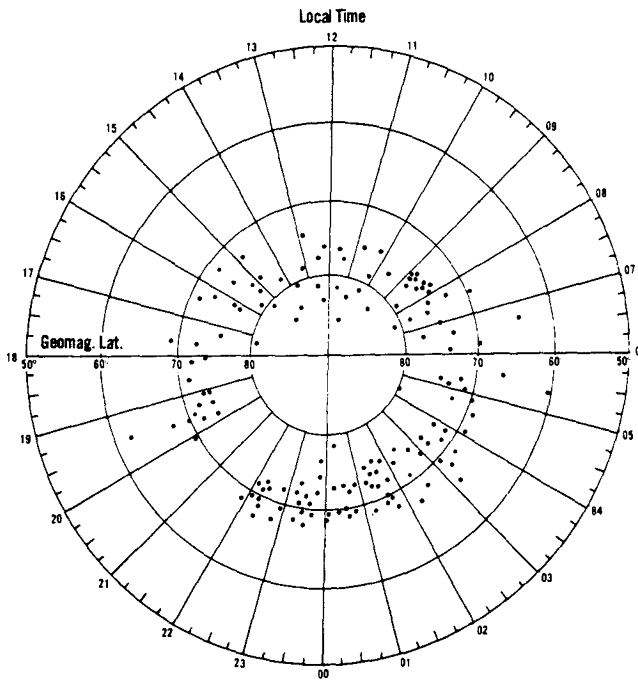

Fig. 9. The Distribution of Intense Topside Spread F at 1000 km Altitude, with respect to Local Time and Geomagnetic Latitude
(after Petrie [24]).

Topside equatorial spread F frequently occurs when long-range echoes are visible on the ionograms. It is also observed between 1900 and 2130 hours LT (Fig. 10), independently of the occurrence of long-range echoes. These spread F occurrences are thought to be connected with one stage in the diurnal development of the equatorial anomaly[16].

The preceding results, of course, apply only to the stated conditions, i.e., for sunspot minimum epoch and magnetically quiet days. (A preliminary investigation of the occurrence of high-latitude intense spread F at 2400 hrs LT, during magnetically disturbed conditions, indicates that the belt of intense spread shifts to lower latitudes during storms.) The oval-shaped distribution of intense high-latitude spread F obtained here for quiet conditions is very similar to the results reported for other geophysical parameters during generally disturbed conditions (e.g., high-density sporadic E[27], visual aurora[28], and bottomside spread F[29]. Other investigators, however, have found evidence for two spiral-like curves in magnetic and radio blackout data[30,31,32]. A more detailed study of the topside spread data was made from 2200 to 0300 LT, specifically to investigate this point, but no evidence of two spirals was found.

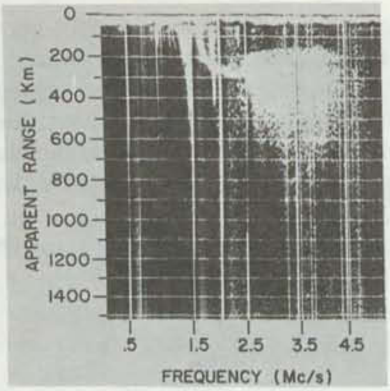

Fig. 10. Low-Latitude Topside Spread F Recorded at about 2000 LT, (64°W, 21°N)
(after Petrie [87]).

2.2.3.3 Guided Propagation of HF Waves

Echoes at abnormally long ranges are occasionally visible on Alouette I ionograms (Fig. 11). The possibility of guided propagation of HF waves had been forecast by earlier theoretical and experimental work (for example [33,34,35]). The Alouette long-range echoes provide conclusive evidence of guided propagation in the topside ionosphere, and have revealed some of the properties of the guiding irregularities[20]. In Figure 11 the labelled reflection traces on the left side of the ionograms can be explained consistently on the assumption that the irregularities are aligned along the earth's magnetic field. The guided waves travel north or south along the irregularities, undergo reflection, and then return along the same general path. Because of the long delay times, several pulses may be transmitted before the initial pulse is returned to the receiver. Accordingly, it is necessary to add an appropriate increment to the apparent ranges shown on the ionograms. Propagation paths deduced from Figure 11 (b) are shown in Figure 12.

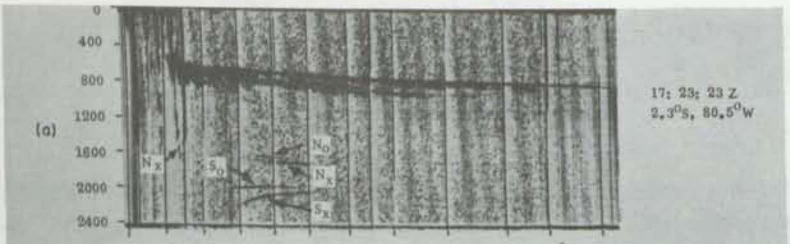

Fig. 11. Examples of Long-Range Guided Echoes on Alouette I Ionograms
(after Muldrew [20]).
(a) 1723:23, U.T.; 2.3°S, 80.5°W. (b) 1724:34, U.T.; 6.3°S, 80.1°W.
(The unlabelled, nearly vertical, reflection traces are due also to long-range guided echoes; these echoes have traversed the equator more than once.)

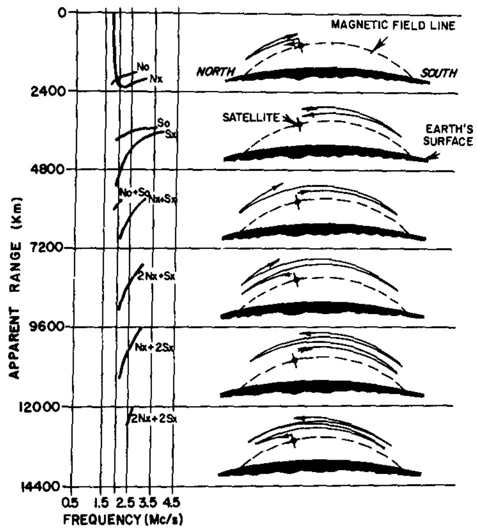

Fig. 12. Apparent Ranges and Modes of Propagation of the Labelled Traces, Fig. 11(b).
The symbols N_O, N_X, S_O, and S_X denote north-going or south-going, ordinary and extraordinary waves (after Muldrew [20]).

In the satellite the ionosonde pulses are radiated from an antenna system with a broad aperture and the mean radiated power is only 10 watts. The fact that well-defined echoes have been observed at apparent ranges in excess of 12,000 km, even though the sweep-frequency receiver is appreciably detuned by the time the long-range echo has returned, indicates that the wave energy is effectively confined to the vicinity of the guiding irregularities. (The National Bureau of Standards fixed-frequency topside sounder Explorer XX, launched on August 25, 1964, can achieve even longer ranges via the guided mode of propagation.)

Ray-tracing analysis of the sweep-frequency ionograms, using a model field-aligned sheet of ionization, has shown that the guided waves are reflected at about the height at which reflection would be expected at vertical incidence. The computed ray path of a guided wave is shown in Figure 13. The ray is confined to a constant-width track along the field line, even though the electron density increases by a factor of six along the path, and the distances between consecutive crossings of the ray and the field line become progressively smaller until reflection occurs. For this model computation the track-width of the ray was 2.3 km and the minimum increase of electron density required for efficient guidance varied from about 2 per cent at 1000 km to about 0.4 per cent at 600 km.

If it is assumed that the actual ionospheric irregularities are field-aligned sheets, some information on the characteristics of these sheets may be deduced from a detailed examination of the long-range echoes. The reflection traces on Figure 11, for example, are consistent for propagation along field-aligned sheets of *enhanced* ionization; a cross-section of the deduced sheets corresponding to the traces of Figure 11 (a) is shown in Figure 14. (Other workers[26] consider that the waves are guided in field-aligned ducts of reduced ionization; this issue is still unresolved.)

2.2.3.4 Ionization Troughs

The occasional occurrence of sharp decreases in the F-region critical frequencies at moderately high latitudes had previously been observed on bottomside ionograms[36], and these decreases were sometimes referred to as 'holes' in the ionosphere. The available ground stations were too far apart to permit a detailed study of the horizontal distribution of this phenomenon.

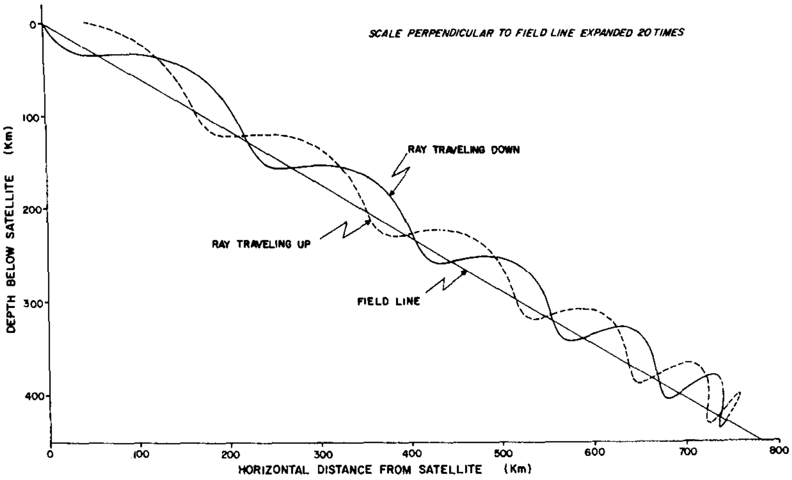

Fig. 13. Ray Path of an Extraordinary Wave along a Model Field-Aligned Sheet of Ionization (after Muldrew (20)).

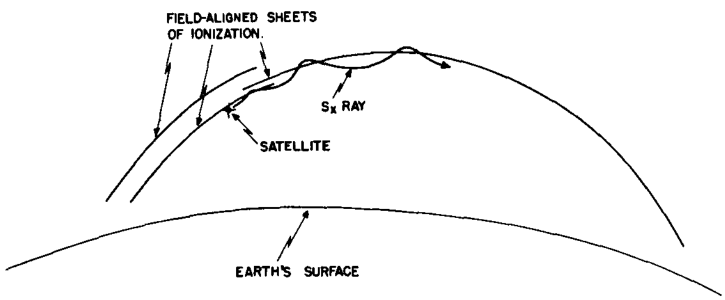

Fig. 14. Distribution of Incomplete Field-Aligned Sheets of Ionization Consistent with the Traces of Fig. 11(a)(after Muldrew (20)).

Topside ionograms at mid- and high-latitudes frequently reveal an abrupt drop in electron number density over the entire height range from 1000 km down to the F layer maximum. (See Fig. 6.) This abrupt drop is frequently seen at nearly the same latitude, on successive satellite orbits, and it can be readily shown that the region of low electron density is elongated in the east-west direction. Accordingly, such regions have been called *troughs*. The occurrence and intensity of high latitude troughs is being examined in detail; in the initial analysis[21] attention has been concentrated on the trough at the peak of the F layer and variations of the trough with height are neglected.

The critical frequencies (f_xF2) of the F2 layer recorded during one satellite pass over North America and the North Atlantic are shown in Figure 15. A minimum critical frequency of about 2.2 Mc/s occurs at 46° geographic latitude, and two or three additional troughs appear at higher latitudes. Detailed examination of many such satellite passes over North America shows that the minimum value of f_xF2 usually occurs in a well-defined trough, at geographic latitudes between 45° and 60° and that there are no persistent troughs at lower latitudes. Accordingly, the lowest latitude trough has been named the *main trough* and the others are called *high latitude troughs*. The main trough appears primarily to be a night-time phenomenon; during the last quarter of 1962 it was usually observed between 14 and 07 hours LT. Usually, when the main trough exists, its location can be determined to within one degree of latitude, by examining a sequence of ionograms.

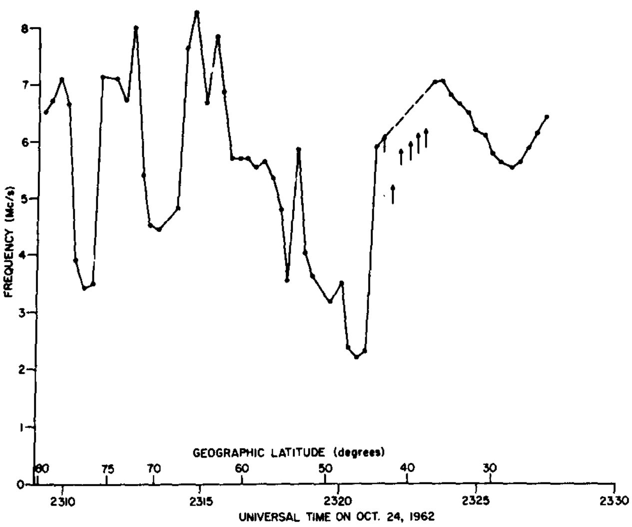

Fig. 15. Variation of the Penetration Frequency of the Extraordinary Wave, f_x F2, during an Alouette I Pass (after Muldrew (21)).

A summary plot of the latitude of the main trough, as a function of local time, from October, 1962, to March, 1963 is shown in Figure 16. A smooth variation of the latitude of the main trough with local time is evident from the plot. The unsmoothed data show large fluctuations about a mean latitude trend line. These fluctuations are statistically correlated with magnetic activity; when the magnetic activity increases there is a tendency for the main trough to appear at a lower latitude. From 14 to 20 hours local time the mean latitude of the main trough decreases from 72° to 60° geomagnetic latitude. The variation from 20 to 07 hours is more gradual, and the mean latitude of the main trough reaches a minimum of 56° about halfway in this interval.

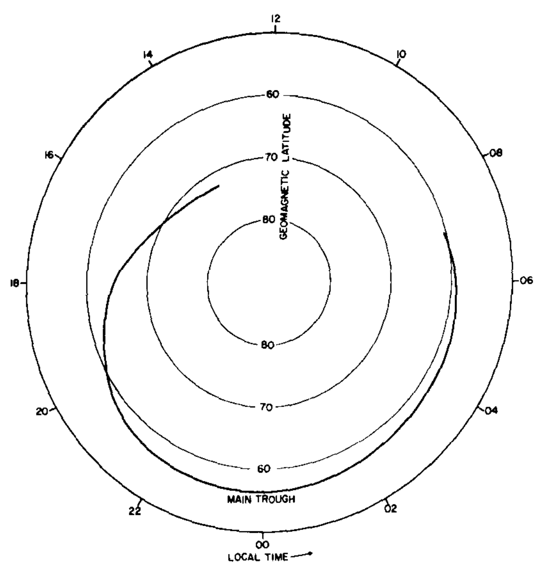

Fig. 16. Local-Time Variation of the Mean Geomagnetic Latitude of the Main Trough in f_xF2, from Oct. 1962, to March, 1963 (based on Muldrew (21)).

High-latitude troughs, such as those shown in Figure 15, are frequently observed. At these higher latitudes, the topside ionosphere is more disturbed, and the troughs are less well defined than the main trough. Accordingly, the analysis of high-latitude troughs is still in the exploratory stage.

2.2.3.5 The Equatorial Anomaly

It has been noted already that anomalous increases in ionization may appear either as sporadic layers or as ledges. Sporadic layers appear only very occasionally on topside ionograms, and detailed analysis has not been carried out; accordingly, they are not discussed in the present report. Ionization ledges, however, occur quite regularly at equatorial latitudes. These ledges have now been identified with the so-called *equatorial anomaly* (or geomagnetic anomaly) in the ionization below the F-region maximum.

The existence of an equatorial anomaly in electron number density has been firmly established from analysis of bottomside ionograms. If ionization movements are neglected, simple ionospheric theory predicts that the maximum electron density should occur near the geographic equator. Instead, at certain local times, there is a minimum in f_0F2 at the magnetic equator, and two well-defined maxima at 15^0-20^0 on each side.

A persistent feature of the equatorial topside ionosphere is the occurrence of cusps in the reflection traces on the individual ionograms. Figure 17 (a) shows a well-developed equatorial cusp and the corresponding electron density height profile is plotted in Figure 17 (b). The cusps correspond to an increase, or ledge, in the ionization, occurring in this case within the height range 750 to 900 km. During a single satellite transit across the equator, these ledges are all located along the same magnetic field line as shown in Figure 18. Examination of successive satellite transits has shown that the enhanced ionization indicated by the ledges lies along a magnetic shell(37), and that dome-like sheets of enhanced ionization are formed in a regular diurnal pattern.

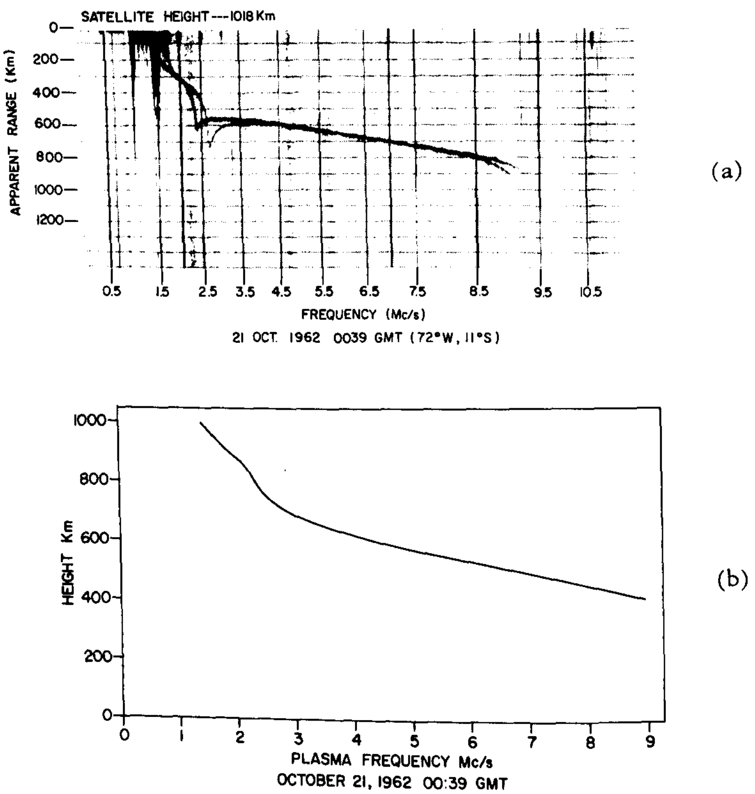

Fig. 17. The Topside Equatorial Anomaly (After Lockwood and Nelms (37)).
(a) Ionogram recorded at 72^oW, 11^oS, 0039 U.T., 2 October, 1962.
(b) Electron Number Density versus height profile computed from Fig. 17(a).

A dome of enhanced ionization begins to form at about sunrise. The dome-like shape becomes more pronounced and the height of each contour of constant electron density rises until mid-afternoon. Ledges begin to form during the afternoon and are observed until about 2200 hours; the height of the ledge increases with increasing time. As the ledge moves up to higher field lines, the ionization beneath the ledge is redistributed, giving rise to flattened or depressed contours beneath the ledge, high heights for the F-layer peak at the magnetic equator, and large concentrations of ionization between 15^{0} and 20^{0} on either side of the equator. During magnetically quiet conditions the ionization ledge may be observed as early as 1100 hours; during disturbed conditions, it may not appear until 1730 hours.

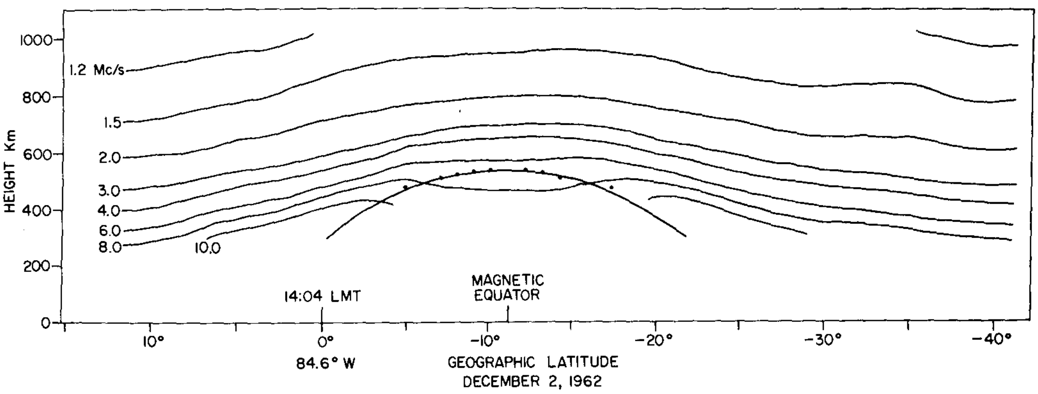

Fig. 18. Contours of Constant Electron-Number Density at 1404 L.M.T., on a Magnetically Quiet Day. The observed locations of ionization ledges (similar to the one shown in Fig. 17(a)) are marked by the solid dots; the curved line through these dots is a magnetic field line (after Lockwood and Nelms (37)).

2.3 Ionospheric Resonances

2.3.1 Introduction

The HF and VLF receivers in Alouette I have obtained information concerning a number of modes of oscillation (or resonances) of the ionospheric plasma. The HF resonances are excited by the sounder transmissions, and appear as elongated echoes, i.e., as vertical 'spikes' on the ionograms (Figs. 19). The occurrence of VLF resonances is deduced from the frequency dispersion of certain discrete VLF emissions, and from the cutoff frequencies of VLF noise bands. The observed HF and VHF resonant frequencies appear to be in excellent agreement with the theoretical resonant frequencies of a slowly varying, anisotropic, loss-free cold plasma (see Appendix III for details). The preceding sections, however, have made it clear that the ionosphere contains many irregularities: it may well be that there are significant discrepancies between Alouette I observations[38-43] of the relative amplitudes and durations of a given resonance and its harmonics, and computations based on relatively simple theoretical models[44-48].

One of the plasma resonances depends only on the total ionization. Accordingly, this resonance is considered to be a basic characteristic of a plasma, and it is called the *plasma frequency* *. All of the other ionospheric plasma resonances vary with the strength of the local magnetic field, and have been given names

* This resonance, in effect, is the *electron* plasma frequency, because the motions of the ions are negligible—cf the motions of free electrons. (The parameter 'proton plasma frequency' is also used. This parameter is simply the (electron) plasma frequency divided by the ratio of proton mass to electron mass; resonances have *not* been predicted or observed at the proton plasma frequency.)

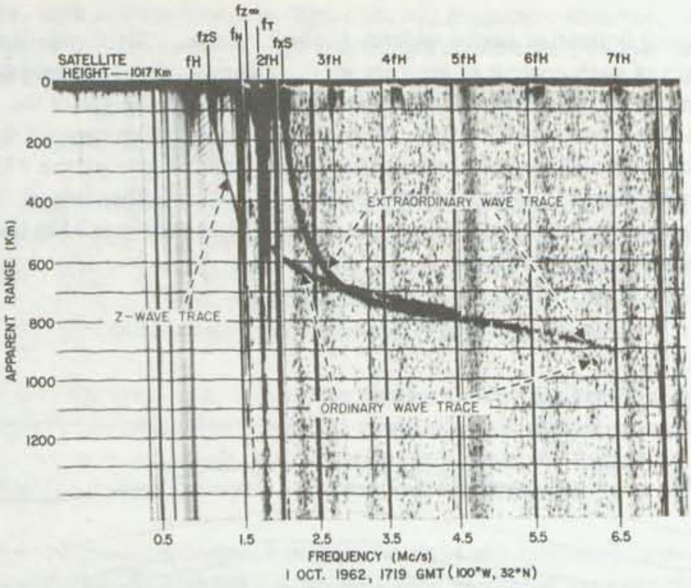

Fig. 19(a). Topside Mid-Latitude Ionogram Showing Ionospheric Resonances at the height of the Satellite.

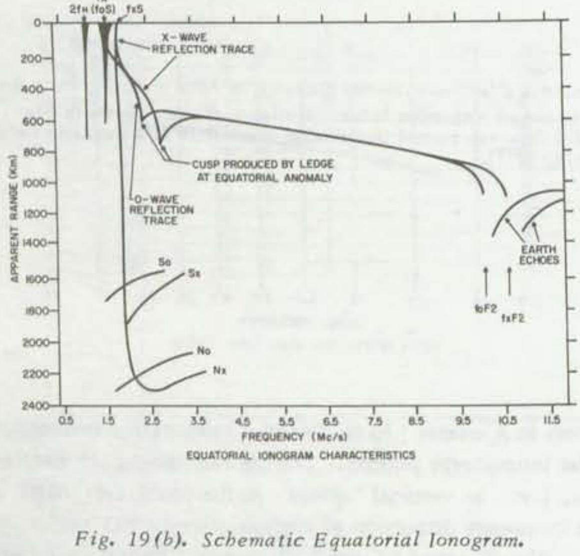

Fig. 19(b). Schematic Equatorial Ionogram.

that indicate the assumed mode of oscillation of the plasma.

The HF resonances shown in Figure 19 (a) are a bit obscure, especially towards the low-frequency end of the ionogram. Details of these resonances are more readily determined by examining sequences of ionograms, and the results of such studies are summarized in the schematic ionograms of Figures 19 (b), 19 (c) and 19 (d).

Figure 19 (b) is an equatorial ionogram. The electron gyrofrequency resonance is not visible, possibly because of reduced receiver sensitivity below 1.0 Mc/s. A strong $2f_H$ resonance spike appears at about 1.3 Mc/s and a plasma frequency spike f_N at 1.6 Mc/s. The upper hybrid resonance and higher harmonics of the gyrofrequency are not visible.

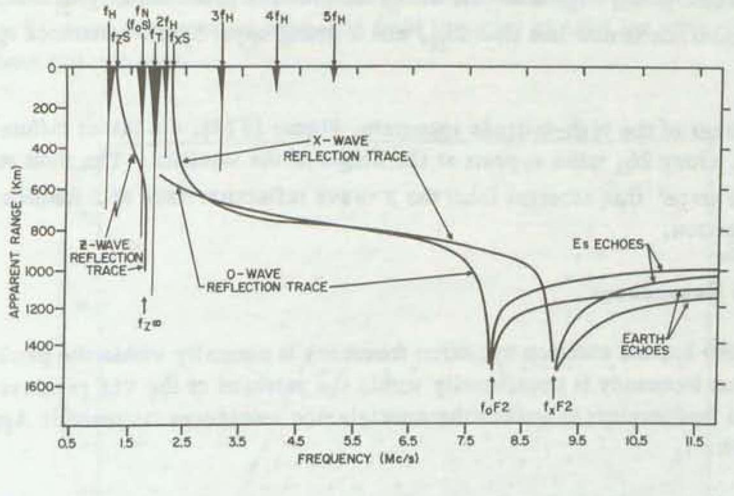

Fig. 19 (c). Schematic Mid-Latitude Ionogram.

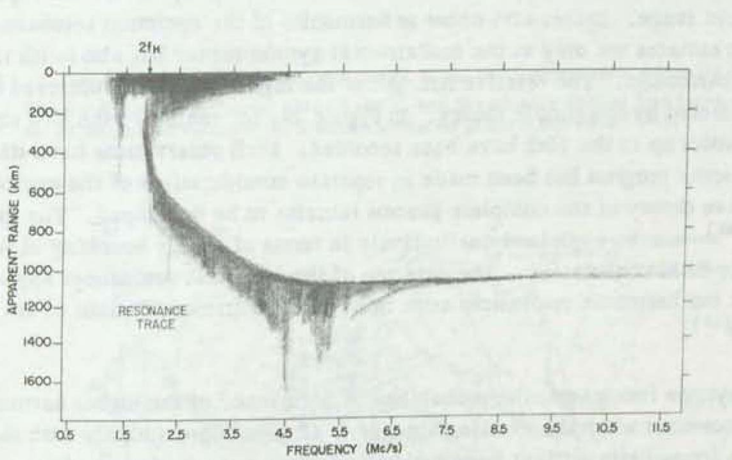

Fig. 19 (d). Schematic High-Latitude Ionogram.

The following symbols are used to identify the resonances and reflection traces.

nf_H, $n = 1,2,3..$ electron gyrofrequency and harmonics:

f_N . . . . plasma frequency.

f_T . . . . upper-hybrid resonance.

$f_oS \equiv f$ . . ordinary-wave frequency at the satellite.

f_xS . . . . extraordinary-wave frequency at the satellite (upper branch).

f_ZS . . . . extraordinary-wave frequency at the satellite (lower branch; also known as "Z trace").

f_{Z_∞} . . . . frequency of infinite retardation of the Z wave.

f_oF2 . . . ordinary-wave penetration frequency.

f_xF2 . . . extraordinary-wave penetration frequency.

The mid-latitude ionogram, Figure 19 (c), shows the electron gyrofrequency f_H and a number of harmonics. The plasma frequency resonance is now less than $2f_H$, and a strong upper hybrid resonance spike f_T appears in between f_N and $2f_H$.

The reflection traces of the high-latitude ionogram, Figure 19 (d), are rather diffuse, and spread F is visible at all heights. A strong $2f_H$ spike appears at the height of the satellite. The most striking feature, however, is a 'resonance trace' that emerges from the X-wave reflection trace at a frequency corresponding to $2f_H$ at the height of reflection.

2.3.2 Cyclotron Resonances

At a height of 1000 km the electron cyclotron frequency is normally within the passband of the HF receiver, while the proton cyclotron frequency is occasionally within the passband of the VLF receiver. The helium and atomic oxygen cyclotron frequencies (as well as the multiple-ion resonances discussed in Appendix III) are too low for observation by Alouette I.

2.3.2.1 Electron Cyclotron Resonances

The electron cyclotron resonance appears as a constant frequency 'spike' on the topside ionograms, starting from zero apparent range. Spikes also occur at harmonics of the cyclotron resonance. It is well known that a spiralling electron radiates not only at the fundamental gyrofrequency but also (with rapidly diminishing amplitude) at all of the harmonics. The relative strength of the higher harmonics observed by Alouette I, however, is much greater than predicted by the simple theory. In Figure 19, for example, the first six harmonics are visible; on some occasions harmonics up to the 15th have been recorded. Such observations have stimulated a number of theoretical studies, and some progress has been made in separate considerations of the excitation and loss processes. However, a comprehensive theory of the complete process remains to be developed. The generation of the electron cyclotron harmonics[38,44] can be explained qualitatively in terms of energy bunching of the gyrating electrons in phase with the electric field of the wave. The duration of the harmonic resonances appears to be consistent with the assumption that the harmonic resonances arise from electrostatic oscillations of the electrons across the magnetic field direction[45].

On Alouette I daytime ionograms, the probability of occurrence of the higher harmonics of the electron cyclotron frequency is increased when the exciting antenna is aligned approximately with the earth's magnetic field[42]. (At night the ionospheric critical frequencies are lower, and interference from ground-based transmitters severely restricts the observation of the higher harmonics.) The topside sounder antenna system consists of two crossed dipoles, 75 ft and 150 ft in length, permanently connected through a 4.7 Mc/s crossover network. The higher-frequency cyclotron harmonics, i.e., those above about 5 Mc/s, are observed only when the angle between the short antenna and the magnetic field is within a range of $\pm 15^{\circ}$. This point is illustrated in Figure 20, which shows data taken when the spin vector of the satellite was perpendicular to the magnetic field. The slope of the dashed line joining one set of harmonics arises from the fact that there is an appreciable rotation of the satellite during the 12 second frequency sweep of the sounder. It is evident from the figure that harmonics above the 10th were observed only when the short antenna was approximately aligned with the magnetic field.

The frequencies of the electron cyclotron harmonics can be determined with an accuracy of about 0.02 Mc/s. In all cases examined the frequencies of the members of the harmonic series are integral multiples of the cyclotron frequency, to within the experimental error[46]. This result apparently differs from current interpretations of laboratory experiments[47], based on solutions of Bernstein's dispersion relation[48] for electrostatic waves. There appear to be significant differences between the satellite observations and laboratory experiments, and it has been suggested that the results could be reconciled by taking into account the large difference in the ratio of antenna length to electron gyro radius in the two cases.

Regardless of the precise reasons for the above discrepancy, it has been established that the observed resonances are accurate multiples of the electron cyclotron frequency. These spikes, therefore, provide a convenient and accurate method of measuring the strength of the earth's magnetic field at the height of the satellite(49). Figure 21 shows the observed magnetic field intensity at 1000 km over North America, measured to an accuracy of about one per cent.

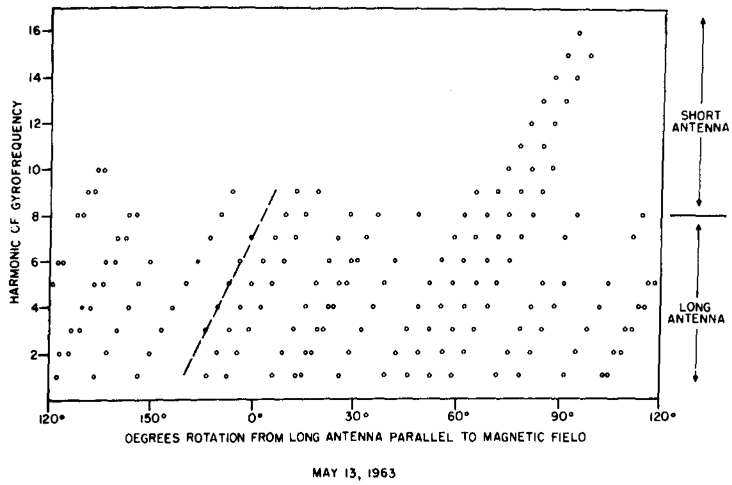

Fig. 20. Electron Cyclotron Harmonics Recorded on 18 Consecutive Alouette I Ionograms.
The 9th harmonic occurs at about 5 Mc/s, and the sloping dashed line joins one set of harmonics recorded on a single ionogram (after Lockwood (42)).

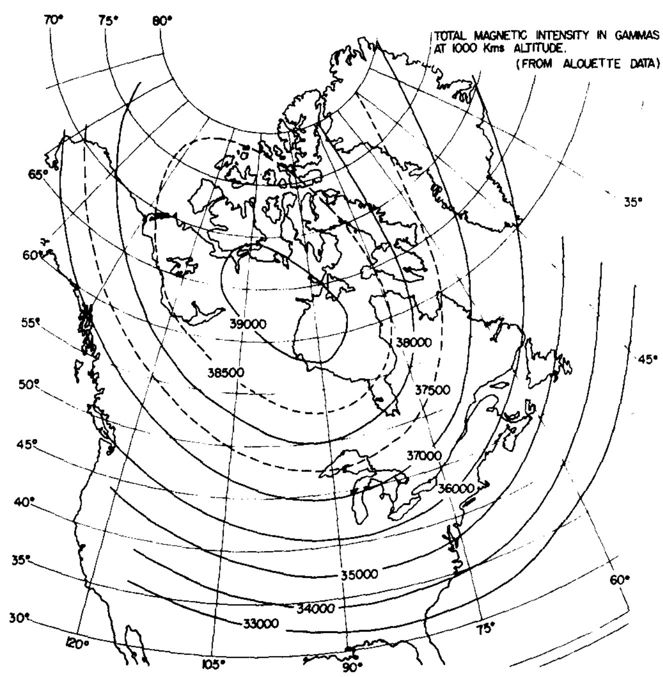

Fig. 21. Magnetic Field Strength at 1000 km over North America, Computed from Electron Cyclotron Harmonic Resonances Recorded by Alouette I
(after Hagg (2)).

2.3.2.2 Proton Whistlers, and the Proton Cyclotron Resonance

In both the Alouette I and the Injun III satellites, slightly dispersed lightning impulses (often called 'short fractional-hop' (SFH) whistlers, as in Sec. 2.4) are occasionally followed at lower frequencies by a slowly rising tone. In the example shown in Figure 22 the SFH whistlers have a small, but normal, frequency dispersion. Two of the SFH whistlers are followed by rising tones that start at about 400 cps, and rise asymptotically towards a frequency of about 500 cps. This asymptotic frequency is, to within the experimental accuracy, the proton cyclotron frequency in the vicinity of the satellite. The duration of these rising tones, or 'proton whistlers', is highly variable and may exceed 5 seconds. A theory for the production of ion cyclotron whistlers has been developed by Gurnett et al (50) (see Appendix III, Sec. 1.4 for more details). The proton whistlers are evidently generated by SFH whistlers, and the crossover frequency at which this conversion occurs depends on the number density of protons (51).

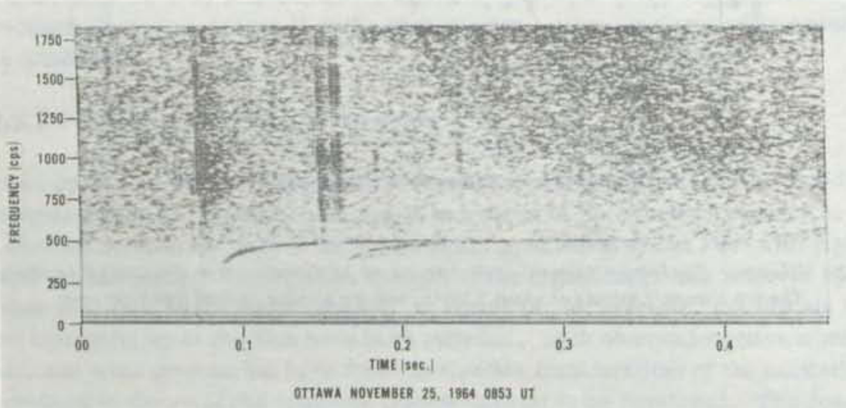

Fig. 22. Alouette I Spectrogram of Two Short Fractional-Hop Whistlers that are Followed by a Wave, the 'Proton Whistler', Whose Frequency Rises Asymptotically toward the Proton Cyclotron Frequency.

The long-enduring 'tail' of a proton whistler has a frequency dispersion that depends on the difference between the whistler frequency and the proton gyrofrequency near the satellite, and on the number density of protons. From measurements of the crossover frequency and the frequency dispersion of the proton whistler tail, Gurnett et al(52) have computed electron densities at the satellite. The dispersion data may also be used to obtain the proton gyrofrequency (and hence magnetic field strength) at the satellite. Plots of the square root of the difference between a constant oscillator frequency $\Omega_{osc.}$ and the frequency of a proton whistler are shown in Figure 23. The theory predicts that such plots will be linear when the oscillator frequency is set at the proton gyrofrequency. Evidently, the proton gyrofrequency is close to 498 cps. This technique permits the measurement of magnetic field strength to an accuracy of about 0.2 per cent, and of proton number density to about 20 per cent (53).

The duration of proton whistlers observed at 1000 km is normally determined by cyclotron damping, and in this case the proton temperature can be computed. Preliminary results indicate that the computation depends critically on the assumed amount of cyclotron absorption. For example, a proton whistler with a duration of 3.34 seconds yielded proton temperatures in the range 715° - 815°K for an assumed absorption of 30 db, and temperatures of 855° - 985°K for an assumed absorption of 40 db (54) (in Alouette I there is no provision for measuring the amplitude of the VLF signals).

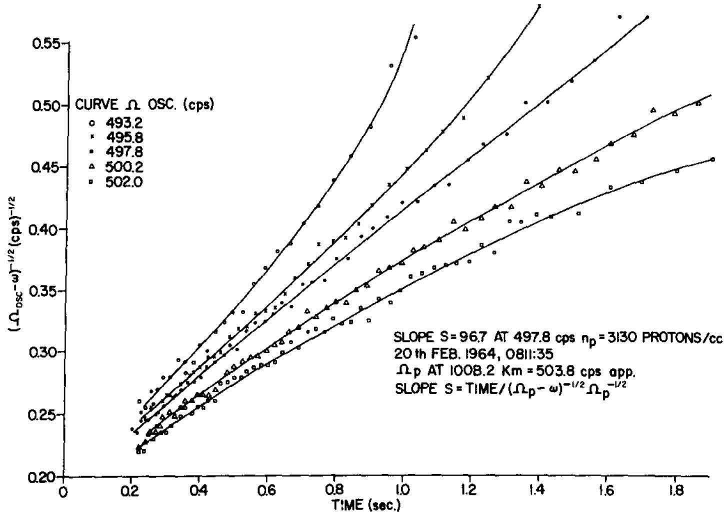

Fig. 23. Curves Showing the Square Root of the Period Plotted against Time for a Waveform that is the Difference in Frequency between a Pre-set Oscillator Frequency and a Proton Whistler.
A straight line indicates that the oscillator frequency was equal to the proton gyrofrequency at the satellite when the proton whistler was recorded, and the slope of this line yields the number density of protons (after Brice [53]).

2.3.3 Other HF Resonances

In addition to the electron cyclotron resonances, the schematic ionograms in Figures 19 (b) to (d) show HF resonance spikes at the plasma frequency f_N, the upper hybrid resonance f_T, and a resonance trace at a frequency corresponding to $2f_H$ at the height of reflection. (Occasionally a spike is also observed at $2f_T$. This may be a harmonic of the f_T resonance, or it could be an instrumental effect. The evidence on this point is not yet conclusive.)

The functional dependence of the f_N spikes on ionospheric parameters was readily established in the initial analysis of Alouette I ionograms [38]. The f_N spike occurs at the plasma frequency, corresponding to the frequency of reflection of the ordinary wave at the satellite.

At first the f_T spike was incorrectly identified. During earlier rocket tests of a fixed-frequency sounder (Knecht et al [34]), spike-like signals were received at the cut-off frequencies of the ordinary and extraordinary waves. Accordingly, it was anticipated that similar phenomena would appear on the topside ionograms. The f_T spike occurs at a somewhat lower frequency than the cutoff of the upper branch of the extraordinary wave, but it was postulated that such a displacement could be caused by a perturbation in the ionosphere caused by the satellite spacecraft [55].

From a detailed analysis of a long sequence of Alouette I ionograms, Calvert and Goe[56] found that the f_T spike occurs at the upper hybrid resonance, and not at the extraordinary wave cutoff. There is no discrepancy (to within the experimental accuracy) between the observed and computed resonance frequencies; evidently the perturbation of the ionosphere by the satellite spacecraft has a negligible effect on this resonance frequency.

Although the f_N and f_T spikes are now believed to be correctly identified, a number of problems remain. In the rocket experiment[34] spikes were observed at cutoff frequencies of the two wave modes, but not at the upper hybrid resonance. The sweep-frequency topside ionograms show spikes at the cutoff frequency of the ordinary wave, and at the upper hybrid resonance, but not at the extraordinary wave cutoffs.* A comprehensive theoretical solution consistent with all of these HF observations has not yet been developed. Several authors have discussed this problem in terms of electrostatic waves, which result from an approximate solution of Maxwell's equations, and Boltzmann's equation governing this situation, and substantial progress has been made. In a recent paper Fejer and Calvert[45] try to provide a unified explanation of all the ionospheric resonance phenomena observed by the Alouette I topside sounder. (The resonance trace observations, discussed later in this section, had not been reported at the time of the Fejer and Calvert analysis.) Their analysis considers the nature of the resonance oscillations, their dispersion properties, and their duration. (Excitation mechanisms are not discussed.) The authors develop an electrostatic approximation such that the wave electric fields are in the direction of the wave normal, and wave magnetic fields are neglected. These electrostatic waves travel at velocities comparable with the velocity of the satellite. The authors conclude that f_N and f_H correspond to electrostatic oscillations along the earth's magnetic field, whereas f_T and the harmonics of f_H correspond to electrostatic oscillations across the field. At intermediate angles the electrostatic waves have group velocities comparable with the thermal velocity of electrons, the wave energy is carried away more rapidly, and the duration of any plasma oscillations is greatly reduced. These results for f_N and f_T are consistent with the Alouette I observations. In addition, computed relative strengths of the f_N, f_T and gyro-resonances are in approximate agreement with the observations.

This analysis, however, does not account for the spikes observed in the rocket experiment. Moreover, the conclusion that the fundamental electron gyrofrequency f_H arises from an electrostatic oscillation along the magnetic field direction is somewhat surprising. This result may be inherent in the initial assumption that wave magnetic fields can be neglected. Other authors, e.g., Smith and Brice[57], find that f_H is an electromagnetic rather than an electrostatic resonance.

The preceding discussion has been concerned with HF plasma resonances in the vicinity of the sounder transmitter. The resonance trace, however, appears at the height of reflection of the upper branch of the extraordinary wave, as shown in Figures 19 (d) and 24.

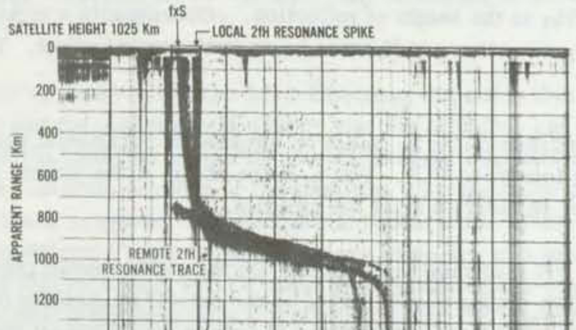

Fig. 24. Topside Ionogram Showing the Remote $2f_H$ Resonance Trace.

The resonance trace, unlike the electro gyrofrequency spikes, occurs primarily at high latitudes, at times when there is moderate to severe spread F on the topside ionograms, and the spread extends to the height of the satellite[43, 43(a)]. Between May 2-11, 1963, resonance traces were found on one-quarter of the 4000 ionograms recorded at the Resolute Bay, N.W.T., and College, Alaska, telemetry stations. A parallel examination of bottomside ionograms, recorded at Baker Lake, Resolute Bay and Thule, did not reveal any phenomena that could be associated with the topside resonance traces. The highest frequency of the cyclotron trace evidently

* Early results from the fixed-frequency sounder experiment in the Explorer XX satellite are similar to Alouette I results.

occurs at its smallest apparent range. (Spread F tends to mask details at the junction of the cyclotron trace with the X-trace.) A significant characteristic of the resonance trace is that the upper frequency limit is equal to $2f_H$, provided that the electron gyrofrequency f_H is measured at the height of reflection of the X-trace. In Figure 25 measured values of the highest frequency of the cyclotron trace are plotted against values of $2f_H$, computed using the Jensen and Cain (1962) spherical harmonic coefficients, at the height of the X-trace. The error bars indicate the uncertainty in the computed reflection heights.

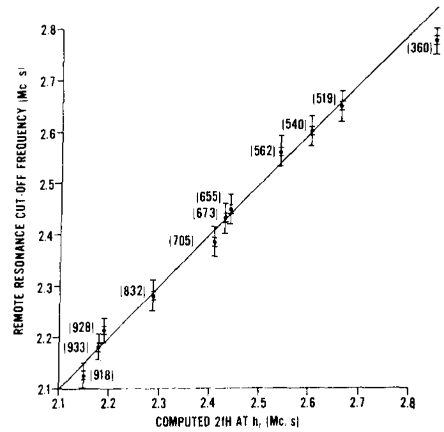

Fig. 25. Comparison of the Upper Frequency Limit of the Resonance Trace with Computed Values of $2f_H$.

The bracketed numbers give the height of the X-reflection trace at its intersection with the resonance trace; this is the height used in the computation of $2f_H$ (after Hagg and Muldrew[43]).

A theoretical explanation for the occurrence of the resonance trace is in preparation[58]. A necessary condition for occurrence is that the radio energy that produces the resonance trace is confined along a field-aligned ionospheric waveguide. The waveguide produces a gradient in the electric field of the propagating wave, in a direction perpendicular to the magnetic field, and also maintains sufficiently high signal levels to permit observation of the resonance trace by the Alouette I receiver. The theory assumes that the wave paths are as illustrated in Figure 26. A radio pulse of frequency f is transmitted in the extraordinary mode from the satellite and propagates downward along the field line direction through the height A, where $f = 2f_H$. A fraction of the pulse energy is absorbed by the free electrons in a small range of heights around A. The absorbed energy is not significantly dissipated by collisions. Instead, at a time τ after the initial pulse passed through A, an extraordinary wave pulse is generated at A. The delay time τ depends on the index of refraction of the wave, and on the plasma and gyrofrequencies at height A. The analysis shows that a delayed pulse is generated at A only if the initial pulse is propagating in the direction of increasing magnetic field (here, downward), and that the delayed pulse can only propagate in the direction of decreasing field (upward). Resonance traces computed from this model are consistent with the observations.

The intersections of the resonance trace with the extraordinary wave reflection trace have been used to compute the plasma frequency at the height of reflection. Such values of plasma frequency are independent of the usual assumptions made in computing N (h) profiles from ionograms, and are therefore of value in assessing the accuracy of N (h) profiles.

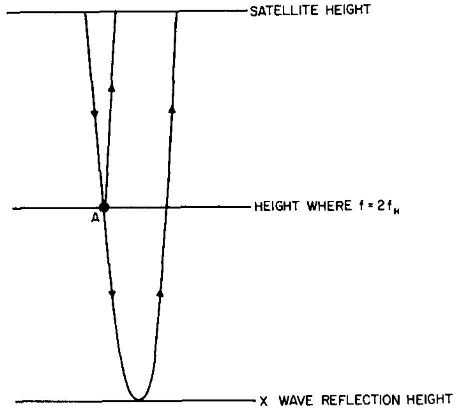

Fig. 26. Mode of Propagation Assumed for the Radio Energy Responsible for Producing the Resonance Trace (after Hagg and Muldrew [43]).

2.3.4 The VLF Lower-Hybrid Resonance

The VLF emissions recorded by Alouette I include certain noise bands that are not observable on the ground; the low-frequency cutoff of these noise bands depends on the properties of the plasma in the vicinity of the satellite[10,59,60]. These bands have a number of characteristic features that distinguish them from other emissions recorded by the VLF receiver. Whistlers and atmospherics can trigger the generation of the noise bands, or increase their intensity, indicating that the generation region is near the satellite. The low-frequency cutoff of the noise bands often shows a marked dependence on the geomagnetic field, as shown in Figure 27. (Note the symmetry of the cutoff frequencies with respect to the geomagnetic equator, for geomagnetic L values less than 4.0. The L coordinate, first introduced by McIlwain[61], gives the maximum height, in earth radii, from the center of the earth, of the magnetic field line through the point of observation.) Brice and Smith[40] suggested that the lower cutoff frequency of this noise band is identical with the lower hybrid resonance. (See Appendix III.) This resonance is the lower-frequency branch of a theoretical plasma resonance for the extraordinary-wave mode, but it had not previously been identified either in the laboratory or in space experiments. Detailed analysis of simultaneous observations by the Alouette I VLF receiver and the HF topside sounder[62,63] strongly support this interpretation. In the following discussion these VLF emissions are referred to as the lower hybrid resonance (LHR) noise bands.

The frequency of the lower hybrid resonance for a moderately dense plasma, such as the ionosphere above about 80 km, is given by:

$$f_{LHR} = \left(\frac{f_N^2 \, f_H^2}{f_N^2 + f_H^2}\right)^{\frac{1}{2}} \quad \left(\frac{1}{M\,(\bar{m}_i)_{eff}}\right)^{\frac{1}{2}} ,$$

where M is the ratio of proton to electron mass, and $(\bar{m}_i)_{eff}$ is an effective ion mass given by:

$$\frac{1}{(\bar{m}_i)_{eff}} = \Sigma_i A_i \frac{m_p}{m_i} ;$$

and A_i is the fractional numerical abundance of the i^{th} ion species.

An analysis of the LHR noise bands was made over a two-year period. Data were available from over 200 satellite passes, each of about ten minutes duration; during these passes the VLF receiver and the topside sounder operated simultaneously. (This simultaneous operation had not been planned; the occurrences were accidental, and the data are distributed fairly randomly over the two years.) The LHR noise bands were visible on one or

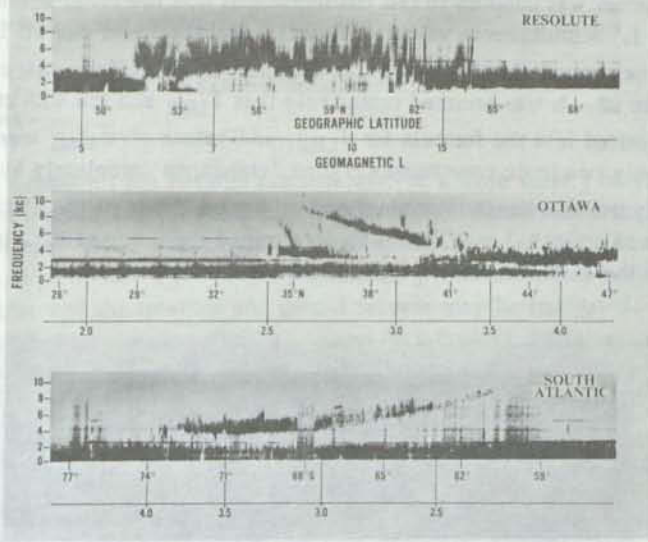

Fig. 27. Spectrogram of VLF Emissions Recorded by Alouette I at 1057-1148 U.T. on 31 Jan., 1963.

The captions on the three segments refer to the telemetry stations where the data were recorded (after Barrington et al[59]).

more ionograms in the majority of the passes. The most frequent occurrence was at high latitudes; LHR noise was seen only rarely at L values less than 2 and never at L values less than 1.5. Very little is known about the excitation mechanism of the LHR noise. Sometimes the noise bands are continuous throughout the satellite pass. On other occasions they are seen only during a portion of the pass, or only when triggered by long or short fractional-hop whistlers (See Fig. 28).

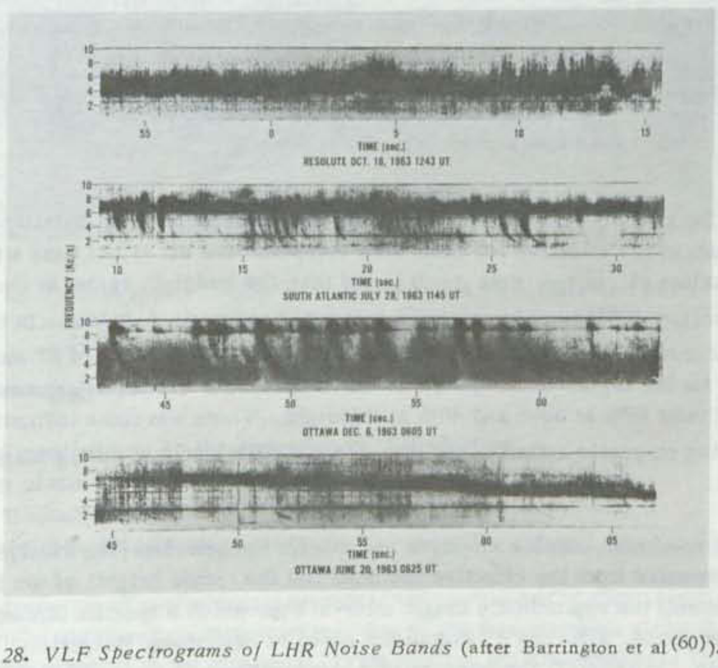

Fig. 28. VLF Spectrograms of LHR Noise Bands (after Barrington et al[60]).

The following procedure was adopted to test the hypothesis that the lower hybrid resonance was, in fact, being observed by Alouette I. Simultaneous values of f_N, f_H, and the lower cut-off frequencies of the LHR noise bands were obtained from the topside sounder ionograms and the VLF sonograms. An example of the simultaneous recordings is shown in Figure 29. It was assumed tentatively that f_{LHR} and the VLF cut-off frequencies are identical; the data were inserted into the formula for f_{LHR}, and values of $(\bar{m}_i)_{eff}$ were obtained. The composition of a plasma having only two ionic constituents is then determined completely by $(\bar{m}_i)_{eff}$. When there are three constituents, it is only possible to set maximum and minimum limits on the abundance of each constituent. On occasion the abundance of either H^+ or 0^+ could be determined quite accurately, but there was always a considerable uncertainty in the abundance of $H_e{}^+$.

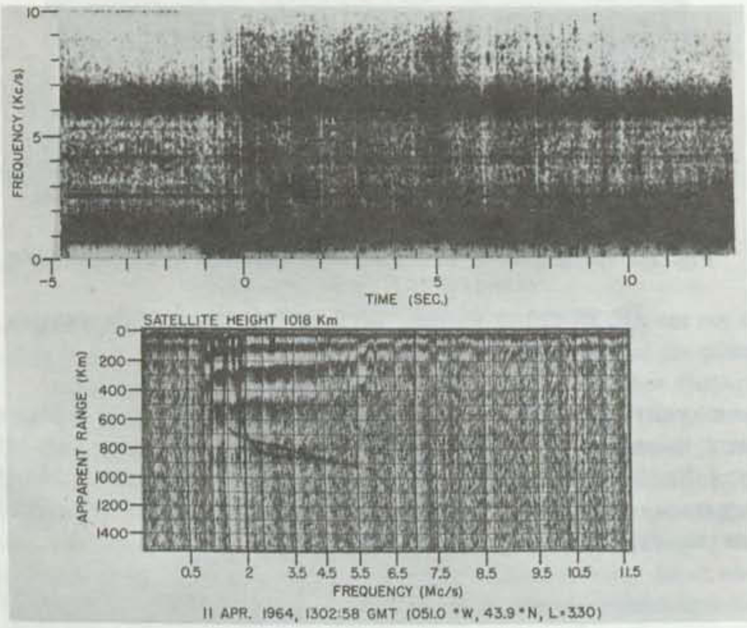

Fig. 29. VLF Spectrogram and Topside Ionogram Simultaneously Recorded in Alouette I.
The VLF record shows a continuous LHR noise band, with lower frequency cutoff of about 6 kc/s (after Barrington et al [62]).

The results of the analysis were entirely plausible, although some of the details were somewhat unexpected. Over four hundred values of the effective ion mass were computed and all values were within the limits 1 and 16. In general, the noon values of $(\bar{m}_i)_{eff}$ were much larger than the midnight values at the same latitude, and for a given time of day $(\bar{m}_i)_{eff}$ tended to increase with increasing magnetic L values. In the polar regions $(\bar{m}_i)_{eff}$ ranged from about 7 at midnight to about 13 at noon; the corresponding content of 0^+ was over 60% for the lower values and about 95% for the higher ones. At the lowest latitudes for which $(\bar{m}_i)_{eff}$ could be computed, the H^+ number density was at least 68% at noon and 40% at midnight. There was some indication in the data that $(\bar{m}_i)_{eff}$ increases with increasing magnetic activity, but there were insufficient data during magnetically disturbed periods for conclusive results.

Maximum and minimum possible effective ionospheric temperatures (the average of the ion and electron temperatures) were computed from the effective ion mass and the 'scale height' of the free electrons at 1000 km (the scale height represents the approximate height interval over which a specific atmospheric parameter decreases by a factor e). On occasion, when the 0^+ abundance could be determined accurately, the effective temperature could also be computed. In general, the temperatures obtained were in reasonable agreement with data available from other experiments. At middle latitudes, the effective ionospheric temperature ranged from about 1200°K to 1600°K. Substantially higher temperatures were computed at higher latitudes, but insufficient data have been analyzed to permit a quantitative statement.

2.4 Other VLF Emissions

The polar orbit of Alouette I has enabled the reception of a wide variety of VLF emissions[10], of which the emissions associated with plasma resonances, namely the proton whistlers and the LHR resonance, have been discussed in preceding sections. Other VLF emissions, such as whistlers and certain noise bands, do not appear to be specifically associated with plasma resonance phenomena. Such emissions may be observed at ground level, as well as at satellite height; and the satellite and ground records may be compared. In Figure 30, for example, a wide-band burst of atmospheric noise (or 'sferic'), caused by a flash of lightning, appears at 0.25 sec. on the ground record. This sferic travelled from the troposphere and through the ionosphere to the nearby satellite, orbiting at a height of 1000 km.* The lower frequencies in the sferic were delayed more than were the higher frequencies, thus producing the 'whistler' shown on the satellite record that started near 0.25 sec. Whistlers propagate generally in the direction of the magnetic field. This particular whistler travelled to the opposite (i.e., southern) hemisphere, was reflected, and then returned along approximately the same path to the satellite. After a travel time of about 3.5 seconds, the whistler again appears on the satellite and ground records but the frequency dispersion is now obviously much greater. The type of signal shown at 0.25 sec. on the satellite record has been named a 'short fractional-hop' (SFH) whistler, to distinguish it from the more familiar whistlers that can be observed by ground-based equipment — the latter whistlers have 'hopped' at least once across the magnetic equator.

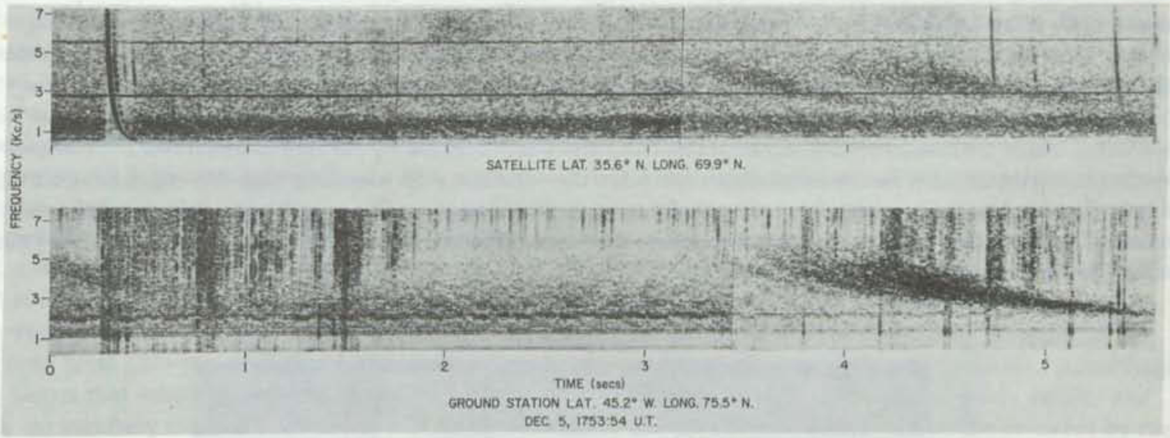

Fig. 30. Comparison of Simultaneous Spectrograms from Alouette I and from an Ottawa Ground Station (after Barrington and Belrose [10]).

The following features of the VLF observations will now be considered.

(i) The effect of positive ions on the dispersion of SFH whistlers.
(ii) SFH whistlers of unusual dispersion.
(iii) Whistlers of limited bandwidth.
(iv) Continuous and sporadic VLF noise bands.

Analysis of the dispersion of SFH whistlers provides information on the mean ionic mass below the satellite. Storey[64] noted that while whistler dispersion is largely due to the free electrons along the whistler path, positive ions also made a small contribution to the dispersion. This positive ion contribution is largest at low frequencies

* On the scale of this record, the travel time of the higher frequencies over the short path from the troposphere to the satellite may be neglected.

and depends on the total mass of the ions along the whistler path. It is difficult to measure this quite small positive ion effect in whistler dispersion; whistlers with a very high signal-to-noise ratio and an accurately known propagation path are necessary. SFH whistlers satisfy these requirements and accordingly some of the best examples of these signals were selected from the Alouette I records and their frequency was measured[65].

The positive ion effect in SFH whistlers amounts to only two to three per cent of the total dispersion. To measure the ion effect to within five to ten per cent, the frequency dispersion must be measured to an accuracy of a few tenths of one per cent. The required accuracy was achieved by developing a new technique in which the dispersion is measured directly from the waveform of the SFH whistlers. A given SFH whistler can be analyzed in several hours by this method. (For comparison, it requires several weeks to obtain equivalent results using the standard narrow-band filter technique.) Interpretation of the analytic results depends on the assumption of quasi-longitudinal propagation of the whistlers. This assumption is valid for whistlers observed above 35° geomagnetic latitude.

The waveforms of about 75 SFH whistlers recorded at latitudes between 35° and 50° were analyzed, and the arithmetic-mean gyrofrequency of all the positive ions along the whistler path was derived. During the day this gyrofrequency was about 50-60 cps; at night it was in the range 150-250 cps. Such results, taken together with a knowledge of the total ionization below the satellite, can be used to test various ionospheric models.

Whistlers emissions sometimes have an unusual amount of frequency dispersion, in between that of a normal SFH whistler and a long-path whistler. The example in Figure 31 was selected because two SFH whistlers occur within about 0.1 sec. of each other, and are followed by two whistlers whose dispersion is about 3 times as large as that of the SFH whistlers. The SFH whistlers appear on the recording at 1.4 - 1.5 seconds and the subsequent emissions at 1.6 - 1.7 seconds (the time origin in Figure 31 is quite arbitrary). The time separation between each pair of whistlers is identical, suggesting that both pairs originated from the same two lightning flashes. Time origins for the lightning flashes, computed from the dispersion of each whistler, are in agreement with this suggestion. A possible interpretation is that the SFH whistlers were partially reflected by refractive index gradients in the neighborhood of the satellite. The reflected waves then returned to the lower edge of the ionosphere, where they underwent a second reflection, and were recorded by the satellite receiver. This interpretation is consistent with the observed dispersion since the whistlers with unusually high dispersion have traversed the ionosphere below the satellite three times. Moreover, these whistlers do not extend to as high a frequency as the normal SFH whistlers. This is reasonable, since the higher frequencies are less likely to be reflected by the assumed ionospheric irregularities.

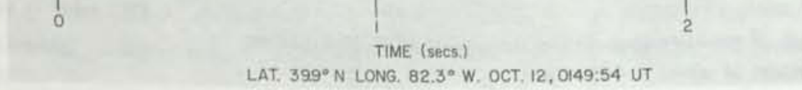

Fig. 31. Two SFH Whistlers with 3 Times the Normal Dispersion
(after Barrington and Belrose [10]).

Another unusual feature of the VLF emissions appears in Figure 32. Two whistlers are shown at about 0.4 and 1.6 seconds. Each whistler extends over a relatively short frequency band and the two frequency bands are in different portions of the VLF spectrum. The dispersion of these whistlers, however, shows that they both originated at about the same latitude. The occurrence of such truncated whistlers has not yet been investigated in any detail, but it is evident that they occur most frequently at low latitudes. The cause of the observed frequency cutoff is not known. Since the upper ionosphere is far from homogenous, it is possible that different frequency components of a whistler follow somewhat different paths. Simultaneous ground and satellite observations will probably help to resolve this issue.

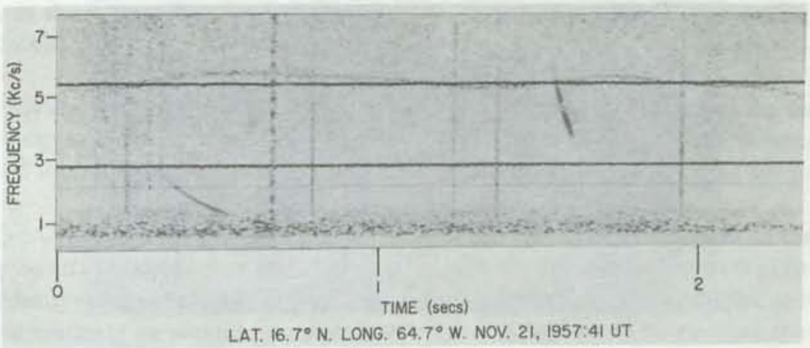

Fig. 32. Two Whistlers of Limited Bandwidth (after Barrington and Belrose [10]).

In addition to the discreet VLF emissions, ionospheric noise appears consistently on the VLF records. At the satellite, the noise extends to lower frequencies than at the ground stations; on the other hand, the total bandwidth of the noise appears to be greater at the ground. An example of a continuous noise band at low latitudes appears in Figure 32. The upper edge of the noise band is at about 1.3 kc/s and the lower edge is near the cutoff of the VLF receiver. On other occasions the VLF noise occurs in two distinct frequency bands, as in Figure 33. These records were obtained at middle latitudes, where ionospheric noise bands are of very frequent occurrence. The character of the noise is quite different in Figures 33 (A) and 33 (B). The origin of the noise bands, and hence the cause of these differences, is unknown, but in general, sporadic noise bands are more frequent at the higher latitudes. Figure 34 is a comparison of simultaneous ground and satellite records obtained near the same geographic location. There are very many more sferics (i.e., electromagnetic impulses in the atmosphere) on the ground record than there are SFH whistlers on the satellite record. Closer inspection reveals that most of the sferics have a low-frequency cutoff at about 1600 cps, and that only those sferics that produce SFH whistlers extend beyond the cut-off frequency. The explanation of this result is reasonably straightforward. The waveguide formed by the earth and the lower edge of the ionosphere is able to support the propagation of sferics to great distances with very little attenuation; but this waveguide has a low frequency cutoff. Accordingly, only sferics that originate near the ground station will extend to frequencies below this wave-guide cutoff; and these are precisely the sferics that have a high probability of producing SFH whistlers that can be recorded by the satellite overhead.

2.5 Extra-Terrestrial HF Emissions

2.5.1 Introduction

Extra-terrestrial radio noise nas been monitored by ground-based equipments for several decades, over a very wide spectrum. The low-frequency end of this spectrum is cut off by the ionosphere at the penetration frequency of the F layer. One reason for using a satellite-borne receiver to monitor the HF noise background is to extend knowledge of extra-terrestrial noise to lower frequencies; a second reason is to determine the noise background against which a sweep-frequency sounder must operate. Accordingly, before the Alouette I sounder design was completed, the HF noise at 3.8 Mc/s was measured by a DRTE receiver in the NASA satellite, 1960 eta one[66, 67].

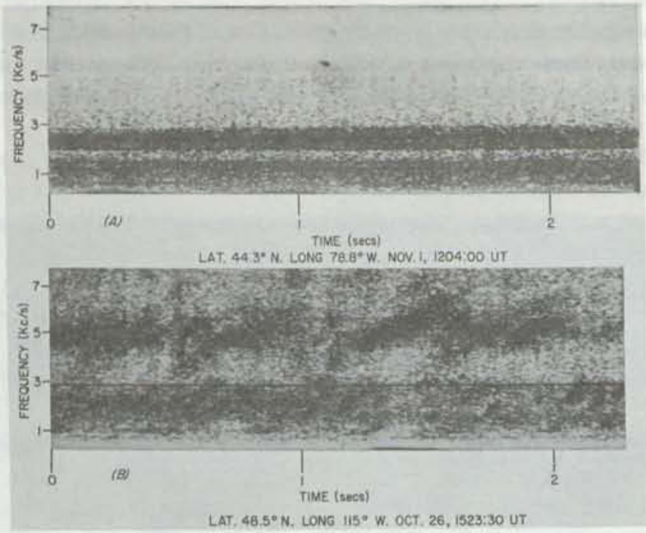

Fig. 33. Examples of VLF Ionospheric Noise Bands Recorded by Alouette I.
(a) Continuous,
(b) Sporadic.
(after Barrington and Belrose (10)).

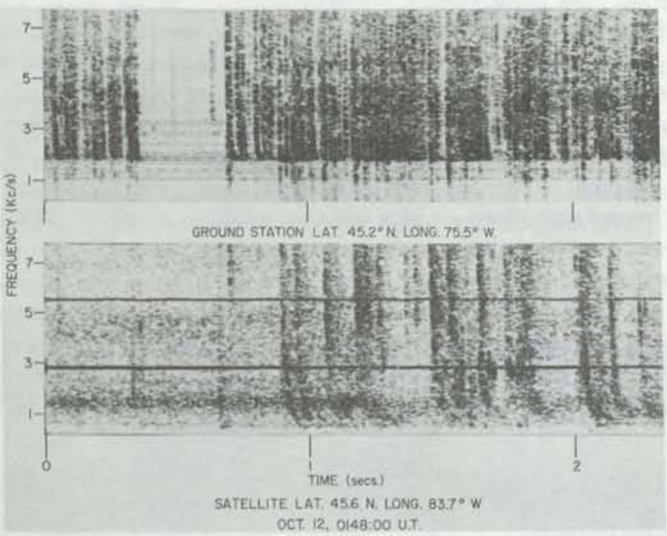

Fig. 34. The Association between Sferics and SFH Whistlers
(after Barrington and Belrose (10)).

In Alouette I the background radio noise level between 1.5 and 10 Mc/s is monitored by the automatic gain control (AGC) voltage of the sweep-frequency sounder receiver. The ionosphere shields the receiver from HF ground-based transmissions below the F-layer critical penetration frequency, so that the background noise is almost entirely of extra-terrestrial origin. Most of the noise, the so-called cosmic noise, originates outside of our solar system; sporadic emissions from the sun are superimposed on the cosmic noise. The representative cosmic noise record shown in Figure 5 was discussed briefly in Section 1.3.4, and will now be described in more detail.

In addition to the background noise level, between about 1.5 and 6.5 Mc/s, Figure 5 shows ionospheric plasma resonances at f_H, f_N, f_T and $2 f_H$, spurious responses, and radio interference[9]. When the sounder transmitter is switched off, the AGC variations caused by the ionospheric resonances disappear. The remaining relatively rapid variations are due to two effects: toward the low frequency end there are a number of spurious responses, generated at fixed frequencies by the satellite equipment, and toward the high frequency end there is interference from ground transmitters. To cause this type of interference, the frequency of the ground transmitters must be above the F-layer critical frequency. On the AGC record the interference is usually restricted to the high-frequency end, as shown here, but when the interference is particularly strong non-linearities in the receiver (or possibly in the plasma) result in a spreading of the interference across the entire record.

The smooth, slowly varying trace in the intermediate frequency range represents the background noise level that, in this example, is due to galactic noise. The intensity of the noise can be determined from the AGC records, provided that the characteristics of the antennas and the matching network are known.

Once the galactic noise level in a given direction has been established, increases in the receiver noise above this level may be attributed to other extra-terrestrial sources. The Alouette antennas have too broad an aperture to directly identify the source, and it is necessary to use inference. For example, sporadic solar emissions are recorded routinely by several ground observatories at a number of frequencies above 15 Mc/s. Noise enhancements recorded by Alouette at the same time as (or a few minutes later than), the higher frequency solar recordings, and originating from the general direction of the sun, are identified as solar emissions.

The AGC voltage provides accurate data on relative noise levels, but uncertainties in the receiver gain and antenna beam width make it difficult to obtain precise values of the absolute noise level. The receiver gain was calibrated before launch, but there is no provision for in-flight calibration. A comparison of cosmic noise data obtained over a two-year period shows sufficient consistency to suggest that significant changes in receiver gain have not yet occurred. The effective antenna beam width is much more dependent on the parameters of the plasma than on the geometry of the antennas. Using the topside sounder data, the effective antenna beam width has been computed at 1000 km for various ionospheric conditions[68]. For example, the effective antenna beam width (half-cone angle) is about 90° when the ratio of operating frequency to plasma frequency is 5:1, and this decreases to about 60° when this ratio is 2:1. This computation has been checked, to some extent, by monitoring solar noise as the sun passes through the antenna beam.

2.5.2 Cosmic Noise

Cosmic noise measurements have been made for a variety of local electron densities and for a wide range of magnetic field strengths[11,69]. These data have been extrapolated to zero electron density, and the resulting values have then been taken as a measure of the cosmic noise levels in extra-terrestrial space near the earth's orbit. The noise spectrum obtained by this method is shown in Figure 35. The estimated error limits on this diagram allow for scatter in the observations as well as for uncertainties in the extrapolation process. The curve appears to be well defined between 1.5 and 5 Mc/s, but it has not been possible to extend this up to 10 Mc/s with any accuracy. (The cross-over frequency of the antenna dipoles (Section 1.3.2) is 4.5 Mc/s.) The spectrum of Figure 35 is representative of medium and high galactic latitudes; any fine detail that may exist in these regions has been smoothed out by the broad effective antenna beam width.

The absolute flux density of the galactic radiation measured by Alouette I varied systematically over the celestial sphere. The highest flux density was measured for a region centered approximately on the south galactic pole, whereas the lowest flux density came from a region centered approximately on R.A. 9 hrs., declination +75°. These results are shown in Figure 36, along with values for the north galactic pole region; data obtained by other workers are also plotted for comparison.

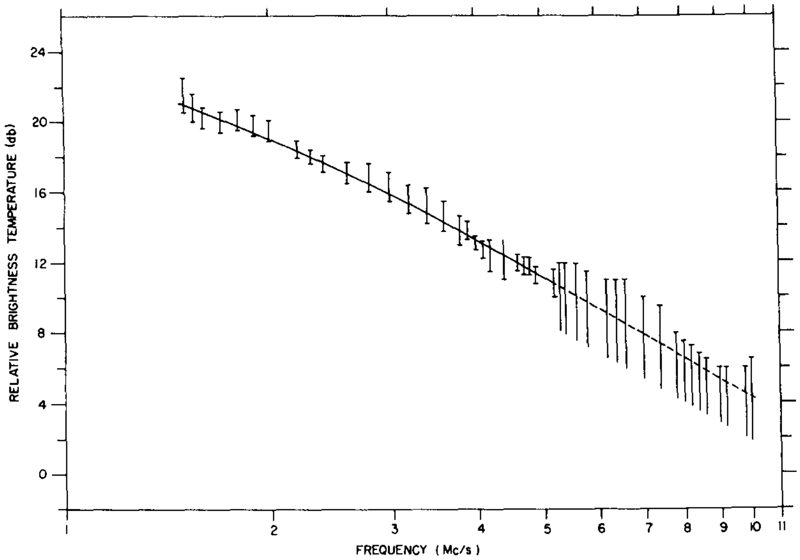

Fig. 35. Relative Galactic Brightness Temperature as a Function of Frequency (after Hartz (11)).

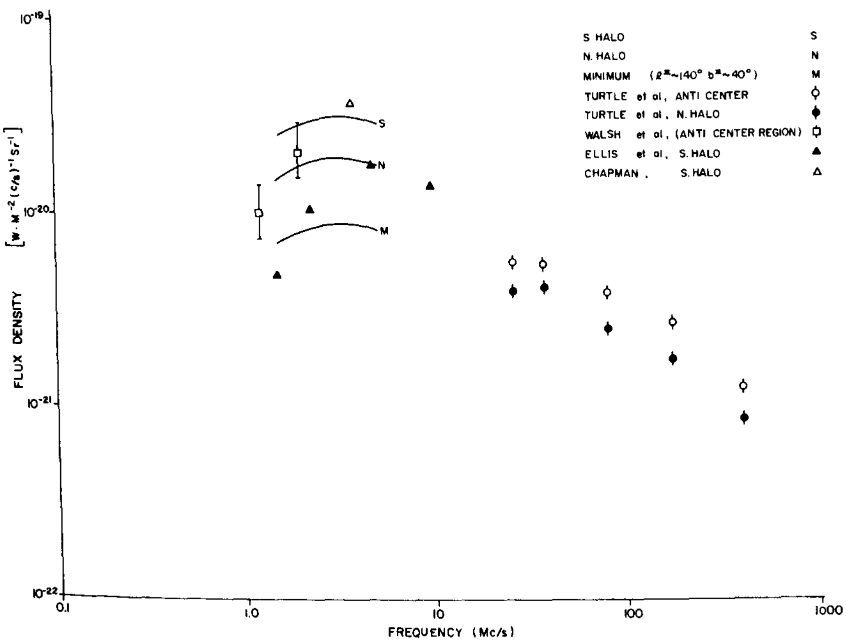

Fig. 36. Composite Diagram Showing the Variation of the Galactic Radiation Flux Density as a Function of Frequency, as Determined by Various Observers, and for Several Different Regions of the Galaxy.
The Alouette I results are shown as three curves, of which two represent the maximum and minimum values found in the data (after Hartz (11)).

2.5.3 Solar Noise

Certain sporadic solar radio noise emissions appear to be associated with disturbances on the sun, and on occasion with the ejection of solar matter. The radio emissions are often very complex, and they have been categorized as bursts type I, II, etc. (see[70] for an elementary discussion of solar radio emissions). Solar radio noise appears sporadically on the AGC recordings, superimposed on the normal galactic noise level. The well-known type III bursts can be readily identified, but other spectral types are much more difficult to identify from only the AGC records. The recording of Figure 37 (b) was made part way through a type III solar radio noise burst; Figure 37 (a) is a normal galactic noise record for comparison. The cut-off frequency of the antenna aperture was 1.9 Mc/s and the maximum intensity was recorded at about 2 Mc/s. Data scaled from such recordings of type III bursts are presented in three dimensions in Figure 38. The frequency at which the noise amplitude is maximum decreases with time, during each noise burst. From the rate of frequency drift of such bursts a source velocity between 0.10 and 0.15 of that of light in free space has been computed.

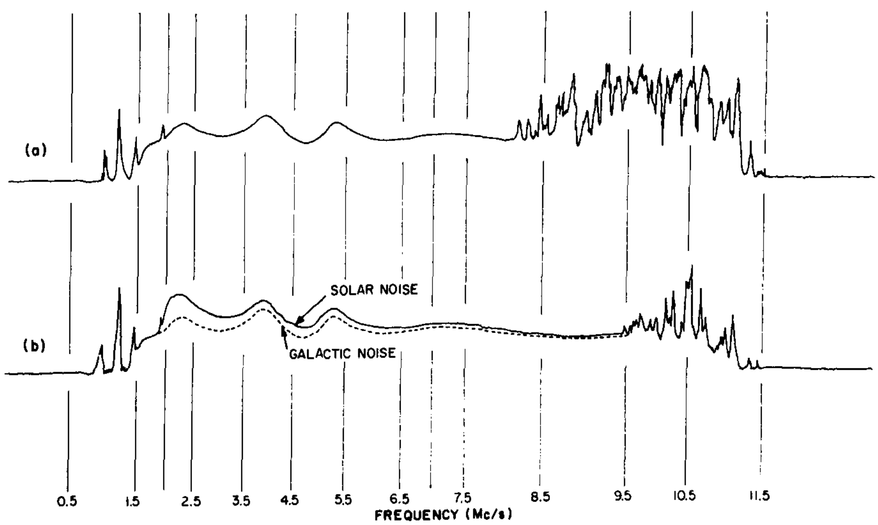

Fig. 37. Alouette I AGC Records Showing
(a) The normal galactic radio noise levels,
(b) Solar noise above the galactic level, from 1.9 Mc/s (the antenna aperture cutoff) to about 9.5 Mc/s
(after Hartz [71]).

The type III bursts, along with other types of solar radio noise enhancements seen in the Alouette I records, appear to have characteristics very similar to those of the corresponding events at higher frequencies; i.e., they are apparently a low frequency extension of well-known noise events observable with ground-based equipment. This point is illustrated in Figure 39. A type III burst, starting at about 1535 (UT), is first recorded on ground-based equipment, at 45 Mc/s. The frequency of maximum intensity decreases continuously with time, for a fraction of a second, until the noise level at 22 Mc/s prevents further measurements. It is obvious, however, that the noise burst recorded a short time later, at 10 Mc/s, by Alouette I, is the same type III burst. Again, the frequency of maximum intensity decreases continuously with time, down to the low-frequency limit of the satellite equipment. The second noise burst on the satellite record was not visible on the ground equipment, but the third burst is an extension of the ground-based record starting at about 1538.

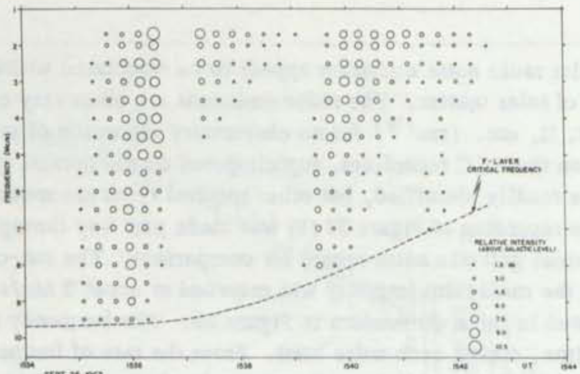

Fig. 38. Spectra of the Type III Solar Noise Bursts, as Recorded by Alouette I.
The Data are portrayed as various sized circles, to represent the intensity of the solar noise relative to galactic noise, as indicated. (after Hartz (71)).

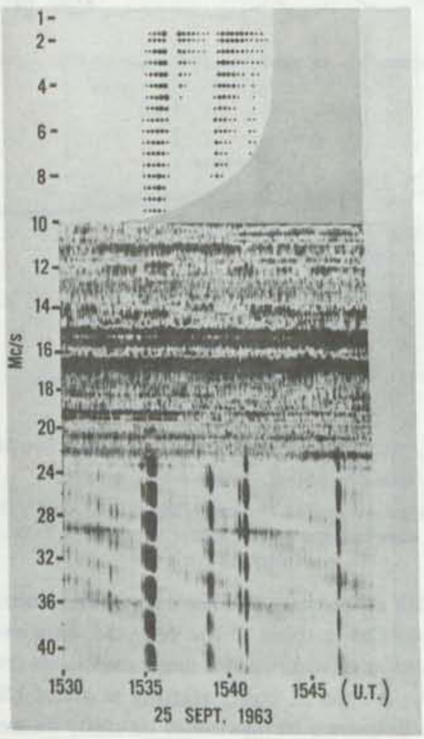

Fig. 39. Composite Spectra of Type III Solar Radio Noise Bursts.
The data above 10 Mc/s were recorded on ground-based equipment; below 10 Mc/s they were scaled at discrete frequencies from satellite recordings (Hartz and Warwick (72)).

2.6 Associated Research

This section will describe several ionospheric investigations that do not fit into the preceding subject categories, but in which Alouette I data play a significant part.

2.6.1 The Effect of Spread F on the Apparent Reflection Coefficient of the F-Region

The reflection coefficient of the F region is an important parameter in many HF propagation studies. In these studies it has frequently been assumed that the ionosphere can be considered as a plane reflector, with a constant reflection coefficient.

The apparent reflection coefficient of the F region has been measured from both above and below the F-layer maximum[73]. The bottomside data were obtained at Prince Rupert (54.3°N, 130.3°W) from April, 1949, to March, 1950, at six frequencies between 2.0 and 5.2 Mc/s. The topside data were obtained from Alouette I ionograms taken in 1962 - 63, at frequencies from 2.7 to 2.9 Mc/s. It was found that the vertical-incidence first-hop F-layer apparent reflection coefficient increases substantially with increasing intensity of spread F. The vertical incidence second-hop F-layer apparent reflection coefficient, however, decreases slightly during spread-F conditions. The topside vertical-incidence (first-hop) F-layer apparent reflection coefficient increases by about 10 db in going from no spread F to spread-F conditions. An illustration of the data obtained from one satellite pass is given in Figure 40.

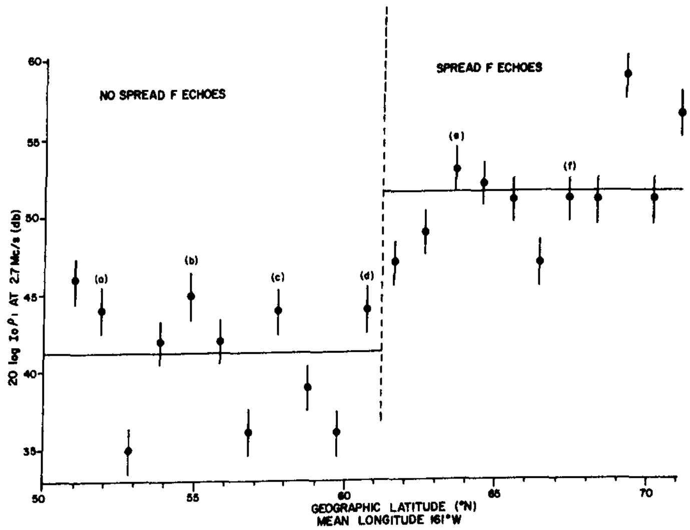

Fig. 40. Variation of the Vertical-Incidence Apparent Reflection Coefficient, ρ, of the Topside of the Ionosphere with Latitude, 0310-0316 (UT) on Nov. 6, 1962.
The data points are for the ordinary wave mode at 2.8 Mc/s. The horizontal lines indicate the average values in the presence or absence of spread F echoes (after Petrie, Hagg, and Warren [73]).

The increase in the F-layer first-hop reflection coefficient with spread F can be explained either by a focussing effect in the energy scattered from an irregular surface, or else by propagation of the energy along field-aligned ducts.

Two standard methods[74] of measuring HF absorption depend on a knowledge of the reflection coefficient of the F region. The first method compares the amplitudes of the first-hop echo by day and by night; night-time absorption is assumed to be negligible. The second method compares the amplitudes of successive multiple-hop echoes. Both methods assume the ionosphere to be a plane reflector. On occasion these methods yield inconsistent results. This inconsistency is undoubtedly associated with the dependence of the one-hop reflection on spread-F conditions. The amplitude of the one-hop night-time echo is not a suitable calibration constant for daytime measurements of absorption. The multiple-hop technique, however, is not subject to the same criticism and (at Prince Rupert) has yielded reliable absorption data for all times of day.

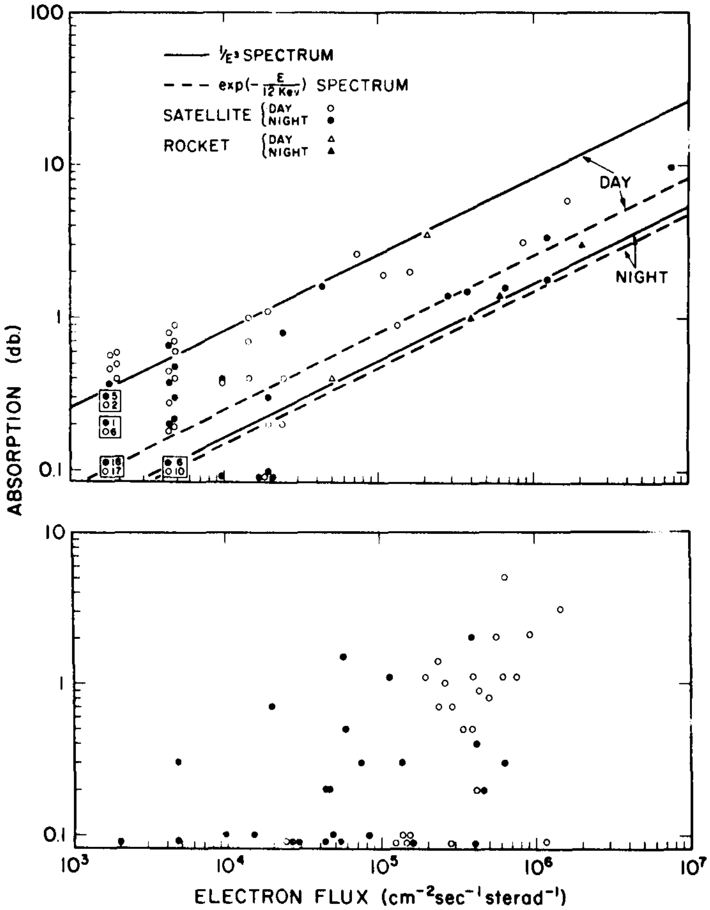

Fig. 41. Variation of Absorption with Electron Flux for both Precipitated (A) and Trapped (B) Electrons (after Jelly, McDiarmid and Burrows (75)).

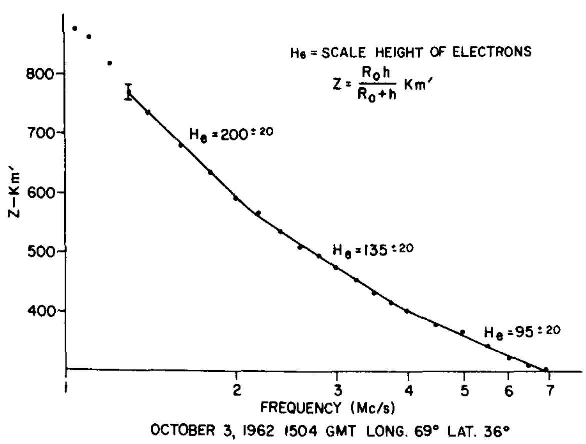

Fig. 42. Scale Height Profile of the Topside of the Ionosphere (after Nelms (77)).

2.6.2 Precipitated Electrons and Auroral Absorption

There is a very high probability that the anomalous absorption of HF radio waves at auroral zone latitudes is caused by increases in the ionization density of the D region, and that these increases arise from the precipitation of energetic particles. Details of the physical processes involved, however, are still largely undetermined.

The flux of energetic electrons at 1000 km, measured by particle detectors in Alouette I, was compared with the auroral absorption of HF radio waves measured by ground-based riometers[75]. An Anton 223 Geiger counter[76] sensitive to electrons with energies greater than 40 Kev was used. Electron count data were selected in two categories, using the following selection criteria.

(i) Precipitated electrons, i.e., with pitch angles inclined at less than 45° to the magnetic field. These electrons are normally precipitated below 100 km and the resultant ionization would contribute to auroral absorption.

(ii) Trapped electrons, i.e., with pitch angles of $90 \pm 20^{\circ}$. These electrons mirror at altitudes between 700 and 1000 km.

Auroral absorption data were obtained from five riometer stations in Canada and one in Alaska. Electron data were selected from satellite passes within 5° longitude of each riometer station.

For a given flux of precipitated electrons, the observed auroral absorption is in agreement with theoretical computations, to within the experimental accuracy. The plots in Figure 41 present a visual summary of the observations, and both precipitated and trapped electrons are shown for comparison.

2.6.3 Scale Heights in the Upper Ionosphere

The N (h) profiles of electron number density versus height derived from topside ionograms may be used to calculate ionospheric scale heights[77]. The effect of a gravity gradient is removed by converting from ordinary height h to a 'reduced-height' parameter

$$Z = \frac{R_o h}{R_o + h} \quad ,$$

where R_o is the earth's radius. The scale height of electrons, H_e, can then be obtained directly from the straight line portions of the N (Z) profiles, as illustrated in Figure 42. The scale height is approximately doubled in going from the 400 to the 800 km level. Similar N (Z) profiles were computed for latitudes from 17°N to 68°N, for this October 3, 1962, satellite pass. The scale height increased slightly with increasing latitude, and the 2:1 ratio of scale heights between the 400 and 800 km levels remained unchanged.

Scale heights have been determined for only a few selected passes. Variations in scale height may be due to variations in temperature or composition, or to both. Accordingly, the interpretation of scale height data depends on the availability of information on temperature and composition. Most of the scale height analysis has been associated with the studies of ionic composition described in Section 2. Temperature information derived from incoherent electron scatter is also being supplied by the Prince Albert Radar Laboratory of DRTE, at Prince Albert, Saskatchewan, for selected passes.

3. ACKNOWLEDGEMENTS

This report includes information supplied in advance of publication by the following members of DRTE: R.E. Barrington, J.S. Belrose, E.L. Hagg, T.R. Hartz, L. Herzberg, D.H. Jelly, G.E.K. Lockwood, D.B. Muldrew, G.L. Nelms, L.E. Petrie and E.S. Warren.

4. REFERENCES

1. 'Alouette, Canadian-U.S. Ionospheric Topside Sounder Satellite.' IG Bulletin No. 65, Nov., 1962, p. 9.

2. 'Alouette Topside Ionosphere Studies.' Results from studies conducted by the Canadian Defence Research Telecommunications Establishment during the satellite's first year in orbit, IG Bulletin No. 79, Jan., 1964, p.1.

3. Franklin, C.A., Bibby, R.J., Sturrock, R.F., and D.F. Page. 'Electronic and System Design of the Canadian Ionospheric Satellite.' **Vol. 11**, Part V, pp. 64-72, IEEE International Convention Records, New York, March, 1963.

4. Brown, R.K. 'The Canadian Topside Sounder Satellite Engineering Performance.' Engineering Jour., **46**, 44, 1963.

5. Franklin, C.A., Bibby, R.J., and R.F. Sturrock. 'Telemetry and Command Systems for the Canadian Ionospheric Satellite.' Proc. International Telemetry Conference, London, 1963, p. 457.

6. Franklin, C.A. 'Alouette I, The First Three Years in Orbit - Part II: Electrical Design and Performance.' DRTE Report No. 1159-2, 1967.

7. Mar, J. 'Alouette I, The First Three Years in Orbit - Part III: Mechanical Design and Environment.'DRTE Report No. 1159-3, 1967.

8. Chapman, J.H., and E.S. Warren. 'The Topside Sounder Satellite Alouette: Electron Density Distribution in the Ionosphere and Exosphere, North-Holland Pub. Co., Amsterdam, 1964, p. 307.

9. Hartz, T.R. 'A Study of Interference in the Alouette Topside Sounder Records.' DRTE Report No. 1123, Oct., 1963.

10. Barrington, R.E., and J.S. Belrose. 'Preliminary Results from the Very-Low-Frequency Receiver in Canada's Alouette Satellite.' Nature, **198**, 651, 1963.

11. Hartz, T.R. 'Observations of the Galactic Radio Emission between 1.5 and 10.0 Mc/s from the Alouette Satellite, Ann. d'Astrophys., **27**, 823, 1964.

12. McDiarmid, I.B., Burrows, J.R., Rose, D.C., and Margaret D. Wilson. 'High Latitude Particle Flux Measurements from the Satellite 1962 Beta Alpha (Alouette).' Space Research, **Vol. 4**, North-Holland Pub. Co., Amsterdam, 1964, p. 606.

12a. Jensen, D.C., and J.C. Cain. 'An Interim Geomagnetic Field.' Jour. Geophys. Res., **67**, 3568, 1962.

13. Warren, E.S. 'Some Preliminary Results of Sounding of the Topside of the Ionosphere by Radio Pulses from a Satellite.' Nature, **197**, 636, 1963.

14. Warren, E.S. Private Communication, 1965.

15. Haselgrove, J. 'Ray Theory and a New Method for Ray Tracing.' Report of the Physical Society Conference on the Physics of the Ionosphere, London, Sept., 1954.

16. Lockwood, G.E.K., and L.E. Petrie. 'Low-Latitude Field-Aligned Ionization Observed by the Alouette Topside Sounder.' Planet. Space Sci., **11**, 327, 1963.

17. Hagg, E.L. 'A Preliminary Study of the Electron Density at 1000 kilometers.' Can. Jour. Phys., **41**, 195, 1963.

18. Nelms, G.L., and E.S. Warren. 'Some Irregular Variations of the Electron Density in the Topside of the Ionosphere. COSPAR Space Research, **Vol. 5**, 1965, p 637.

18a. Nelms, G.L. 'Seasonal and Diurnal Variations of the Distribution of Electron Density in the Topside of the Ionosphere.' Electron Density Profiles in Ionosphere and Exosphere, **Vol. 3**, NATO Science Series, 1966, p 358.

19. Hines, C.O. 'Ionospheric Movements and Irregularities.' Research in Geophysics, **Vol. 1**, Sun, Upper Atmosphere and Space, M.I.T., 1964, p 299.

20. Muldrew, D.B. 'Radio Propagation along Magnetic Field-Aligned Sheets of Ionization Observed by the Alouette Topside Sounder.' Jour. Geophys. Res., **68**, 5355, 1963.

21. Muldrew, D.B. 'F-layer Ionization Troughs Deduced from Alouette Data.' Jour. Geophys. Res., **70**, 2635, 1965.

22. Penndorf, R. 'Frequency of Spread-F Occurrence in Antarctica.' Proc. AGARD Ionospheric Research Committee, Copenhagen, 1964. (In press)

23. Cohen, R., and K.L. Bowles. 'On the Nature of Equatorial Spread F.' Jour. Geophys. Res., **66**, 1081, 1961.

24. Petrie, L.E. 'Topside Spread Echoes.' Can. Jour. Phys., **41**, 194, 1963.

25. Petrie, L.E. 'Preliminary Results on Mid- and High-Latitude Topside Spread F.' Proc. AGARD Ionospheric Research Committee, Copenhagen, 1964. (In press)

26. Calvert, W., and C.W. Schmid. 'Spread F Observations by the Alouette Topside Sounder Satellite.' Jour. Geophys. Res., **69**, 1839, 1964.

27. Hagg, E.L., Muldrew, D.B., and E.S. Warren. 'Spiral Occurrence of Sporadic E.' Jour. Atmos. Terrest. Phys., **14**, 345, 1959.

28. Malville, J.M. 'Antarctic Auroral Observations, Ellsworth Station 1957.' Jour. Geophys. Res., **64**, 1389, 1959.

29. Petrie, L.E. Private communication.

30. Hope, E.R. 'Spiral Patterning of Solar Corpuscular Precipitation.' Nature, **177**, 571, 1956.

31. Burdo, O.A. 'Re Certain Laws of Magnetic Disturbance in the High Latitudes.' Canadian Defence Research Board English Translation, T321R dated April, 1959; from Physics of Solar Corpuscular Streams and their Action Upon the Upper Atmosphere of the Earth. Moscow; Acad. of Sci. Press, 1957, p 159.

32. Meek, J.H. 'The Location and Shape of the Auroral Zone.' Jour. Atmos. Terrest. Phys., **6**, 313, 1955.

33. Pitteway, M.L.V., and R. Cohen. 'A Waveguide Interpretation of 'Temperate-Latitude Spread F' on Equatorial Ionograms.' Jour. Geophys. Res., **66**, 3141, 1961.

34. Knecht, R.W., Van Zandt, T.E., and S. Russell. 'First Pulsed Radio Soundings of the Topside of the Ionosphere.' Jour. Geophys. Res., **66**, 3078, 1961.

35. Booker, H.G. 'Guidance of Radio and Hydromagnetic Waves in the Magnetosphere.' Jour. Geophys. Res., **67,** 4135, 1962.

36. Reber, Grote, and G.R. Ellis. 'Cosmic Radio-Frequency Radiation near one Megacycle.' Jour. Geophys. Res., **61,** 1, 1956.

37. Lockwood, G.E.K., and G.L. Nelms. 'Topside Sounder Observations of the Equatorial Anomaly in the 75° W Longitude Zone.' Jour. Atmos. Terrest. Phys., **26,** 569, 1964.

38. Lockwood, G.E.K. 'Plasma and Cyclotron Spike Phenomena Observed in Topside Ionograms.' Can. Jour. Phys., **41,** 190, 1963.

39. Brice, N.M., Smith, R.L., Belrose, J.S., and R.E. Barrington. 'Recordings from Satellite Alouette I. Triggered Very-Low-Frequency Emissions.' Nature, **203,** 926, 1964.

40. Brice, N.M., and R.L. Smith. 'Recordings from Satellite Alouette I. A Very-Low-Frequency Plasma Resonance.' Nature, **203,** 926, 1964.

41. Smith, R.L., Brice, N.M., Katsufrakis, J., Gurnett, D.A., Shawhan, S.D., Belrose, J.S., and R.E. Barrington. 'An Ion Gyrofrequency Phenomenon Observed in Satellites.' Nature, **204,** 274, 1964.

42. Lockwood, G.E.K. 'Excitation of Cyclotron Spikes in the Ionospheric Plasma.' Can. Jour. Phys., **43,** 291, 1965.

43. Hagg, E.L. 'Remote Cyclotron Resonance Phenomenon Observed by the Alouette Satellite.' Nature, **210,** 927, 1966.

43a. Muldrew, D.B., and E.L. Hagg. 'A Novel Ionospheric Cyclotron Resonance Phenomenon Observed on Alouette I Data.' Can. Jour. Phys., **44,** 925, 1966.

44. Johnston, T.W., and J. Nuttal. 'Cyclotron Harmonic Signals Received by the Alouette Topside Sounder.' Jour. Geophys. Res., **69,** 2305, 1964.

45. Fejer, J.A., and W. Calvert. 'Resonance Effects of Electrostatic Oscillations in the Ionosphere.' Jour. Geophys. Res., **69,** 5049, 1964.

46. Barrington, R.E., and Luise Herzberg. 'Frequency Variation in Ionospheric Cyclotron Harmonic Series Obtained by the Alouette I Satellite.' Can. Jour. Phys., **44,** 987, 1966.

47. Crawford, F.W., Kino, G.S., and H.H. Weiss. 'Transmission Characteristics of Cyclotron Harmonic Waves in Plasma.' Phys. Rev., 1965. (In press)

48. Bernstein, I.B. 'Waves in a Plasma in a Magnetic Field.' Phys. Rev., **109,** 10, 1958.

49. Hagg, E.L. Private Communication.

50. Gurnett, D.A., Shawhan, S.D., Brice, N.M., and R.L. Smith. 'Ion Cyclotron Whistlers.' Jour. Geophys. Res., **70,** 1665, 1965.

51. Shawhan, S.D., and D.A. Gurnett. 'Fractional Concentration of Hydrogen Ions in the Ionosphere from VLF Proton Whistler Measurement.' Jour. Geophys. Res., **71,** 47, 1966.

52. Gurnett, D.A., and S.D. Shawhan. 'Determination of Hydrogen Ion Concentration, Electron Density, and Proton Gyrofrequency from the Dispersion of Proton Whistlers.' Jour. Geophys. Res., **71**, 741, 1966.

53. Brice, N.M. 'Ion Effects Observed in Radio Wave Propagation in the Ionosphere.' Proc. of URSI Symposium on Electromagnetic Wave Theory, Delft, Holland, Sept., 1965. (In press)

54. Brice, N.M., and D.A. Gurnett. 'Duration of Proton Whistlers.' Oral presentation at URSI Meeting, Washington, D.C., 20-23 Apr., 1965.

55. Warren, E.S. 'Perturbation of the Local Electron Density by the Alouette Satellite.' Can. Jour. Phys., **41**, 188, 1963.

56. Calvert, W., and G.B. Goe. 'Plasma Resonances in the Upper Ionosphere.' Jour. Geophys. Res., **68**, 6113, 1963.

57. Smith, R.L., and N.M. Brice. 'Propagation in Multi-Component Plasmas.' Jour. Geophys. Res., **69**, 5029, 1964.

58. Muldrew, D.B. 'Delayed Cyclotron Pulse Generation in the Topside Ionosphere Deduced from Alouette I Data.' Nature, **210**, 471, 1966.

59. Barrington, R.E., Belrose, J.S., and D.A. Keeley. 'Very-Low-Frequency Noise Bands Observed by the Alouette I Satellite.' Jour. Geophys. Res., **68**, 6539, 1963.

60. Belrose, J.S., and R.E. Barrington. 'VLF Noise Bands Observed by the Alouette I Satellite.' Radio Science Jour. of Res., NBS/USNC-URSI, **69D**, 69, 1965.

61. McIlwain, C.E. 'Coordinates for Mapping the Distribution of Magnetically Trapped Particles.' Jour. Geophys. Res., **66**, 3681, 1961.

62. Barrington, R.E., Belrose, J.S., and G.L. Nelms. 'Ion Composition and Temperature at 1000 km as Deduced from Simultaneous Observations of a VLF Plasma Resonance and Topside Sounding Data in the Alouette I Satellite.' Jour. Geophys. Res., **70**, 1647, 1965.

63. Barrington, R.E., Belrose, J.S., and G.L. Nelms. 'Ion Composition and Temperature at 1000 km as Deduced from VLF Resonances and Topside Ionograms.' Electron Density Profiles in Ionosphere and Exosphere, **Vol. 3** NATO Science Series, 1966, p 387.

64. Storey, L.R.O. 'A Method to Detect the Presence of Ionized Hydrogen in the Outer Atmosphere.' Can. Jour. Phys., **34**, 1153, 1956.

65. Barrington, R.E. Private Communication.

66. Chapman, J.H., and A.R. Molozzi. 'Interpretation of Cosmic Noise Measurements from 1960 Eta One at 3.8 Mc/s.' Nature, **191**, 480, 1961.

67. Molozzi, A.R., Franklin, C.A., and J.P.I. Tyas. 'Cosmic Noise Measurements from 1960 Eta One at 3.8 Mc/s.' Nature, **190**, 616, 1961.

68. Hartz, T.R., and R.S. Roger. 'The Effective Antenna Beam Width for a Satellite-Borne Radio Telescope.' Can. Jour. Phys., **42**, 2146, 1964.

69. Hartz, T.R. 'Spectrum of the Galactic Radio Emission between 1.5 and 10 Mc/s as Observed from a Satellite.' Nature, **203**, 173, 1964.

70. Hartz, T.R. 'Particle Emissions from the Disturbed Sun, and the Sun-Earth Environment; Physics of the Earth's Upper Atmosphere.' Ed. C.O. Hines, I. Paghis, T.R. Hartz, J.A. Fejer, Prentice-Hall Inc., New Jersey, 1965, p 216.

71. Hartz, T.R. 'Solar Noise Observations from the Alouette Satellite.' Ann. d'Astrophys., **27**, 831, 1964.

72. Hartz, T.R., and J.W. Warwick. Private communication.

73. Petrie, L.E., Hagg, E.L., and E.S. Warren. 'The Influence of Focusing on the Apparent Reflection Coefficient of the F Region.' Jour. Geophys. Res., **70**, 4347, 1965.

74. Pigott, W.R., Beynon, W.J.G., and G.M. Brown. 'The Pulse Method of Measuring Ionospheric Absorption. Annals of the International Geophysical Year, **3**, Part II, Pergamon Press, 1957.

75. Jelly, D.H., McDiarmid, I.B., and J.R. Burrows. 'Correlations between Intensities of Auroral Absorption and Precipitated Electrons.' Can. Jour. Phys., **42**, 2411, 1964.

76. McDiarmid, I.B., Burrows, J.R., Budzinski, E.E., and M.D. Wilson. 'Some Average Properties of the Outer Radiation Zone at 1000 km.' Can. Jour. Phys., **41**, 2064, 1963.

77. Nelms, G.L. 'Scale Heights of the Upper Ionosphere from Topside Soundings.' Can. Jour. Phys., **41**, 202, 1963.

For additional references see pages 58 and 69.

APPENDIX I

RELATED IONOSPHERIC SATELLITE PROGRAMS

The Alouette I project is part of an international program of ionospheric research by satellites. The overall management of this program is the responsibility of the U.S. National Aeronautics and Space Agency (NASA). At the date of writing, (Autumn 1965), two ionospheric satellites were operational: Alouette I and Explorer XX, launched in September, 1962, and August, 1964, respectively. The next satellite in this program, ISIS-X, is scheduled for launch in late 1965.* Three additional satellites, ISIS-A, ISIS-B and ISIS-C are planned for launch between 1967 and 1971.

The main experiment in Alouette I is a sweep-frequency HF sounder; in Explorer XX the main experiment is a fixed-frequency (6 frequencies) HF sounder. ISIS-X includes two satellites, Alouette II and Explorer XXXI. Alouette II is similar to Alouette I, and the Explorer is a direct probe measurement satellite. The ISIS-A satellite contains sweep-frequency and fixed-frequency sounders together with a number of direct measurement probes; in effect, ISIS-A is similar to ISIS-X except that all the experiments of ISIS-A are contained within a single payload. ISIS-B and ISIS-C are still in the early planning stage.

* ISIS-X was successfully launched into orbit on 28 November, 1965, from the Pacific Missile Range in California.

APPENDIX II

REDUCED DATA FROM ALOUETTE I IONOGRAMS

Copies of the Alouette I topside sounder ionograms are deposited in the World Data Center A, Boulder, Colorado, U.S.A. Reduced data from ionograms scaled at the Defence Research Telecommunications Establishment are published in two formats:

A Routine Tabulations of Selected Ionospheric Parameters

This book-sized publication is titled *Alouette I Ionospheric Data Alosyn* (ALOuette SYNoptic data [79]). Each issue contains data from about 14,000 ionograms.

B Tabulations of N (h)

Electron number density versus height tabulations are made for selected groups of ionograms[78]. Each N (h) book contains about 5,000 profiles.

A - ALOSYN

An ionogram that illustrates the scaling of f_xS, f_oF2 and f_xF2, together with a sample data page from an ALOSYN book are shown in Figures 43 and 44.

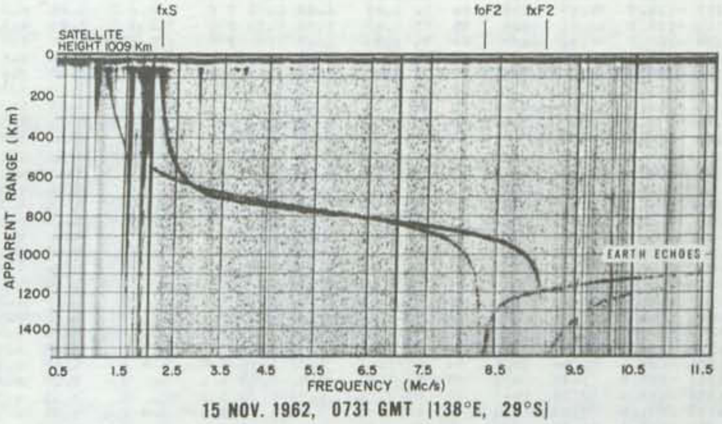

Fig. 43. Scaling of f_xS, f_oF2, and f_xF2 from an Alouette I Ionogram for ALOSYN Booklet.

The symbols used in Figure 44 are:

YR	Year
MO	Month
DY	Day of the month
GMT	Greenwich Mean Time, in hours, minutes, and seconds, with the minutes and seconds separated by a solidus. The time given is 3.0 ± 1 seconds before the occurrence of the 0.5 Mc/s frequency marker.

DEFENCE RESEARCH BOARD
DEFENCE RESEARCH TELECOMMUNICATIONS ESTABLISHMENT

ALOUETTE I TOPSIDE IONOSPHERIC PARAMETERS

YR	MO	DY	GMT	LMT	LONG	LAT	HGT	CHI	DIP	FH	JFOS	FXS	A	Q	FOF2	A	Q	JFOF2	FXF2	A	Q	FES	Q	G	KP
62	9	29	742/ 4	2127	-153.7	59.26	1044	117	72	0.98	1.43	2.00	4	D	-0.	-0		2.77	3.5	5	D	-0.		2	30
62	9	29	744/16	2143	-150.3	52.13	1043	123	68	0.94	0.92	1.50	4	D	-0.	-0		3.32	4.0	5	D	-0.		3	30
62	9	29	745/12	2148	-149.2	49.07	1042	126	66	0.92	0.94	1.50	4	D	-0.	-0		1.79	2.5	5	D	-0.		2	30
62	9	29	745/31	2150	-148.9	48.03	1042	127	65	0.91	0.46	1.10	3	D	-0.	-0		2.42	3.1	3	D	-0.		3	30
62	9	29	745/49	2151	-148.6	47.05	1042	128	64	0.90	0.95	1.50	4	D	-0.	-0		2.73	3.4	2	D	-0.		3	30
62	9	29	746/ 8	2153	-148.3	46.00	1041	129	64	D.89	0.61	1.20	3	D	-0.	-0		2.84	3.5	2	D	-0.		3	30
62	9	29	746/27	2154	-148.1	44.96	1041	130	63	0.89	0.96	1.50	4	D	-0.	-0		3.10	3.7	2	D	-0.		2	30
62	9	29	746/45	2156	-147.8	43.97	1041	131	62	0.88	0.74	1.30	3	D	-0.	-0		2.86	3.5	3	D	-0.		2	30
62	9	29	747/ 4	2157	-147.5	42.92	1041	132	61	0.87	0.97	1.50	4	D	-0.	-0		3.57	4.2	3	B	-0.		2	30
62	9	29	747/23	2158	-147.3	41.87	1040	133	61	0.86	1.51	2.00	4	D	-0.	-0		3.58	4.2	3	D	-0.		2	30
62	9	29	1606/ 0	1100	-76.4	38.31	1017	42	69	0.97	1.11	1.70	3	A	6.5	3	A	6.30	7.0	3	A	-0.		3	2E
62	9	29	1606/18	1101	-76.2	39.31	1017	43	69	0.98	1.11	1.70	3	A	6.6	2	A	6.30	7.0	3	A	-0.		2	2E
62	9	29	1606/37	1103	-76.0	40.37	1018	44	70	0.99	1.10	1.70	3	A	6.3	2	A	6.29	7.0	3	A	-0.		2	2E
62	9	29	1606/56	1104	-75.8	41.43	1019	45	71	0.99	1.10	1.70	3	D	6.3	2	A	6.29	7.0	3	A	-0.		2	2E
62	9	29	1607/15	1105	-75.5	42.48	1019	46	72	1.00	1.09	1.70	3	D	6.1	3	B	6.03	6.7	3	B	-0.		2	2E
62	9	29	1607/33	1106	-75.3	43.48	1020	47	72	1.01	0.98	1.60	3	D	6.1	3	B	6.03	6.7	3	B	-0.		3	2E
62	9	29	1607/52	1108	-75.0	44.53	1021	48	73	1.01	0.97	1.60	3	0	5.6	3	B	5.57	6.3	3	B	-0.		2	2E
62	9	29	1608/11	1109	-74.8	45.59	1021	49	74	1.02	0.97	1.60	3	D	5.4	2	D	5.47	6.2	2	0	-0.		2	2E
62	9	29	1608/29	1111	-74.5	46.58	1022	50	74	1.02	0.96	1.60	3	D	5.3	2	D	5.27	6.0	3	0	-0.		2	2E
62	9	29	1608/48	1112	-74.2	47.63	1022	51	75	1.02	0.96	1.60	3	D	5.3	2	D	5.31	6.0	2	D	-0.		2	2E
62	9	29	1609/ 7	1114	-73.9	48.68	1023	52	75	1.03	D.96	1.60	3	D	5.3	2	D	5.26	6.0	2	D	-0.		2	2E
62	9	29	1609/25	1115	-73.5	49.67	1024	53	76	1.03	0.95	1.60	3	D	5.2	2	D	5.21	5.9	2	D	-0.		2	2E
62	9	29	1609/42	1117	-73.2	50.60	1024	53	76	1.03	0.90	1.55	3	0	-0.	-0		4.85	5.6	3	E	-0.		2	2E
62	9	29	1610/ 3	1119	-72.8	51.75	1025	55	77	1.04	0.95	1.60	3	D	4.4	2	D	4.45	5.2	2	D	-0.		2	2E
62	9	29	1610/22	1121	-72.4	52.79	1026	56	78	1.04	0.83	1.50	3	D	4.2	2	D	4.40	5.1	2	D	-0.		3	2E
62	9	29	1610/40	1123	-72.0	53.77	1026	56	78	1.04	0.95	1.60	3	D	4.1	2	D	4.14	4.9	2	0	-0.		2	2E
62	9	29	1610/59	1125	-71.6	54.81	1027	57	79	1.04	0.83	1.50	3	D	4.0	2	D	4.04	4.8	2	D	-0.		3	2E
62	9	29	1611/18	1127	-71.1	55.84	1027	58	79	1.04	0.83	1.50	3	D	-0.	-0		4.75	5.5	4	G	-0.		3	2E
62	9	29	1611/36	1129	-70.6	56.81	1028	59	79	1.04	0.83	1.50	3	D	3.7	2	D	3.84	4.6	2	D	-0.		3	2E
62	9	29	1611/55	1131	-70.1	57.84	1029	60	80	1.04	0.83	1.50	3	D	3.7	2	D	3.79	4.5	3	D	-0.		2	2E
62	9	29	1612/18	1135	-69.4	59.08	1029	62	80	1.04	0.83	1.50	3	D	3.7	2	G	3.79	4.5	3	G	-0.		2	2E
62	9	29	1612/32	1137	-69.0	59.83	1030	62	80	1.04	0.83	1.50	3	G	3.7	2	G	3.79	4.5	2	G	-0.		2	2E
62	9	29	1612/51	1140	-68.3	60.84	1030	63	81	1.04	1.06	1.70	3	G	4.0	2	D	4.04	4.8	2	0	-0.		2	2E
62	9	29	1613/10	1143	-67.6	61.85	1031	64	81	1.04	1.17	1.80	3	G	4.5	2	D	4.55	5.3	2	D	-0.		2	2E
62	9	29	1753/49	1109	-101.2	45.94	1021	49	73	1.03	1.07	1.70	2	A	5.3	3	D	5.25	6.0	3	D	-0.		3	2E
62	9	29	1754/ 7	1110	-100.9	46.93	1022	50	73	1.03	1.06	1.7D	2	A	-0.	-0		4.95	5.7	3	A	-0.		2	2E
62	9	29	1754/23	1112	-100.6	47.81	1023	51	74	1.04	1.06	1.70	2	A	5.0	3	A	4.74	5.5	3	A	-0.		2	2E
62	9	29	1755/22	1117	-99.6	51.06	1025	54	76	1.05	1.05	1.70	2	A	-0.	-0		3.00	3.8	3	D	-0.		2	2E
62	9	29	1755/59	1121	-98.8	53.08	1026	56	78	1.06	1.04	1.70	2	A	4.1	2	D	4.22	5.0	3	D	-0.		3	2E
62	9	29	1756/19	1123	-98.4	54.17	1026	57	78	1.07	1.04	1.70	2	D	4.0	2	D	4.11	4.9	3	0	-0.		2	2E
62	9	29	1803/23	1313	-72.5	75.73	1038	79	86	1.05	1.05	1.70	2	D	4.0	1	P	3.95	4.7	2	B	-0.		2	2E
62	9	29	1941/ 3	1117	-125.9	51.57	1025	54	72	1.01	1.08	1.70	2	D	4.0	2	D	3.96	4.7	3	D	-0.		2	3E
62	9	29	1941/22	1119	-125.5	52.61	1026	55	73	1.02	1.08	1.70	2	D	3.5	3	G	3.85	4.6	3	G	-0.		2	3E
62	9	29	1941/59	1123	-124.7	54.63	1027	57	74	1.03	1.07	1.70	2	D	4.0	2	D	3.74	4.5	3	D	-0.		2	3E
62	9	29	1942/19	1125	-124.2	55.71	1027	58	75	1.03	1.01	1.65	3	D	3.7	3	D	3.84	4.6	3	D	-0.		3	3E
62	9	29	1942/37	1128	-123.7	56.69	1028	59	76	1.04	1.00	1.65	3	D	3.7	2	D	3.73	4.5	2	D	-0.		3	3E
62	9	29	1942/55	1130	-123.3	57.66	1029	60	77	1.04	1.00	1.65	3	D	3.6	1	A	3.53	4.3	2	A	-0.		3	3E
62	9	29	1945/44	1160	-116.6	66.60	1034	69	83	1.07	0.92	1.60	3	G	3.3	3	G	3.41	4.2	3	G	-0.		2	3E
62	9	29	1946/ 2	1204	-115.5	67.53	1034	70	83	1.07	1.15	1.80	3	G	4.2	3	G	4.22	5.0	3	G	-0.		2	3E
62	9	29	1948/10	1249	-104.9	73.77	1037	77	87	1.07	D.81	1.50	3	J	-0.	-0		2.60	3.4	3	J	-0.		2	3E
62	9	29	2128/41	1131	-149.4	58.44	1029	61	72	0.99	0.88	1.50	3	D	3.5	2	D	3.43	4.1	2	D	-0.		2	5E
62	9	29	2129/ 0	1134	-148.8	59.46	1030	62	73	1.00	0.87	1.50	3	D	3.5	3	D	3.42	4.1	2	D	-0.		2	5E
62	9	29	2129/18	1137	-148.2	60.42	1030	63	74	1.0D	0.86	1.50	3	D	-0.	-D		3.42	4.1	2	D	-0.		2	5E
62	9	29	2129/37	1140	-147.5	61.43	1031	64	75	1.01	0.86	1.50	3	D	3.5	2	D	3.46	4.2	2	D	-0.		3	5E
62	9	29	2129/56	1143	-146.8	62.44	1031	65	75	1.02	0.85	1.50	3	D	3.4	2	D	3.25	4.0	2	G	-0.		2	5E
62	9	29	2130/14	1146	-146.0	63.39	1032	66	76	1.02	0.85	1.50	3	G	3.5	2	D	3.4D	4.1	2	G	-0.		2	5E
62	9	29	2130/33	1150	-145.2	64.39	1032	67	77	1.03	0.78	1.45	3	D	-0.	-0		3.40	4.1	2	G	-0.		3	5E
62	9	29	2130/52	1154	-144.3	65.38	1033	68	78	1.03	0.84	1.50	3	D	3.4	3	D	3.34	4.1	2	D	-0.		2	5E
62	9	29	2131/10	1158	-143.4	66.31	1033	69	78	1.04	0.77	1.45	3	G	-0.	-0		3.34	4.1	2	G	-0.		2	5E
62	9	29	2131/29	1202	-142.3	67.29	1034	70	79	1.04	0.95	1.6D	3	D	-0.	-D		4.25	5.0	4	G	-0.		2	5E
62	9	29	2131/48	1207	-141.2	68.26	1034	71	80	1.04	0.83	1.50	3	G	-0.	-0		3.38	4.1	3	G	-0.		2	5E
62	9	29	2132/ 6	1212	-140.0	69.16	1035	72	80	1.05	0.88	1.55	3	G	3.1	2	G	3.23	4.0	2	G	-0.		2	5E
62	9	29	2132/25	1218	-138.6	70.11	1035	73	81	1.05	1.11	1.75	3	G	3.5	2	G	3.58	4.3	2	G	-0.		2	5E
62	9	29	2132/44	1224	-137.1	71.04	1036	74	82	1.05	1.05	1.70	3	G	3.5	2	G	3.48	4.2	2	G	-0.		2	5E
62	9	29	2133/ 2	1231	-135.5	71.91	1036	75	82	1.05	0.82	1.50	3	G	-0.	-0		3.22	4.0	2	G	-0.		2	5E
62	9	29	2133/21	1239	-133.6	72.81	1037	76	83	1.06	1.16	1.80	3	G	-0.	-0		3.53	4.3	2	G	-0.		2	5E
62	9	29	2133/40	1247	-131.6	73.69	1037	77	84	1.06	0.93	1.60	3	G	3.9	2	G	3.38	4.1	2	G	-0.		2	5E
62	9	29	2133/58	1256	-129.4	74.50	1037	78	84	1.06	0.87	1.55	3	G	-0.	-0		3.37	4.1	2	G	-0.		2	5E
62	9	29	2134/17	1307	-126.9	75.33	1038	79	85	1.06	0.81	1.50	3	G	-0.	-0		3.32	4.1	2	G	-0.		2	5E
62	9	29	2134/36	1318	-124.1	76.13	1038	80	86	1.06	0.81	1.50	3	G	-0.	-0		3.27	4.0	2	G	-0.		2	5E
62	9	29	2135/12	1344	-117.7	77.53	1039	82	87	1.06	0.81	1.50	3	G	-0.	-0		4.24	5.0	4	J	-0.		2	5E
62	9	29	2135/47	1415	-110.2	78.71	104D	83	88	1.06	0.99	1.65	3	G	-0.	-0		3.84	4.6	2	G	-0.		2	5E
62	9	29	2136/ 5	1433	-105.7	79.22	1040	84	89	1.06	D.56	1.30	3	G	3.3	2	G	3.54	4.3	3	G	-0.		2	5E
62	9	29	2136/24	1455	-100.4	79.69	1040	85	89	1.05	0.82	1.50	3	G	-0.	-0		3.33	4.1	2	G	-0.		2	5E
62	9	29	2136/43	1517	-94.8	80.06	1041	86	89	1.05	0.70	1.40	3	G	3.2	2	G	3.23	4.0	2	G	-0.		2	5E
62	9	29	2137/ 1	1541	-89.1	80.31	1041	87	89	1.05	0.70	1.40	3	G	3.2	2	G	3.24	4.0	2	G	-0.		2	5E
62	9	29	2137/20	1606	-82.8	80.47	1041	88	88	1.05	0.70	1.40	3	G	-0.	-0		3.29	4.0	2	G	-0.		2	5E
62	9	29	2137/39	1632	-76.4	80.52	1041	89	87	1.04	1.06	1.70	3	G	-0.	-0		4.77	5.5	4	J	-0.		2	5E
62	9	29	2137/57	1656	-70.4	80.45	1042	90	87	1.04	0.83	1.50	3	G	-0.	-0		4.11	4.8	3	G	-0.		2	5E
62	9	29	2138/16	1722	-64.2	80.26	1042	91	86	1.04	1.06	1.70	3	G	4.1	2	G	4.11	4.8	3	G	-0.		2	5E

Fig. 44. Sample Page of ALOSYN Data.

LMT Local mean time in hours and minutes.
LONG Longitude
LAT Latitude
HGT Height of satellite
CHI Solar zenith angle
DIP Angle of dip of earth's magnetic field at the satellite.
FH The computed electron gyrofrequency at the satellite.
JFOS Frequency of the ordinary wave reflection trace at the satellite, calculated from the observed f_xS.
FXS Frequency of the observed extraordinary wave reflection trace at the satellite.
(FXS)A Accuracy of observation, according to the following code:

1. Estimated error less than 0.025 Mc/s.
2. Estimated error less than 0.05 Mc/s.
3. Estimated error less than 0.1 Mc/s.
4. Magnitude of FXS less than tabulated value.
5. Magnitude of FXS greater than tabulated value.

(FXS)Q Quality of the reflection trace near the satellite, according to the following table:

QUALITY TABLE

	No Spread	Slightly Spread	Moderately Spread	Extremely Spread
Unambiguous records	A	D	G	J
Oblique traces present	B	E	H	K
Cusps and/or forking of the records	C	F	I	L

The classifications of spread F in this table refer to the degree of spread F at the height and frequency of the observations. It is not a classification of spread F for the ionogram as a whole.

FOF2 Observed ordinary wave penetration frequency of the F2 layer.
(FOF2) A Accuracy of observation according to the following code:

1. Estimated error less than 0.05 Mc/s.
2. Estimated error less than 0.1 Mc/s.
3. Estimated error less than 0.2 Mc/s.
4. Magnitude of FOF2 less than tabulated value.
5. Magnitude of FOF2 greater than tabulated value.

(FOF2)Q Quality of the reflection trace at the ordinary wave penetration frequency according to the preceding quality table.
JFOF2 Ordinary wave penetration frequency of the F2 layer, calculated from the observed f_xF2.
FXF2 Observed extraordinary wave penetration frequency of the F2 layer.
(FXF2) A Accuracy of observation, according to the f_oF2 accuracy code.
(FXF2)Q Quality of the reflection trace at the extraordinary wave penetration frequency, according to the quality table.
FES Maximum frequency of observation of sporadic E.
(FES) Q Quality of sporadic E, according to the first row of characters in the quality table.
G Strength of signal returned from the earth, according to the following code:

1. Strong well defined echoes.
2. Weak and intermittent echoes.
3. Echoes not observed.

KP Three-hourly planetary magnetic K_p index. The symbols -, 0, ϵ, replace the usual superscripts -, 0, and + in the second column for the K_p index.

```
                              DEFENCE RESEARCH BOARD
                 DEFENCE RESEARCH TELECOMMUNICATIONS ESTABLISHMENT

                          ALOUETTE I  REAL HEIGHT PROFILES

    YR DAY   GMT     LONG    LAT   CHI  DIP   FH   Q   FOF2*    TOTALN    P

4XT 62 272 1941/ 3 -125.9  51.57   54   72  1.01  5   3.88  43.122E11  18
     1.32 1023.     1.42  994.    1.67  935.    1.94  877.    2.23  824.    2.54  777.    2.90  736.
     3.25  699.     3.63  666.    4.06  636.    6.50  529.    9.58  450.   13.18  382.   14.84  356.
    16.52  331.    17.44  318.   18.28  303.   18.57  298.

4XT 62 272 1941/22 -125.5  52.61   55   73  1.02  8   3.83  46.995E11  17
     1.29 1024.     1.42  998.    1.67  939.    1.94  880.    2.23  827.    2.54  783.    2.86  743.
     3.25  707.     3.63  674.    4.02  645.    6.50  534.    6.39  450.   13.10  377.   14.76  350.
    16.43  322.    17.34  307.   18.19  281.

4XT 62 272 1941/59 -124.7  54.63   57   74  1.03  6   3.65  41.118E11  17
     1.26 1025.     1.39  991.    1.64  933.    1.91  874.    2.19  822.    2.50  780.    2.83  740.
     3.17  704.     3.58  670.    3.97  639.    6.39  529.    9.45  445.   13.02  373.   14.67  345.
    15.45  330.    16.34  310.   16.43  303.

4XT 62 272 1942/18 -124.2  55.66   58   75  1.03  6   3.71  47.789E11  17
     1.26 1026.     1.37  992.    1.61  933.    1.88  874.    2.16  823.    2.47  780.    2.83  740.
     3.17  704.     3.54  670.    3.97  640.    6.39  529.    9.38  443.   13.02  367.   14.59  337.
    15.36  321.    16.25  301.   17.07  266.

4XT 62 272 1942/37 -123.7  56.69   59   76  1.04  6   3.70  48.447E11  17
     1.24 1026.     1.37  993.    1.61  933.    1.88  875.    2.16  824.    2.47  779.    2.79  739.
     3.17  702.     3.54  669.    3.93  640.    6.39  529.    9.38  444.   12.94  371.   14.59  343.
    15.36  327.    16.25  310.   16.98  267.

4XT 62 272 1942/55 -123.3  57.66   60   77  1.04  5   3.55  45.007E11  17
     1.24 1027.     1.34  993.    1.58  935.    1.85  876.    2.13  824.    2.47  781.    2.79  740.
     3.13  704.     3.54  672.    3.93  642.    6.33  531.    9.38  445.   12.94  370.   13.75  354.
    14.50  336.    15.28  311.   15.63  284.

4XT 62 272 1945/44 -116.6  66.60   69   83  1.07  6   3.44  42.740E11  20
     1.34 1032.     1.56  959.    1.82  892.    2.10  833.    2.40  784.    2.72  739.    3.06  698.
     3.42  661.     3.84  628.    4.72  570.    5.68  519.    6.73  475.    7.87  437.    9.11  401.
    10.50  369.    11.92  335.   12.62  316.   13.42  296.   14.17  273.   14.59  252.

4XT 62 272 1946/ 2 -115.5  67.53   70   83  1.07  8   4.28  64.272E11  20
     1.73 1032.     1.91  996.    2.19  939.    2.54  892.    2.83  841.    3.17  792.    3.54  747.
     3.97  706.     4.38  669.    4.81  636.    5.26  606.    5.79  580.    6.28  555.    9.31  462.
    12.86  384.    16.98  314.   18.86  287.   20.74  257.   21.67  240.   22.61  218.

4XT 62 272 1949/32  -92.8  77.22   81   89  1.06  6   3.86  51.941E11  18
     1.26 1037.     1.34 1022.    1.58  961.    1.85  899.    2.13  846.    2.43  799.    2.79  755.
     3.13  716.     3.54  682.    3.93  651.    6.33  536.    9.38  452.   13.02  382.   14.59  357.
    16.34  326.    17.16  309.   18.09  285.   18.48  261.

4XT 62 272 1949/50  -89.3  77.88   82   88  1.05  6   3.55  42.816E11  17
     1.22 1038.     1.32  986.    1.53  900.    1.79  838.    2.06  786.    2.40  742.    2.72  703.
     3.10  668.     3.46  636.    3.88  607.    6.33  503.    9.31  425.   12.94  357.   13.75  343.
    14.59  325.    15.36  298.   15.63  276.

4XT 62 272 1950/ 9  -85.1  78.51   83   88  1.05  6   3.82  52.362E11  20
     1.37 1038.     1.64  990.    1.91  935.    2.19  879.    2.50  829.    2.83  784.    3.21  744.
     3.58  707.     3.97  675.    4.43  646.    4.91  619.    5.36  594.    5.89  571.    6.39  551.
     9.45  466.    13.10  396.   14.76  370.   16.43  342.   17.34  324.   18.09  279.

4XT 62 272 1950/46  -75.7  79.54   85   87  1.05  6   3.96  51.981E11  20
     1.91 1039.     2.00 1021.    2.29  964.    2.61  920.    2.98  878.    3.34  837.    3.71  799.
     4.15  764.     4.57  733.    5.06  703.    5.52  676.    6.06  650.    6.62  627.    9.65  536.
    13.34  465.    15.02  440.   16.70  417.   17.62  404.   18.57  388.   19.45  355.

4XT 62 272 1951/ 5  -70.2  79.95   86   87  1.04  6   3.74  47.338E11  19
     1.24 1039.     1.34 1000.    1.61  940.    1.88  888.    2.16  841.    2.50  799.    2.83  760.
     3.21  725.     3.58  692.    4.02  661.    4.91  609.    5.95  565.    7.02  527.   10.21  450.
    14.00  383.    14.84  369.   15.63  353.   16.52  333.   17.34  296.

4XT 62 272 1951/24  -64.3  80.25   87   86  1.04  6   3.84  48.233E11  19
     1.12 1039.     1.32  957.    1.56  893.    1.85  840.    2.13  792.    2.43  752.    2.79  715.
     3.17  682.     3.54  651.    3.97  624.    6.45  521.    9.51  447.   10.94  419.   12.38  393.
    14.00  367.    15.63  340.   16.52  326.   17.44  310.   18.19  271.

4XT 62 272 1951/42  -58.4  80.43   88   86  1.04  6   4.25  61.596E11  20
     1.70 1039.     1.97  972.    2.26  914.    2.57  867.    2.94  822.    3.29  781.    3.71  744.
     4.11  709.     4.57  679.    5.01  652.    5.52  626.    6.00  604.    6.56  582.    9.65  501.
    13.34  431.    17.62  371.   19.45  347.   20.44  334.   21.46  317.   22.40  280.

4XT 62 272 1952/ 1  -52.1  80.52   89   85  1.03  5   3.95  49.789E11  18
     1.12 1040.     1.34  964.    1.58  901.    1.88  849.    2.16  801.    2.47  761.    2.83  724.
     3.21  691.     3.58  661.    4.02  634.    6.50  534.    9.58  456.   13.76  390.   14.93  365.
    16.61  340.    17.53  327.   18.38  310.   19.25  276.
```

Fig. 45. Sample Page from N(h) Data Book.

Where the symbol ' -0' occurs in a column of the tabulations it indicates that the parameter was not observed on the ionogram.

The orbital position, local mean time, and solar zenith angle, are obtained from a computer program supplied by the Institute for Telecommunication Sciences and Aeronomy, Boulder, U.S.A. The gyrofrequency and magnetic dip angle are obtained from a computer program supplied by the National Aeronautics and Space Administration, Washington, D.C., U.S.A.

B - TABULATIONS OF N(h)

These tabulations consist of electron number density profiles computed for selected groups of ionograms. A sample page is shown in Figure 45. The profiles are listed in the order in which the ionograms were recorded. The estimated accuracy of the tabulation is indicated by a subjective quality figure, Q. This index figure has values from 4 for the best quality records to 9 for the lowest usable quality. Data with Q figures from 7 to 9 should be used with caution. (The quality figure 0 indicates that the data were tabulated before this system of quality figures was started.)

Occasionally the higher frequency portion of the F-region reflection trace is either absent or difficult to interpret, and the tabulated profile is incomplete. Under these circumstances the highest frequency to which the record is read is less than the penetration frequency. On other occasions, more than one set of reflections is observed on the same ionogram. A subjective decision is then made, either to compute several N (h) profiles, or else to select the most appropriate reflection trace for computation.

Each profile occupies four lines of the tabulation. The first line gives information about the ionogram used, according to the following sets of symbols:

4	Type of Data: The 4 indicates that the data are N (h) profiles.
X, O	The polarization of the sounder echo for the ionogram trace used: X indicates extraordinary wave O indicates ordinary wave
T, B	Location of sounder: T indicates topside B indicates bottomside
YR	Year
DAY	Day number, e.g., 62 336 indicates the 336th day of 1962, or 2 December, 1962.
GMT, LONG, LAT, CHI, DIP, FH	As for Figure 44.
Q	Quality of the ionogram, according to a subjective code.
FOF2*	The ordinary wave frequency corresponding to the highest number density computed for the ionogram. This is always less than or equal to the ordinary-wave penetration frequency of the F layer.
TOTALN	The integral of N, the number of electrons in a column one square centimeter in horizontal cross section extending from the satellite to the height of reflection corresponding to FOF2*. This number is expressed in units of 10^{11} electrons per square centimeter column.
P	Number of frequencies used for computing the N (h) profile.

The succeeding lines of the tabulation for each ionogram consist of pairs of numbers. The first is the electron density; it is followed by the computed real height at which that number density occurs. The units used for the number density are 10^4 electrons per cubic centimeter, and the height is expressed in kilometers above the surface of the oblate spheroid that best approximates the surface of the earth. The first pair of points gives the electron number density at the satellite, and the height of the satellite. The electron densities listed correspond to the frequencies used for the real height calculation.

The reading errors are such that, for the best quality ionograms, the real heights are reproducible to an accuracy of about one per cent. The systematic error introduced by the assumptions on which lamination methods of computation are based have not yet been adequately investigated. Such systematic error in the computed real height has been estimated to be less than five per cent.

REFERENCES

78. 'Alouette I Ionospheric Data N (h). DRTE Data Publications: (Volume 2, No. 2, for example, contains N (h) data for selected satellite passes from Aug., 1963, to June, 1964).

79. 'Alouette I Ionospheric Data, ALOSYN.' DRTE Data Publications.

APPENDIX III

1. WAVE PROPAGATION IN THE IONOSPHERE; IONOSONDES AND IONOGRAMS

The earth's ionosphere extends upward from about 50 km to the boundary of the magnetosphere*. There are (at least) three distinctive ionospheric regions: the D region in the height range 50 to 90 km; the E region from 90 to 140 km; and the F region above 140 km. Maximum ionization occurs in the F region, at heights varying from about 250-500 km. The dominant charged constituents are free electrons and positively charged atoms of hydrogen, oxygen and helium. Less numerous constituents, such as nitric oxide ions, also play an important role in some ionospheric processes. There is no clearcut lower boundary to the ionosphere; the dividing line obviously depends on the observational methods used. Present radio-physics techniques enable the study of ionization from heights of about 50 km upward. Most of these studies have been concerned with the *total ionization*, as measured by the number density of free electrons. In recent years, however, methods to obtain more detailed information on the number density of the different ions have received increasing emphasis.

Quantitative information on the constitution of the ionosphere can be derived by analysis of data recorded by the HF sounder and VLF receiver in Alouette I. The interpretation of this data depends on a detailed knowledge of interactions between the ionospheric charged particles and the waves propagating in the ionosphere. For this purpose, the ionosphere may be considered as a 'plasma', i.e., a gas in which a significant proportion of the atoms are ionized and in which the interactions involving the neutral species may be neglected. This ionospheric plasma is anisotropic, due to the effect of the earth's magnetic field, and it can support the propagation of a number of distinct wave modes. Under appropriate circumstances energy may be transferred from one wave mode to another.

Plasma waves are also important in many other fields of science, such as astronomy, thermo-nuclear physics, solid state physics, etc., and the relevant literature is increasing at a fantastic rate. Thus this very complex subject cannot be treated adequately here, but the following introductory remarks may be helpful to the non-specialist reader.

1.1 Waves in the Ionospheric Plasma

The ionospheric plasma consists of free electrons and several types of ion. A completely rigorous mathematical solution for wave propagation in such a *multicomponent anisotropic plasma* has not yet been developed. From various partial solutions, however, it is evident that the ionosphere can support the propagation of *electromagnetic* and *electrostatic* waves. Each of these main classes includes several distinct wave modes, in which one characteristic wave parameter is the *phase velocity*: in general, radio waves have phase velocities of about the velocity of light in vacuum, electrostatic waves have velocities comparable with the thermal velocity of the charged particles, and the velocity of hydromagnetic waves is the 'Alfvén' velocity. (This velocity is proportional to the static magnetic field divided by the square root of the mass density of the charged particles.) In special circumstances, however, the phase velocities of two different wave modes may become equal, and strong coupling between the waves may then occur.

The integrated result of individual interactions between charged particles and waves is conveniently discussed in terms of a *dispersion equation* that gives the relation between the frequency and wavelength of plane waves in an infinite homogeneous plasma. This equation may be written in the general form (see for example [80]),

$$An^4 - Bn^2 + C = 0$$

* This boundary is at a varying distance of about 5-15 earth radii in the sunlit hemisphere. The size of the magnetospheric tail is still uncertain, but it probably extends well beyond a distance of 50 earth radii.

where $n = \frac{c}{u}$

and n = refractive index of the plasma
c = velocity of light in vacuum
u = phase velocity of a wave.

In the general case, the thermal motions and interactions with a wave of all the charged particles must be taken into account. The coefficients A, B, C depend on the phase velocity, and hence on n^2. The number of possible wave modes is N + 2, where N is the number of components of the anisotropic plasma. More specifically, there are two electromagnetic wave modes, and N electrostatic modes consisting of an electron plasma wave and one ion plasma wave for each type of ion.

In ionospheric research two special cases are of particular interest. The first involves a 'cold' plasma, in which the thermal motions of the charged particles can be neglected. This is an approximation where the electrostatic wave solutions vanish, leaving only the two electromagnetic wave solutions. The coefficients A, B, C are now independent of n^2 and, in general, the equation yields four values of n. These values occur in pairs with the same magnitude, but of opposite sign; each pair describes the same wave mode but with opposite directions of propagation.

The second case can be considered as a 'high-frequency approximation', where the effect of ions on wave propagation becomes negligible, and the only charged particles that need to be considered are the free electrons. The plasma is no longer necessarily 'cold', since the effects of collisions between electrons and other constituents, and of the thermal spread of electron velocities, may be included in the analysis. Collisional effects may be treated very approximately, by assuming that the collisional frequency is independent of electron velocity, and that all electrons have the same average velocity, as in the well-known Appleton-Hartree analysis[81]. Recently, more refined collisional computations have been made, as in the generalized magneto-ionic analysis of Sen and Wyller[82]. The high-frequency approximation is similar to the cold plasma approximation in that there are only two wave solutions. These electromagnetic wave modes are frequently referred to as the 'ordinary' and 'extraordinary' modes. (There are certain difficulties in the application of this terminology[83]. In general, the mode whose propagation is least affected by the presence of a static magnetic field is called 'ordinary'.)

1.2 Reflection and Absorption in a Continuously Varying Plasma; Cutoff and Resonance

Although the discussion of the preceding section applies strictly to wave propagation in an infinite, homogeneous, anisotropic plasma, the analysis can be extended to a slowly-varying plane-stratified plasma, by means of the WKB (Wentzel-Kramers-Brillouin)[84,85] solutions. In these approximate solutions the direction of energy propagation (the so-called 'ray direction') is computed according to the laws of geometric optics. The WKB solutions become invalid when the refractive index approaches zero, or when the refractive index changes appreciably within a distance of one wavelength. In such circumstances, it is necessary to refer back to the original differential equations, and attempt a 'full-wave' solution. For the earth's ionosphere, a full-wave treatment is required for wave frequencies below about 100 kc/s, and for higher frequencies near singular values (zeros and infinities) of the refractive index. When collisional losses are neglected, the refractive index, n, is entirely real or entirely imaginary. The boundaries between the real and imaginary values are the surfaces $n^2 = 0$ and $n^2 = \infty$, and these are precisely the boundaries for the regions of propagation and non-propagation for each wave mode. When the effect of collisions is included, the refractive index becomes complex, n^2 approaches zero and infinity, but does not quite pass through these values. As a result, the boundaries between regions of propagation and non-propagation are not as sharp as in the collision-free case.

In an isotropic plasma the ray path and the wave normal have the same direction, and the reflection and absorption of a wave can be simply illustrated. Consider a plane-stratified plasma in which there is a continuous variation of, say, plasma density, as illustrated in Figure 46. Regions in which n^2 is negative cannot support wave propagation; these regions are cross-hatched in the diagram. A wave propagating toward a region of minimum positive values of the refractive index, n, must be travelling in the direction of decreasing n, and is therefor refracted away from the surface $n^2 \approx 0$. If the boundary surface is sharp, as in Figure 46 (A), the wave is totally reflected; if it is diffuse, as in (B), some of the wave energy is absorbed near the boundary. This reflection phenomenon is also known as 'cutoff', because it occurs over a well-defined range of wave frequencies.

Similarly, a wave propagating towards a region of very high positive values of n must be travelling in the direction of increasing n; it is therefore refracted toward the surface $n^2 \approx \infty$ and reaches it at normal incidence. If the boundary is sharp, the wave energy is stored at the boundary in the form of currents in the plasma, oscillating at the wave frequency. This phenomenon is usually known as 'resonance'. If the boundary is diffuse, some of the wave energy is absorbed near the boundary and the resonant oscillations are damped.

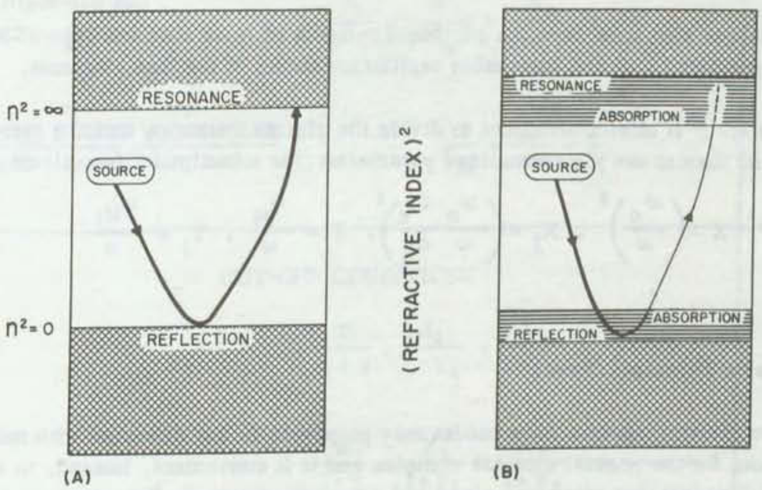

Fig. 46. Schematic Representation of a Single Wave Mode in a Continuously Varying Plane-Stratified Plasma.

Regions in which this mode cannot propagate are cross-hatched.
(A) Sharp boundaries at $n^2 = 0$ and $n^2 = \infty$;
(B) Diffuse boundaries where n^2 approaches zero and infinity.

In an anisotropic plasma the laws of geometric optics are not applicable, and the ray path may depart from the direction of the wave normal. Nevertheless, more rigorous analysis[85] shows that the reflection and absorption processes are still associated with surfaces $n^2 \approx 0$ and $n^2 \approx \infty$.

The plasma itself has a natural frequency of oscillation that arises from random inhomogeneities in the distribution of space charge. This *plasma frequency*, ω_o, is independent of the static magnetic field strength because the free electrons oscillate along the magnetic field direction. In unrationalized c.g.s. units:

$$\omega_o = \omega_N = \left(\frac{4\pi N_e^2}{\epsilon_o m}\right)^{\frac{1}{2}}$$

where N = electron number density

ϵ_o = electric permittivity of a vacuum

m = mass of the electron

e = charge of the electron.

At the plasma frequency*, the refractive index of the plasma approaches zero, even in the absence of a magnetic field. The plasma frequency is a low-frequency cutoff for the 'ordinary' wave mode. (Cutoffs for the 'extraordinary' wave are discussed in the following Section.)

Waves in the plasma may excite resonances at the frequency of circular motion of each type of charged particle around the magnetic field H. These are the gyrofrequency resonances,

$$\omega_{H_j} = \frac{\mu_o H |q_j|}{m_j} ,$$

where μ_o = magnetic permittivity of a vacuum

q_j = charge on the j th type of particle

m = mass of the j th type of particle.

Other ionospheric resonances also arise from the combined motions of more than one type of particle (multiple-ion and ion-electron resonances[57]) and from other oscillation modes of the free electrons.

In ionospheric work it is often convenient to divide the plasma frequency and the gyrofrequencies by the operating frequency, and then to use the normalized parameters (the subscript for free electrons is omitted here).

$$X = \left(\frac{\omega_o}{\omega}\right)^2 , \quad X_j = \left(\frac{\omega_o}{\omega}\frac{m_e}{m_j}\right)^2 , \quad Y = \frac{\omega_H}{\omega} , \quad Y_j = \frac{\omega_{Hj}}{\omega} .$$

1.3 The Electromagnetic Principal Waves

Each of the two electromagnetic wave modes may propagate in any direction with respect to the magnetic field. Detailed solutions for the general case are complex and it is convenient, instead, to consider the special case of waves (principal waves) that propagate along and across the magnetic field direction. If θ is the angle between the wave direction and the magnetic field direction, these waves are defined as those for which $\theta = 0$ or $\theta = \pi/2$. Results obtained for the two principal waves of a given wave mode can often be applied (at least, qualitatively) to waves travelling in arbitrary directions.

The four principal waves are named according to the polarization† of their electric fields. The two waves with $\theta = 0$ are circularly polarized with respect to the magnetic field direction, and the electric fields rotate in opposite directions. Accordingly they are called the left-handed (L), and right-handed (R), principal waves. One of the waves where $\theta = \pi/2$ is linearly polarized along the magnetic field and has a dispersion equation that is independent of the field strength; this is the ordinary (O) principal wave. The second wave where $\theta = \pi/2$ is either left- or right-handed elliptically polarized and its dispersion equation depends on the magnetic field strength; this is the extraordinary (X) wave. The polarization sense of the (R), (L), and (X) waves is such that the (R) wave interacts primarily with negatively charged particles, the (L) wave with positively charged particles, and the (X) wave may interact with either or both. A wave mode (when it exists) may have one or two principal waves; i.e., one of the principal waves may disappear because of resonance or cut-off conditions, while the other principal wave continues to propagate.

The ionospheric resonance and cut-off conditions for each principal wave are listed in Table I, where M is the ratio of ion to electron mass, for the special case of a single dominant ion. (Harmonic resonances and related cutoffs are neglected here.)

* The effect of ionic motions on the plasma frequency is very small, and has been omitted from the above formula.

† Polarization is defined here with respect to the positive direction of the static magnetic field.

TABLE 1

Principal Waves

MODE	RESONANCES		HIGH FREQUENCY APPROXIMATIONS
(L)	ion gyrofrequencies	$Y_j = 1$	
(R)	electron gyrofrequency	$Y = 1$	
(O)	none		
(X)	Multiple-ion and electron-ion	$\frac{X}{1-Y^2} + \frac{X_1}{1-Y_1{}^2} + \frac{X_2}{1-Y_2{}^2} + \text{----} = 1$	$X = 1 - Y^2$
	<u>LOWER HYBRID RESONANCE</u> (for one dominant ion)	$\frac{1}{M} = \frac{1}{Y^2} + \frac{1}{X}$	
	CUT-OFF CONDITIONS		
(L)		$\frac{X}{1+Y} + \frac{X_1}{1-Y_1} + \frac{X_2}{1-Y_2} + \text{-----} = 1$	$X = 1 + Y$
(R)		$\frac{X}{1-Y} + \frac{X_1}{1+Y_1} + \frac{X_2}{1+Y_2} + \text{-----} = 1$	$X = 1 - Y$
	(for one dominant ion)	$X = 1 - \frac{1}{M}$	$X = 1$
(X)	Same as (L) and (R) above		$X = 1 \pm Y$

As an illustration, suppose that waves are generated by a variable frequency transmitter within the ionosphere, in the height range 500-1000 km, and that the ratio of plasma frequency to electron gyrofrequency is about 1.7.

At frequencies well below the ion gyrofrequencies the phase velocity of the waves is approximately equal to the Alfvén velocity. The (R) and (L) principal waves have identical phase velocities and combine to form a linearly polarized plane wave. The (X) principal wave is circularly polarized. The (O) wave is cut off because the operating frequency is below the plasma frequency, i.e., $X > 1$. As the operating frequency increases toward the lowest ion gyrofrequency the phase velocity of the (R) wave increases and that of the (L) wave decreases and the two wave modes become spatially separated. When O^+, $H_e{}^+$, and H^+ are all present in significant quantities, the sequency of events listed in Table 2 should occur as the transmitter frequency is gradually increased:

TABLE 2

Operating Frequency (approx.) (cps)	Principal Waves	Remarks
< 25	(R,X): (L)	
25		cyclotron and collisional damping of (L) near $Y_{(O^+)} = 1$
	(R,X)	
30		damping of (X) by multiple-ion (O^+, H_e^+) resonance
	(R)	
40		transmission of (L) and (X)
	(R,X): (L)	
100		cyclotron and collisional damping of (L) near $Y_{(H_e^+)} = 1$
	(R,X)	
150		damping of (X) by multiple-ion (H_e^+, H^+) resonance
	(R)	
180		transmission of (L) and (X)
	(R,X): (L)	
400		cyclotron damping of (L) near $Y_{(H^+)} = 1$
	(R,X)	
5000		damping of (X) by electron-ion (lower hybrid) resonance
	(R)	
1.0 Mc/s		cyclotron damping of (R) near $Y = 1$

1.3		transmission of (L) and (X), when $X < 1 + Y$
	(L,X)	
1.7		transmission of (O), when $X < 1$
	(L,O): (X)	
2.1		damping of (X) near upper hybrid resonance, $X = 1 - Y^2$
	(L,O)	
2.6		transmission of (R) and (X), when $X < 1 - Y$
	(R,X): (L,O)	

In the column headed 'Principal Waves' the two electromagnetic wave modes are separated by a colon. When both principal waves of a mode are shown, this means that propagation may also occur for other values of θ, between $\theta = 0$ and $\theta = \pi/2$. In these circumstances, (and especially at HF) the entire wave mode is often labelled as 'ordinary' or 'extraordinary'. For example, at frequencies above 2.6 Mc/s, the (O) mode includes the principal waves (L,O), and the (X) mode the principal waves (R,X).

Note that, for the ratio of plasma to gyrofrequency selected here, only one principal wave, the (R) wave, is transmitted between 5 kc/s and 1.0 Mc/s. This principal wave is part of the well-known *'whistler'* mode, that is guided along the magnetic field direction. Between 1.0 - 1.3 Mc/s, electromagnetic waves do not propagate at all. This region of non-propagation disappears for smaller ratios of plasma to gyrofrequency.

1.4 Proton Whistlers

Both the (R) and the (L) principal waves propagate along the magnetic field direction. Their polarizations are such that at low frequencies the (R) wave interacts primarily with electrons and the (L) wave with ions. As noted in the preceding section, the (R) wave is the normal (i.e., electron) whistler mode, and it is not cut off anywhere in the VLF band. Moreover, it seems clear that an (L) wave entering the lower ionosphere would be cut off due to cyclotron damping by heavy ions, well below the 1000 km height of Alouette I. Nevertheless, the proton whistlers observed by Alouette I (Section 2.2 - 2.3 and Fig. 22) are preceded by sferics and SFH whistlers, and have frequency dispersions that are entirely consistent with the (L) mode of propagation.* The observed relation between the occurrence of (R) mode SFH whistlers and (L) mode proton whistlers has been explained in detail by Gurnet el al[50]. A single lightning impulse accounts for both emissions. The (R) mode is, in effect, partially converted into an (L) mode at a *crossover* frequency. This crossover occurs between two adjacent ion gyrofrequencies, and is the frequency at which both the (R) and (L) modes become linearly polarized and have the same refractive index.

This process is shown schematically in Figure 47. The solid curves represent the VLF emissions recorded by Alouette I; the broken portions of the curve would have been recorded by a VLF receiver with improved low-frequency sensitivity. The vertical dashed line at time zero indicates the sferic that produces the VLF emissions; the horizontal dashed line at about 450 cps is the proton gyrofrequency f_{H_p}, at the height of the satellite.

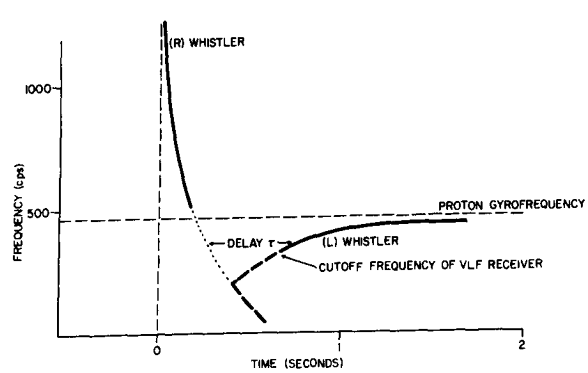

Fig. 47. Schematic Representation of the Partial Conversion of an (R) Mode SFH Whistler to an (L) Mode Proton Whistler.

The transmission bandwidth of the proton whistler at a given height depends on the crossover frequency and the proton gyrofrequency. This crossover frequency (about 200 cps in Fig. 47), in turn, depends on the number density of protons; it decreases with height and determines the low-frequency limit of the proton whistler. The proton gyrofrequency determines the upper-frequency limit of the proton whistler, and this limit also decreases with height. The (L) whistler has a smaller propagation velocity than the (R) whistler, and the delay times τ between the arrival of the two waves at the satellite are indicated in Figure 47. When $\tau = 0$, the crossover frequency occurs at the height of the satellite.

* Both the SFH and the proton whistlers may propagate over a range of angles, centered on the magnetic field direction. By definition, the (R) and (L) principal waves propagate precisely in the $\theta = 0$ direction. The terms (R) mode and (L) mode are used here to indicate that the polarizations and frequency dispersions of the waves under consideration do not differ significantly from that of the (R) and (L) principal waves.

Note that attenuation of the (R) whistler extends to a frequency F above the proton gyrofrequency at the satellite. The attenuation between F and f_{H_p} is due to conversion of (R) to (L) waves at heights below the satellite; the (L) waves within this bandwidth are absorbed as the proton gyrofrequency decreases with height.

1.5 HF Ionosondes and Ionograms

At sufficiently high frequencies, the effect of ions on wave propagation may be neglected. At such frequencies the variation of electron number density, N, with height, h, in the ionosphere is conveniently studied by means of an HF ionosonde. The sounder transmissions at a particular frequency penetrate into regions of increasing electron density, until each of the two wave modes is totally reflected. The distance of a reflecting region from the HF ionosonde can be computed from the observed time delay between the transmitted signal and the ionospheric echo (in essentially the same way that radar equipment is used to measure the distances of solid reflecting objects). The distance is approximately one-half the time delay, multiplied by the velocity of light in vacuum. The approximation arises from the fact that under some circumstances the radio wave is slowed down and refracted by the ionosphere. In vertical soundings, the approximate ionospheric height obtained in this way is called the 'equivalent or apparent height, h'. A record of the variation of apparent height with frequency (or with critical electron density) is termed an 'ionogram'. Conventionally, heights computed by taking into account the effect of wave retardation on the ionograms are often called 'real heights' to distinguish them from the apparent heights.

In oblique soundings the transmitter and receiver may be separated by large distances and it is much more difficult to compute 'real heights' from the measured time delays.

The height (about 250 - 500 km) of maximum ionospheric ionization is also the maximum height at which HF radio waves that originate near the ground can be totally reflected by the ionosphere. Accordingly, although the ionosphere below the F-layer maximum has been studied extensively by means of radio probes, there is relatively little information on the ionosphere above this maximum. Some information has been obtained through studies of the propagation of VLF whistlers generated by lightning flashes, and by the scattering of UHF waves from free electrons. More recently, probes in rockets and satellites have obtained data at great heights. The sweep-frequency topside sounder in Alouette I, however, is the first experiment to provide ionospheric data, above the F-layer maximum, comparable in quantity and quality to the existing data obtained below this height.

Schematic drawings of the main features of topside ionograms, along with representative Alouette I ionograms, were presented in Figures 3, 17, 19, 24, and 43; and Figure 19 (a) is repeated here as Figure 48 for convenience in discussion. A vertical section of an ionogram displays the apparent distances of ionospheric echoes and scatter returns, or the duration of local ionospheric resonances, at a fixed frequency. Echo distances on the ionograms change with operating frequency, and the resultant curves of apparent distances versus frequency (h' f) are called 'reflection traces'. The cutoff conditions given in the preceding section for principal waves in a homogeneous plasma may (with some precautions) be applied to vertical soundings in the earth's ionosphere. It will be recalled that there are three cutoff conditions; accordingly there are normally three reflection traces, as in Figure 48. At satellite height, the ordinary wave mode is reflected at the plasma frequency f_N, where $X = 1$. (The ordinary wave reflection trace is not usually visible at the height of the satellite, but the plasma frequency resonance spike always appears.) The extraordinary wave mode has two cutoff conditions, at $X = 1 \pm Y$, and there are two corresponding reflection traces. The lower frequency reflection at $X = 1 + Y$ is usually called the Z-wave; it is labelled $f_Z S$ at the height of the satellite; the upper frequency reflection at $X = 1 - Y$ is the X-wave, labelled $F_X S$ at satellite height*. At middle latitudes the three reflection traces are usually quite distinct, whereas at high latitudes the traces tend to overlap. The crossover of the O and X reflection traces (between about 3.0 to 4.5 Mc/s in Figure 48) is caused by the greater retardation of the X wave at the lower frequencies. (The apparent range of an echo is greater than the 'real' range, whenever the wave is significantly retarded by the ionosphere.)

* The $X = 1 + Y$ reflection condition is not normally visible on bottomside ionograms taken at low and middle latitudes. It was identified on high-latitude bottomside ionograms after the other two reflection traces had already been named 'O' and 'X'.

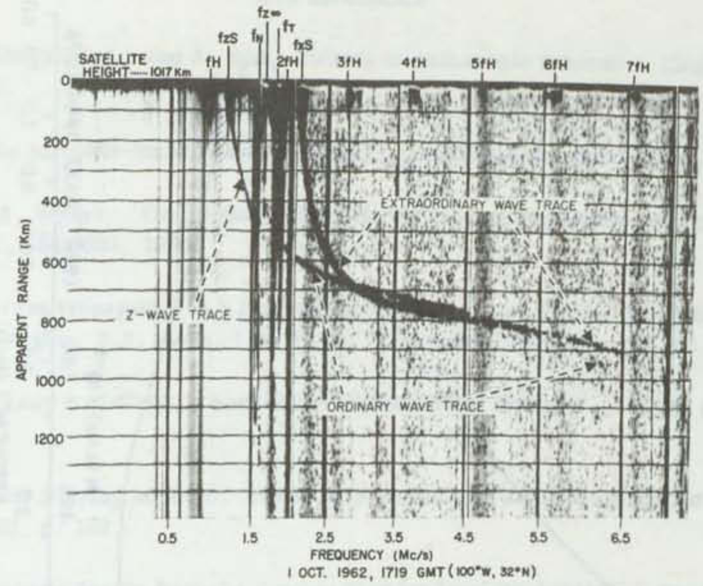

Fig. 48. Topside Mid-Latitude Ionograms Showing Ionospheric Resonances at the Height of the Satellite.
This is the same as Fig. 19(a) and is repeated here for convenience in reference.

Figures 49(a) and 49(b) show representative ionograms taken from a height of 1031 km, and from the ground, during 'quiet' ionospheric conditions and at almost the same time and geographic location. The vertical scale of the ground ionogram, by long-established convention, shows the apparent height of reflection. On the other hand, the scale of the satellite ionogram shows the apparent range of the reflecting region from the satellite. Ordinary and extraordinary reflection traces are visible on both ionograms. The effect of wave retardation on the vertical scales was computed, and it was then possible to combine the top- and bottom-side data to show the profile of electron density vs. height from 100 to 1000 km (Fig. 49(c)).

One major difference between top- and bottom-side ionograms arises from the fact that the Alouette sounder antennas are embedded in a plasma, i.e., the ionosphere. At certain resonant frequencies, radiated energy may be stored near the satellite where it can be detected for an appreciable time after the transmitter is shut off. This resonance effect is visible on the ionograms as an apparent elongation of the transmitter pulses near the relevant frequencies; these elongations are known as 'spikes'.

In addition to reflection traces and resonant spikes, topside ionograms may show reflections from the ground, echoes from sporadic E-layer ionization, long-range echoes arising from guided propagation along the direction of the magnetic field (Sec. 2.2.3.3), as well as the 'resonance trace' that appears as a spur on the X-trace at a frequency $2f_H$ (Sec. 2.3.2), etc.

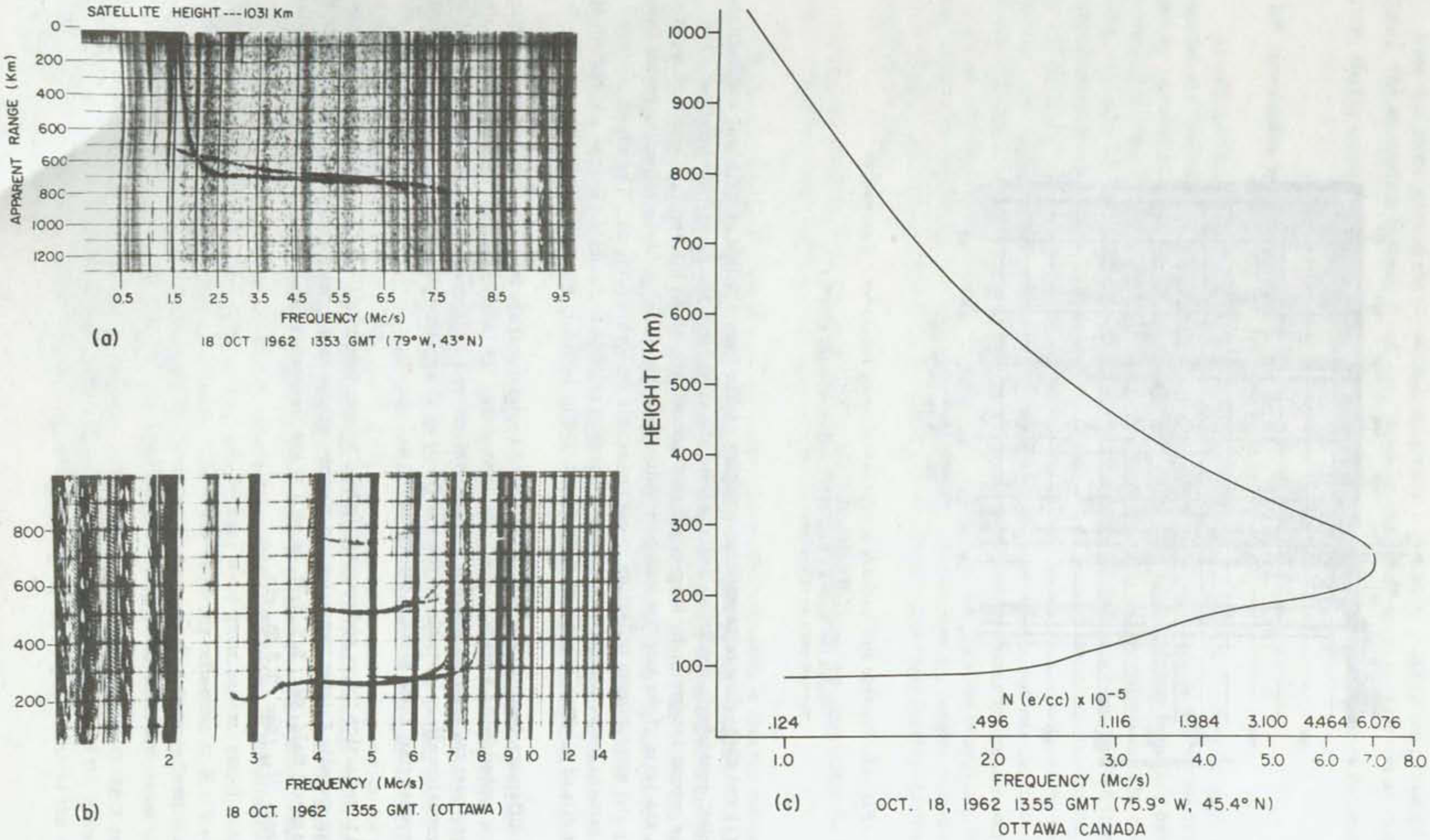

Fig. 49. Representative Top and Bottom-Side Ionograms at Ottawa, Canada, and the Computed N(h) Profile,
(after Nelms (86)).

(a) Alouette I ionogram.
(b) Ionogram from a ground-based ionosonde. (The traces visible at about 500 and 750 km are due to multiple reflections between the ionosphere and the ground.)
(c) The height profile of electron density, N(h), computed from 47(a) and 47(b).

REFERENCES

80. Allis, W.P., Buchsbaum, S.J., and A. Bers. 'Waves in Anisotropic Plasmas.' Cambridge, Mass., The M.I.T. Press, 1963.

81. Ratcliffe, J.A. 'The Magneto-ionic Theory.' London, Cambridge University Press, 1959.

82. Sen, S.K., and A.A. Wyller. 'On the Generalization of the Appleton-Hartree Magnetoionic Formulas.' Jour. Geophys. Res., **65**, 3931, 1960.

83. Barrington, R.E. 'Wave Propagation in a Homogeneous Ionized Gas; Physics of the Earth's Upper Atmosphere'. ed. C.O. Hines, I. Paghis, T.R. Hartz, J.A. Fejer. New Jersey, Prentice-Hall Inc., 1965, p. 371.

84. Jeffreys, Sir H. and Lady B. Jeffreys. 'Methods of Mathematical Physics.' London, Cambridge University Press, 1956.

85. Budden, K.G. 'Slowly Varying Medium. The W.K.B. Solutions; Radio Waves in the Ionosphere.' Cambridge University Press, 1961, p. 128.

86. Nelms, G.L. 'Ionospheric Results from the Topside Sounder Satellite Alouette.' Space Research, **IV**, Amsterdam, North-Holland Pub. Co., 1964, p. 437.

87. Petrie, L.E. 'A Preliminary Analysis of the Alouette Ionospheric Data.' Electronics and Communications, **II**, 32, 1963.

DEFENCE RESEARCH BOARD

DEPARTMENT OF NATIONAL DEFENCE
CANADA

DEFENCE RESEARCH TELECOMMUNICATIONS ESTABLISHMENT

ALOUETTE I: THE FIRST THREE YEARS IN ORBIT

PART II – ELECTRICAL DESIGN AND PERFORMANCE

by

C.A. FRANKLIN

DRTE REPORT NO. 1159-2

PCC No. D48-02-04-01

Submitted January 1966
Published April 1967
OTTAWA

66-374

TABLE OF CONTENTS
PART II

ALOUETTE I: THE FIRST THREE YEARS IN ORBIT

PART II – ELECTRICAL DESIGN AND PERFORMANCE

by

C.A. Franklin

SUMMARY

This part of the Alouette report is concerned with the design and performance of the electrical systems. The primary experiment uses a sweep-frequency pulse-sounding technique to determine electron density distributions in the topside of the ionosphere. Also included among the electrical systems is equipment for secondary experiments. These are designed to measure the flux densities of energetic particles, and the amount of background noise at high (HF), and very low (VLF), radio frequencies. In addition to apparatus for the experimental program, sixty 'housekeeping' channels, concerned mainly with engineering data about the day to day operation of the equipment, are carried.

The design of the ionospheric sounder required the solution of some difficult electrical and mechanical problems and called for use of an unusually large antenna system consisting of two crossed dipoles measuring 150 ft. and 75 ft. tip-tip, respectively. These antennae are connected via a matching network to a 100 watt 1-12 Mc/s solid-state transmitter.

Three VHF transmitters are used, two for telemetry and one for tracking. Data bandwidth for the primary experiment is 0.5 c/s - 15 kc/s and for the VLF experiment 400 c/s - 10 kc/s. All other data channels have bandwidths in the range 0.3 c/s - 150 c/s.

A seven tone command system provides means for ON-OFF control of the spacecraft, for selection of spare batteries, transmitters, and other redundant units, and for choice of a number of possible operational modes.

Except for normal wear-out of a junction particle detector, all systems have functioned as intended since Alouette I was launched in 1962.

At the time of writing this report this Canadian satellite has been in orbit for over three years. Since it carries 6480 solar cells and 7000 other components, a high level of system and component reliability has been demonstrated.

1. INTRODUCTION

Canada's first satellite, Alouette I*, was launched from the Pacific Missile Range in California by a Thor-Agena B vehicle on September 29th, 1962, at 0705 U.T. The spacecraft was placed in a near-circular 80° prograde 1000 km circular orbit, and the precise orbital parameters on October 29th, 1962, one month after launch, were as shown in Table 1.

* Prior to launch, Alouette I was known as S-27, and immediately after launch it was designated 1962 BETA ALPHA. It was renamed Alouette as soon as confirmation was received that all systems were functioning as intended and that the desired orbit had been achieved. The name 'Alouette', the French word for the high flying bird, the Lark, has connotations that extend deep into early Canadian colonial history. It is also the title of one of the country's best known and most nonsensical folk songs, originally brought to North America from France many centuries ago.

TABLE 1

Period	105.409 minutes
Inclination	86.463 degrees (prograde)
Right Ascension of Ascending Node	143.939 degrees
Argument of Perigee	183.829 degrees
Mean Anomaly	87.890 degrees
Perigee	993.80 kilometers
Apogee	1033.23 kilometers
Rotation of Line of Apsides	2.566 degrees per day
Nodal Regression	0.984 degrees per day

The successful launching and operation of Alouette I provided scientists with a new and powerful means of studying the physics of the ionosphere. To the long established, world-wide network of ground-based bottomside ionospheric sounding stations, was now added a scientific satellite carrying equipment designed to sound the topside of the ionosphere up to a height of 1000 km. The design of the sounder proved exceptionally difficult and involved the development of some highly sophisticated, solid-state, sweep-frequency, pulse sounding equipment that required significant advances in state of the art electrical and mechanical technology. It is the purpose of this part of the report to describe the electrical design of the spacecraft and to discuss its characteristics and operational performance.

The primary purpose of the spacecraft was to enable observations of the earth's ionospheric envelope from above its top side, and by means of radar-type sounding pulses emitted over a carefully chosen range of frequencies at which echoes can normally be received, to determine the diurnal, seasonal, geographical, and other variations that occur in the electron number density distributions in the upper constituents of the regular and sporadic ionospheric layers.

In addition to the sounding equipment, other apparatus carried in the satellite enables the flux density of high energy particles at the satellite height to be measured, and makes observations of the electrical background noise at low and high radio frequencies. For 'housekeeping' purposes, sixty channels concerned mainly with engineering data about the day to day operation of the satellite and its equipment are included.

Actually, four separate types of measurement are undertaken from Alouette I, which at the time of writing, more than three years after launch, is still operating successfully in its planned orbit.

The four types of measurement undertaken from this orbit involve the main ionospheric sounding experiment, observations of ambient cosmic and solar noise levels at frequencies between 0.4 and 12 Mc/s, particle detectors to determine energetic particle and ion flux densities, and a low-frequency receiving system designed to pick up VLF emissions, such as whistlers, between 400 cps and 10 kc/s.

Because of the wide range of the frequency sweep (1 to 12 Mc/s)* required for the sounding measurements, relatively long, extendible, antenna dipole elements are necessary. One dipole measures 150 feet from tip to tip and is used for soundings below 4.8 Mc/s; the other measures 75 feet from tip to tip and is used for the higher sounding frequencies up to 12 Mc/s. These antennae extend outward from the equator of the satellite and are orthogonal, i.e., are arranged in a crossed-dipole configuration.

The design of these antennae employed a principle initiated within the National Research Council of Canada for another application. This is similar to the principle used in the design of the common

* Although the sounding receiver covers a frequency range of 0.4 to 12 Mc/s, echoes are rarely observed below 1 Mc/s because of the bandwidth limitations of the sounding transmitter and its associated antenna system.

collapsible steel rule, wherein a slightly concave spring steel tape is pulled out from a spool turning inside a compact container. In the antenna application the separate dipole elements are fabricated from 0.004 inch by 4 inch pre-stressed, especially treated, strips of spring steel. On extension, these strips, which are normally wound in flat form on spools within the spacecraft, are pushed through a circular orifice so that they emerge in tubular form with overlapping edges. The strips are pre-stressed in such a way that as they unwind and emerge from the satellite the edges curl tightly together and form overlapping seams under strong spring tension. The result is a semi-rigid continuous tube slightly under one inch in diameter.

The four sections of the two sounding dipoles are pushed out simultaneously from their separate housings inside the satellite by a single dc motor and associated gear trains, at a rate of about four inches per second. During the launch phase of Alouette I these antennae were extended from the satellite immediately following the separation of the spacecraft from the launch vehicle. On full extension the individual dipole elements measure 73.5 and 36 feet, respectively, to form half sections of electrical dipoles separated at their centers by the girth of the spacecraft.

Alouette I is relatively large for a scientific satellite. It weighs 320 pounds, is 42 inches in diameter and 34 inches high. Its near-spherical shape (Fig. 1) was chosen to simplify passive temperature control and to ensure relatively constant battery charging currents from its 6480 solar cells, throughout all possible orientations of the satellite with respect to the sun. The solar cells are mounted on panels attached to the outer surface of the spacecraft, and are designed to provide an average power of twelve watts for the worst case condition in which the orbit is sunlit for only 66 per cent of the time.

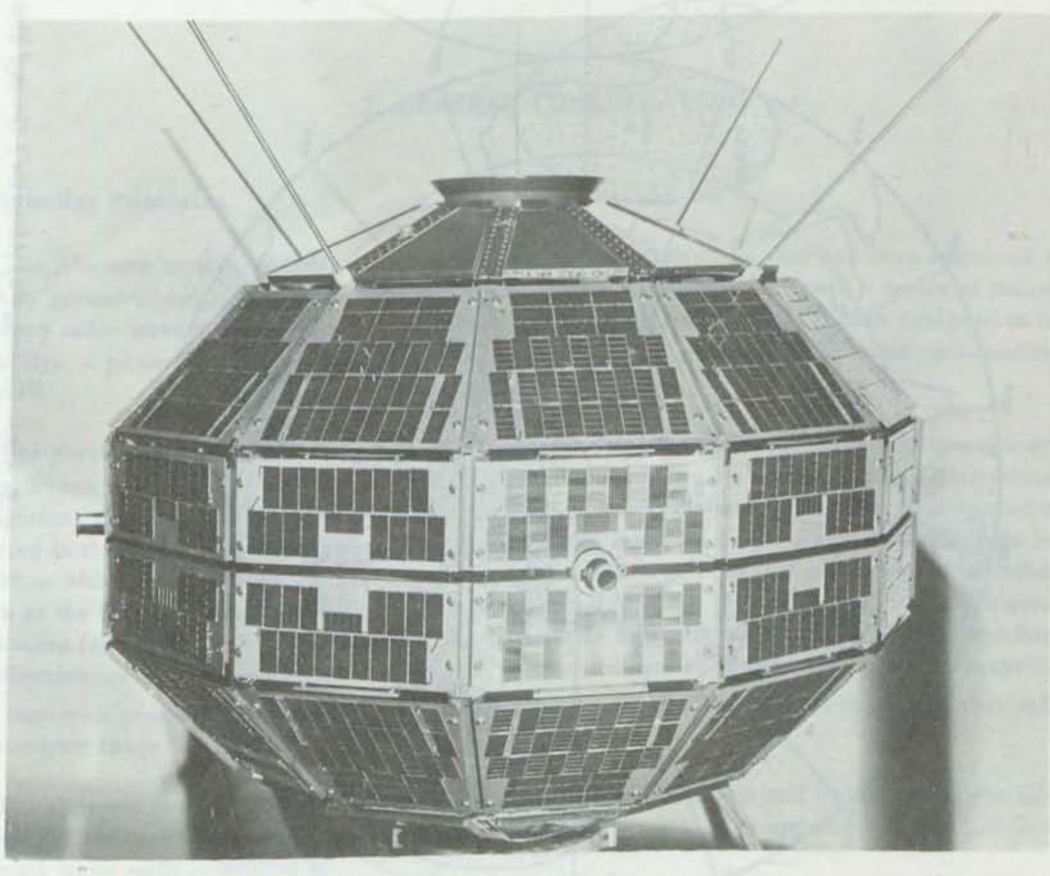

Fig. 1. Alouette I.

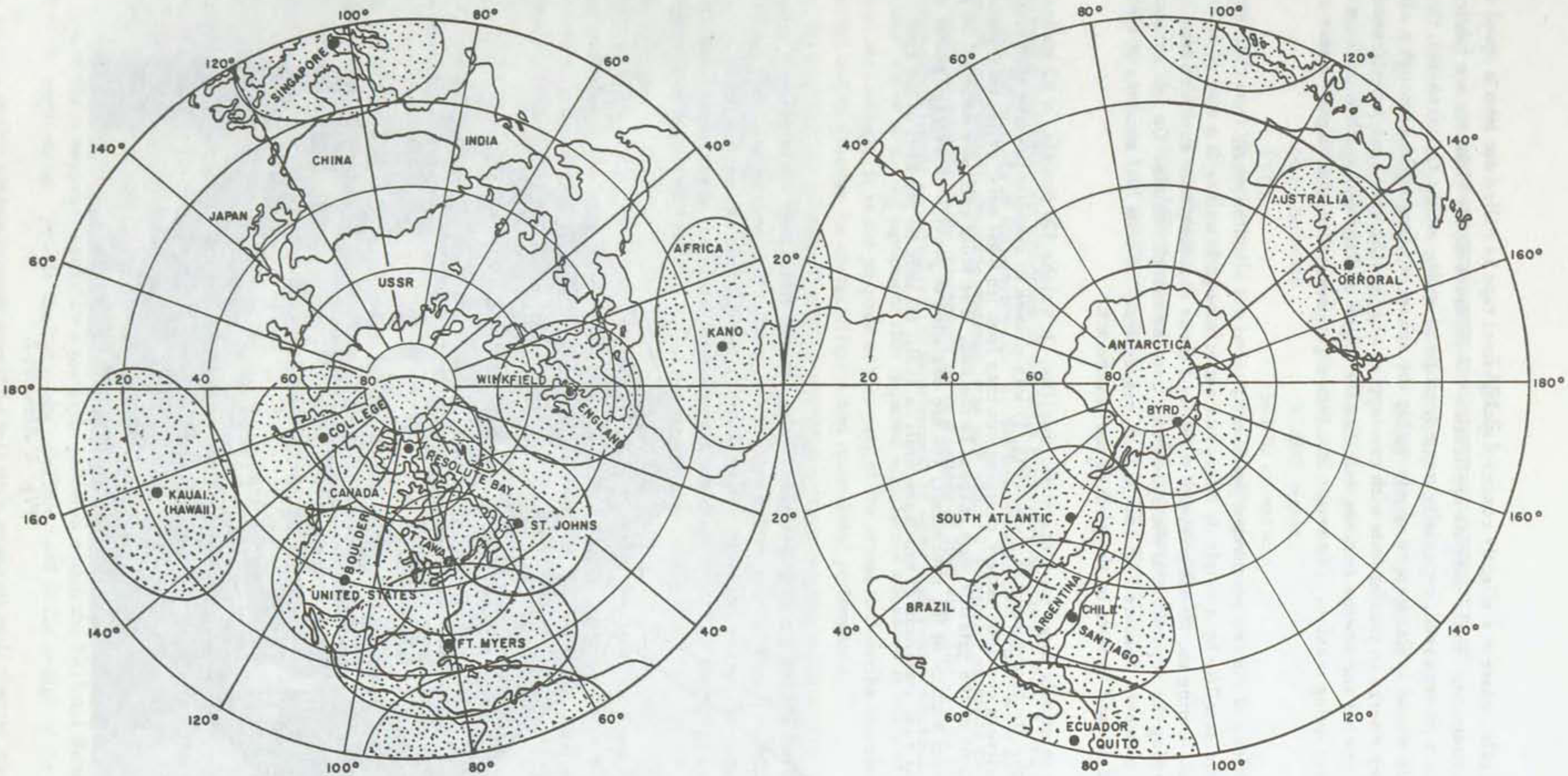

Fig. 2(a). Coverage of Alouette I Ground Stations for Antenna Elevations ≥ 15°.

Data storage was considered impracticable because of the relatively high bandwidth and extended low-frequency response of the primary experiment and the complexity of the ionospheric data. Hence it was decided to control the spacecraft from a network of widely dispersed ground stations (Fig. 2) that also collect the data. The shaded areas on Figure 2(a) indicate the region of space about each station where the satellite subtends an angle ≥ 15 degrees above the horizon (slant range ≤ 1400 miles). In fact, the satellite telemetry and command systems have operated adequately to near zero horizon angles (corresponding to a slant range of approximately 2200 miles) with the result that for many stations the coverage is as illustrated in Figure 2(b). Each station, as directed, turns on the satellite by coded commands, and collects data in real time for approximately 10 minutes, at the end of which interval the satellite is turned off by an internal timer. In the design of the command, tracking, and telemetry systems, compatibility with the NASA STADAN stations was mandatory. This factor determined the command frequency of 122.900 Mc/s and placed the telemetry and tracking frequencies within the 136-137 Mc/s band.

The design objective of Alouette I was an operational life of about one year. To achieve this it was considered necessary to add redundant batteries, transmitters and command receivers. Such redundancy led to a relatively complicated command system but resulted in a payload that is operationally very flexible.

All satellite systems, including the sounder, were completely transistorized to increase reliability and to meet limitations on weight, size and power consumption. During construction of the satellite many challenging design problems were encountered. Some of these, as met and solved in the telemetry transmitters and power amplifier, involved state-of-the-art design limitations. Others, as encountered in the sounder's receiving equipment, arose because of the multi-octave requirements of the circuitry and the associated radio frequency interference that ensued [1,2,3]. All were solved in time for the scheduled launching.

2. GENERAL CONSIDERATIONS

2.1 Sounding Principles

The Alouette topside sounder uses essentially the same technique that has been employed for many years by ground-based ionosondes. In this, a conventional ionosonde transmits a series of pulsed high frequency radio waves, over a wide range of frequencies, from a wide-band antenna designed to radiate vertically. A pictorial representation of bottomside and topside sounding is shown diagrammatically in Figure 3.

The presence of the earth's magnetic field in the ionosphere splits the wave into two characteristic modes, known as 'ordinary' and 'extraordinary' waves. (See Part 1 for a more detailed discussion of wave propagation in the ionosphere.) The two wave modes encounter different refractive indices, and are refracted in the ionosphere from different heights. As the sounding frequency is increased, the ionization density at which each mode is reflected, for vertical incidence waves, also increases, until reflection occurs at the height of maximum ionization, referred to as the peak of the F layer. At still higher frequencies (above the 'critical' frequency) the ionosphere becomes transparent. The critical frequencies for reflection are abbreviated as f_oF2 and f_xF2, for the ordinary and extraordinary waves respectively. They vary with geomagnetic latitude, time of day, season and sunspot number; at present they fall within the frequency range 1.5 - 13 Mc/s.

The apparent heights (or ranges) of the reflecting surfaces are obtained by measuring the time delays between the vertically transmitted pulses and the received echoes. The apparent height h' of reflection of a specific wave mode is defined by

$$h' = \tfrac{1}{2} ct,$$

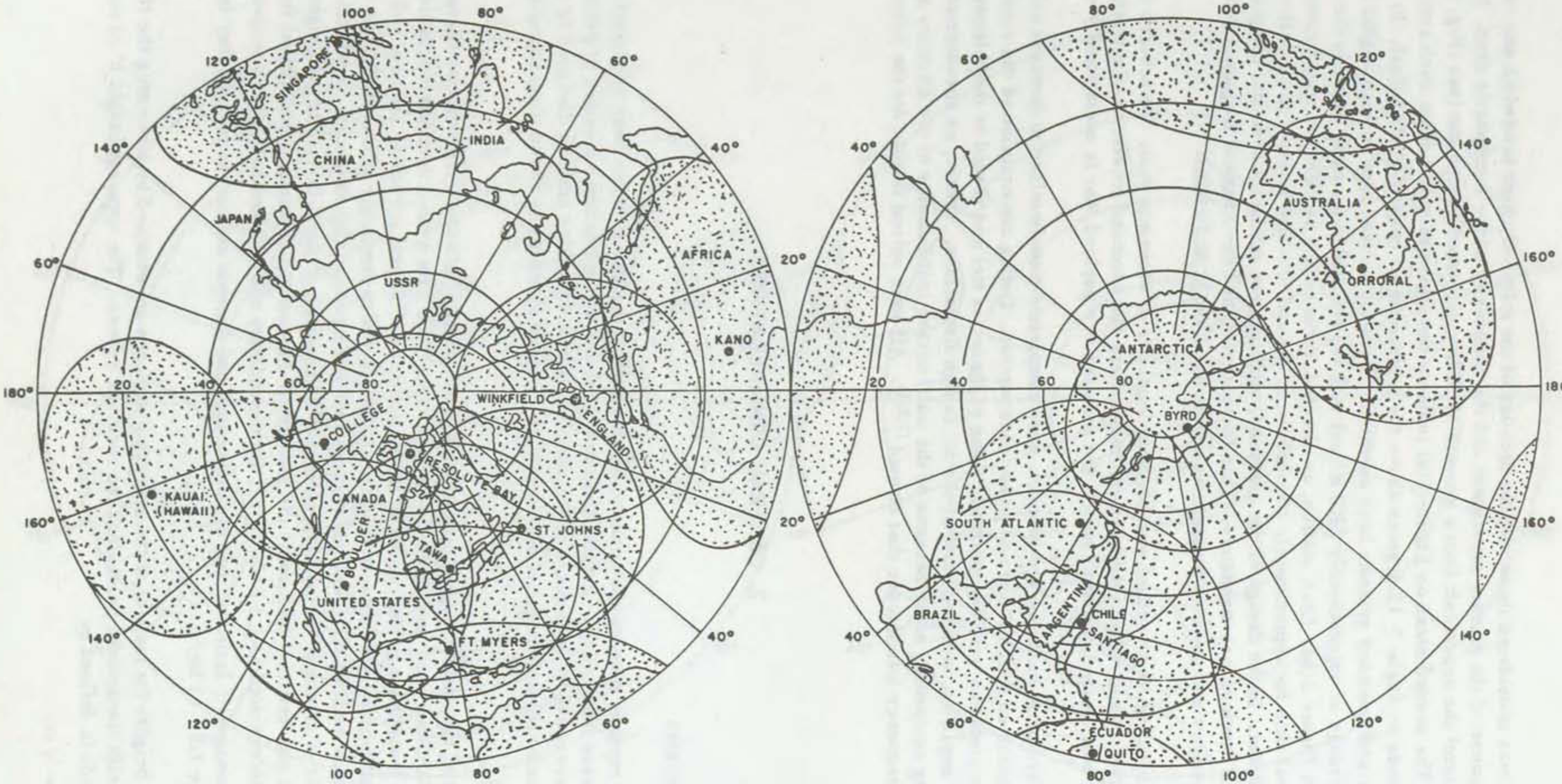

Fig. 2(b). Coverage of Alouette I Ground Stations For Antenna Elevations $\geq 0°$.

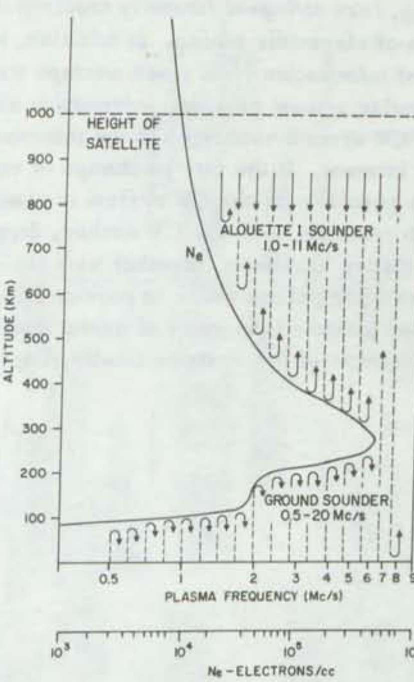

Fig. 3. Ionospheric Sounding.

where c is the velocity of light in vacuum and t is the measured time delay of the echo. This reflection information is usually presented as a plot of apparent height versus frequency, known as an 'ionogram'. A mid-latitude topside ionogram showing the reflection traces, the penetration of the ionosphere at the critical frequencies, together with echoes from the ground at still higher frequencies is shown in Figure 4.

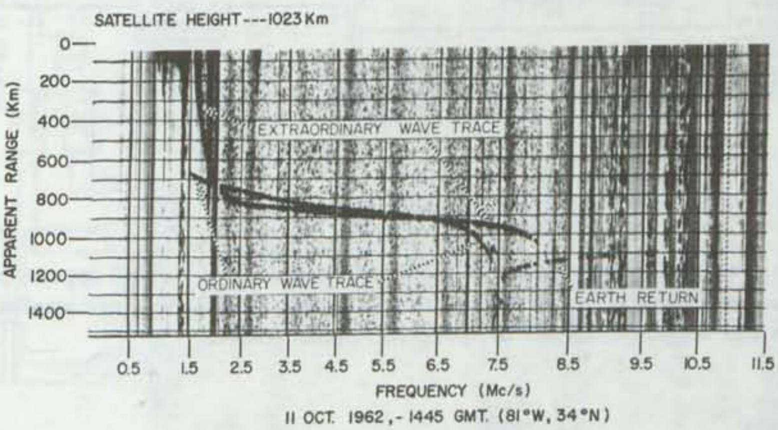

Fig. 4. Alouette I Ionogram.

2.2 Alternatives Considered

During the early phases of system design several possible sounding methods were considered. Among these was the sweep-frequency CW sounding technique in which range to a reflecting region is determined by measuring the frequency difference between the transmitted and received signal. As a result of these preliminary studies, and despite the greater peak power required, the pulse method was chosen, instead of a sweep-frequency CW system because it involved more commonly used and proven techniques, less serious receiver-transmitter isolation problems, *less stringent linearity requirements for the sweep frequency oscillator,* and enables a simpler form of electronic tuning. In addition, it can be shown that while both systems offer the same total amount of information for a given average transmitter power, they differ in what this information is about. The pulse system provides information almost entirely about range—the parameter of main interest—while the CW system sacrifices range information to provide doppler information about velocity—a parameter of lesser interest. If the rate of change of virtual range with sounding frequency is sufficiently low, it is theoretically possible for the CW system to provide better range resolution than does a conventional pulse system. In practice, with the CW method, doppler effects, linearity variations, and frequency jitter in the sweep frequency oscillator, together with rapid changes in virtual range with sounding frequency will normally enable the pulse system to provide better range resolution. A further advantage is that the pulse system can produce ionograms of useful quality with very simple receiving and data read-out equipment[4]. Block diagrams of the systems finally adopted for Alouette I are shown in Figures 5 and 6.

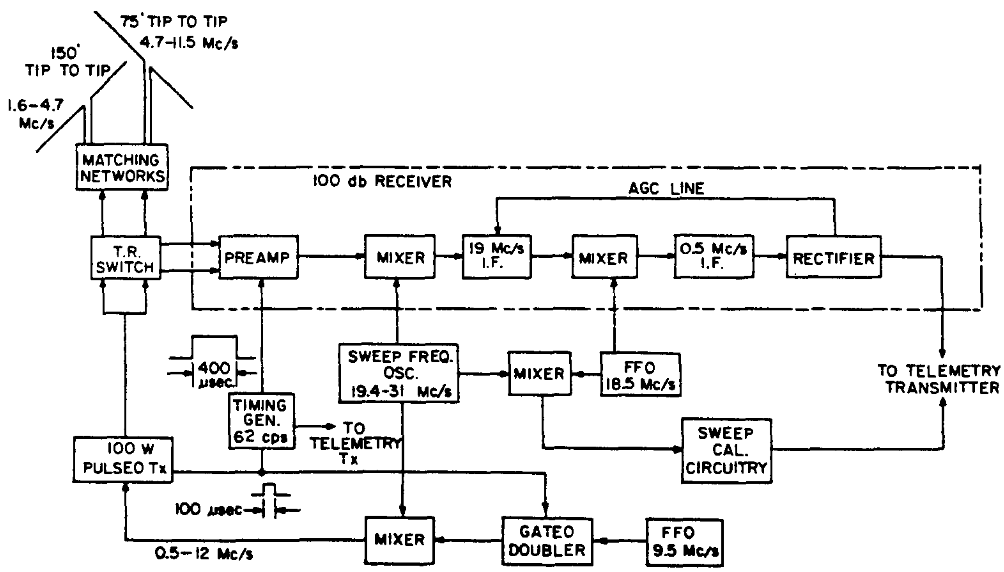

Fig. 5. Ionospheric Sounder.

In future applications, a possible alternative to the conventional pulse method appears to be the binary-coded pulse-compression technique [5]. However, this possibility does eliminate amplitude information, and there may be serious doppler problems in spacecraft applications.

2.3 System Parameters

The height of maximum electron density in the F layer varies between 250 and 500 km. Therefore, for a satellite height of 1000 km in a circular orbit, the true height of the spacecraft above this region varies between 500 and 750 km. To obtain satisfactory resolution of f_oF2 and f_xF2 under these conditions it was considered necessary to design for a ratio of apparent range to true range of at least two to one, corresponding to an apparent range of approximately 1600 km (1000 miles). The transmission path loss was

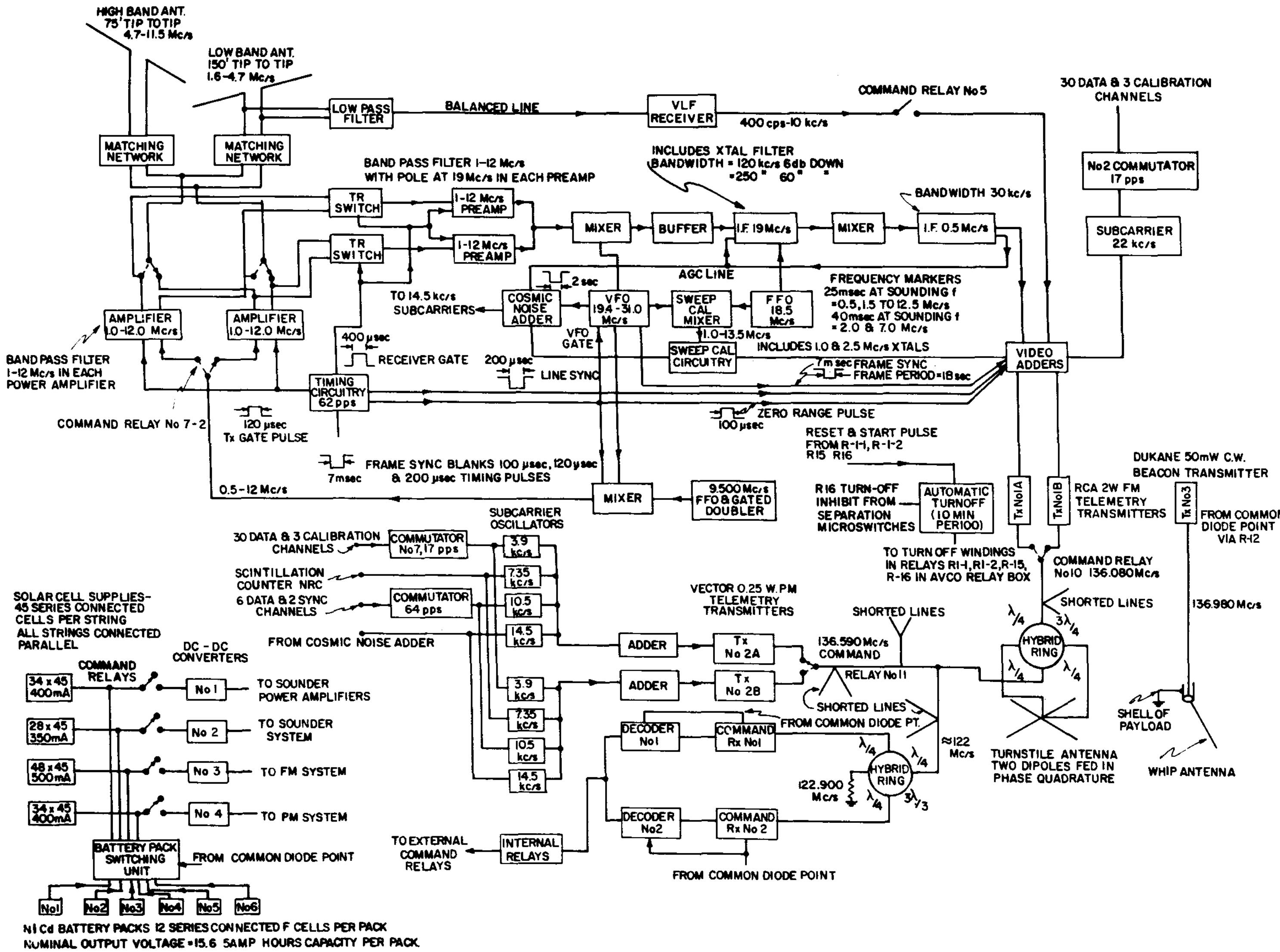

Fig. 6. Alouette I Simplified Block Diagram.

calculated by assuming a simple inverse square law relation between the received signal strength and the apparent range. Although this assumption is not strictly true [6], the error involved is less than 20% and can be neglected when considered with other system uncertainties. In calculating the necessary transmitter power, an apparent range of 1000 miles was used; however, in setting the pulse repetition frequency of the sounder a line period of 16 ms was chosen to correspond with an apparent range of 1600 miles. This period was selected for compatibility with the U.S. fixed-frequency sounding satellite known as S48 (line period 14.9 ms) and also to permit reception of echoes with increased delay times under conditions of reduced antenna pattern fading and lower background noise.

Since the character of the ionosphere varies relatively rapidly with geomagnetic latitude in the polar regions, it was considered that the maximum change in position of the satellite that could be allowed during the course of any sounding sweep was one degree of latitude. Thus, because of the 1000 km circular orbit, and a tangential velocity of 7 km/sec, a sweep time of 15 seconds or less was required. In Alouette I the sounding frequency is swept linearly from 0.4 - 12.0 Mc/s every 11.8 seconds, the sweep being repeated every 18.2 seconds*. The frequency is continuously swept, rather than stepped, to achieve a desired frequency resolution of less than 20 kc/s. At the time the design was carried out it appeared impracticable to design a stepped system with a resolution even approaching this figure.

The RF pulse length of 100 μs was chosen to provide a virtual range resolution to within 10 miles. For a line period of 16 ms, delay times from 100 μs to 16 ms can, in theory, be measured with a minimum resolution of 100 μs. In practice, the minimum delay time that can be measured is 220 μs, (as measured from the leading edge of the transmit pulse) and this is only achieved at high sounding frequencies. For frequencies below 2 Mc/s, noise and ringing effects, following each transmitter pulse, desensitize the sounder receiver for periods of up to 600 μs. This minimum delay time of 220 μs means that the sounder cannot detect targets closer than 22 miles from the spacecraft.

A calculation of the pulse power required from the sounder transmitter is summarized in Table 2. Assuming a maximum time delay of 16 ms, and allowing for tolerances on filters, oscillator frequencies and sweep rates, the receiver IF bandwidth of 33 kc/s is near optimum for a pulse width of 100 μs and a sweep rate of 1 Mc/s/s. The path loss is calculated for zero reflection loss, isotropic transmitting and receiving antennae, and assumes that the true range has been increased by a factor of approximately 2.5, owing to retardation in the ionosphere. Cosmic noise and transmission path losses are calculated for a frequency of 2 Mc/s.

TABLE 2

Peak Power Calculation for Ionospheric Sounder

KTB (BW = 1 c/s)		- 204 db w
Cosmic noise, 2 Mc/s	+ 45 db	
Receiver bandwidth, 33 kc/s	+ 45	
O and X splitting	+ 3	
Polarization loss	+ 3	
Antenna mismatch	+ 10	
Receiver signal/noise	+ 10	
Path loss, 1000 miles range, 2 Mc/s	+ 108	
Antenna pattern fading	+ 6	
Subtotal		+ 230 db
		+ 26 db w
Visual integration, ionogram analysis		- 6
Required transmitter pulse power		+ 20 db w = 100 watts

* This sweep range should not be confused with the previously quoted figure of 1.0 - 11.5 Mc/s, which takes into account the bandwidth limitations of the sounder transmitter.

The received signal power P_R is given by

$$P_R = \frac{P_T}{4\pi R^2} \frac{\lambda^2}{4\pi}$$

where P_T is the transmitted power and R the range.

The transmission loss for mirror reflection is given by

$$L_T = 20 \log_{10} R + 20 \log_{10} f + 42.6$$

where R is the range in miles to the reflecting surface, f is the frequency in Mc/s, and L_T is in db.

Since the antenna capture area is inversely proportional to f^2, the combined effect of cosmic noise and path loss would be constant if the cosmic noise temperature varied inversely as f^2. At the time the system design was carried out, the NBS curve (see curve 'a' of Fig. 7) was assumed to be valid for cosmic noise. The resultant path loss plus cosmic noise curve is shown in Figure 8. A partial check of the NBS curve was carried out by an experiment carried in Transit II (1960η 1) in June 1960 at 3.8 Mc/s[7,8]. The measured value of 44 db above kTB[8] was 6 db above the NBS curve[9] implying that the NBS curve was low. In fact as seen in Figure 7 the NBS curve compares favourably with the lowest measured noise levels on Alouette I. The original system calculations were, in this respect, slightly optimistic.

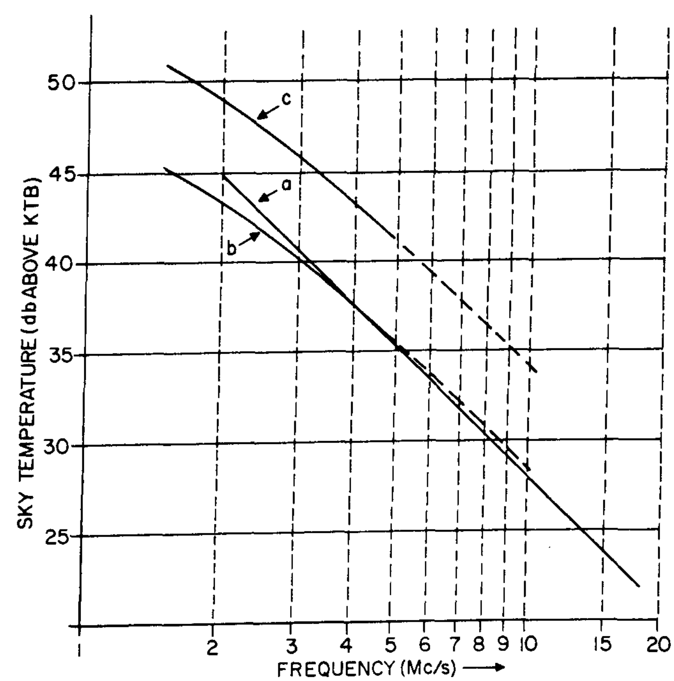

Fig. 7. Cosmic Noise Temperature versus Frequency.
(a) *NBS* $f^{-2.4}$ *curve*
(b) *minimum Alouette I curve*
(c) *maximum Alouette I curve.*

The antenna mismatch loss of 10 db was also somewhat optimistic, as compared with the calculated curves of antenna mismatch loss vs frequency shown in Figure 9. The actual measured value at 2 Mc/s into a dummy load was found to be 15 db. This measured value may, however, have been pessimistic due to the effect of the capacity of the rolled-up antennae.

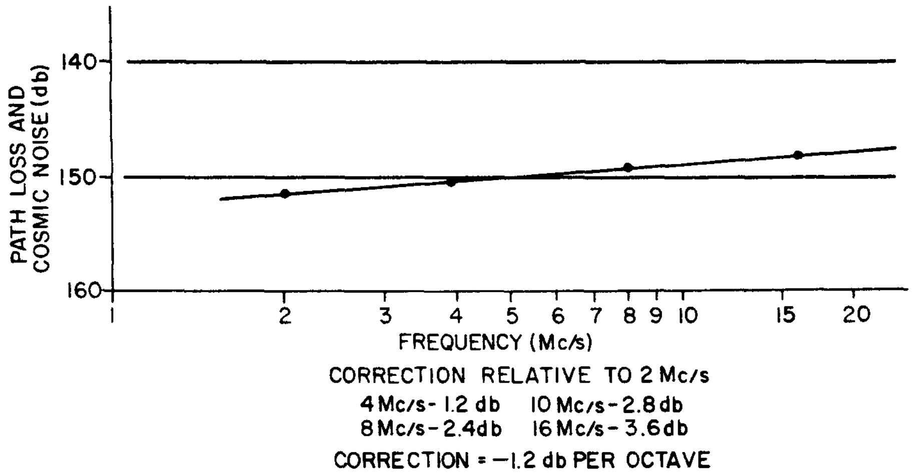

Fig. 8. Path Loss plus Cosmic Noise for a Range of 1000 Miles.
(Sky Temperature 45 db above KTB at 2 Mc/s and Proportional to $f^{-2.4}$.)

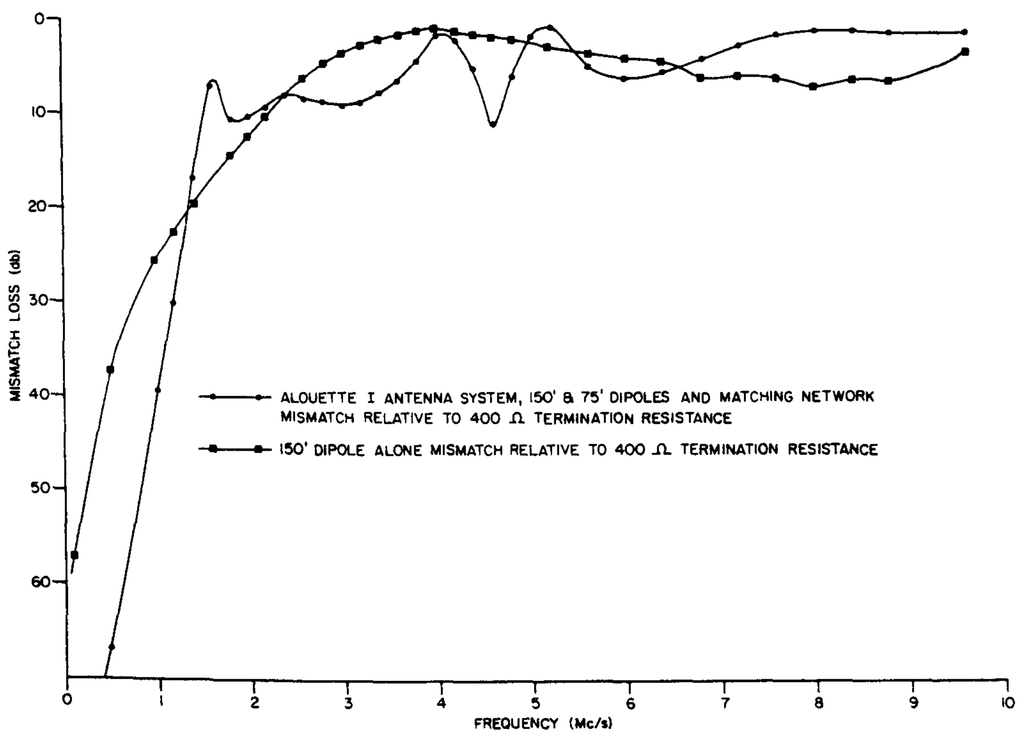

Fig. 9. Mismatch Loss in Alouette I Antenna System.

Since cosmic noise is approximately isotropic (with the typical 100° antenna apertures of Alouette I the variation is observed to be ± 3 db), the received noise power for frequencies below f_0F2 is virtually independent of the orientation of the antenna. The received signal power, however, varies with orientation because of peaks and nulls in the antenna patterns. The theoretical gain of a half-wave dipole over an isotropic antenna is 2.15 db. In Table 2 the fading margin of 6 db is for an isotropic antenna and was obtained by allowing 3 db for reception and 3 db for transmission. In practice, if the dipole gain of 2.15 db is taken into account, this leads to a fading margin of approximately 5 db both in reception and transmission. For a spinning satellite, and a $\lambda/2$ dipole antenna pattern, this means that for 75% of the time the fading loss will be no worse than that given in Table 2.

The polarization and wave splitting losses arise from magneto-ionic effects caused by the earth's magnetic field and the ionized medium, and are average values that take into account the spin of the satellite and the variations in the electric-field polarization ellipse for the ordinary and extraordinary waves.

No allowance was made for antenna system losses that arise from changes in antenna impedance caused by the ionized medium.

2.4 Sounder Antennae

The physical characteristics of the sounder antennae were described in Section 1. On extension, the behaviour of each antenna element was monitored by telemetering the voltages from four potentiometers connected via gear trains to their respective antenna poles. In the event that the antennae failed to extend, because the vehicle did not separate, or because a separation microswitch failed to operate, power could be switched into the antenna motor by a command from the ground.

Various approaches to antenna systems were tried and discarded before the final configuration was chosen. Preliminary studies established that either a particular system was unable to meet the bandwidth specifications or else it would not have a convenient collapsible form[11,12,13]. The simple thin dipole satisfied nearly all requirements except those for bandwidth. For a 10 db attenuation in a matching network, the thin dipole has a frequency range of 2.5:1 instead of the desired 10:1. This limitation was effectively overcome through the use of two orthogonal dipoles, which permitted band splitting. The long antenna covered the 1.4 - 4.7 Mc/s range, and the shorter one covered the band between 4.7 and 11.5 Mc/s. A further advantage of this arrangement is that dynamically it is much better than a single dipole design.

The two antennae are excited by a single solid-state wide-band transmitter through a passive matching and cross-over network. From Figure 9 it can be seen that the main theoretical contribution of the matching network is to extend the low frequency response of the antenna system between 1.4 and 2.4 Mc/s. The cross-over network heavily attenuated the response of the low band antenna beyond 4.5 Mc/s, and hence reduced lobe splitting effects at high frequencies. The matching network was designed by the Fano techniques[12,13].

The input impedance of the antenna system varied from $10\,\Omega$ to $13\,K\Omega$ between 1 and 11.5 Mc/s (see Fig. 10). This complicated the design of the transmitter and made noise matching of the receiver a rather academic consideration. Antenna mismatch curves were calculated assuming a source resistance of 400 ohms and a dipole in free space. Since the input resistance of the sounder receiver is approximately 350 ohms, the calculated mismatch loss for received signals is a close approximation to the actual loss in the Alouette's receiving system. For this reason, the computed mismatch curves can be used directly to determine received cosmic noise levels, provided there is no detuning of antennae by the ionized medium. Observations of cosmic noise in Alouette have shown that plasma detuning is not a major factor for frequencies between 2.4 and 5.0 Mc/s. In the case of the transmitter, however, its output resistance is 1.5 K ohms, shunted by an inductive reactance of 400 ohms at 1 Mc/s, and a capacitive reactance of 400 ohms at 11 Mc/s. Furthermore, the output voltage from the transmitter is limited by zener clippers to 1000 volts peak-to-peak. In practice, it was found that the measured mismatch loss for transmission, using dummy antenna loads, was within ± 5 db of the calculated values shown in Figure 9.

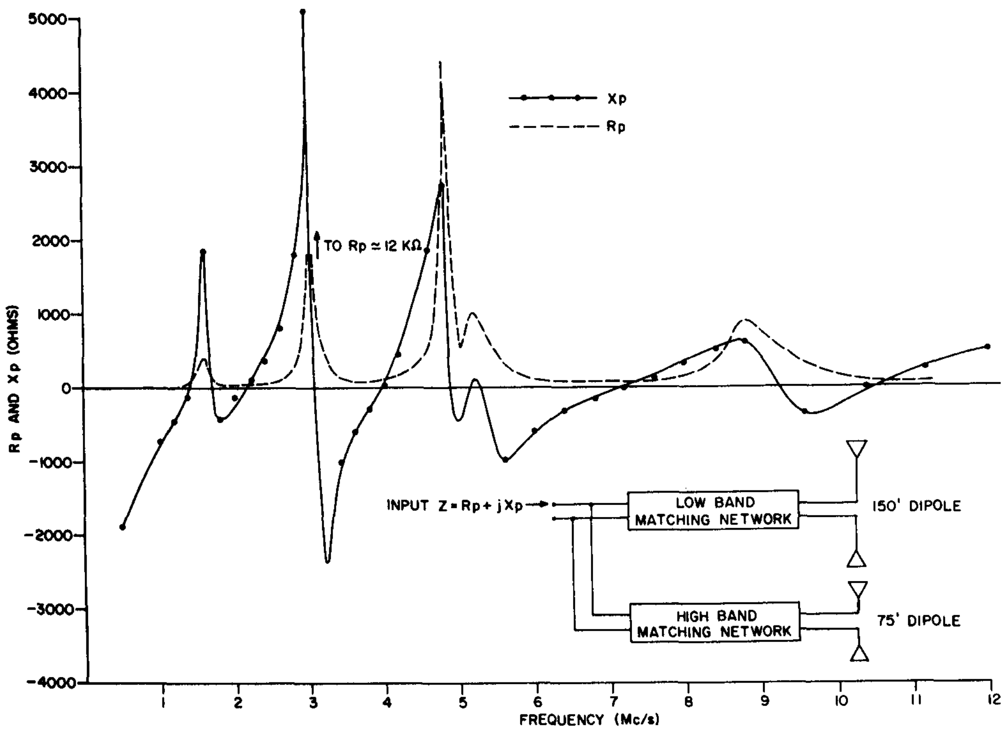

Fig. 10. Input Impedance to Sounder Antenna Matching Network.

Attempts were made to design antenna tuning networks using varactors, increductors, and/or solid-state or mechanical switches. Such attempts failed because of frequency tracking problems, non-realistic Q's for coils and capacitors, and/or voltage and reliability considerations in switches.

2.5 Sounder Transmitter

The power calculations showed that the sounder transmitter should deliver 100 watts into a matched load and, at the time the system was completed, this was judged the maximum power available from a transmitter using transistors with proven reliability. The calculation provided no power margin for absorption effects in the ionosphere; this would have required a vacuum tube transmitter. The choice was made in favor of the more reliable and efficient semiconductor transmitter on the grounds that ionospheric absorption, where important, could affect soundings only under the worst conditions (maximum range, highest antenna mismatch, etc.).

The original design specification called for a sweep-frequency pulsed transmitter with a power output of 100 watts into 400 ohms, a frequency range of 1.0 to 12 Mc/s, and a pulse width of 100 μs at 62 pps.

Because of the highly reactive and variable impedance of the antenna system, the transmitter had to be capable of operating into complex load impedances varying in magnitude from near zero to several thousand ohms. Other considerations were an ambient temperature range of - 10°C to +75°C, an operating life of at least one year, and severe limitations on dimensions, weight, and power consumption.

A review of available transistors showed that only two types could be considered, of which the most promising was the PSI 2N1709, an npn triple-diffused VHF silicon unit capable of dissipating approximately 12 watts at 25°C case temperature. To achieve a power output of 100 watts it was initially thought that a prohibitively large number of these transistors might have to be connected in parallel. It was finally determined that only eight transistors were needed in the output stage for the following reasons:

(1) The minimum collector thermal time constant in the 2N1709 power transistors is $\geq 600\,\mu s$.

(2) The high-frequency parameters of the 2N1709 are not seriously degraded when the peak collector dissipation is four to five times the maximum allowable steady state value.

(3) The manufacturer's 80 volt V_{CBO} rating was for an arbitrary and small collector current. The true avalanche breakdown voltage for the collector-base junction is ~200 volts.

(4) Because of the high breakdown voltage, operation in the common base connection with peak collector excursions of 120 volts is technically sound.

Confidence in the above assumptions was based on manufacturer's estimates of thermal time constants, on measurements and extensive life testing (including 1000 hours at +85°C) and on the fact that seven amplifiers had been constructed and tested with virtually identical performance. At the time of writing, the transmitter in Alouette has been in orbit for over 3½ years and has operated for approximately 8000 hours without any observable drift in performance.

A block schematic of the power amplifier is shown in Figure 11. All collector voltages are derived from a single power supply rail, via appropriate potential dividers. The transmitter is pulsed ON by a transformer-coupled power supply connected to the bases of the output transistors, to the emitters of the low-level common-base stages, and to the emitter of the first common-collector stage. The signal voltages in the class-B common-collector stages are large enough to virtually eliminate cross-over distortion. Since operation of these stages is true class-B, no emitter bias is required—a useful simplification both in terms of components and in reduction of feedback between stages.

The output stage of the power amplifier consists of four pairs of 2N1709 transistors connected in a push-pull parallel arrangement, and operated in class-A with a common-base drive configuration. Push-pull operation was used primarily to cancel L/R transients which occur when the emitter and collector currents are turned on and off by the pulser. A secondary advantage of push-pull operation is reduction of harmonic distortion.

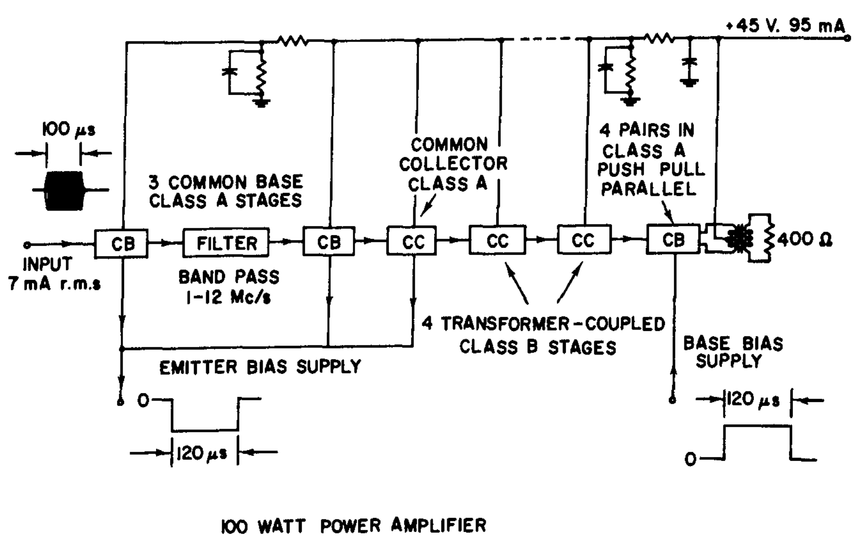

Fig. 11. 100 Watt Power Amplifier.

The choice of a common-base configuration in the output stage was made from consideration of the following factors:

(1) In class-A operation, the maximum allowable output voltage swing is smaller in practice for the common-emitter and common-collector connections than for the common-base connection, although a common-collector stage could, in theory, tolerate the same swing if it were driven from a true voltage source. In the case of the common-emitter connection, the maximum output voltage swing is less than the peak permissible collector-to-base voltage by the magnitude of the base drive voltage, since this is in antiphase with the output.

(2) In the common-collector connection there is a serious transistor protection problem when the load impedance falls to zero. Also, the base drive voltage is approximately equal to the output voltage and the driver must supply large reactive currents through transformer winding inductances, transformer capacitance, and C_{OB} of the output transistors.

(3) In the common-emitter connection there is feedback via C_{OB} and g_{OB} and the driver must supply this added current. For the 2N1709 this would reduce the available current gain to two at 12 Mc/s.

The disadvantage of the common-base connection was the need to supply a large input current at a low impedance level over a wide frequency range. The design of the driver transformer proved difficult and the high frequency response of the transmitter was finally limited by leakage inductance and shunt capacity in this transformer.

In the pulser schematic of Figure 12, the direct current through the tertiary winding of the transformer resets the core flux, while core saturation limits the maximum available pulse width to approximately 180 μs. Details of the output stage and common-collector drivers are shown in Figures 13 and 14. The pulser establishes an emitter current of 0.8 amps in each of the output transistors. In the absence of an RF signal this corresponds to 32 watts per transistor during the 120 μs pulse interval. During normal operation the peak collector current in each of the transistors is 1.6 amps. The additional circuitry needed for reliable operation into a highly reactive antenna system is shown in Figure 15. The zener diodes DA1 and DA2 limit the maximum voltage at the collectors of the output transistors, while diodes D_1 and D_2 serve as peak rectifiers to prevent the zener capacitance from shunting the output load. This scheme was only partially successful because of forward transient effects in D_1 and D_2 producing significant voltages, in the forward direction, across these diodes. Zeners are now available with low enough capacitance to permit their use directly across the load, which eliminates any need for peak rectifier diodes.

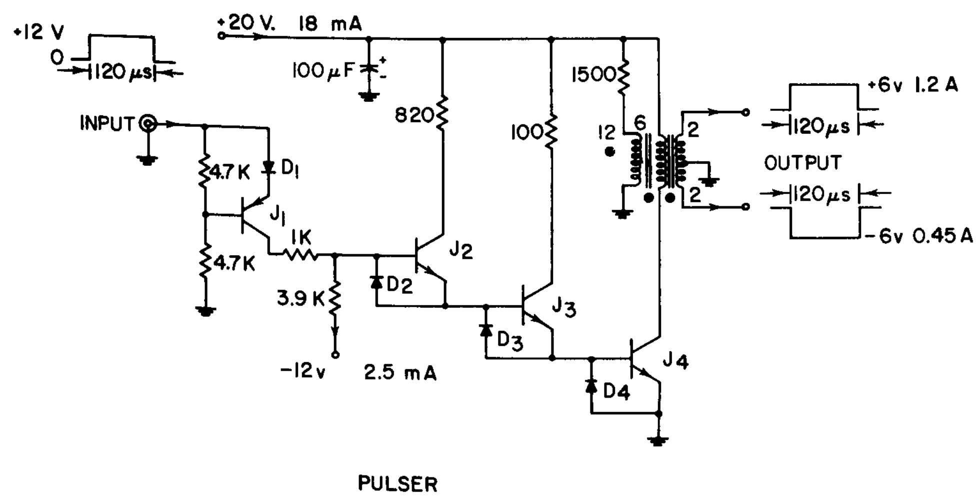

Fig. 12. Pulser for Power Amplifier.

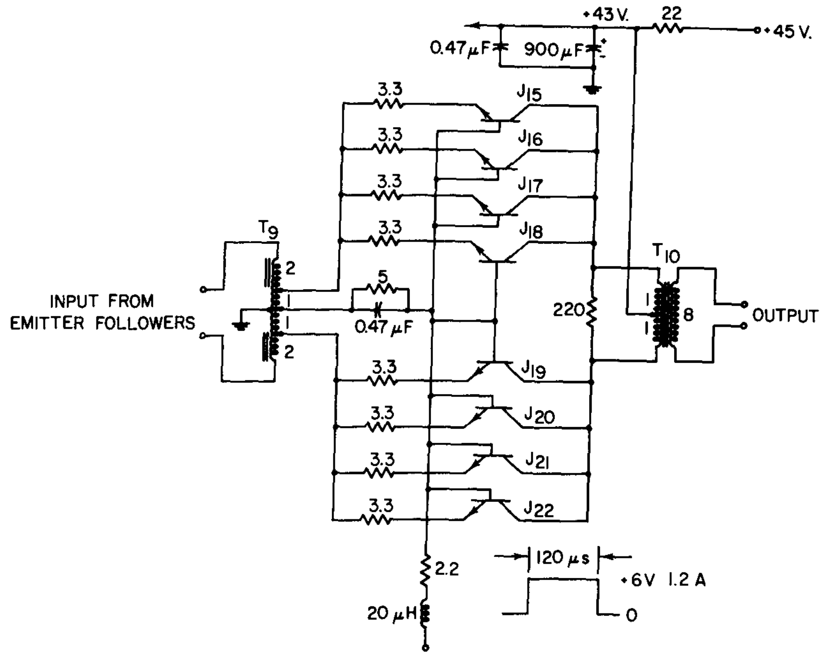

OUTPUT STAGE OF POWER AMPLIFIER

Fig. 13. Output Stage.

J15-22 2N1709

T9 18 turns of copper tape
Ferroxcube 4B Pot core
Dim. 25 x 16 mm Pot core
Air gap 0.007"

T10 Primary 6 turns of copper tape
Secondary 24 turns of copper tape
Ferroxcube 4B Pot Core
Dim. 25 x 17.5 mm
Air Gap 0.001".

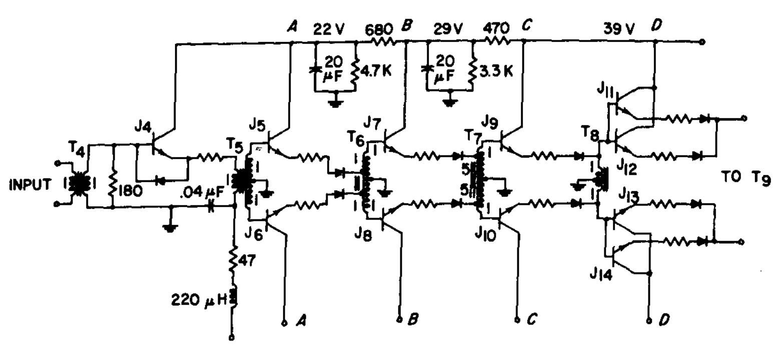

COMMON-COLLECTOR DRIVER CHAIN

Fig. 14. The Common-Collector Driver.

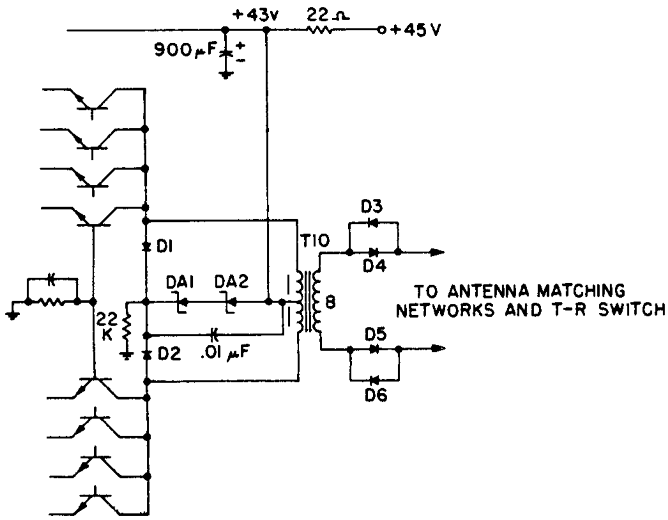

Fig. 15. Modified Output Stage for Driving Sounder Antenna System.

When the transmitter is gated off, thermal noise at approximately 14 db above KTB, appears at the transformer output terminals. This noise is attenuated by diodes D_3 - D_6 to permit common antenna operation with a low noise receiver.

Overall weight of the transmitter was 4.2 pounds and power consumption was 4.6 watts. The total power gain was 46 db, of which 6 db represented gain in the final stage. The transmitter was tested from -50°C to +80°C and operated satisfactorily throughout this range(14).

2.6 Sounder Receiver

A block schematic of the sounder receiver is shown in Figure 16. The incoming signal passes through a T-R switch and wide-band preamplifier. The T-R switch(15) uses only passive components and semiconductor diodes and is shown in Figure 17. In the receive state, forward bias currents through two sets of diodes cause the diodes to appear as low impedances to the incoming RF signal. When the transmitter is pulsed ON its high level RF output is peak rectified by the two input diodes. This produces a negative dc voltage, which reverse biases the other two diodes. Therefore, the RF signal that passes through the T-R switch is heavily attenuated and, to provide further protection, the front end of the preamplifier is gated off by a 400 μs pulse that is initiated 200 μs before the start of each transmitted pulse, and finishes 100 μs after the end of the transmitted pulse. The sweep frequency oscillator (SFO) drive to the first mixer is gated off during the transmission interval to reduce the disturbance on the AGC line due to RF leaking through the T-R switch and preamplifier.

Although the operation of the T-R switch is simple in theory, its operation in practice is complex, largely because of minority carrier storage effects in the high voltage silicon diodes.

The preamplifier has a push-pull common-base input stage using a pair of 2N1613 transistors. An m-derived bandpass filter provides an overall response 3 db down at 1.0 and 12.4 Mc/s. The filter has a pole at 19 Mc/s (-50 db) to reduce the possibility of receiver desensitization by spurious signals appearing in the first IF stage. Because of the high transmitter voltages that appear across the T-R switch diodes, redundancy was considered necessary. Two preamplifiers and two T-R switches were mounted in a single shielded box. Because of command limitations each T-R switch has its own preamplifier and 100 watt transmitter, i.e., it is not possible to interchange T-R switches without interchanging transmitters

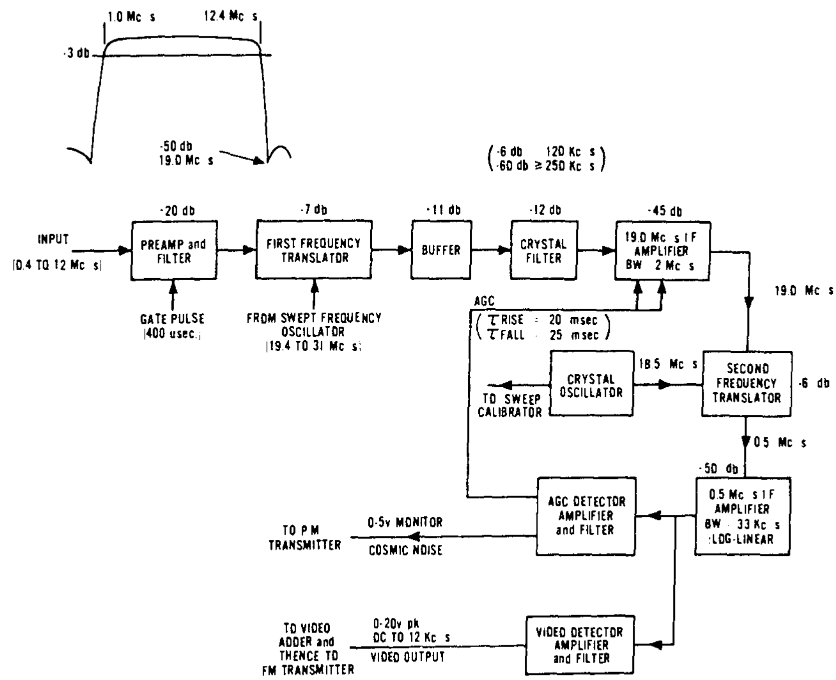

Fig. 16. Block Diagram of the Sounder Receiver System.

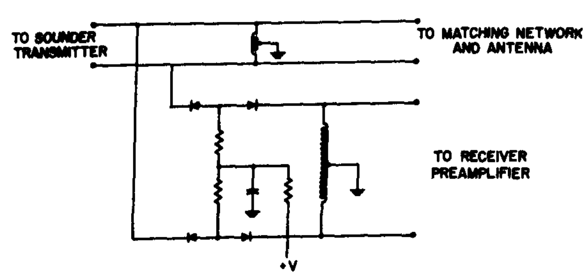

Fig. 17. T-R Switch.

and preamplifiers as well. The input terminals to each T-R switch are switched via relay contacts. The output of each preamplifier is then added in a single load resistor. This arrangement eliminated switching of the preamplifier outputs, but a disadvantage is that noise generated in the standby preamplifier adds to the active preamplifier channel. The output from the preamplifier box is fed via a coaxial line to the sounder receiver.

The incoming signal is mixed with the sweep-frequency oscillator and translated in frequency to 19 Mc/s. Conversion loss in the silicon diode ring mixer is approximately 7 db. Local oscillator and signal leak rejection is better than 30 db, with no selection or balancing of diodes, since inherent balance against signal and local oscillator frequencies is provided in the mixer. The circuit proved very tolerant to variations in temperature, power supply voltages, and diode characteristics. The mixer output is buffered by an 11 db amplifier and then fed to a crystal filter. This filter provides image rejection and attenuates the local oscillator leak signal so that the SFO can sweep to within 120 kc/s of 19 Mc/s before desensitization of the receiver occurs. Bandwidth of the crystal filter is 120 kc/s at the 6 db points and 250 kc/s at the 60 db points. Insertion loss is 12 db and ripple in the passband is ± 0.7 db.

The 19 Mc/s IF strip consists of five transformer-coupled common-base stages, giving a total gain of 45 db. Delayed AGC is applied to the first two stages of this amplifier via a dc amplifier and loop filter such that the receiver output level is held within 5 db for a 40 db change in input signal level.

Following the 19 Mc/s amplifier, the signal is mixed with the output of a crystal-controlled local oscillator operating at a frequency of 18.50 Mc/s. This results in a second frequency translation to 500 kc/s. In fact, this oscillator should have been offset + 10 kc/s, to 18.51 Mc/s, to compensate for the change in frequency of the SFO during the time interval between transmission of an RF pulse and reception of its delayed echo. The 500 kc/s amplifier has five cascaded transformer-coupled common-base stages giving a 3 db bandwidth of 33 kc/s and a gain of 50 db. The amplitude response is shaped and limited in this final IF to produce an output that is linear with input signal for the first half of the output voltage range, and logarithmic with input signal for the final half of the output range (Fig. 18). Envelope detectors at the output of the 500 kc/s strip provide the video signal (sounder pulse) and an AGC voltage to control the gain of the 19 Mc/s amplifier over a dynamic range of 40 db. The video signal has a post-detection bandwidth from dc to 12 kc/s and modulates a wide-band FM telemetry transmitter via a video adder. The output of the AGC detector is connected via a threshold circuit to a dc amplifier and loop filter. The threshold is adjusted so that the background noise in the sounder video channel is approximately 0.16 of peak output with an AGC voltage of 2.5. The dc amplifier has a peak clipper to eliminate overload and paralysis effects on strong signals. A single dominant time constant limits the high-frequency cut-off of the AGC loop to 20 cps, and the dc amplifier output impedance is such that the AGC attack and decay time constants are 20 ms and 25 ms, respectively. The performance of the receiver could probably have been improved by making these time constants asymmetric with attack and decay times of 40 ms and 5-10 ms, respectively. This would have complicated the design of the AGC loop but would have improved delineation of plasma resonance and spread-F echoes. The cosmic noise background level is monitored by measuring the filtered AGC voltage at the output of the dc amplifier. This voltage, together with added frequency markers, is transmitted continuously to the ground via a standard 14.5 kc/s FM subcarrier in the PM telemetry link. In addition to providing cosmic noise levels, the AGC voltage has proved a useful tool in monitoring the effects of ground-based interference on the performance of the receiver.

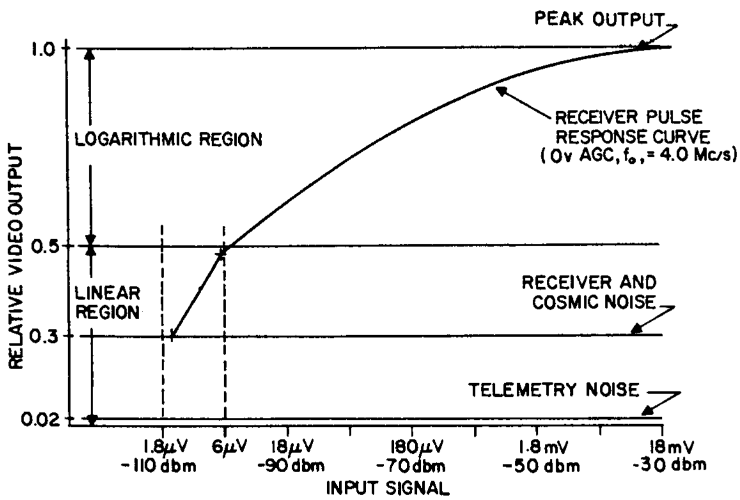

Fig. 18. Amplitude Response of Sounder Receiver.

No RF tuning was provided before the first mixer, partly for simplicity and partly because signals from ground-based transmitters with frequencies above the local f_oF2, and having normal spatial attenuation, were not expected to cause any significant interference. Tests using three different pairs of frequencies, and received signal levels of - 35 dbm, revealed no significant intermodulation effects. In practice, ground-based interference and resulting receiver desensitization has proved a serious problem during night time over North America and during day and night over Continental Europe [16]. The interference appears to be due to ground transmissions at frequencies above f_oF2 reaching the satellite and intermodulating in the first mixer of the sounder receiver to produce an output at 19 Mc/s, the frequency of the first IF.

Tangential sensitivity of the receiver was - 110 dbm, corresponding to a noise figure of 16 db for a source resistance of 400 ohms. Pulse overload and paralysis effects were negligible for input signal levels of - 25 dbm or lower.

Power consumption was 1.4 watts, dimensions 2½ in. x 7.0 in. x 8.0 in. and weight 3.1 pounds.

2.7 Sweep Frequency Oscillator

The sweep frequency generator consists of a linear sweep circuit and an oscillator tuned by a saturable inductor.

A 0.8 cps emitter-coupled multivibrator drives a four-stage binary counter, the outputs of which are added in a gate circuit. The gate output switches on a Miller integrator which, in turn, varies the dc current through the control winding of a Vari-L increductor. The signal winding of the increductor is in the tank circuit of an oscillator, and for a 0-30 ma current sweep a frequency sweep of 19.4 to 31.0 Mc/s is obtained.

The linearity of the sweep was only fair and in spite of the use of a specially designed increductor and the addition of linearizing circuitry, the sweep rate varied between 0.7 and 1.4 Mc/s/s (see Fig. 47).

The resistance of the control winding of the Vari-L increductor was 400 ohms, and to obtain the final sweep-frequency characteristic a peak control power of 720 mw was required. It can be argued that a higher starting frequency for the SFO would have led to a smaller percentage frequency change and a more linear and lower power sweep. At the time the design was carried out 19.4 Mc/s was considered the highest starting frequency which could safely be used if long term drifts in this frequency were to be kept below 100 kc/s.

The timing capacitor in the Miller integrator consisted of four 5 μF Mylar units connected in parallel. To avoid possible drift in sweep rate due to radiation damage to transistors, the Miller charging current was conservatively set at 45 μa, thus producing a 24 volt sweep in 11 seconds. Referring to Figures 47 and 48 showing the in-flight performance, it can be seen that drift in the SFO has been negligible over the first three years in orbit.

2.8 Sweep Frequency Calibrator

A block diagram of the frequency calibrator is shown in Figure 19. The approach used is to gate, at an accurately known rate, a frequency sweep that is offset by 0.5 Mc/s from the basic sounder sweep. The frequency spectrum of this gated RF signal, together with explanatory waveforms is given in Figure 20. For convenience of illustration an input signal frequency of 10.050 Mc/s has been chosen and second order effects due to finite pulse rise time and frequency sweep rate have been neglected.

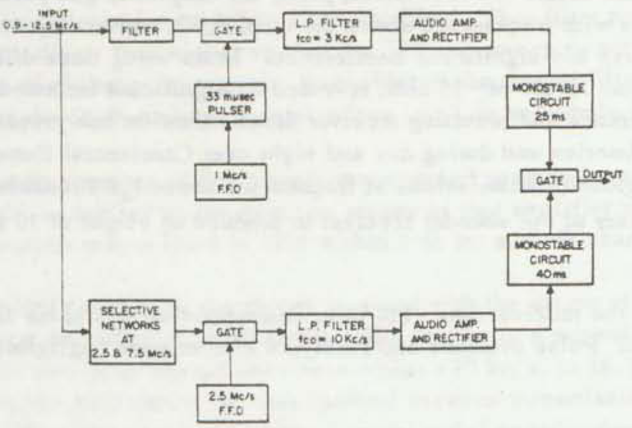

Fig. 19. Frequency Calibrator.

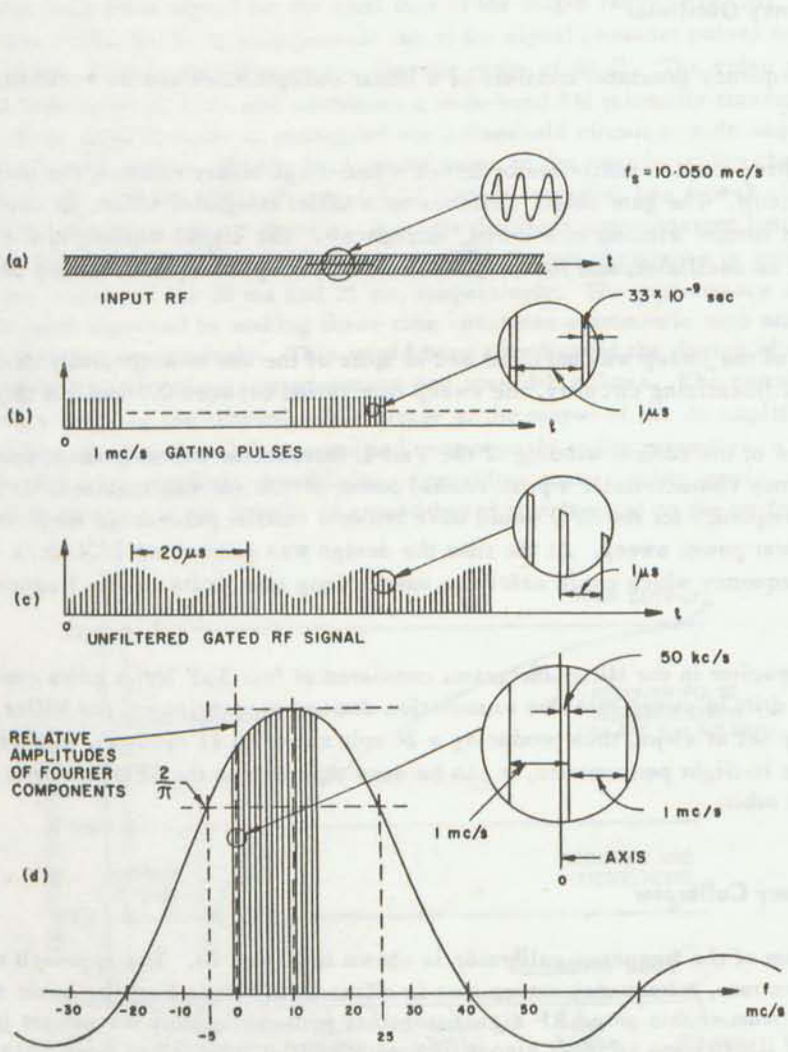

Fig. 20. Fourier Components of Pulsed RF Signal.

With the above simplifications the output signal from the gate may be expressed in the form*

$$i(t) = \frac{T}{T_p} \cdot I \left[\cos 2\pi f_s + \sum_{n=1}^{n=\infty} \frac{\sin \frac{n\pi T}{T_p}}{\frac{n\pi T}{T_p}} \cos 2\pi(f_s + nf_p)t \right.$$

$$\left. + \sum_{n=1}^{n=\infty} \frac{\sin \frac{n\pi T}{T_p}}{\frac{n\pi T}{T_p}} \cos 2\pi(f_s - nf_p)t \right]$$

where I = the amplitude of the RF input signal

T = duration of gating pulse

T_p = period of gating pulse

f_s = frequency of RF input signal

and f_p = gating frequency.

When $f_s \rightarrow nf_p$, $i(t)$ has an audio frequency component of amplitude

$$A = \frac{T}{T_p} \cdot I \cdot \frac{\sin \frac{n\pi T}{T_p}}{\frac{n\pi T}{T_p}}$$

If the gated RF signal, represented by $i(t)$ and illustrated in Figure 20(c), is transmitted through a low pass audio filter, an audio output pulse is obtained (Fig. 21) whenever the carrier frequency is swept through an integral multiple of the pulse repetition frequency. This audio pulse is then amplified and rectified to produce an output, the leading edge of which triggers a monostable pulse generator to produce a calibration pulse of suitable width. Since the amplitudes of the Fourier components of the gated RF signal vary as $\frac{\sin x}{x}$, the audio output level decreases with increasing sounding frequency until the first amplitude zero is reached at

$$\frac{nT}{T_p} = 1$$

i.e., when $\quad nf_p = \frac{1}{T}$

T, the width of the gate pulse, must therefore be short enough to maintain a reasonably constant audio amplitude over the sounding frequency range and in practice $\frac{1}{T}$ should be at least twice the highest sounding frequency.

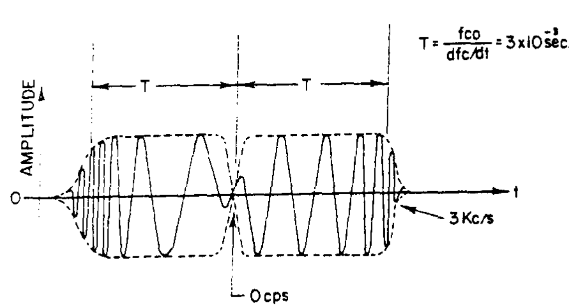

Fig. 21. Audio Signal at Output of Low-Pass Filter.

* Dc term due to 50 mA gating pulses has been omitted.

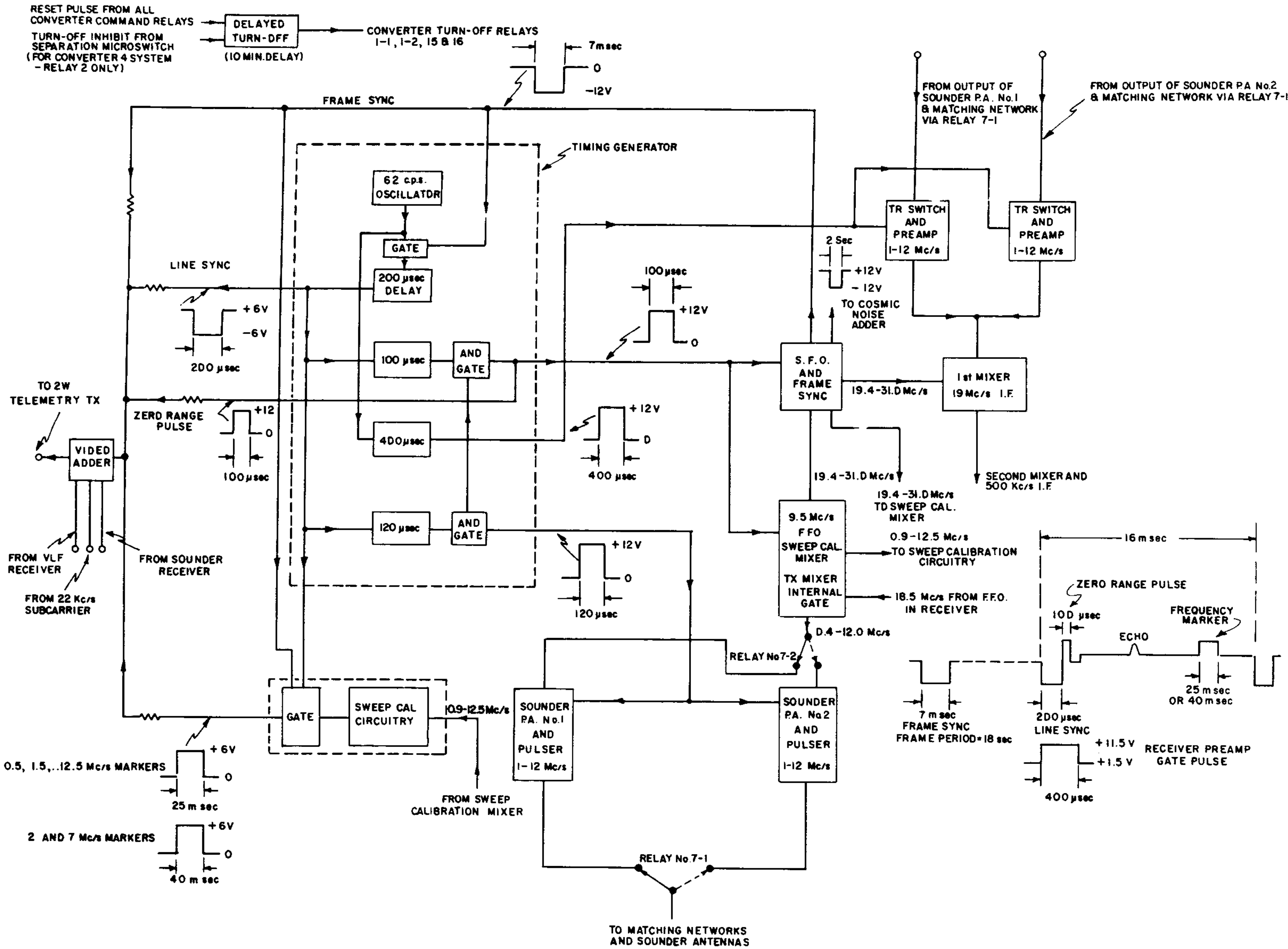

Fig. 22. Alouette I Timing and Gating Diagram.

Referring to Figure 19 it will be seen that there are two frequency marker channels, one to provide a 'fine' grid with calibration markers 25 ms wide, every megacycle, and the second to provide a pair of identification markers, each having a width of 40 ms. To generate the main marker grid a 1 Mc/s crystal oscillator triggers a blocking oscillator, which produces a 50 ma gating pulse having a width of 33×10^{-9} secs., and rise and fall times of approximately 7 and 10 nanoseconds, respectively. The pulse width is narrow enough to ensure less than 3 db fall-off in the amplitude of Fourier components up to 12 Mc/s from the carrier frequency. Therefore, the amplitude of the audio output signal does not vary more than 3 db over the sounding band. The audio amplifier consists of three transformer-coupled common-base stages with a steep-cut low-pass filter having a cut-off frequency of 3 kc/s. Since triggering occurs on the leading edge of the audio pulse, each calibration marker is generated 3 kc/s 'low' in frequency. The cut-off frequency of the audio amplifier is close to optimum for a sounding sweep rate that varies between 0.7 and 1.4 Mc/s/s, and for an output pulse width of 25 ms.

The 40 ms identification markers are generated at input frequencies of 2.5 and 7.5 Mc/s by selecting the first and third harmonics of a square wave derived from a 2.5 Mc/s crystal oscillator. A much simpler low-pass filter, with a relatively slow roll-off, is used in the associated audio amplifier, with the result that the two identification markers are generated 4-6 kc/s low in frequency.

Owing to the 0.5 Mc/s offset at the input to the sweep calibrator, the 25 ms markers correspond to sounding frequencies of 0.5, 1.5, 2, 5 ..... 11.5 Mc/s, and the 40 ms identification markers correspond to 2.0 and 7.0 Mc/s.

Although simple in principle, the practical implementation of the sweep calibrator caused a good deal of trouble, mainly because of spurious audio outputs caused by harmonics and other unwanted frequencies in the input RF signal.

During initial system tests it was noted that the audio envelope was frequently asymmetric, and often widened to the point where multiple triggering of frequency markers could occur. This fault was traced to unsuspected and serious frequency modulation of the SFO due to transients on power supply rails. It was subsequently realized that the asymmetry of the audio envelope in the sweep calibrator was a very sensitive indication of SFO frequency modulation during turn on of the sounder transmitter.

Attempts to use the sounder frequency sweep, instead of a 0.5 Mc/s offset sweep, failed because of leakage into the first IF of the sounder receiver from a continuously operating 19 Mc/s oscillator in the sweep calibration mixer.

2.9 Timing and Gating Circuits

A block diagram of the sounder timing system and line timing circuitry is shown in Figure 22. The 62 pps line frequency is set by an emitter-coupled multivibrator.

The possibility of using a tuning fork oscillator to achieve a line frequency stability of ±0.1% or better was considered but was rejected because of added complexity and questionable reliability of available forks. Referring to Figure 49, showing the in-flight performance of the line oscillator, it will be seen that the maximum line frequency variation observed over a three-year period in Alouette I has been ±1%. Capacity-coupled monostable circuits are used to produce fixed time delays and to generate gating and synchronizing pulses. A 200 μs negative-going line sync pulse is produced immediately prior to each transmitter pulse, and a 7 ms negative-going frame sync pulse is generated at the start of each frequency sweep. These sync pulses are required at the ground facilities to construct a CRO display of echo pulses showing virtual range versus sounding frequency. The sync, gating, and frequency calibration pulses are added at the output terminals of the sounder receiver to produce the composite video signal shown in Figure 23. The adding function is carried out by feeding defined currents into a low input impedance dc-coupled buffer amplifier. To ensure that the frame sync is never suppressed by the rest of the video signal, all other inputs are gated out when the frame pulse is generated. Similarly, second precedence is given to the line sync and, when this pulse is generated, all other inputs with the exception of the frame sync are gated out.

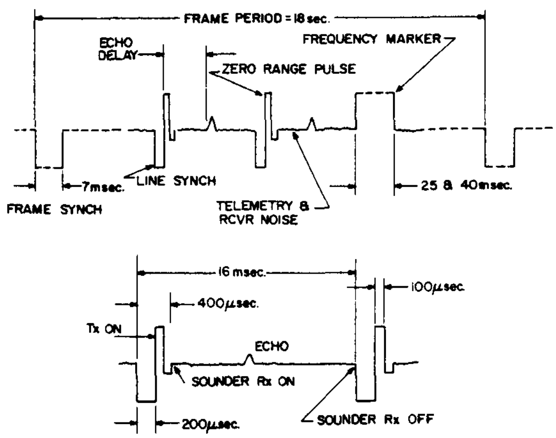

Fig. 23. Video Format for Ionospheric Data Link.

2.10 Sweep Calibration and Transmitter Mixers

The transmitter mixer converts a pulsed 19.4 - 31 Mc/s sweep, from the SFO, into a 0.4 - 12 Mc/s pulsed frequency sweep to drive the sounder transmitter. The local oscillator frequency is 19 Mc/s. This is derived from a continuously operating 9.5 Mc/s crystal oscillator via a gated frequency doubler that is turned on only during the 100 μs transmission interval. The use of a local oscillator operating continuously at 19 Mc/s proved impracticable because of desensitization of the sounder receiver due to 19 Mc/s leakage into the first IF. The 9.5 Mc/s oscillator was carefully shielded and no detectable leak of either 9.5 Mc/s or 19.0 Mc/s (second harmonic) were detected by the receiver. As a further RFI precaution, and also to reduce power consumption, buffer amplifiers, between the mixer and local oscillator and the input and output signal lines, are turned on only during transmission.

The mixer consists of a ring of four silicon diodes terminated by a low input impedance (~ 50 ohms) buffer amplifier and driven by essentially current sources in the local oscillator and input signal lines. For an input signal of 12 ma 0-peak, and a local oscillator drive current of 40 ma 0-peak, the frequency-translated output signal is 6 ma 0-peak. This conversion loss of 6 db is virtually flat across the sounding band, and is insensitive both to changes in diode characteristics and to drifts in power supply voltages and in temperature. No attempts were made to optimize the balance of the circuit by selecting diodes and adding trimming capacitors. In retrospect, the decision not to select diodes probably resulted in a quite unnecessary loss of performance without any corresponding improvement in reliability. In the output of the mixer, local oscillator and input signal rejection is $\geq$ 30 db.

The sweep calibration mixer converts a continuous frequency sweep from the SFO into a 0.9 - 12.5 Mc/s signal to drive the sweep calibrator. The local oscillator frequency is 18.5 Mc/s and is derived from the crystal-controlled local oscillator in the sounder receiver. The use of a 19 Mc/s local oscillator for the mixer was rejected because of leakage problems in the first IF of the sounder receiver. This approach would have put the main marker grid at integral megacycles of the sounding frequency instead of being offset by 0.5 Mc/s.

The basic mixer design is similar to that used in the transmitter mixer. For an input signal of 3 ma 0-peak, and a local oscillator drive current of 15 ma 0-peak, the frequency-translated output is approximately 1.5 ma. This output signal is fed to the sweep calibrator via a low input impedance buffer amplifier having a current gain of 3. Exceptional care was needed to ensure that there were no spurious outputs capable of causing false triggering in the sweep calibrator.

Because of the inherent non-linearity of the frequency conversion technique, the mixer generated spurious signals over a wide range of frequencies and amplitudes. This process produced a large number of interfering spikes in the sounder receiver output, many of which were never satisfactorily suppressed. This interference was mostly conducted (via coaxial lines and power leads), and represented the major RFI problem in the spacecraft.

2.11 Commutators

To determine the state of the spacecraft, diagnose failures, and set up realistic operating schedules it is necessary to transmit to the ground various engineering data such as battery voltages, solar charging currents, load currents, temperatures, etc.

The approach used was to time-multiplex this analogue 'housekeeping' data onto an FM subcarrier channel by means of a solid-state commutator. The commutator performs the functions of a rotary switch by sequentially connecting the various housekeeping channels to the input of its associated subcarrier oscillator.

Because of the critical importance of certain housekeeping functions redundancy was considered necessary and two separately powered 35-channel commutators were used, one for the FM telemetry system, and the other for the PM telemetry link.

The commutators were designed and constructed at DRTE because, at the time, there were no commercially available units of acceptable reliability and with low enough power consumption. A non-standard commutation rate of 18 samples per second and a duty cycle of 75% were chosen to maximize the sampling rate and at the same time permit the use of conventional low-cost paper chart recorders.

The commutators use a single pnp alloyed-junction low-frequency silicon transistor in each analogue switch. Each switch is driven by an AND gate which detects a simultaneous pulse occurrence from a 5-stage and 7-stage ring counter. The outputs from the 35 analogue switches are then fed to the input of an emitter-follower amplifier that is gated off during the first 25% of each clock period. All input signals to the commutators are in the range 0 to +5 volts.

Although data quality has been satisfactory there are a number of undesirable features in the commutator design. The sample input impedance is relatively low ($\simeq$ 82 K to -6V) because of base current drawn by the ON channel switch; analogue data below 5% of full scale is lost due to the clamping action of a diode; and manual decommutation is mandatory because of the non-standard format. Also the low cut-off frequency of the channel switch transistor makes it susceptible to radiation damage.

Channel allocations for commutators I and II are given in Tables 3 and 4 respectively. Commutator I has twenty-nine channels for housekeeping, one for the single axis magnetometer, and five for amplitude calibration. Channels 33-35 provide a 5 volt amplitude calibration level and a frame sync pulse lasting for 2.75 channel periods.

Commutator II, which is essentially a back-up unit, has twenty-nine housekeeping channels with channels 1 - 10 and 27 - 30 being identical to those in Commutator I.

Each commutator had approximately 350 components and a power consumption of 500 mw. Dimensions and weight were 2¾ in. by 6 in. x 8 in. and 3.5 lbs. respectively.

TABLE 3

Commutator I Channel Allocations

Channel No.	Function
1.	Current monitor for battery 1
2.	Current monitor for battery 2
3.	Current monitor for battery 3
4.	Current monitor for battery 4
5.	Current monitor for battery 5
6.	Current monitor for battery 6 and battery 7
7.	Battery switching matrix, position (a)
8.	Battery switching matrix, position (b)
9.	Battery switching matrix, position (c)
10.	Battery switching matrix, position (d) (This position also reads the common diode analogue voltage when the command gate is opened, if this position is in the 'one' state.)
11.	Converter 1 + 45v out, unregulated
12.	Converter 2 + 6v out, unregulated
13.	Converter 3 + 28v out, unregulated
14.	Converter 4 + 6v out, regulated
15.	Magnetometer output
16.	Temperature sensor hood 2 location 1
17.	Temperature sensor hood 2 location 2
18.	Temperature sensor deck 2 location 1
19.	Temperature sensor deck 2 location 2
20.	Temperature sensor shell 2 location 1
21.	Temperature sensor shell 2 location 2
22.	Temperature sensor battery 3
23.	Temperature sensor battery 1, after full antenna extension, otherwise antenna 1 extension monitor
24.	Temperature sensor deck 1 after full antenna extension, otherwise antenna 2 extension monitor
25.	Temperature sensor deck 1 after full antenna extension, otherwise antenna 3 extension monitor
26.	Temperature sensor hood 1 after full antenna extension, otherwise antenna 4 extension monitor
27.	Converter 1 input voltage monitor
28.	Converter 2 input voltage monitor
29.	Converter 3 input voltage monitor
30.	Converter 4 input voltage monitor
31.	Ov calibration
32.	2.50v calibration
33.	5.00v calibration
34.	5.00v calibration
35.	5.00v calibration

TABLE 4

Commutator II Channel Allocations

Channel No.	Function
1.	Battery 1 current monitor
2.	Battery 2 current monitor
3.	Battery 3 current monitor
4.	Battery 4 current monitor
5.	Battery 5 current monitor
6.	Battery 6 and battery 7 current monitor
7.	Battery switching matrix, position (a)
8.	Battery switching matrix, position (b)
9.	Battery switching matrix, position (c)
10.	Battery switching matrix, position (d) (This also reads common diode analogue voltage when the command gate is opened if this matrix position is in the 'one' state.)
11.	Converter 1 monitor, + 20v out, unregulated
12.	Converter 2 monitor, + 12v out, unregulated
13.	Converter 3 monitor, + 12v out, unregulated
14.	Converter 4 monitor, + 12v out, regulated
15.	Blank
16.	Temperature sensor hood 1 location 1
17.	Temperature sensor hood 1 location 2
18.	Temperature sensor deck 1 location 1
19.	Temperature sensor deck 1 location 2
20.	Temperature sensor shell 1 location 1
21.	Temperature sensor shell 1 location 2
22.	Temperature sensor antenna
23.	Temperature sensor antenna
24.	Temperature sensor deck 2 location 1
25.	Temperature sensor deck 2 location 2
26.	Temperature sensor hood 2
27.	Converter 1 input voltage monitor
28.	Converter 2 input voltage monitor
29.	Converter 3 input voltage monitor
30.	Converter 4 input voltage monitor
31.	0v calibration
32.	2.5v calibration
33.	5.00v calibration
34.	5.00v calibration
35.	5.00v calibration

3. SECONDARY EXPERIMENTS

3.1 Cosmic Noise Experiment

As mentioned in Section 2.6, the cosmic noise background level in the sounder receiver is measured by monitoring the AGC voltage. Although no in-flight calibration of amplitude was provided, data for the 36-month period since launching is consistent enough to suggest that there have been no significant changes in the characteristics of the sounder receiver and no observable drifts in overall system performance. Provision was made for commanding the sounder transmitter off during cosmic noise measurements but this facility is rarely used. Operationally, cosmic noise information is not obtained below 1.5 Mc/s because of mismatch losses in the sounder antenna system.

3.2 VLF Experiment

In the VLF experiment, the receiver has a gain of 85 db, a pass-band from 400 cps to 10 kc/s, a noise figure of 12 db, and a power consumption of 18 mw. Five transformer-coupled single-ended stages are used, four in the common-emitter connection and one, the input stage, in the common-base connection. Amplified and delayed AGC is applied to the first stage only, using a shunt diode technique. The AGC loop has attack and decay time constants of 0.2 seconds, and holds the output signal level constant to within 3 db for an input signal variation of 60 db. The input terminals of the receiver are permanently connected to the 150-foot dipole by means of a balanced low-pass coupling network as shown in Figure 24. The purpose of this network is

(a) to avoid excessive shunting of VLF signals by the sounder matching network and by the low impedance input circuits to the sounder receiver,

and (b) to prevent the VLF receiver from significantly loading the sounder antenna over the sounding frequency range.

These two objectives were met but at the cost of a possibly high and poorly defined insertion loss between the terminals of the 150 foot dipole and the VLF receiver. The value of the insertion loss is at present unknown due to uncertainties in the impedance of the sounder antenna at VLF. The receiver output terminals can be connected on command, by a magnetic latching relay, to the wide band telemetry link.

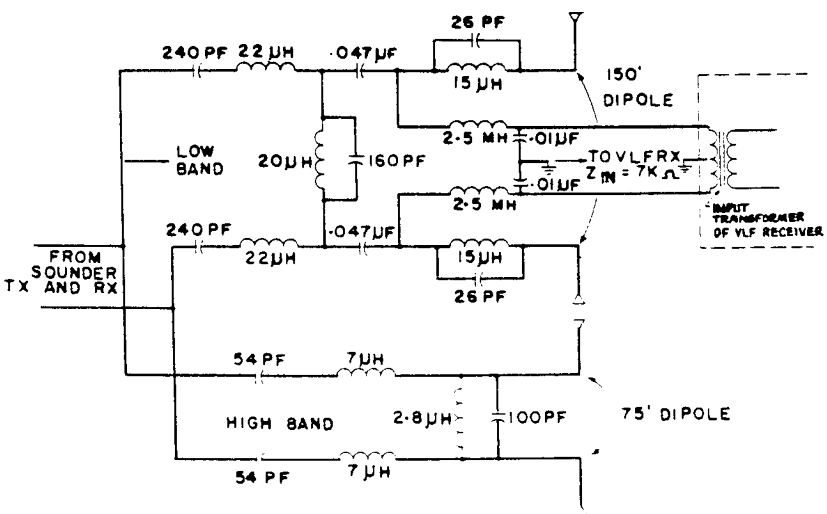

Fig. 24. Antenna Matching and Coupling Networks for the VLF and Sounder Receivers.

Electrical interference, resulting from the operation of other spacecraft equipment, is observed in the VLF passband. Most of this interference originates in the dc-dc converters, and by various mechanisms leaks into the input terminals of the VLF receiver. An unexpected leak path has been via the solar cells and the 150 foot dipole. This effect is due to ripple voltages at the inputs of dc-dc converters being conducted to the externally mounted solar cells*. These voltage variations apparently modulate the spacecraft sheath and set up compensating currents to the sounder dipoles. The currents that flow in the 150 foot dipole appear as converter interference in the VLF receiver, and in space this interference is observed to be modulated at the spin rate of the satellite. Fairly severe interference also exists between the sounder and VLF experiments, although this was expected since the Fourier spectrum of the video format contains components lying within the pass band of the VLF receiver. It was, in fact, expected that simultaneous operation of the sounder and the VLF receiver would be impracticable for this reason. Despite this interference, however, valuable information on ion temperature and composition is being obtained by simultaneous operation of these experiments.

Because the VLF experiment originally had very low priority, the design of the receiver is elementary—it uses only 6 transistors—and its performance in several respects is modest. For example, it has a very small instantaneous dynamic range and, because of its low consumption of power, has relatively poor overload characteristics. The problem of converter interference might have been reduced by improved filtering in the power supply rails.

3.3 Particle Experiments

In the NRC particle experiments six detectors were included to measure the intensities of electrons above 40 kev, protons above 500 kev, and alpha and heavier particles with energies up to 3 Bev [17].

The detectors used are as follows:

(i) *Detector A* is an Anton 302 Geiger counter identical with those used by the Iowa and Minnesota groups in the Explorer and Pioneer satellites. The counter wall thickness plus other shielding materials set an approximate energy threshold of about 40 Mev for protons and 4 Mev for electrons. The counter output is scaled by factors of 2^4, 2^9, and 2^{14} and fed to separate shaping circuits. The outputs from the shaping circuits are mixed at different levels and fed to one channel of a solid state commutator which forms part of the electronic package.

(ii) *Detector B* consists of an Anton 223 thin window (approx. 1 mg/cm^2) Geiger counter placed at the end of a cylindrical brass collimator directed spaceward through a hole in the satellite's top radiation shield. The counter window sets lower limits of about 40 kev and 500 kev for electrons and protons respectively. An approximate 'background' rate is given by the counting rate in Detector A. The geometric factor of the detector is 5.05×10^{-4} cm^2 sterad for particles that enter through the opening in the collimator. The counter output is scaled by factors of 2^4, 2^9, and 2^{14}, and fed to one channel of the commutator as described for Detector A.

(iii) *Detector C* is similar to B except that a magnetic field of a few hundred gauss is applied across the collimator to exclude electrons with energies less than 250 kev. The proton response is the same as for B. The geometric factor for this detector is 2.33×10^{-3} cm^2 sterad.

(iv) *Detector D* is an RCA silicon junction particle detector with a sensitive area of 5 mm^2, and a 100 micron thick depletion layer, when operated at 12 volt bias. A layer of aluminum is evaporated over the sensitive area to exclude sunlight: the thickness of aluminum plus dead layer is 1 mg/cm^2. This counter is also placed at the end of a collimator as described above; the geometric factor for the detector is 1.57×10^{-3} cm^2 sterad for particles that enter through the opening in the collimator.

* The amplitude of these ripple voltages in Alouette I has probably been accentuated by the use of surge suppressors in all battery leads.

The detector output is amplified and fed in parallel to two discriminators, the outputs of which are scaled by various factors and fed to two channels of the commutator as described for Detector A. The amplifier gain and discriminator levels are set with a $P_o{}^{210}$ α-particle source so that protons with energies greater than 1 Mev (and heavier particles) are detected in one channel, and α-particles with energies greater than 5 Mev (and heavier particles) are detected in the other channel. The depletion layer thickness sets upper limits to the detectable proton and α-particle energies of approximately 8 Mev and 24 Mev respectively. This detector is insensitive to electrons of all energies.

(v) *Detector E* is a Geiger telescope consisting of two trays of Philips 18509 Geiger counters separated by 1/2 inch of lead and a small amount of other material. Due to the low efficiency of these counters the overall telescope efficiency is about 15 per cent, while the geometric factor is 4.4 cm^2 sterad. The minimum detectable proton energy is 100 Mev. The coincidence output from the trays is scaled by factors of 2 and 2^6, and is fed to one channel of the commutator as previously described.

(vi) *Detector F* is a 3/8-inch thick plastic scintillator mounted on an RCA C 7151C phototube. The scintillator is placed between the counter trays of detector E and is separated from each tray by 1/4 inch of lead. All pulses from the phototube in coincidence with the Geiger telescope are recorded. To extend the measurable pulse height range, the linear amplifier is tapped to provide two different amplifications. The pulses from the amplifier are fed to separate stretching circuits. The outputs of these, which differ in length, are mixed and fed directly to a subcarrier oscillator. An internally generated calibration pulse is fed through the system every 15 seconds. This detector provides data on proton spectra in the energy range 100 Mev to 700 Mev, and on α-particle spectra in the range 400 Mev to 2.8 Bev. In addition, it permits identification of relativistic protons and heavier particles, together with measurements of their intensity.

4. TELEMETRY SYSTEM

4.1 System Requirements

The 100 μsec sweep-frequency ionospheric pulse sounder produces data in the form of transmitted and received-echo pulses. Synchronizing and frequency calibration pulses are then added to form the composite video signal illustrated in Figure 23. Received echo pulses vary in width from 100 μsec to 10 msec depending on the number, range, and distribution of the reflecting surfaces in the ionosphere. The rise time of the echo pulse is limited by the IF and post-detection bandwidths in the sounder receiver. Overall video response is dc to 10 kc/s and, to avoid further pulse distortion with consequent loss of range resolution, a high frequency cut-off of at least 15 kc/s is required for the telemetry link. A low frequency cut-off of 0.5 cps is also needed to effectively eliminate droop on the frequency markers and 'spread' echo pulses.

In the VLF experiment, a high-gain audio amplifier covers the range 400 cps - 10 kc/s. Since it is impracticable to process VLF data in the satellite, the wide band output of this receiver is telemetered directly to the ground, where it is subsequently scanned with one or more narrow-band filters. Since the bandwidth of the ground scanner is only 70 cps, it was feasible to transmit the wide-band VLF data at a relatively small frequency deviation, typically less than ± 5 kc/s, and still obtain adequate S/N margins. This was done to provide for the possibility of simultaneous operation of the sounder and VLF experiments.

The energetic particles experiments required two telemetry channels, each having a frequency response from dc to approximately 80 cps. Cosmic noise data was obtained by monitoring the AGC level of the sounder receiver. This required one telemetry channel with a response from dc to 50 cps.

In addition, 'housekeeping' or engineering data was needed for in-flight monitoring of the spacecraft. Temperatures, voltages, currents and a magnetometer output were converted to dc voltage levels by appropriate transducers and these were then time-multiplexed into two 35-channel solid-state PAM commutators. The commutation rate was 18 cps; hence two telemetry channels, each having a response from dc to at least 60 cps, were required. The commutation rate was a compromise value that took into account the frequency response of pen recorders, available telemetry bandwidth, and the widely varying data rates encountered throughout the life of the satellite. For example, during the launch and injection phases a commutation rate of approximately 300 cps would have been required to resolve some of the engineering data. Once the operation of the satellite becomes routine only a few frames of engineering data are needed per day and a commutation frequency of 1 cps would have been sufficient. In practice, however, it has been found that a continuous record of engineering data at a commutation rate of 18 cps is exceedingly useful in diagnosing apparent malfunctions in the satellite.

The satellite orbit is computed by the NASA STADAN network, and to supply the necessary tracking information, a continuously-operating VHF beacon was provided in the spacecraft. The beacon transmitter is also a valuable aid to telemetry acquisition, particularly during the first few days of a satellite's life when the orbital parameters have not been accurately established.

4.2 Basic System

A block schematic of the telemetry system is shown in Figure 25. The use of two separate telemetry links reduces the possibility that a catastrophic failure will terminate all experiments in the spacecraft. This approach also leads to lower tape speeds at ground stations, negligible cross-talk between telemetry basebands, and more efficient use of IRIG subcarrier channels. To have achieved the same results with a single RF link would, at the very least, have required frequency translation and sideband filtering both in the spacecraft and on the ground. Furthermore, two RF carriers provide greater freedom in choice of modulation techniques, since the detection of one carrier is carried out independently of the other. The question of tape speed is an important one because of the large cost involved in recording data for one year at thirteen ground stations.

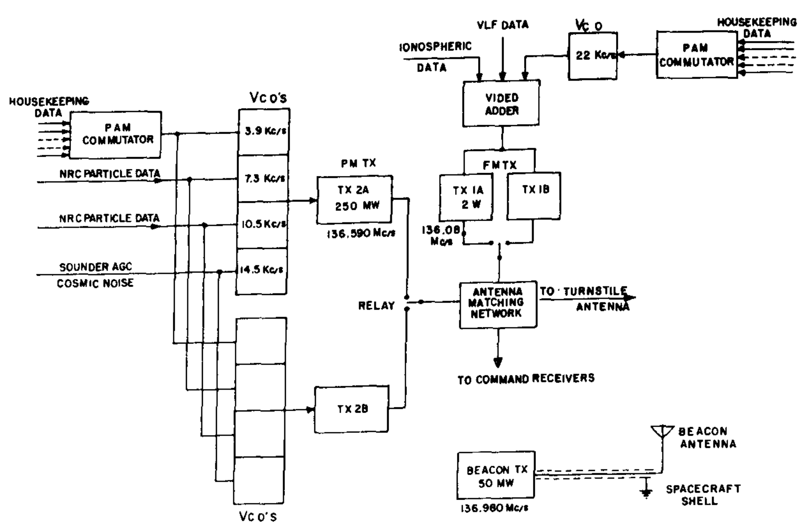

Fig. 25. Alouette I Telemetry System.

Finally, there was the practical consideration that in the 136 - 137 Mc/s band the maximum allowable channel allocation per RF carrier was 100 kc/s. If a single transmitter had been used the spectrum allocation would, therefore, have been reduced from 150 kc/s, as used in Alouette, to 100 kc/s.

An unexpected and potentially serious problem was the generation of cross-modulation products between the two telemetry transmitters. Unless special precautions are taken this can lead to serious desensitizing of command receivers. This is discussed in more detail in Section 4.3 of this report.

4.2.1 Narrow Band Telemetry Link

A 0.25 watt, 136.590 Mc/s transmitter is phase modulated by four standard IRIG subcarrier oscillators at 3.9, 7.35, 10.5 and 14.5 kc/s respectively.

The 3.9 kc/s subcarrier carries commutated engineering data such as battery voltages, charging currents, temperatures, etc. The 7.35 and 10.5 kc/s subcarriers are used for the energetic particles experiments. The 14.5 kc/s subcarrier is used to carry cosmic noise data and frequency markers. Data to the 10.5 kc/s oscillator is time multiplexed at a clock frequency of 64 cps and has a format suitable for automatic decommutation on the ground. The rms phase deviation of the transmitter is ± 0.8 radians, and the phase deviation for each subcarrier is such that the signal/noise ratio is constant for all four subcarriers.

On the ground the received signal is amplified by a conventional FM receiver, frequency translated to approximately 30 kc/s, and then synchronously demodulated using a phase lock tracking filter. Although the tracking bandwidth can be varied from 2.5 cps to 100 cps, it has been found in practice that phase noise sets a lower limit of 20 cps on the bandwidth of the phase locked loop. Pulse averaging subcarrier discriminators are used for the final demodulation process.

Since only one tracking filter is available at each ground station, diversity reception is impracticable, and hence polarization drop-outs are experienced*. The effectiveness of the tracking filter decreases rapidly as the number of subcarriers increases. This occurs because the phase modulation process generates a wide range of sum and difference frequencies which, when demodulated by a synchronous detector, contribute noise to the subcarrier spectrum. In this respect a pilot carrier FM-AM system would have led to more efficient use of available transmitter power. However, the choice was restricted to FM-PM because linear AM telemetry transmitters were not readily available.

In addition to its use in the telemetering of narrow band data, the 1/4 watt transmitter is also used as a redundant tracking beacon. This requires very low sideband levels within a few hundred cycles of the carrier and is a factor to be considered in the choice of subcarrier frequencies.

System parameters for the narrow-band telemetry link are shown in Table 5.

4.2.2 Wide Band Telemetry Link

A 2 watt, 136.080 Mc/s FM transmitter is frequency modulated by the video output of the ionospheric sounder. Peak deviation due to the sounder video signal is $\pm$ 35 kc/s, giving a modulation index of 3.5 for a post-detection bandwidth on the ground of 10 kc/s. Overall sounder video bandwidth is 0.5 cps to 10 kc/s, which is considerably narrower than the modulation bandwidth capability of the transmitter which extends from 0.25 cps to 60 kc/s.

A 22 kc/s subcarrier was added, mainly for redundancy, whose purpose is to monitor, continuously, redundant commutated engineering data. The deviation due to this subcarrier is +5 kc/s, hence final peak deviation of the telemetry transmitter is $\pm$ 40 kc/s.

* Diversity reception of synchronously detected signals is now possible using 'Electrac' combiners. At the time of writing, only the Ottawa telemetry station is regularly using an Electrac for reception of Alouette PM signals.

TABLE 5

System Parameters for PM Telemetry Link
Frequency = 136.590 Mc/s, Maximum Slant Range = 1400 Miles

KTB (BW = 1 cps)		- 204 dbw
Background (receiver and cosmic noise)	+ 13 db	
* Spectrum folding in tracking filter	+ 3	
** Subcarrier improvement threshold	+ 10	
Effective bandwidth (16 kc/s)	+ 42	
Subtotal		+ 68 db
Required receiver sensitivity		- 136 dbw
Path loss	+ 141 db	
Receiver antenna gain	- 20	
Polarization loss	+ 3	
Mismatch & fading loss	+ 6	
Subtotal		+ 130 db
Required transmitter power		- 6 dbw = 0.25 watts

* Doubles noise power per unit bandwidth.
** Signal-to-noise ratio in predetection bandwidth of subcarrier discriminator.

To obtain VLF data, the sounder is normally switched off and the VLF receiver is switched on so that it modulates the FM transmitter directly. The VLF experiment may be operated simultaneously with the sounder. Total peak deviation under these conditions will exceed the assigned ± 50 kc/s at times; however, the signal degradation due to over-deviation is negligible. Useful information has been obtained in this mode of operation.

System parameters for the wide band telemetry link are shown in Table 6.

TABLE 6

System Parameters for FM Telemetry Link
Frequency = 136.080 Mc/s, Maximum Slant Range = 2000 Miles

KTB (BW = 1 cps)		- 204 dbw
Background (receiver and cosmic noise)	+ 13 db	
Receiver improvement threshold	+ 10	
Receiver bandwidth (100 kc/s)	+ 50	
Subtotal		+ 73 db
Required receiver sensitivity		- 131 dbw
Path loss	+ 145 db	
Receiver antenna gain	- 20	
Polarization loss	+ 3	
Mismatch & fading losses	+ 6	
Subtotal		+ 134 db
Required transmitter power		+ 3 dbw = 2 watts

The choice of modulation technique is governed, not only by theoretical considerations, but also by such factors as complexity, availability of equipment, and peak power limitations of satellite transmitters. In practice, this eliminated coded systems such as PCM, and only relatively simple FM, PM and suppressed-carrier AM systems could be considered.

Direct FM was finally chosen because the technique led to higher S/N ratios and to lower tape speeds on the ground.

The calculated value of the received signal level, at a range of 2000 miles, is -101 dbm. This signal is at the FM threshold for a predetection bandwidth of 100 kc/s and a receiver input noise level of 13 db above KTB. The output S/N ratio is approximately 32 db at threshold for a deviation ratio of 4:1 and a post-detection bandwidth of 10 kc/s.

Various schemes were considered for lowering the FM threshold but these were abandoned either for technical reasons or because the necessary equipment was not commercially available.

Polarization diversity is used on the ground, and the received signals are amplified and detected using two FM receivers, having IF bandwidths of 100 kc/s, and conventional discriminators. The receiver outputs are fed to an AGC-type diversity combiner which effectively eliminates polarization fading.

Alouette is probably the first satellite in which direct FM has been used down to such low modulating frequencies.

An overall low-frequency cut-off of 0.5 cps introduced a number of problems. First, the diversity combiner had to be of the AGC-type, since the more common noise sampling combiner does not have the necessary low-frequency response. AGC combiners work very well in practice but need to be carefully matched to the receiver AGC characteristics. This type of combiner also proved surprisingly difficult to obtain and has only recently become commercially available.

A much more serious problem is the presence of low-frequency noise at the video outputs of telemetry receivers. The noise originates in power supply lines and becomes more noticeable as the video response is extended to lower frequencies. Therefore, special care is needed in regulating all power supplies to FM receivers. In practice, this has been a problem in less than 5% of tapes so far received.

The demodulated video signal is FM recorded at 15 inches per second using a 27 kc/s subcarrier oscillator. This FM mode of operation is necessary because of a low-frequency cut-off of approximately 300 cps associated with direct recording on tape.

At the time the wide-band FM system was specified it appeared that solid-state true FM transmitters would be available from several manufacturers. It soon became evident that advertising had outstripped engineering and that it would be extremely difficult to get a reliable transmitter to meet the Alouette specifications. Designers on the S-48 Topside Sounder program in the U.S.A. experienced the same difficulty. Satisfactory transmitters were finally produced at very short notice, late in the program (mid-1962), by the RCA Victor Research Laboratories in Montreal[18].

A block diagram of the RCA Victor transmitter is shown in Figure 26. The input signal modulates the capacitance of a varactor placed in series with a crystal in the feedback loop of an oscillator. The oscillator frequency is centred on 17 Mc/s to realize the advantage of crystals operating in their fundamental mode.

The oscillator modulator is followed by a cascade consisting of buffer amplifier and varactor frequency-multiplier stages, ending in a final buffer power amplifier. Buffer amplifiers on each end of a varactor multiplier are necessary to accurately define the source and load impedances. If this is not done, frequency instability and the generation of excessive noise can occur. The final buffer amplifier has a gain of approximately 4 db and provides sufficient isolation between the last varactor and the antenna load to virtually eliminate spurious outputs, instabilities, and noise from the varactor multiplier.

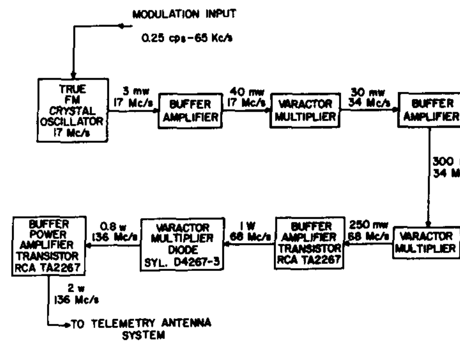

Fig. 26. True FM Telemetry Transmitter.

At the operating frequency the antenna and duplexer load impedance is approximately resistive, but at frequencies several megacycles away this is no longer true—a fact which makes the design of varactor power output stages at 136 Mc/s very difficult.

The overall efficiency of the transmitter was 25% and the power output is within ± 1.5 db of 2 watts over the temperature range -50°C to +75°C. A typical curve of power output and frequency stability versus temperature is shown in Figure 27.

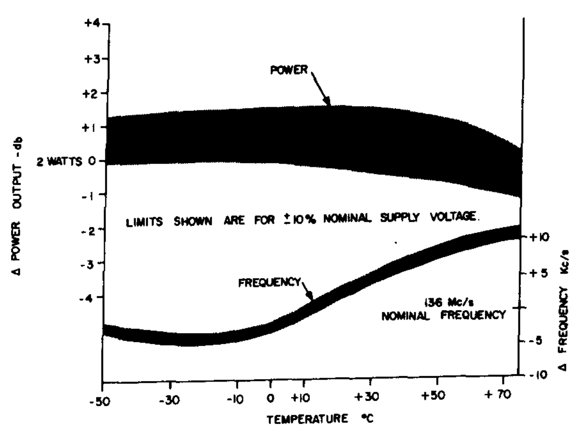

Fig. 27. FM Transmitter Output Power and Frequency Stability versus Temperature.

4.3 VHF Antenna System

In the Alouette satellite the command receivers and telemetry transmitters share a four-element turnstile antenna, while the beacon transmitter is connected to a single whip antenna(13). A schematic of the antenna feed system is shown in Figure 28. The two telemetry transmitters and command receivers are isolated from one another by coaxial line filters and hybrid rings.

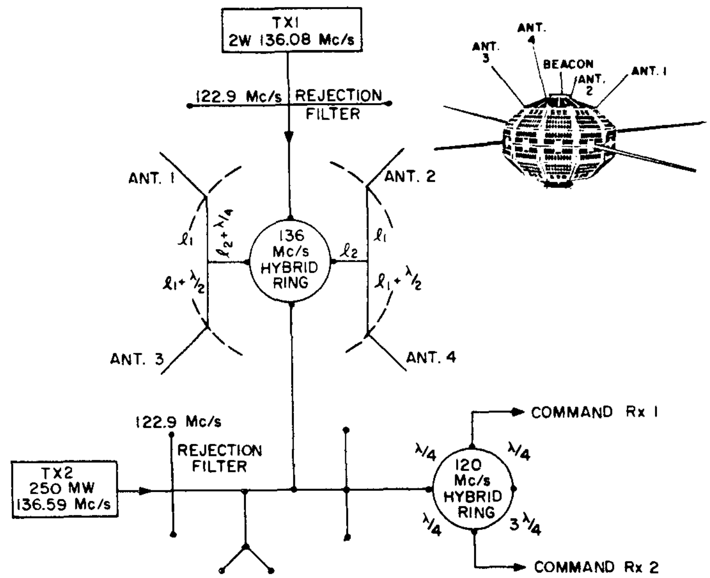

Fig. 28. Coaxial Line TM—Command Antenna Matching Network.

Polar radiation patterns for the beacon and telemetry antennae, plotted for the equatorial plane of the satellite, are shown in Figure 29. The beacon antenna pattern is relatively uniform, while the pattern for the turnstile antenna indicates nulls produced by the long sounder dipoles. To illustrate the significance of these nulls in ground station operation, and to indicate the improvement obtainable by diversity combining, the turnstile antenna patterns are plotted in rectilinear form in Figure 30 (a, b and c). For the 136.080 Mc/s telemetry link the contours shown correspond to a received signal of 2 microvolts at a slant range of 2000 miles. This boundary value represents the FM improvement threshold, as calculated in Table 6, while the enclosed shaded portions indicate regions where the received signal is below this threshold. Due to spin and orbital motion, all values of E_ϕ and E_θ are equally likely to occur, hence the ratio of shaded to total area represents the fraction of the operating time during which the signal is below threshold. Figure 30 (a) and (b) show that both E_θ and E_ϕ are below the FM threshold for 25 - 30% of the time at a range of 2000 miles. Figure 30 (c) illustrates the improvement due to polarization diversity and it can be seen that signal fading has been virtually eliminated.

Two basic problems occur as a result of operating two transmitters and a receiver from a common antenna [19]. The first and most serious results from cross-modulation products between the two telemetry transmitters which appear at the command receiver input. These appear as energy clusters spaced at intervals of 0.51 Mc/s, (the difference frequency) and extend for many tens of megacycles on each side of the 136 Mc/s band. Each energy cluster consists of a spectrum comprising the modulation spectra of the two telemetry transmitters.

The second problem is that broadband noise at the output of the telemetry transmitters is high enough in the region of the command frequency to seriously desensitize the receivers unless special precautions are taken.

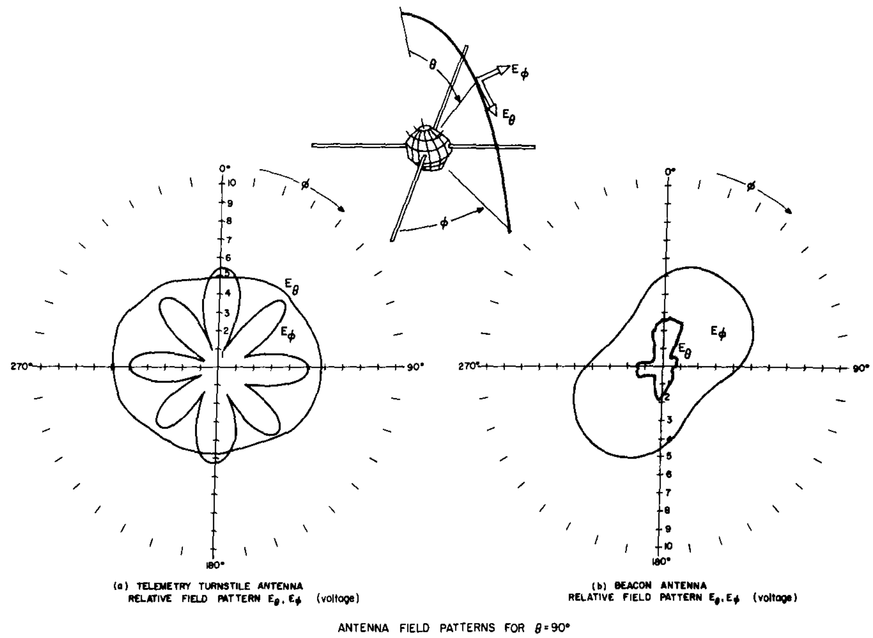

Fig. 29. Antenna Field Patterns.

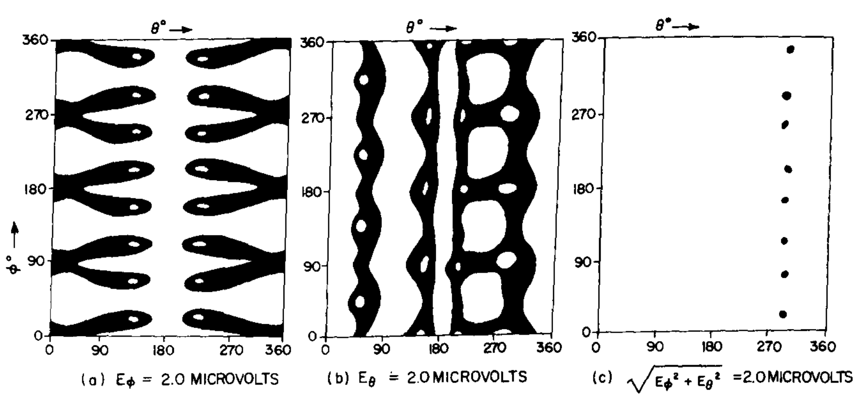

Fig. 30. Turnstile Antenna Field Strength Contours.

It was found that adequate reduction of cross-modulation effects could be achieved by maintaining a high isolation between the two transmitters, and by using coaxial line rejection filters, tuned to the command frequency, in the outputs of both transmitters. To achieve maximum isolation between the two transmitters it was necessary to balance accurately the hybrid ring by careful adjustment of the length of the turnstile antenna elements.

The isolation between the beacon whip and the turnstile antenna was 40 db and was high enough to effectively eliminate cross-modulation between the beacon and the telemetry transmitters.

Noise at 123 Mc/s, from the telemetry transmitters, is adequately reduced by a 123 Mc/s rejection filter in the output of each transmitter.

Mismatch losses, to the telemetry antenna, are negligible since the VSWR at each input is not greater than 1.4:1. Space and weight limitations required the use of miniature coaxial cable types RG/187U and R/188U. The measured insertion losses were 3.5 db for the 1/4 watt transmitters, 2.8 db for the 2 watt transmitters, and 5.3 db for the command receivers.

5. COMMAND SYSTEM

5.1 General

Approximately 30 watts of power is required to operate all the experiments in the satellite, while the average power supplied by the solar cells in a 66% sun orbit was initially only 15 watts. It was decided that the most practical way to overcome this limitation, and at the same time allow read-out over each ground station, was to provide means for turning the satellite on and off by command at each station pass. Moreover, since the design objective was to produce a satellite that would have an operational life of at least one year, it was deemed advisable to include a number of redundant units that could be switched into operation by command if necessary. Another objective was a command capability that would enable the satellite to be operated in a number of modes, both to facilitate change of mission emphasis at any given time, and to permit the best possible use of the satellite in the event of the failures of any particular experiment.

As a result, a command system capable of completely fulfilling these objectives was designed. Inherent was the assumption that the increased electronic system reliability, achieved through redundancy, and the added operational flexibility of the spacecraft, more than offset the disadvantages of greater command system complexity. Thus it was decided to base the design on a commercially available 7-tone command equipment(2) that had a history of successful use in a number of prior satellites and could control up to twelve sets of output relays.

Command messages are coded in the form of ordered combinations of seven discrete audio tones. These tones are used sequentially to amplitude modulate a VHF carrier transmitted to the satellite. Redundant receivers and decoders operate a relay branching network which routes control power to the output relays.

5.2 System Parameters

Table 7 lists the system parameters used in the design of the command link. The calculations apply to STADAN stations where the specified minimum radiated power is 170 watts from a linearly polarized antenna that has a minimum gain of 11 db, and a nominal half-power beam width of approximately 45°. At a slant range of 2000 miles, corresponding to a satellite elevation of 4° above the horizon, the expected signal at the satellite is 17 db above the operating threshold, after allowing losses of 6 db for fading and 3 db for antenna mismatch at the satellite.

5.3 Decoder Operation and Output Functions

The output relays are all double-pole double-throw magnetic latching relays using two control coils, hence control of twenty-four sets of relay coils is required for the twelve sets of output relays. This is achieved by an eight-by-three matrix wherein the first four tones are used to address the positive supply voltage to any one of eight lines, while the last three tones are used to provide three alternative paths to ground.

TABLE 7

System Parameters for Command Link
Frequency = 122.900 Mc/s, Maximum Slant Range = 2000 Miles

Transmitted power		+ 22 dbw
Transmitter antenna gain	+ 11 db	
Path loss	- 144	
Receiver antenna gain	0	
Fading loss	- 6	
Mismatch loss	- 3	
Subtotal		- 142
Input signal level to receiver		- 120 dbw
Receiver threshold sensitivity		- 137
S/N margin		+ 17 db

The address logic of the decoder is shown in Figure 31. Associated with each of the four discrete audio tones is a tuned audio circuit, together with detection and amplifier circuitry, which causes a particular NPN-transistor to conduct whenever a given tone is transmitted. Relay coils are connected to the transistors in such a manner that control of the associated relay contacts can be achieved by a suitable sequence of audio tones. The contacts of the four relays, K_1 to K_4, are arranged in a tree configuration to permit the 15 volt supply to be switched to any of the eight address lines shown. The sequence of tones for each address line is indicated on the diagram and follows directly from the logic of the circuit.

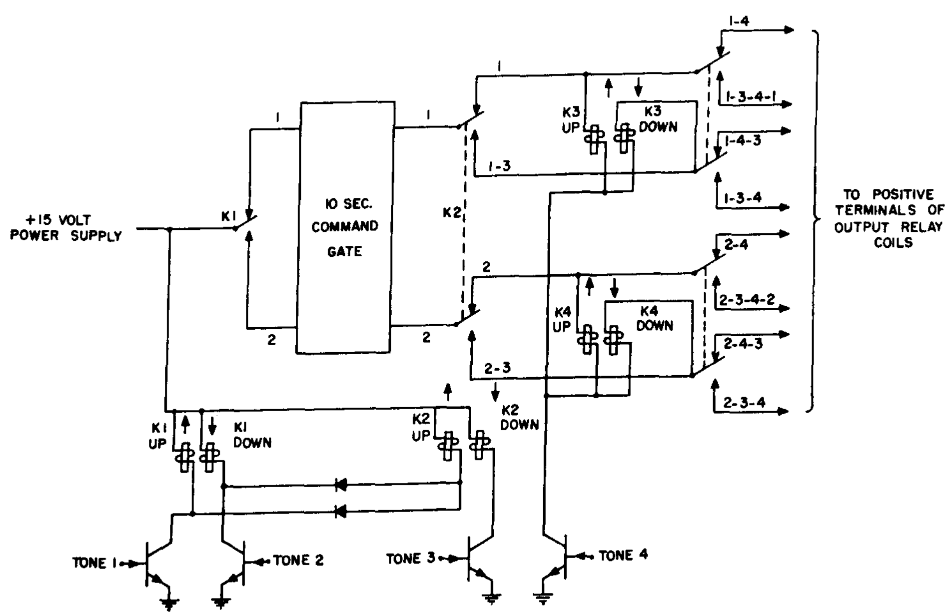

Fig. 31. Decoder Address Logic.

The function of the command gate circuit, inserted between K_1 and K_2 relay contacts, is to inhibit operation of the output relays, except for a pre-determined time interval of approximately 10 seconds following the operation of tone 1 or tone 2. This feature was added to the basic command system to reduce the probability of operation by spurious signals falling within the bandwidth of the command receiver.

The complete decoder control system is illustrated in operational form in Figure 32. Each basic command operation shown corresponds to a particular contact position of one output relay and is achieved by passing current through an appropriate relay coil. This is done by transmitting an address tone sequence which connects the power supply to the positive side of the relay coil, followed by transmission of one of the last three tones to provide a conduction path to earth from the negative terminal of the relay coil. The eight address lines combined with the last three tone circuits form a matrix allowing control of twenty-four relay coils.

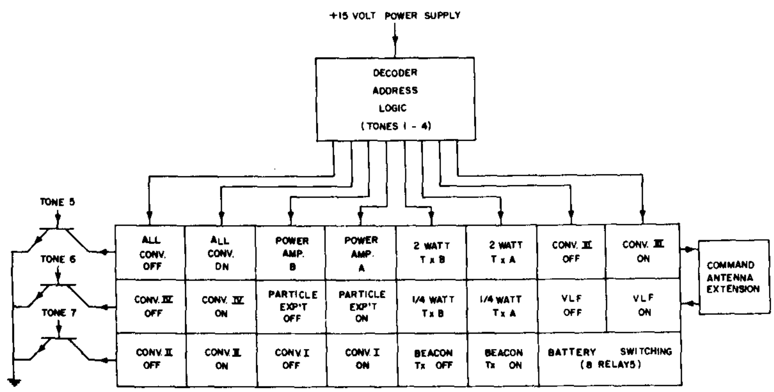

Fig. 32. Alouette I Command System.

Ten positions in the matrix are used to control five sets of ON-OFF relay contacts used in conjunction with the four dc-dc converters employed in the satellite power supply system. These relays allow the converters to be turned on either simultaneously or individually as may be required for any particular mode of satellite operation.

Six of the matrix positions are used for ON-OFF control of relays used to turn on two individual satellite experiments and the tracking beacon, and six more are used to allow command selection of operating units in the telemetry and power amplifier systems, where redundancy is employed.

The remaining two positions in the decoder control matrix are sequentially cycled to provide control of eight relays in a battery switching unit. These allow a variety of interconnections to be made between the six batteries—four primary and two redundant—and the four solar cell banks of the satellite. The switching functions performed by this unit are shown in Figure 33. Each solar cell bank may be connected to an associated primary battery, or to either of two spare batteries, or may be disconnected. It may be of interest to note that a total of 256 different modes of connection are possible, thus giving considerable flexibility in the choice of operation in the event of failures occurring in either individual batteries or solar cell banks.

One additional function of the system was a method for command initiation of the extension of sounder antennae, in case of malfunction of a mechanically tripped switch employed for this purpose. Command initiation was arranged to occur by commanding on converter 3 and the VLF experiment.

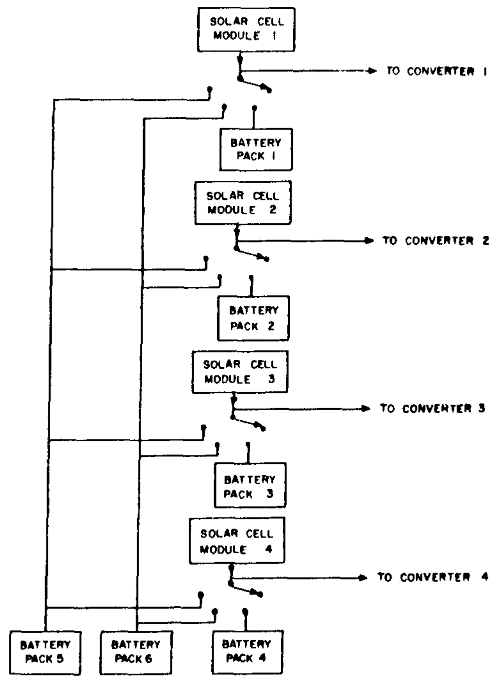

Fig. 33. Battery Pack Switching Functions.

5.4 Switching Techniques

The implementation of most of the command functions which have been described, involved, for the most part, fairly simple wiring of the relay contacts in a manner appropriate to the particular switching requirements of each circuit.

In particular, circuits which required switching of direct currents presented only very straightforward switching problems. In these cases relays having silver contact material were used because of their high contact rating, and any extra contacts available were paralleled for redundancy. Physically, most of the relays performing these simple switching functions were located within the decoders to save space.

The switching of RF circuits, as in the case of redundant VHF telemetry transmitters, posed a special problem in connecting the coaxial line feeds from either of two transmitters to a coaxial output line, without excessive reflection losses. Figure 34 illustrates the technique used for this case. The relay was mounted in a small box fitted with coaxial connectors to the input and output lines, and short leads were made from these connectors to the relay contacts and armature as shown. A piston-type capacitor, variable from 2 - 17 pf, was connected to each relay contact and tuned for minimum reflection losses with the output line properly terminated. Typically the standing wave ratio achieved was less than 1.1:1. Gold alloy contact material was used because of its high reliability in dry circuit applications.

Command initiation of sounder antenna extension was accomplished by a pulse method of relay operation which is illustrated in Figure 35. In this circuit, extension of the antennae occurs when the battery is connected to the extension motor by closure of the relay contacts. This is effected by a pulse of current, which flows through the closing coil when the 15 volt supply voltage is connected to the positive terminal of a 47 μF electrolytic capacitor. The connection from the capacitor to the supply voltage is made through a spare contact of the VLF receiver relay, which is in series with the relay contacts turning on converter 3. This provides the condition that both of these relays must be closed to trigger the antenna extension. For convenience in testing and resetting the unit, a similar arrangement is used to open the relay contacts by operating converter 4. The principal advantage of the pulsed technique of relay operation is the negligible power consumption involved.

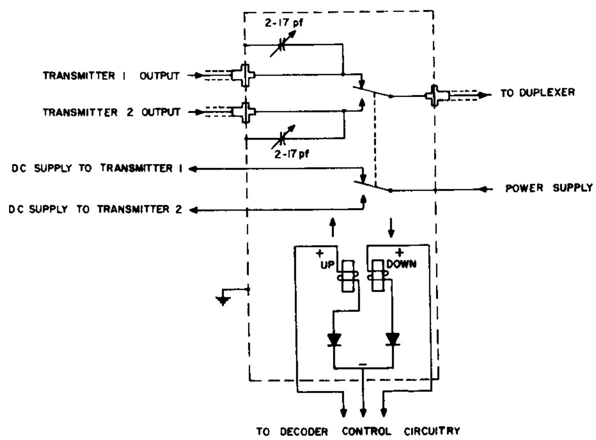

Fig. 34. Switching of VHF Transmitters.

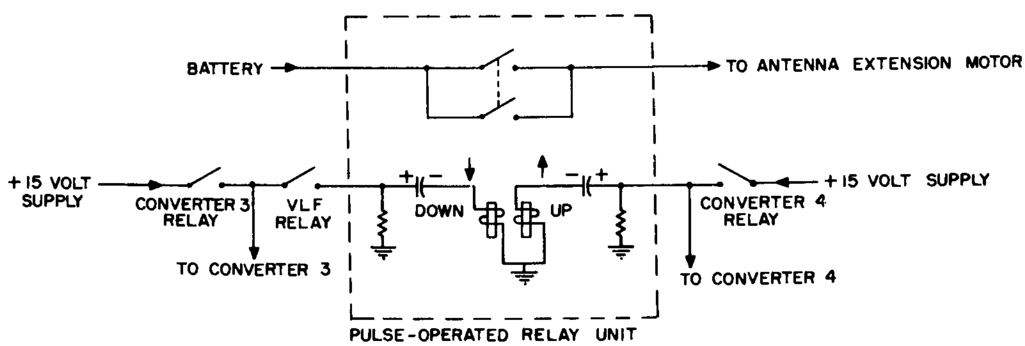

Fig. 35. Command Back-up System for Sounder Antenna Extension.

A somewhat more involved command switching technique was employed in the operation of the battery pack switching circuit shown in Figure 36. Two relays in series are used in conjunction with each solar cell bank to permit four different modes of connection. Thus eight, two-position relays, or sixteen coils in all, must be controlled in operating the switching unit.

The basic method consists of sequencing the decoder control from one relay to the next by means of the address portion of the command, and then operating the execute portion of the command when the desired relay has been reached. Sequencing is done by a 3-stage binary counter which steps the control from one relay to the next each time the '2-4' address rail is energized. The negative terminals of each relay coil are connected to an AND gate which conducts to earth when all four of its inputs are at zero potential. Three of these inputs consist of particular connections to either the input or output sides of each of the three flip-flops of the scaler, which provides a unique combination of these three connections for each of the eight AND gates. The fourth input comes from the 'tone 7' line which is positive in potential except during transmission of this tone. Thus, for any given state of the scaler there is only one AND gate ready to operate when the execute command is given. Control is arranged to pass in an orderly manner from one relay to the next each time the '2-4' rail is freshly energized. Both the voltage on this line and the binary state of the scalers are telemetered back to the ground station to allow monitoring of the battery switching operation.

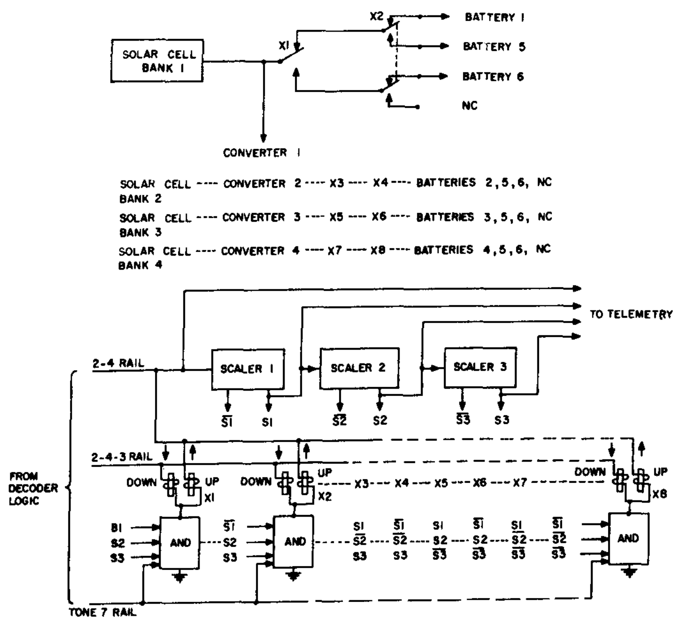

Fig. 36. Battery Switching Unit.

Operation of the battery switching circuit involves more time and care than is required for the simpler command functions. On the other hand, switching of batteries is seldom required, and the complexity of the operation is further justified by the fact that only through a command sub-multiplex method was it possible to provide the necessary switching capacity.

5.5 Command System Auxiliary Units

5.5.1 Automatic Turn-Off Unit

Another feature of the command system was an automatic turn-off circuit which is shown in Figure 37. Since the satellite consumes more power in its sounding operation than is supplied by its solar cells, a serious drain on the batteries might result if the satellite were not turned off at the end of each ground station pass. This circuit was designed to eliminate the danger by providing for automatic turn-off of converters ten minutes after turn-on.

A continuously-operating clock pulse generator is used, together with a divide-by-one-thousand magnetic counter, to give one output pulse every ten minutes. Turn-on of any converter triggers a circuit which resets the counter to zero while simultaneously blocking the output pulse circuit, thus ensuring a full ten minutes delay before the appearance of an output pulse. This output pulse is applied to the OFF control coils of all the relays whose contacts are used to turn on converters.

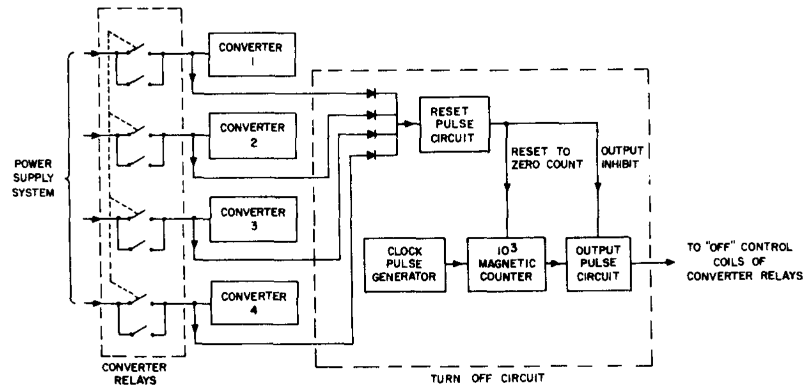

Fig. 37. Automatic Turn-Off Unit.

5.5.2 Command Gate

The command gate circuit shown in Figure 38 is another circuit that was added to the command system for operational reasons. The closing coil of the command gate relay is operated by a surge resulting from a switch-over of decoder relay K_1, which is controlled by the first two tones of the command system. This initiates an output pulse, delayed by 10 seconds, which is used to open the gate relay contacts and thus prevent subsequent operation of the command system output relays. This creates the operational requirement that all of the tones in a given command sequence must be transmitted within the 10-second gate interval, and hence this considerably reduces the chance of command response to stray signals.

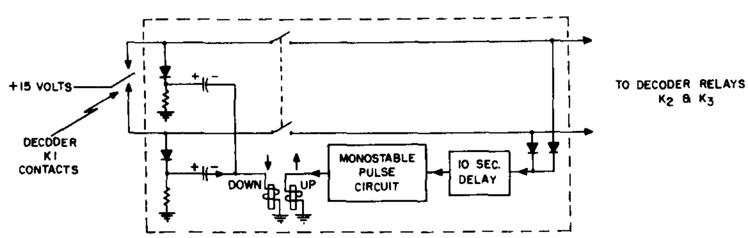

Fig. 38. Command Gate.

5.6 Ground Equipment

Ground equipment for the Alouette command system was relatively simple and will be described only briefly. Essentially the equipment for each station consisted of a seven-tone command encoder, an AM transmitter, and a steerable command antenna.

Transmitted power from the STADAN stations was greater than or equal to 170 watts, and from the Canadian stations greater than or equal to 500 watts. All stations used a Yagi-type transmitting antenna that has a minimum gain of 11 db and a half-power beam width of approximately 45°. The command antenna was located in the centre of the telemetry receiving array.

6. POWER SUPPLY SYSTEM

6.1 System Description

For in-flight operation, power is derived from the sun, using silicon solar cells. Since the spacecraft must be able to operate in darkness, and since the power drawn by the major subsystems exceeds that available from the solar cells, power storage is required and is provided by nickel-cadmium batteries.

On the ground, electrical power is provided by specially designed external battery chargers which supply controlled currents to the batteries in the spacecraft.

The Alouette I power supply system (Fig. 39) may be considered to consist of three basic subsystems: a main power supply to provide, on command, 30 watts to the spacecraft experiments and telemetry system, a continuously operating power supply to provide a maximum of 1 watt for the command system and tracking transmitter, and a 15-watt-hour expendable power supply for sounder antenna extension. Design objective was to provide for at least 3 hours of operation per day in a minimum sun orbit at the end of one year.

The main power supply is divided into four independent subsystems, each supplying roughly the same average power, and consisting of an array of solar cells, a 5-amp-hour 15.6 volt Ni-Cd battery, and a dc-dc converter. This separation into independent subsystems was carried out to minimize potential electrical interference problems, and improve reliability by limiting the seriousness of individual component failures. Also because of capacity, i.e., amp-hour limitations of available Ni-Cd batteries, this arrangement provided increased storage capacity to sustain continuous operation of the experiments over extended periods of time. Two spare batteries are also included in the main power supply. These are normally in a standby mode but may be switched in by command to take over the functions of any or all of the four active batteries.

The command system and the tracking beacon require power continuously, and require a supply having particularly high reliability. This is provided by an OR-gate arrangement of high power diodes connecting the six batteries to the continuous power line. This line draws its power at any time from the battery having the highest terminal voltage. Two diodes are used in series in each of the OR-gate lines to prevent possible battery damage, which might occur in the event of a diode short-circuit failure.

A seventh battery, consisting of six nickel-cadmium 'F' cells connected in series to give a nominal output of 7.8 volts, provides power to the drive motor used for extension of the sounder antenna poles.

Following completion of antenna extension, this battery remains connected to the motor and hence discharges completely. The 5-amp-hour capacity of the 'F' cells provides a safety factor of approximately 2.5 over that required for a normal extension.

6.2 Solar Charging Supply

The solar charging supply consists of 6480 p-on-n silicon 1 ohm-cm cells arranged to provide 144 groups of 45 series-connected cells. Gridded 1 cm x 2 cm cells were used having an air mass zero efficiency of 8.5 - 9%. These cells were distributed over the external surface of the satellite (Fig. 1) on 48 aluminum honeycomb panels and were arranged so that the current available from each of the four charging sources is sensibly independent of sun-satellite orientation. Although the total cell area was 12960 sq. cm, it is only the projected area in the direction of the sun which is effective in providing power. This projected area was 3120 sq. cm giving an aspect ratio of 4.15 which was constant to within ± 5% for all orientations of the spacecraft with respect to the sun. Cover glasses (Corning 0211), 0.012" thick with anti-reflective and spectrally selective coatings, were attached to the cells with an epoxy-based adhesive. The cover glasses greatly reduced the damaging effects due to radiation and

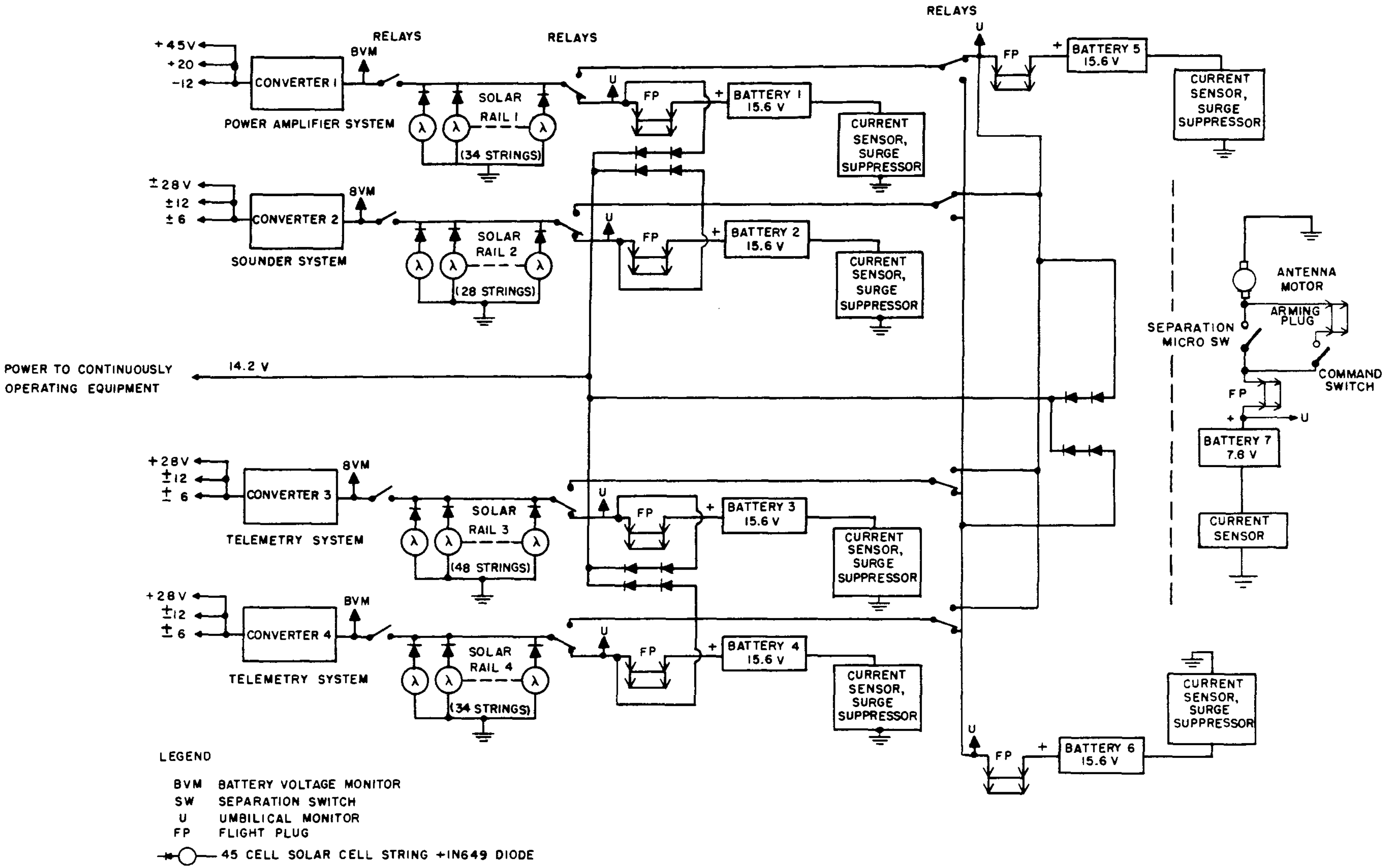

Fig. 39. Power Supply Block Diagram.

micrometeorites and were also used in the adjustment of the a/e ratio for spacecraft thermal control. The solar constant was assumed invariant and equal to 140 mW/sq. cm. In addition to direct radiation from the sun there is the Albedo or earth's reflected light and this was assumed to have an average value of 35 mW/sq. cm, giving a total solar input energy rate of 175 mW/sq.cm.

It was originally expected that the charging power would be reduced by 20-25%, after one year in orbit, due to the effects of radiation damage, micrometeorite erosion, adhesive darkening and general aging.

Because of the anticipated change in solar cell characteristics with time, the solar supply was initially mismatched to its battery-load system to provide a maximum average long-term power output. The design was carried out for what appeared, at the time, a rather extreme worst-case condition of 40% reduction in charging current after one year in orbit. In practice this worst-case figure was nearly reached (observed drop in charging current 38% after one year) due to the unexpected presence of an artificial radiation belt created by the so called Starfish Event, i.e., the July, 1962, U.S.A. Hydrogen Bomb test over the Pacific.

Furthermore, it was assumed that the satellite would be spinning at approximately 2 rpm and that its spin axis would be perpendicular to the ecliptic. Under these conditions solar cell temperatures were calculated to reach minimum and maximum values of - 20°C and + 40°C, respectively, for a maximum shadowed orbit. For a 100% sun orbit the average cell temperature was calculated to be + 45 to + 50°C. Due to unexpected despin torques, arising from thermal bending of the sounder antennas and the effects of solar pressure, the satellite despun to zero rpm after approximately two years in orbit. Calculations and in-flight measurements indicate, that for a 100% sun orbit, this has resulted in illuminated solar cell temperatures increasing to approximately + 75°C and has had the effect of further reducing solar power output by approximately 25%*.

Initially the solar cells provided a total power output of 23 watts distributed according to the following table:

Charging Current (mA)	Power (Watts)	Battery No.
350	5.5	1
290	4.5	2
500	7.8	3
350	5.5	4
–	–	5
–	–	6
Total 1490	23.3	

Degradation of solar charging current with time is shown in Figures 40 and 41. The close agreement between observed and calculated values in Figure 40 shows that the reduction in solar power output in Alouette I has been almost entirely due to radiation damage. To date, solar cell currents have decayed logarithmically with time, and the rate has been such that most of the efficiency loss occurred within the first few months in orbit.

A diode was placed in series with each solar cell string to avoid battery discharge when the satellite is in darkness. Dark resistance of a 45-cell series string is $\simeq$ 500 ohms.

* Solar cell power output drops 0.5%/°C for a matched supply. A somewhat greater degradation with temperature is observed for a mismatched system. See Appendix II (page 97) for further discussion.

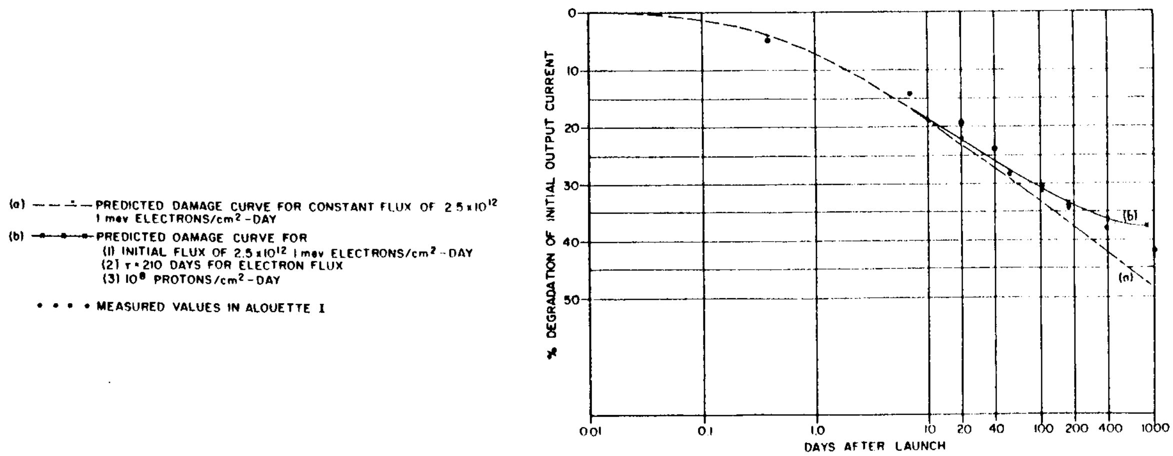

Fig. 40. Degradation of the Output Current of the Alouette I Solar Cell System.

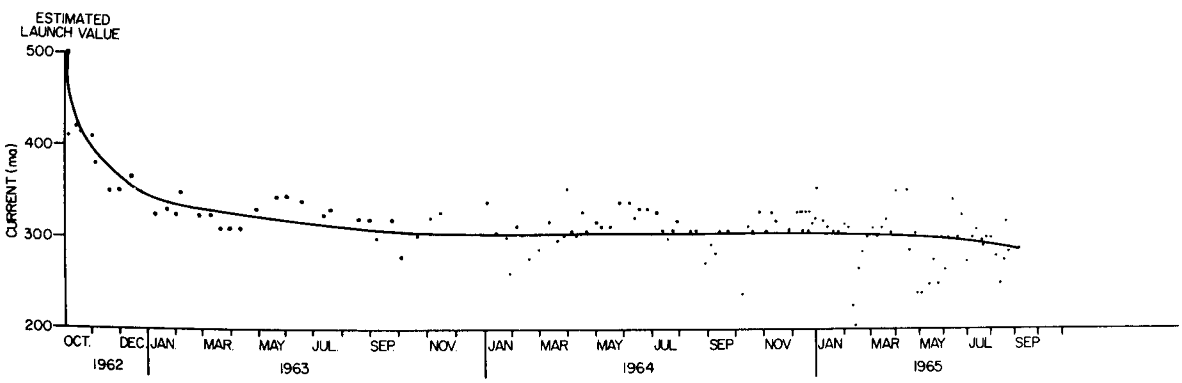

Fig. 41. Decay of Solar Cell Charging Current since Launch for the Converter III System.

Performance of the system has been very satisfactory in spite of the fact that Alouette I was launched shortly after the creation of the artificial radiation belt. After three years there is still sufficient power available to operate all experiments for 3 hours per day in a 100% sun orbit.

Major reasons for this success are:

(a) conservative design,

(b) design chosen for mechanical integrity over temperature range - 100°C to + 100°C to ensure no serious mismatch of thermal coefficients of expansion for the various materials,

(c) use of a flexible cell interconnection technique (proprietary to the manufacturer)

and (d) extensive series of flight acceptance tests at + 90°C and - 50°C.

6.3 Batteries

Each battery in the main power supply has a nominal voltage of 15.6 volts and consists of twelve 5-amp-hour 'F' size hermetically sealed nickel-cadmium cells connected in series. The individual cells were wrapped in glass-fibre insulating tape, and cemented in groups of six in aluminum castings located in the centre of the spacecraft structure. This arrangement resulted in very efficient heat removal from the individual cells.

The batteries are connected to the dc-dc converters via magnetic latching relays and in series with each battery is a surge suppressor whose main function is to limit current transients to safe levels during switch-on (Fig. 42). Also in series with each battery is a low value resistor which serves as a sensor for a current monitor circuit.

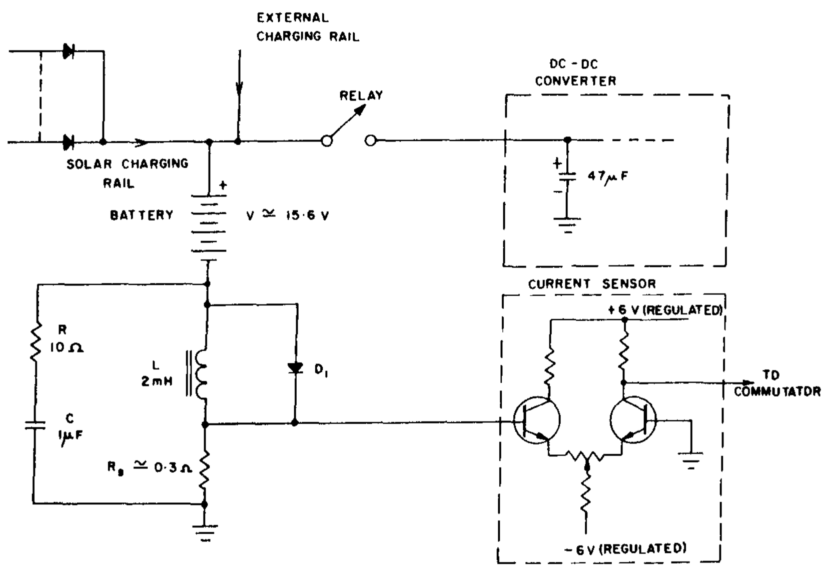

Fig. 42. Battery Surge Suppressor.

A nominal voltage of +15.6 was chosen and was a compromise value which took into account i^2R losses in the wiring harness between the batteries and dc-dc converters, as well as overvoltage and efficiency considerations in command receivers, other continuously operating equipment, and dc-dc converters. For example, an open circuit in one of the four active batteries in the main power supply system could raise the common diode voltage to very nearly the open circuit output voltage of the solar cell supply. For a 15.6 volt system and a solar-cell temperature of -20°C this open circuit voltage is approximately 30 volts.

All battery voltages are positive, i.e., the negative terminal of each battery is at the same potential as the spacecraft deck and shell. Therefore, the solar cells are positive with respect to the spacecraft body, and because the mobility of electrons is much greater than that of positive ions it is likely that the potential of the spacecraft shell will be driven many volts negative with respect to the surrounding plasma*.

A negative supply would have tended to clamp the spacecraft shell at plasma potential. In practice, this would have meant redesign of commercially available command receivers and decoders and tracking beacon transmitters.

* The advantages of a negative supply were first pointed out to the author by Prof. J. Sayers, Birmingham University, in March 1963.

With the assistance of the Canadian Defence Chemical, Biological and Radiation Laboratories (DCBRL) a major effort was made to improve the reliability of commercially available Ni-Cd cells. This resulted in some important differences between Alouette I cells and cells commonly used in U.S. spacecraft at the time. These differences are: (a) non-woven polypropylene separator material was specified because it provided best prospect of long life and stable performance, (b) 'coined' plate edges were used to virtually eliminate short-circuits between plates, (c) a very high quality electro-chemical system was specified having a high purity electrolyte with particularly low carbonate content, and (d) the negative plate capacity to positive plate capacity ratio was 1.5:1 for reliable operation at temperatures below 25°C.

Cell uniformity both on charge and discharge was considered desirable for long life operation under worst-case conditions and was verified by an extensive series of flight acceptance tests at -10°C and +25°C.

Charging currents to batteries never exceeded C/10 = 500 mA, where C is the cell capacity in amp-hours. Furthermore, since each battery could be charged indefinitely at this maximum rate, without compromising its reliability, no devices or circuits were added to the spacecraft to limit either the current or total charge delivered to any battery.

The $\frac{I_{charge}}{I_{discharge}}$ ratio was made essentially equal for all batteries, although somewhat higher for those batteries (e.g., No. 2) having a low charging current, in order to compensate for slightly lower charging efficiency under these conditions.

Operation in flight is such that the energy removed from the cell is replaced by 1.15 times its value to allow for cell inefficiency. Maximum depth of discharge in flight was originally specified as 25% but after six months in orbit was increased to 33%.

6.4 Converters

Dc-dc converters are employed to provide a variety of rail voltages to the electronic systems. At the start of the program converters of acceptable reliability were not commercially available. This situation was considered sufficiently serious that in S-48, the U.S. Topside Sounder, dc-dc converters were banned altogether. Therefore, the possibility of eliminating converters in Alouette I and operating all systems off a single power supply rail was examined. This approach was rejected, not only because it seemed that there was a reliable in-house converter design available, but also because the availability of multiple voltages of both polarities makes circuit design much easier, eliminates 'floating grounds', and permits low-voltage high-current circuits to be driven with reasonable efficiency. Allowing for losses in current and voltage limiters the single supply voltage approach would have required a nominal battery voltage of approximately 30 volts to drive the FM and PM telemetry transmitters and the FM subcarrier oscillators. Also, it is unlikely that the 100 W sounder-transmitters could have been designed, within the scheduled time, to operate from 30 volts. Hence, at least one dc-dc converter would still have been needed. Finally, an overvoltage cut-out would have been required to protect against the possibility of a 60-volt open-circuit output from the solar supply appearing on a battery voltage rail.

Output voltages were fixed at ± 6, ± 12 and ± 28 volts for converters 2, 3, and 4; five of these rails being generated in converters 3 and 4 and six in converter No. 2. Converter No. 1, which powered the sounder transmitters, had output rails at +45, +20, and -12 volts, respectively. The choice of voltage levels was considered optimum and took into account such conflicting factors as ease of circuit design, overall simplicity, minimum power consumption, breakdown margins in diodes, transistors and electrolyte capacitors and system reliability.

The basic converter design consists of a magnetic saturating-core square-wave oscillator using a pair of germanium power transistors to drive a non-saturating multi-tapped output transformer (Fig. 43). The converter had a typical power conversion efficiency of 80% at nominal load currents, and was designed to tolerate overloads and short-circuit conditions in the output rails[20].

In general, converter output voltages were unregulated, but all were limited in order to protect against the application of excessive input voltages. All converters used the basic circuit configuration shown in Figure 43. The schematic diagram, which is for converter No. 4, also illustrates some of the techniques used for voltage and current limiting, monitoring, regulation, surge suppression, etc.

T_1 is a non-saturating transformer that generates the required output voltages via secondary windings, rectifiers and filters. T_2 is a small saturating transformer that determines the oscillation frequency of the converter and provides the necessary positive feedback to the switching transistors. Transformer cores were supermalloy toroids with 0.001" laminations and were enclosed in grease-packed nylon bobbins. Q_1 and Q_2 are 2N174A germanium power transistors with their collectors bolted directly to one wall of the aluminum box housing the converter.

Oscillation frequency for each converter was approximately 3 kc/s and was an optimum value for maximum efficiency, taking into account such factors as storage losses in transistors and rectifier diodes, core losses, and i^2R losses.

Base drive currents to Q_1 and Q_2 were one-tenth the nominal input current to the converter, which ensured normal converter operation for $\beta_{DC} \geq 10$ in the switching transistors. A design minimum of ten was chosen for β_{DC} to provide the largest possible safety margins against radiation damage, and unexpected increases in load currents, without at the same time reducing the conversion efficiency excessively. Operation at low beta levels was considered particularly important because Q_1 and Q_2 are low-frequency germanium power transistors ($f_\alpha \simeq 500$ kc/s) and hence were likely to experience significant β degradation due to radiation damage when in orbit. Q_1 and Q_2 were selected for $\beta_{DC} \geq 50$ at nominal load currents, and if a lower limit of 20 had been set for β_{DC}, then converter efficiency would only have been increased by 3-4%. The loss in efficiency comes about as follows: as the base drive currents are increased, to permit low β operation, R_{B1} and R_{B2} (in Fig. 43) must be reduced in value to minimize power losses in the base circuits of the switching transistors. However, reducing R_{B2} also reduces the starting current drawn from the base of Q_2 hence R_S must be increased in value, which in turn increases the power dissipated in this starting resistor. Starting losses could have been virtually eliminated by replacing R_S with a pulsed or gated starting circuit. This approach would have increased conversion efficiencies by about 5% but would have led to a relatively complex starting circuit. It was rejected in favour of the less efficient but much simpler resistive starting technique.

The value of R_S was made low enough to ensure reliable starting on full load at -50°C at half the nominal input voltage to the converter, i.e., at +7.8 volts. Above +10°C, R_S was hardly needed since the collector leakage currents in the switching transistors were normally high enough to ensure starting at nominal input voltages. All spacecraft load currents were either a linear function of load voltage, i.e., resistance constant, or varied non-linearly with this voltage in such a way that no converter was excessively loaded during starting. The converters were required to work into reactive loads, the most extreme example being the +45v rail in converter No. 1 which was connected via a 22Ω resistor to a reservoir capacitance of 900 μF in the sounder transmitter.

Voltage 'spikes' at the collectors of Q_1 and Q_2 were eliminated by tightly coupling both halves of the primary of transformer T_2 using a bipolar winding on a toroidal core. Toroidal transformers also minimized leakage flux, an important RFI consideration in a spacecraft containing wide band VLF and HF receivers. 10-90% transition times were initially 3 μs for the switching transistors in all converters. To suppress

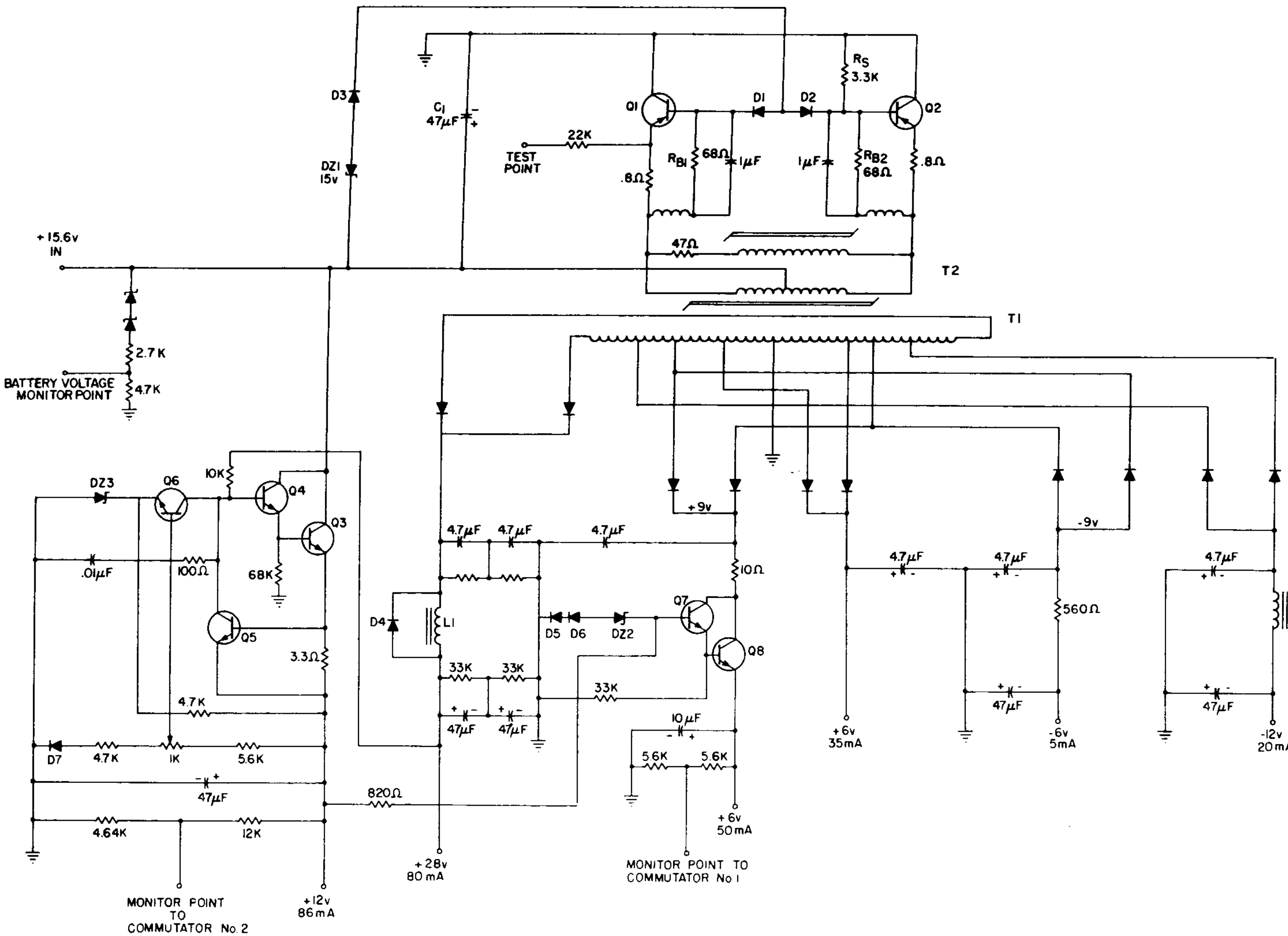

Fig. 43. Schematic of Converter No. 4.

converter interference in the sounder receiver it was necessary to increase the switching times in converter No. 2 to approximately 6 μs.

Double-silk-covered enamelled wire was used for all transformer windings, to reduce the possibility of shorted turns developing due to faulty insulation, or to abrasion resulting from magnetostrictive vibrations in the toroidal cores.

To test for damaging or anomalous transients the in-circuit $V_C - I_C$ dynamic load line was examined for each switching transistor in each converter.

Weight and dimensions of each converter were approximately 2.8 lbs and 2 5/8 in. x 5 1/2 in. x 5 in., respectively.

6.5 Protective Circuits

To eliminate the need for overvoltage cut-outs, all circuits connected to the 15.6 volt batteries were designed to operate reliably over a battery rail voltage range of +12 to +35 volts. The +35 volt limit was set by the voltage ratings of solid tantalum capacitors and could not be exceeded in flight even under the worst conceivable combination of low solar cell temperatures, open-circuit batteries and light power supply loading. Furthermore, output voltages from converters were limited by forcing the switching transistors to function as series regulators when the converter input voltages exceeded a predetermined level. In Figure 43, D_{Z1} avalanches when the input voltage is $\approx$ 16.4 volts. As the battery voltage is raised, the current through the zener diode increases and is steered via D_1 or D_2 into the base of the conducting transistor bringing it out of saturation. Therefore, the increase in battery voltage appears across the ON transistor, thus maintaining a constant voltage across the primary winding of transformer T_1. One drawback is that the ON transistor tends to oscillate when series regulating, a hazard which was reduced to barely acceptable levels in Alouette I and was not completely eliminated until Alouette II.

Low-value emitter resistors (0.8Ω in Fig. 43), limited peak-transient and steady-state currents in Q_1 and Q_2[20], with the result that the maximum dc input current that could be drawn by a converter was typically four times the nominal input current. Any attempt to draw higher currents resulted in the converter automatically switching off until the excess load was removed. At the cost of a 3% loss in efficiency this current-limiting feature permitted high β transistors to be used in a low β circuit without significantly increasing hazards due to high dc and transient overload currents.

No significant voltage transients were generated in any output rail during switch-off and switch-on of a converter. In Figure 43, D_4 was shunted across L_1, mainly to eliminate the voltage surge that would occur if, for example during testing, most of the 28 volt load current was suddenly interrupted. In this case the remaining electronics still connected to the 28 volt rail might, in the absence of D_4, be damaged by the resulting voltage surge.

The only fuzes inserted in Alouette I were a pair of 1/8 amp units connected in parallel in the power supply lead to the magnetometer. These were added because of concern over a voltage regulator circuit in the magnetometer and the possibility that this unit might draw excessive current and stop converter No. 4 oscillating. In the tracking beacon transmitter the emitter and base leads of the 2N1195 output transistor acted as fuzes in the event of breakdown of the collector junction. The leads were 0.0004 in. diameter gold wire and they fuzed at approximately 700 mA.

Considerable care is needed in the choice of fuzes. The i^2t rating must be large enough for the fuze to pass transient currents as well as dc. However, the larger the i^2t rating the greater the possibility of damage to associated circuits, e.g., emitter-base junctions in a current monitor circuit could be damaged if there is sufficient time for the voltage across the current sensing resistor to build up to excessive levels before the fuze blows.

The surge suppressor shown in Figure 42 was placed in series with each battery. The purpose of the choke is to limit surge currents through the relay contacts and associated circuitry when the converter is switched on. Diode D_1 eliminated positive-going voltage surges during switch-on and switch-off. R and C limit, to safe levels, the negative-going inductive voltage swing which can occur if the charging current to a battery is suddenly interrupted, e.g., during ground testing under low or zero load conditions (relay contacts open).

No under-voltage cut-out was used. This device, which is present in most spacecraft power systems, is normally used to disconnect all loads, for many hours, as soon as the battery voltage drops below a predetermined level. In Alouette I, the four converters are automatically switched off 10 minutes after being turned on. If the automatic turn-off unit fails, the converters can be individually turned off by commands from the ground. If the four working batteries became discharged, before this fault was noticed, the command system would be powered by the standby batteries via the common diode line. Since the power drain on this line is approximately 700 mW, at 15.6 volts, the satellite ground controller would have 150-200 hours to correct the situation before command control was irreversibly lost due to discharge of the standby batteries. Special design precautions were taken to ensure that circuitry connected to the common diode line had a very low probability of short circuiting or overloading this supply rail.

If the automatic turn-off unit should fail when the spacecraft deck temperatures are $< +15°C$, and if the FM and PM telemetry transmitters are on, command turn-off might not be possible due to the desensitizing effect discussed on page 38. In this case the spacecraft could become a total loss. In retrospect the performance of the spacecraft is too dependent on reliable operation of the automatic turn-off circuit. Although an under-voltage cut-out would have improved the situation, a more reliable and operationally better solution would have been to provide a back-up automatic turn-off unit.

6.6 Regulation

One of the basic design goals in Alouette I was that all spacecraft systems should be extremely tolerant to variations in power supply voltages. In general, all electronics units were required to operate normally in the presence of simultaneous and asymmetric supply variations of ± 25% from nominal values. Exceptions were the high energy particles experiment, the subcarrier oscillators, the video adder, and the current and temperature monitoring circuits*. The sweep-frequency oscillator unit was heavily regulated but this was done mainly for RFI protection and convenience in analyzing data on the ground. However, the regulation problem was in general not severe and was further eased by the inherent regulation provided by the Ni-Cd batteries.

The batteries have an output voltage characteristic which is relatively constant over a wide range of discharge levels. For example, a battery with a nominal voltage of 15.6 has an output of approximately 17.0 volts at +25°C when fully charged. On being loaded, this voltage drops very rapidly to an initial 'plateau level' of 15.6 volts and then falls off relatively slowly to 14.0 volts at which time the battery is almost completely discharged. For a depth of discharge of 33% and a load current of 500 mA, the output voltage drops to approximately 14.5 volts at +25°C. The 'plateau' voltage is essentially independent of temperature over the range of 0 to +40°C but the battery voltage prior to reaching this plateau level is a function of temperature and has a typical maximum of 18.5 volts at 0°C and 16.6 volts at +40°C. The use of highly regulated main power sources such as width-modulated converters or pre-regulators was therefore considered unnecessary.

* Regulators were supplied, therefore, for all these units.

Because of the constancy of the battery voltage, and the rapidity with which the initial excess voltage of a fully charged battery is dissipated, the zener limiters in the converters were chosen to clamp at battery voltages in the range 15.8 - 16.4 volts. Regulation, when required, was supplied by transistor series regulators or zener diodes. Examples of two types of series regulator are shown in Figure 43. The + 12 volt supply is derived from the battery using a current-limited feedback regulator, the output of which could be adjusted by means of the 1KΩ trimpot to provide a precisely defined voltage for the NRC particle experiment. The regulator is turned on by current derived from the + 28 volt converter output rail and this permits regulation to be maintained for input battery voltages down to + 12.8 volts, i.e., 18% below the nominal 15.6 volt level. Q_5 and the 3.3Ω resistor limit transient and steady-state currents to approximately 180 mA under all conditions of overload.

A + 6 volt supply was required for the subcarrier oscillators in the PM telemetry system and this voltage had to be kept constant to within ± 0.5%. A temperature-compensated series regulator circuit without feedback was used and is shown in Figure 43. The + 12 volt regulated rail provides a constant current for the zener D_{Z2}. The 10 Ω wirewound resistor in series with the collector of Q_8 provides overload protection and limits the maximum current which can be drawn to approximately 900 mA. An example of a simple zener regulator is shown in Figure 44 (p 60). The output voltage of + 8.2 volts was constant to within ± 0.3 volts from - 50°C to + 75°C in the presence of ± 25% battery voltage variations.

Because there was no regulation in most of the electronics boxes, numerous mutual interference problems were encountered during system tests, due to coupling via common power-supply lines. If, in each box, series regulators had been used in most of the supply rails to provide wide-band low-pass filtering, spacecraft RFI problems would have been considerably simplified.

6.7 Monitoring

Facilities were provided to monitor continuously the voltages of all batteries and at least two of the output rails from each converter. The voltages were time multiplexed by the commutators and telemetered to the ground. Since input voltages to the commutators had to be within the range 0 to + 5 volts and since all the monitored levels were $\geq$ 6V the latter had to be offset and/or divided down. For voltages $\leq$ 12V, simple resistive dividers were used as shown in Figure 43 for the + 12V and + 6 V output rails. In the case of the batteries, a more sensitive voltage monitoring circuit was required, since relatively small fluctuations in battery output voltage correspond to large changes in battery charge level. The technique used was to subtract a fixed voltage $\simeq$ 12V from the battery rail using zener diodes as shown in Figure 43. Although the zener voltage was not constant due to varying currents through the zeners, at different battery voltages, this does not effect measurement accuracy because it is included in the calibration. Overall accuracy of this simple voltage monitoring system, including the telemetry link, was ± 0.20 volts from - 50°C to + 75°C. In practice, the spacecraft operational temperature range is 0°C to + 35°C and the battery voltages can be monitored to an accuracy of ± 0.1V. A disadvantage of the system is that the battery voltage monitor readings have to be corrected for IR drops in the battery wiring harness and current-sensing resistors. Typical values for R were 0.6Ω, with the harness and sensing resistances each being equal to approximately 0.3Ω. The battery current I varies, depending on whether the load is connected and whether there is any solar charging current.

Battery currents were obtained by using a differential amplifier to measure the voltage drop across a small wirewound sensing resistor placed between the negative terminal of each battery and ground. The circuit used is illustrated in Figure 42 and it will be seen that only the net current through the battery is measured. To determine the solar charging current the load must therefore be disconnected and to determine accurately the load current the solar charging current must be zero. Overall accuracy of the current-monitoring system, over the temperature range - 50°C to + 75°C, was better than ± 20 mA.

Case temperatures of Nos. 1 and 3 batteries were monitored using the thermistor circuit described in Section 7. The permissible battery operating temperature range for long term reliability is - 10°C to + 50°C.

6.8 Power Consumption and Weight

For a battery voltage of 15.6, and zero solar charging current, the converter input voltages were typically reduced to between 15.0 and 15.2 volts as a result of IR drops in the wiring harness and current-sensing resistors. Total loop resistance, excluding the internal resistance of the batteries*, varied between 0.75 and 0.9 Ω.

For the above conditions and a temperature of + 25°C, the current drains and total power consumption figures (including harness losses) are as shown in Table 8.

TABLE 8

Subsystem	Current (mA)	Power (Watts)
Common diode (beacon ON)	43	0.67
Common diode (beacon OFF)	24	0.37
Converter No. 1	360	5.62
Converter No. 2	390	6.08
Converter No. 3	830	12.95
Converter No. 4 (NRC ON)	380	5.93
Total (beacon ON)	2003	31.25

At a converter input voltage of 15.2 V the input currents to converters 1 and 2 varied from 330-390 and 350-430 mA, respectively, during each frame of a sounding frequency-sweep. Time average values of these currents are given in Table 8 (21,22).

The dc motor in the sounder antenna system was powered by a Ni-Cd battery that had a nominal output under load of 7.2 volts. At this voltage level, and with both sounder dipoles extending, the current drain and power consumption were 4.3 amp and 31 watts, respectively. Under these conditions the voltage at the motor terminals was only 6.3 due to IR drops in the battery leads. The idling current of the motor, with all four sounder poles declutched, was one ampere and the additional current required to drive out any one pole was approximately 0.8 amp. Weight distribution for the power supply system, excluding wiring harness and relays, is given in Table 9.

TABLE 9

Units	Weight (lbs.)
Solar cells with panels	19.6
Batteries	75.6
Converters	11.3
Surge suppressors	2.40
Battery current monitor	0.98
Battery voltage monitor	0.16
Battery switch unit	2.02
Total	112.1

Therefore the power system accounted for 35% of the weight of the spacecraft.

* Internal resistance of main Ni-Cd batteries was approximately 0.2 Ω including inter-cell wiring. Internal resistance of each Ni-Cd cell varies between 10 and 15 milliohms.

7. TEMPERATURE SENSING

Temperatures were monitored continuously at 22 different locations in the spacecraft, time multiplexed by the commutators, and telemetered to the ground. Eleven channels were carried by each of the two commutators and the temperature sensors for these channels were located as shown in Table 10.

TABLE 10

Commutator 1		Commutator 2	
Channel	Location	Channel	Location
16	Hood 2 (top)*	16	Hood 1 (bottom)*
17	Hood 2 (top)*	17	Hood 1 (bottom)*
18	Electronics deck 2 (telemetry)	18	Electronics deck 1 (sounder)
19	Electronics deck 2 (telemetry)	19	Electronics deck 1 (sounder)
20	Shell 2	20	Shell 1
21	Shell 2	21	Shell 1
22	Battery 3	22	Antenna module 3
23	Battery 1	23	Antenna module 1
24	Electronics deck 1 (sounder)	24	Electronics deck 2 (telemetry)
25	Electronics deck 1 (sounder)	25	Electronics deck 2 (telemetry)
26	Hood 1 (bottom)*	26	Hood 2 (top)*

* 'Top' refers to the hood that was uppermost when the spacecraft was mounted on the rocket in the vertical position. The converse applies for the bottom hood.

Of a number of possible methods which might have been used for temperature measurements, the method chosen was based on the use of thermistors as temperature-sensing elements. The principal reasons for this choice were that (i) it led to a very simple temperature-sensing circuit that was compatible with the Alouette commutators, (ii) the power consumption required for each temperature point was very low—an important consideration when so many measurements were involved—and (iii) thermistors are relatively immune to deterioration in a radiation environment.

The design which is illustrated in Figure 44 (a) was required to cover the temperature range from $-50°$ to $+75°C$ and to provide maximum accuracy between $-10°$ and $+50°C$. The basic circuit consists of a potential divider made up of a fixed 22 KΩ resistor in series with the thermistor, which constitutes a temperature varying resistance. Components R_{T1} to R_{T11} are disc thermistors that have a nominal resistance of 10,000 ohms at $+25°C$, a temperature coefficient of approximately $-4.5\%/°C$ and a dissipation constant greater than 3.5 mw/°C†. The resistance-temperature characteristic of these thermistors follows very closely the law

$$R(T) = R_o(T_o)\, e^{B\left(\frac{1}{T} - \frac{1}{T_o}\right)}$$

where B is a constant that depends on the composition of the thermistor,

$R_o(T_o)$ is the resistance at temperature T_o,

and $R(T)$ is the resistance at temperature T.

For the thermistors used, the resistance-temperature law could be approximated by halving the nominal resistance for each 16°C increase in temperature, and doubling this resistance for each 16°C decrease in temperature.

The value of the series resistor is chosen to optimize sensitivity and linearity over the required temperature range. In the case of the Alouette I thermistors, 22 KΩ for the series resistance gave fairly

† The dissipation constant is the power required to raise the thermistor temperature 1°C.

good linearity and sensitivity from - 20° to + 50°C (See Fig. 44(b)). The regulated voltage was chosen so that the monitor output level was always less than the maximum acceptable commutator input signal of + 5 volts.

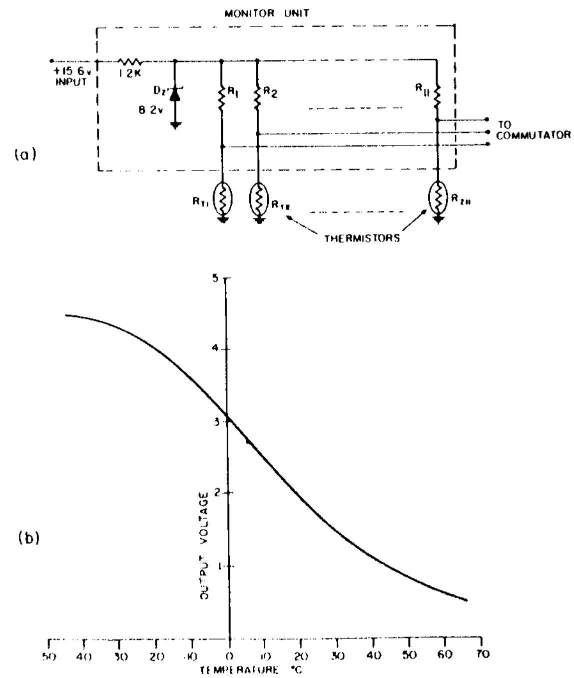

Fig. 44. Temperature Monitoring Unit.
(a) 11-channel temperature monitoring circuit.
(b) Monitor circuit output voltage vs temperature.

Because of the relatively large number of sensors used, matched thermistors were employed to produce a single calibration curve, to aid in ground data processing. The thermistors as supplied by the manufacturer had a tolerance of ± 20% on R_0. These were subsequently sorted and matched to within ± 1%, corresponding to a temperature mismatch of ± 0.25°C.

Each thermistor bead (0.01 inches high and 0.1 inches in diameter) was silver-soldered to a thin copper plate about 3/4" square, and a pair of leads was then silver-soldered to the other side of the thermistor disk and to the base-plate, respectively. The copper plates were epoxy-cemented to the spacecraft at the desired mounting points.

Although the performance of the temperature monitoring system has been satisfactory, improved accuracy at high and low temperatures would have been useful. Decreased accuracy at high temperatures is a result of the logarithmic character of the resistance-temperature curve. Low temperature accuracy is reduced because of the shape of the curve and also because of the low input resistance (82 KΩ) of the commutators.

The overall accuracy of temperature sensing was ± 3°C from - 10°C to + 50°C. Power consumption was approximately 90 mW, at a nominal 15.6 volt supply voltage, for each of the two 11-point monitors employed in the spacecraft.

8. RELIABILITY

8.1 Introduction

To meet the scientific objectives of the program, a fairly complex system design was required. Most of this complexity arose from the ambitious specifications established for the ionospheric sounder, the efforts made to prevent a catastrophic failure that would disable all experiments in the spacecraft, and the requirement that Alouette have an operating life, in orbit, of at least one year.

Although the reliability of a spacecraft is critically dependent on the quality of the system and circuit design and choice of components, it is also vitally affected by construction techniques, inspection, handling and test procedures and the design and safety of ground support equipment.

8.2 Circuit Design

The approach to reliability at the system design level and the methods adopted to provide for redundancy and flexibility of operation have been discussed in earlier chapters. The final system configuration was the result of an iterative design process involving such conflicting requirements as maximum mission performance and reliability, technical feasibility, and strict adherence to the scheduled launch date.

Initially, having specified the preliminary system design, the problems of circuit implementation, construction, and testing then had to be tackled. Ideally, each sub-system should have been subjected to a detailed mathematical analysis to determine accurately its performance and, hopefully, its reliability. Such an approach would have involved a great deal of network and statistical analysis, followed by extensive testing, inspection, and burning-in of components. DRTE simply did not have the time and resources to carry out such a detailed reliability and quality assurance program. Instead, we relied heavily on our physical understanding and intuitive grasp of devices and circuit operation to achieve designs of minimum complexity and maximum tolerance to variations in component parameters and supply voltages. This work was backed up by concentrating on the use of proven parts, large safety margins, redundancy of all transmitters, thorough transient analysis of current and voltage surges, over-load protection, and wide-range temperature and line-voltage testing. All electronic boxes were temperature tested from $-50°$ to $+75°C$ in the presence of $\pm 25\%$ line voltage variations. Although a small number of units were unable to operate satisfactorily at these extreme test levels, in all cases the degradation in performance was due to unusual but thoroughly understood and reversible mechanisms, e.g., to drastic fall-off, below $-20°C$, in core permeability of the variable inductor in the sweep frequency oscillator. It was further specified that, as a general design objective, operation should be satisfactory over the above temperature range in the presence of $\pm 50\%$ line voltage variations. In most cases this latter goal was reached. The temperature and supply voltage tests were conservative, since in practice, payload deck temperatures vary between $+5°$ and $+35°C$, and in-flight line voltage variations are typically less than $\pm 5\%$. With some exceptions in the sounder transmitter, all transistors were selected for a dc beta greater than 40, although all circuits were designed to tolerate a dc beta of 10, and in most cases would operate satisfactorily with a beta of only 5. With one exception, a maximum i_{co} of 50 μA was allowed for all small-signal silicon transistors, and for most RF circuits i_{co} values of many milliamps could be tolerated. Since leakage currents for these transistors were typically in the range 5 - 50 $m\mu A$ at $+25°C$, the minimum safety factor for i_{co}, at $+25°C$, usually varied between 10^3 and 10^4. In general, the need for trimmer resistors was regarded as a symptom of poor design and their use was discouraged. Electrolytic capacitors were regarded as a minor reliability hazard and were only used where absolutely necessary.

Except for the output stages of transmitters, high tolerance to parameter and supply voltage variations was considered a far more important design objective than power matching. For this reason, the RF circuits in general were so mismatched that the concept of maximum power transfer became academic. The common-base connection was used for most RF amplifier stages since, for a single transistor per stage and no power matching, this connection gives maximum constancy of current gain with changes in beta. In the DRTE-designed equipment the common-emitter connection was restricted to the VLF receiver and to pulse and dc amplifiers. In the commercially built tracking beacon, PM telemetry transmitters, and command receivers, however, virtually all RF stages were in the common-emitter connection. With the exception of the commercially supplied command receivers, all mixers used current operated switches to generate the required Fourier components. The local oscillator drive level was made sufficiently large that the conversion loss was virtually independent of power supply, temperature, and component variations.

All resistors were derated by at least a factor of 10, and all transistors which dissipated more than 50 mW were mounted on heat sinks. These wide-tolerance design techniques have been emphasized, since this is precisely the approach that one must use to produce radiation resistant circuitry. It is perhaps not surprising that, apart from the expected degradation in the solar cells and the junction particle detector, Alouette has, up to the time of writing, been essentially immune to the effects of radiation damage. This type of design approach may be criticized on the ground that it is wasteful in power consumption, space, and components. In the case of Alouette, the power argument is difficult to sustain since the power drain is mainly determined by the sounder and telemetry transmitters, which represented state-of-the-art designs in terms of RF output power versus dc input power. It is also doubtful whether tight tolerance design techniques, based on more optimistic estimates of component behaviour, would have reduced the number of components by more than 20%.

Latching relays were considered superior to solid state switches for general command functions. Relays are simple, and virtually immune to radiation damage and are particularly suited to applications involving occasional switching as, for example, with redundant equipment.

The electronics were subdivided into 48 boxes, on two decks, to reduce electromagnetic couplings, simplify modifications during system testing, and permit repairs and calibrations to be carried out more easily in the event of failures. The possibility of using a much smaller number of boxes, with or without connectors, to improve realiability, was rejected as being too impracticable and inflexible.

A significant and sometimes controversial aspect of the program was the highly flexible attitude adopted to design modifications. Circuit and system changes were permitted—with of course back-up checks in the laboratory—to within a few days of launch. Many of the changes were to improve electronics boxes which had already passed all environmental and system tests and which superficially appeared entirely satisfactory. This approach has a number of obvious hazards and can probably be used only in a laboratory-type operation. In the case of Alouette I, it permitted most of the design errors and weaknesses to be eliminated and probably contributed decisively to the high reliability of the spacecraft.

8.3 Components

Excluding 6480 solar cells, approximately 7000 electronic component parts were used in Alouette I. Details of the numbers and types of parts used are given in Table 11.

8.3.1 Coaxial Cable and Hook-up Wire

Only coaxial cables with Teflon dielectric were used because of the superior high temperature properties of this material.

All hook-up wire was of the stranded variety using Teflon insulation. The relatively high temperatures experienced during manufacture makes Teflon insulated wire relatively brittle. During soldering, care must be taken to see that the solder, while molten, does not flow underneath the insulation, yielding what is essentially a small length of non-stranded wire which can then easily become fatigued and break.

TABLE 11

Electronic Component Parts Used in Alouette I

Component	Number
Resistors & potentiometers	2491
Capacitors	1450
Chokes	253
Transformers	146
Crystals	11
Filters	6
Diodes	1474
Zeners	55
Transistors	820
Relays	36
Fuzes	2
Miscellaneous	167
TOTAL	6911

8.3.2 Capacitors

Sealed wet-tantalum capacitors, rated at 90 volts, were used for the 900 μF reservoir capacitors in the sounder transmitters. Solid tantalum capacitors, rated at 35 volts, were used for power-supply filtering, and for low-frequency coupling and by-pass functions. Both porcelain and ceramic capacitors were used for RF by-passing. Mylar units were used for the timing capacitor in the sweep-frequency oscillator. Coupling capacitors were paper, porcelain, or glass types, depending on the circuit application. Glass, tunable piston-type, capacitors were used in the tuned circuits of the sounder receiver and in all oscillator circuits. Temperature compensating capacitors were ceramic dielectric types.

8.3.3 Resistors

Most of the resistors were 1/4 watt carbon composition units and were used wherever high accuracy was not required. Precision resistors were deposited-metal units manufactured by a photo-etch technique. All power resistors were wirewound, and the low value wirewound nichrome resistors in the dc-dc converters were manufactured at DRTE.

8.3.4 Transformers

Most of the transformers were of special design not readily available commercially. Hence they were fabricated at DRTE. High quality construction techniques were used and special mounting techniques were developed as required. None of the transformers were vacuum-sealed or impregnated.

8.3.5 Connectors

Multi-pin connectors occupied a relatively large amount of space in the payload. This space could have been reduced by eliminating redundancy in pins and connecting-wires and using smaller connectors. Neither approach was considered wise. In general, the experience has been that the more miniature a connector the more carefully it has to be handled. The repeated handlings necessary in the thorough testing approach taken throughout the program made sub-miniature multi-pin connectors inherently unreliable.

Considerable trouble was experienced with sub-miniature coaxial connectors and a type widely used in other space programs had to be discarded for reliability reasons.

8.3.6 Semiconductors

All diodes were silicon units, both diffused and alloyed types were used, and many were specially screened and tested by the manufacturer. The alloyed diodes had relatively large reverse-bias capacitances and high storage times but had the lowest leakage currents and the highest reliability (failure rate less than 0.001%/1000 hours). Virtually all transistors were silicon types and most were of mesa and planar construction. The planar 2N1613 was the most widely used, although types 2N706, 2N707 and 2N834 were used in most of the RF circuits. The 2N1132, a pnp mesa device, was used as a general purpose transistor for gating, switching, and for low frequency amplifier applications. The 2N834 was the only planar epitaxial transistor used. Because the device was so new its use was discouraged and there were only fifteen of these transistors in each spacecraft. This was fortunate as all had to be replaced, after the electronics boxes had been encapsulated, because of failures due to 'purple plague' at the interface between a gold base lead wire and an aluminum base stripe. The replacement transistor was an improved 2N834 with a gold base stripe (instead of aluminum) and gold lead wires.

Unijunctions were used in clock oscillators in the commutators and the automatic turn-off unit. In general, their use was discouraged because of the variability of their characteristics (between devices) and their possible susceptibility to radiation damage.

Silicon-controlled rectifiers (SCR's) were used as relay drivers. Because of the variability in their characteristics and possible susceptibility to radiation damage a more reliable approach would probably have been to use pnp-npn transistor switches in place of SCR's.

8.4 Electronic Construction Techniques

The component mounting platform used in the electronic boxes in the satellite consisted of 1/16" glass-base epoxy-laminate material fitted with swaged terminals to accommodate the small components. Wherever possible the components were mounted on one side of the board leaving the reverse side for interconnecting wiring. The photographs on pages 65 to 68 illustrate this feature. The use of terminals for mounting small components enabled a component to be replaced with the minimum of damage to the rest of the circuit, an important consideration in an experimental system subjected to repeated last-minute modifications. The basic platform was employed in single, double, and in a few cases, triple layer configurations.

All terminals used were either silver or gold plated, the former being stored in sealed plastic bags, each containing 100 items, to ensure that large numbers were not left exposed to the atmosphere before being used. Heat sinks were used when soldering the leads of all small components. All soldering was done with conventional irons of various makes and sizes. Temperature-controlled irons were tried but rejected because of poor reliability. The solder was flux-cored, and free of copper, and contained 60% tin and 40% lead.

The generally accepted practice of employing stranded cable for inter-connectors that are subject to flexing, and solid conductors for supported wiring was adopted.

The stranded wire was teflon-insulated and the solid wire was tinned copper with teflon sleeving added during circuit assembly. Beryllium-Oxide washers coated with silicon grease were used to heat-sink the transistor cans to the aluminum frames of the electronic boxes. A good deal of supporting hardware was needed for the heat sinks and this had to be designed and manufactured at DRTE. Sub-miniature RF cable connectors proved very troublesome and were easily damaged during bench and system testing. To improve reliability, all RF connectors used initially in the flight quality electronic boxes were replaced before potting. This procedure could have been avoided if buffer cables had been installed to protect the RF connectors on the boxes from damage during system and bench testing.

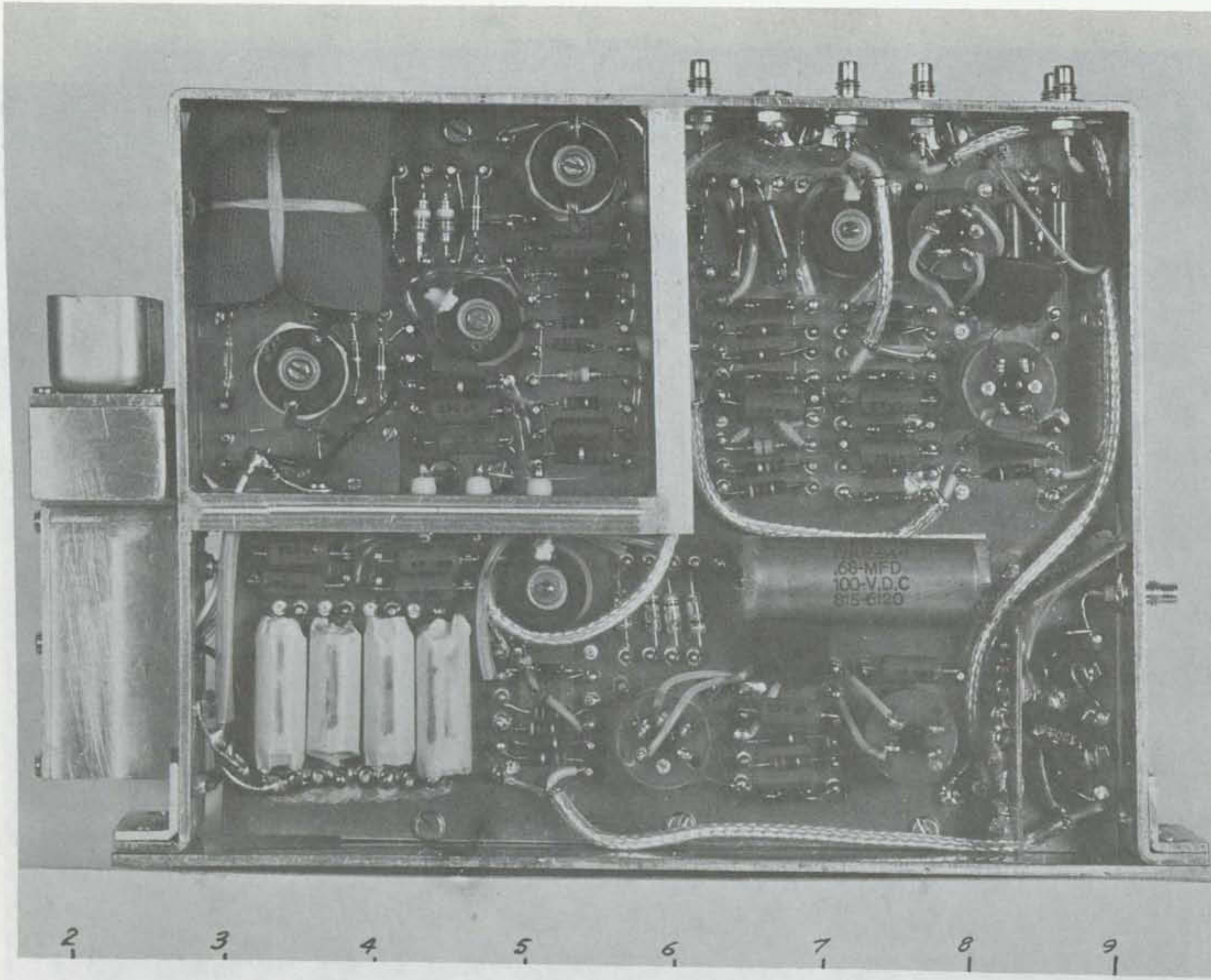

Transmitter and Sweep Calibration Mixers.

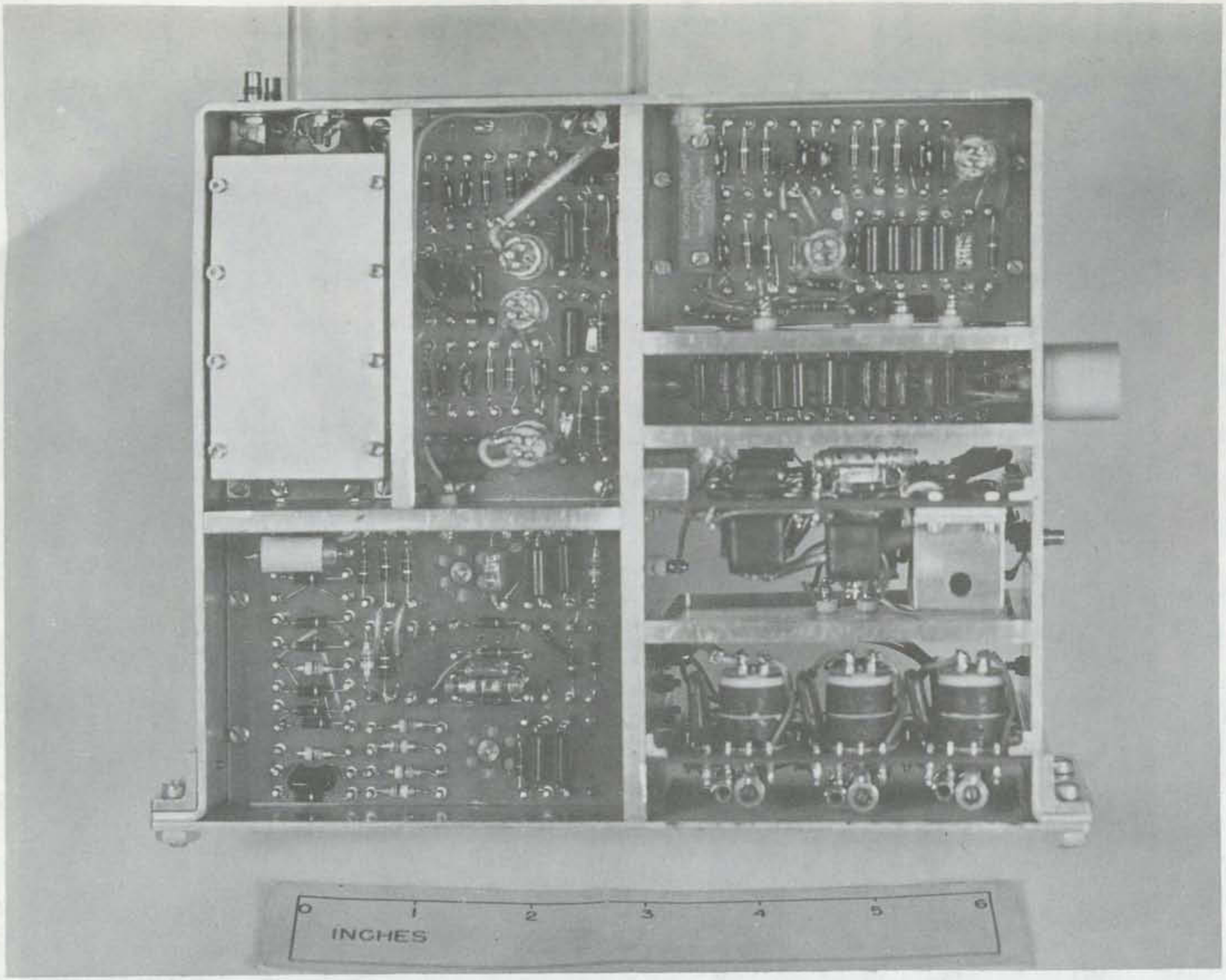

Sounder Receiver.

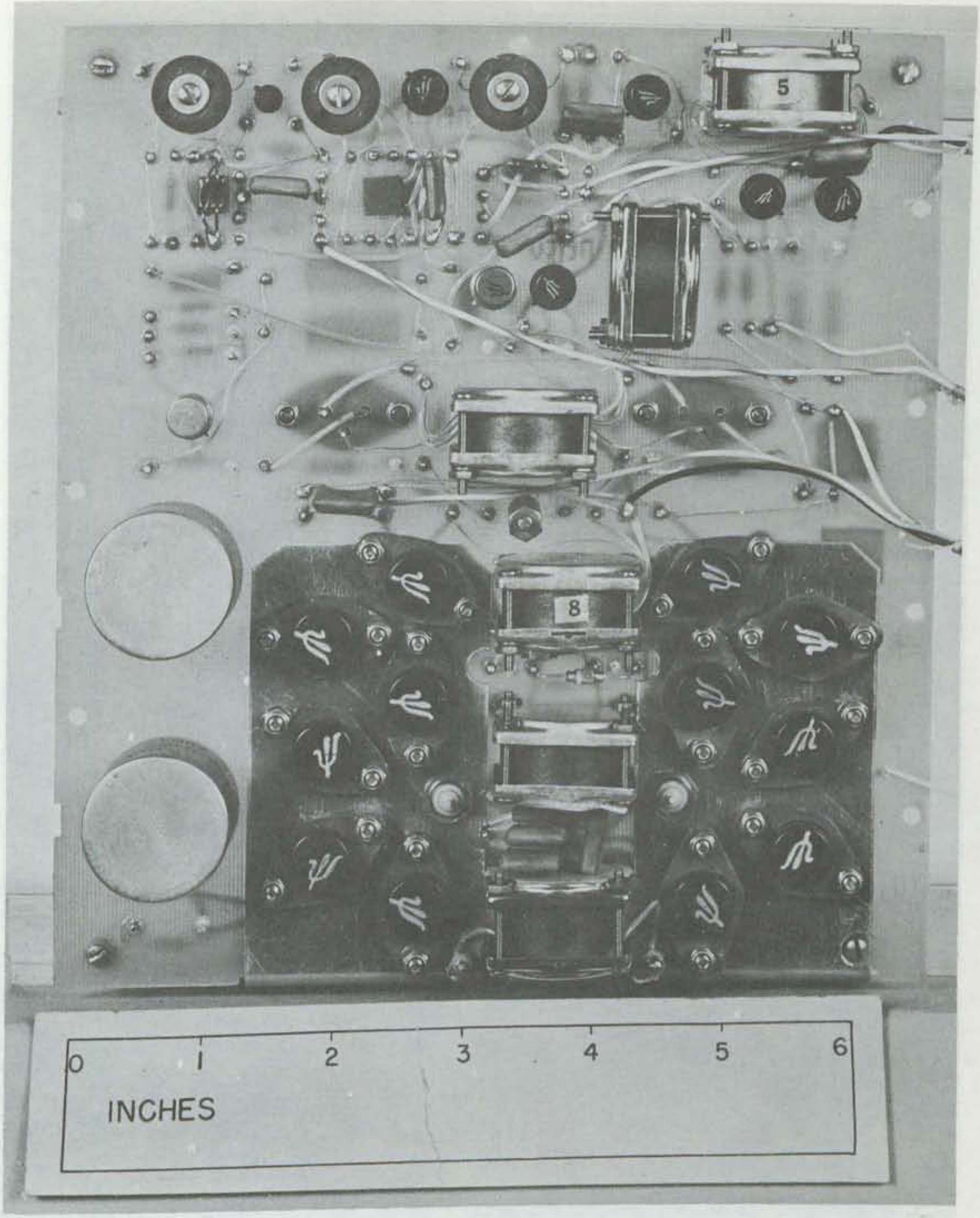

100 Watt Sounder Transmitter.

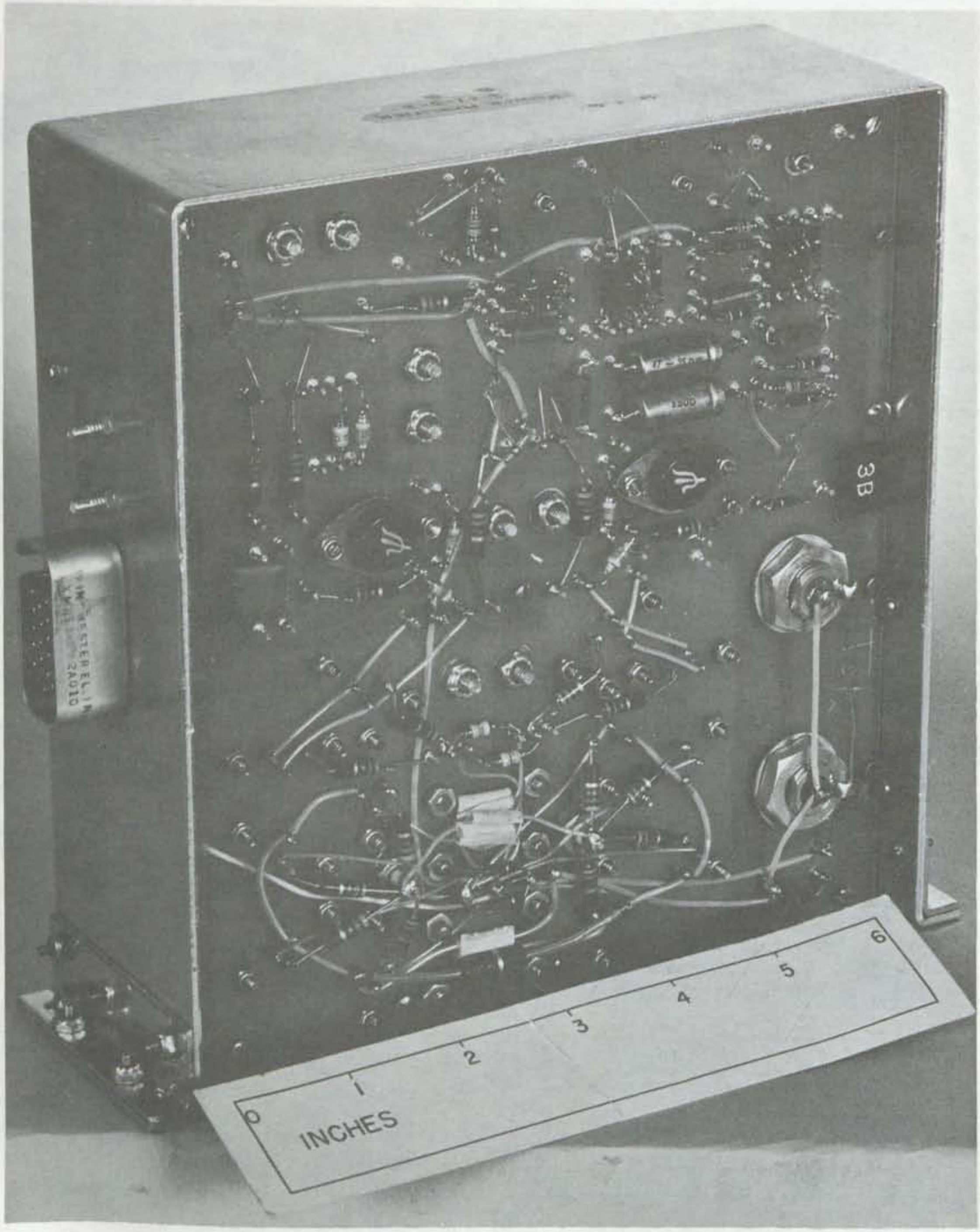

Sounder Transmitter.

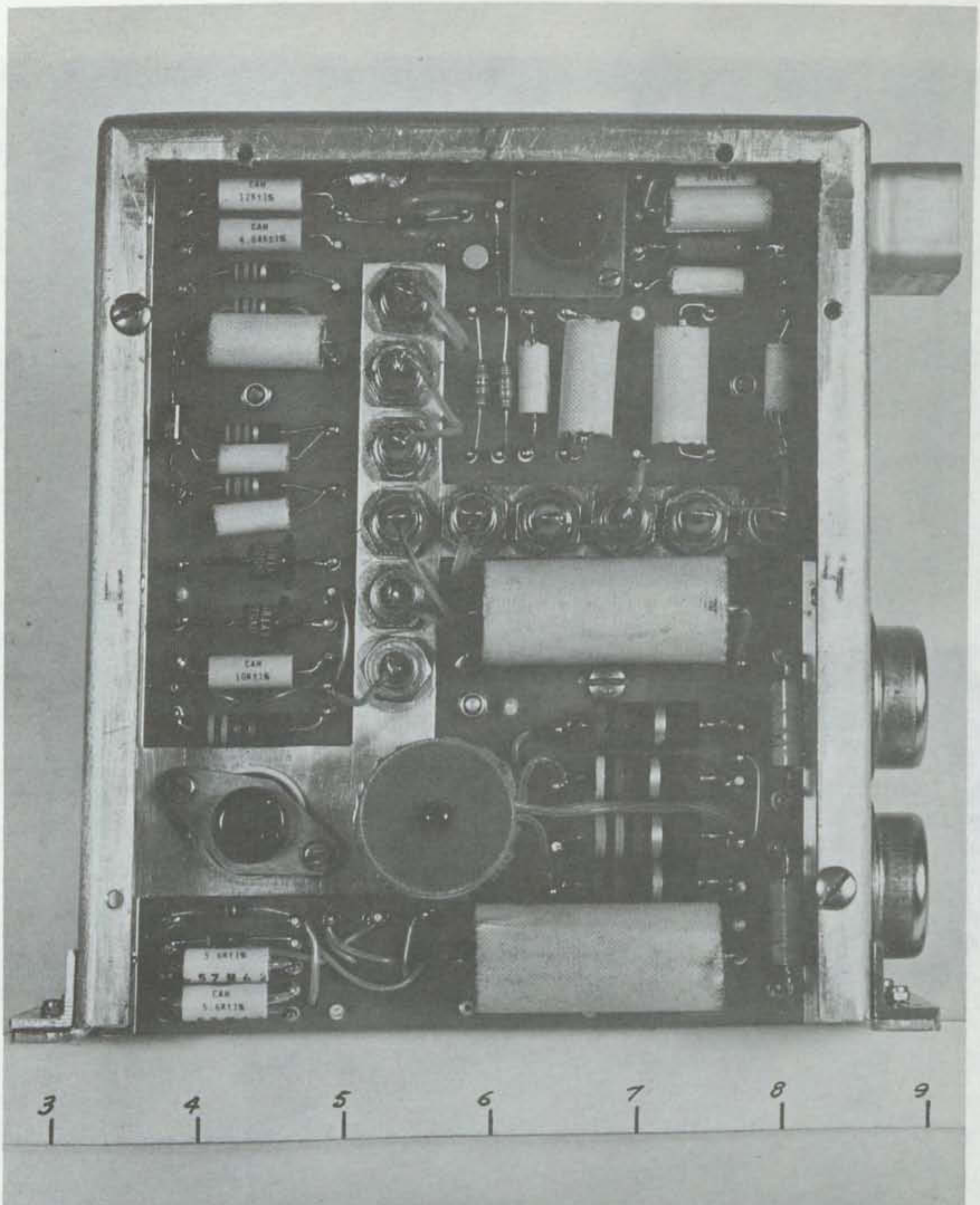

dc-dc Converter.

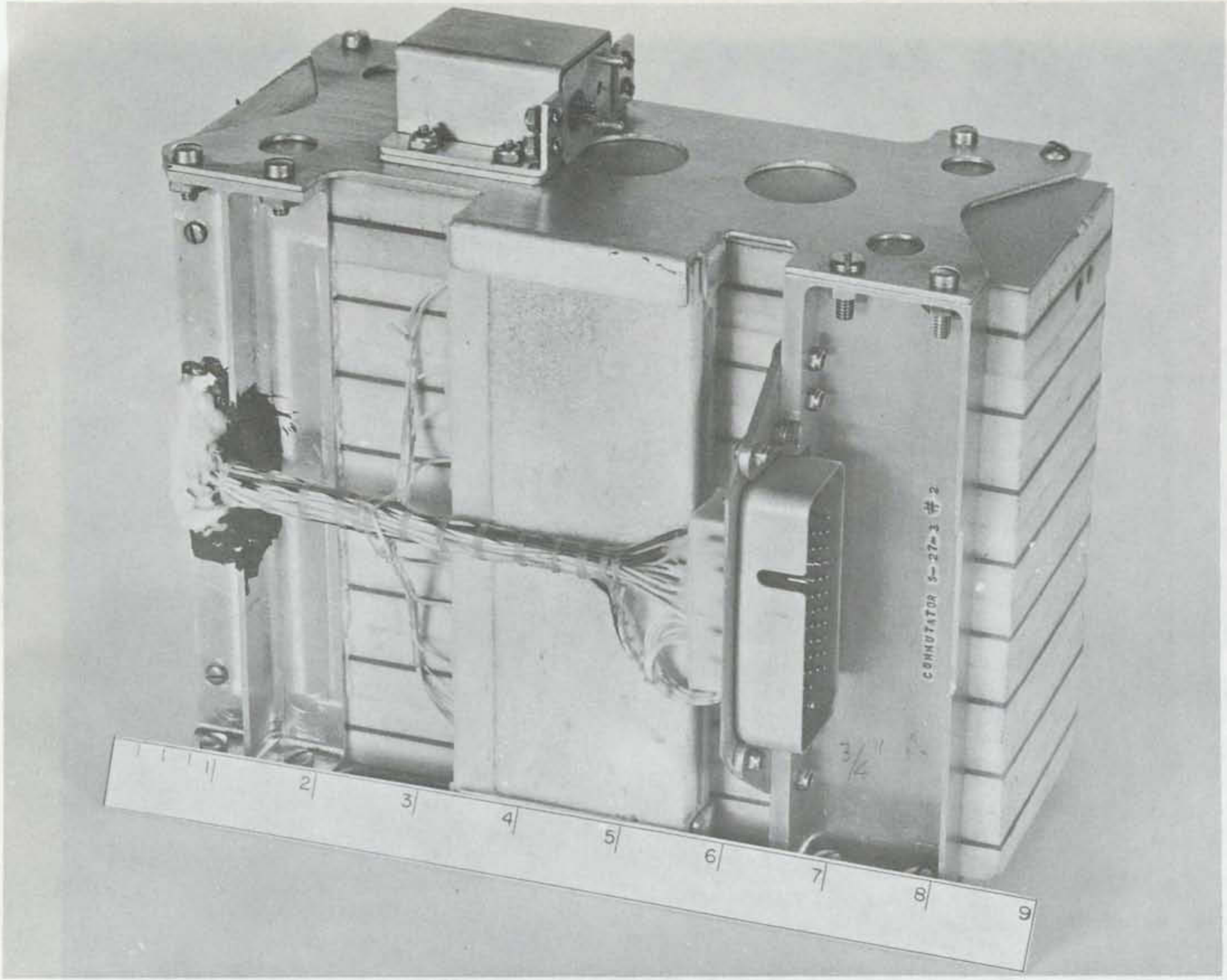

Commutator.

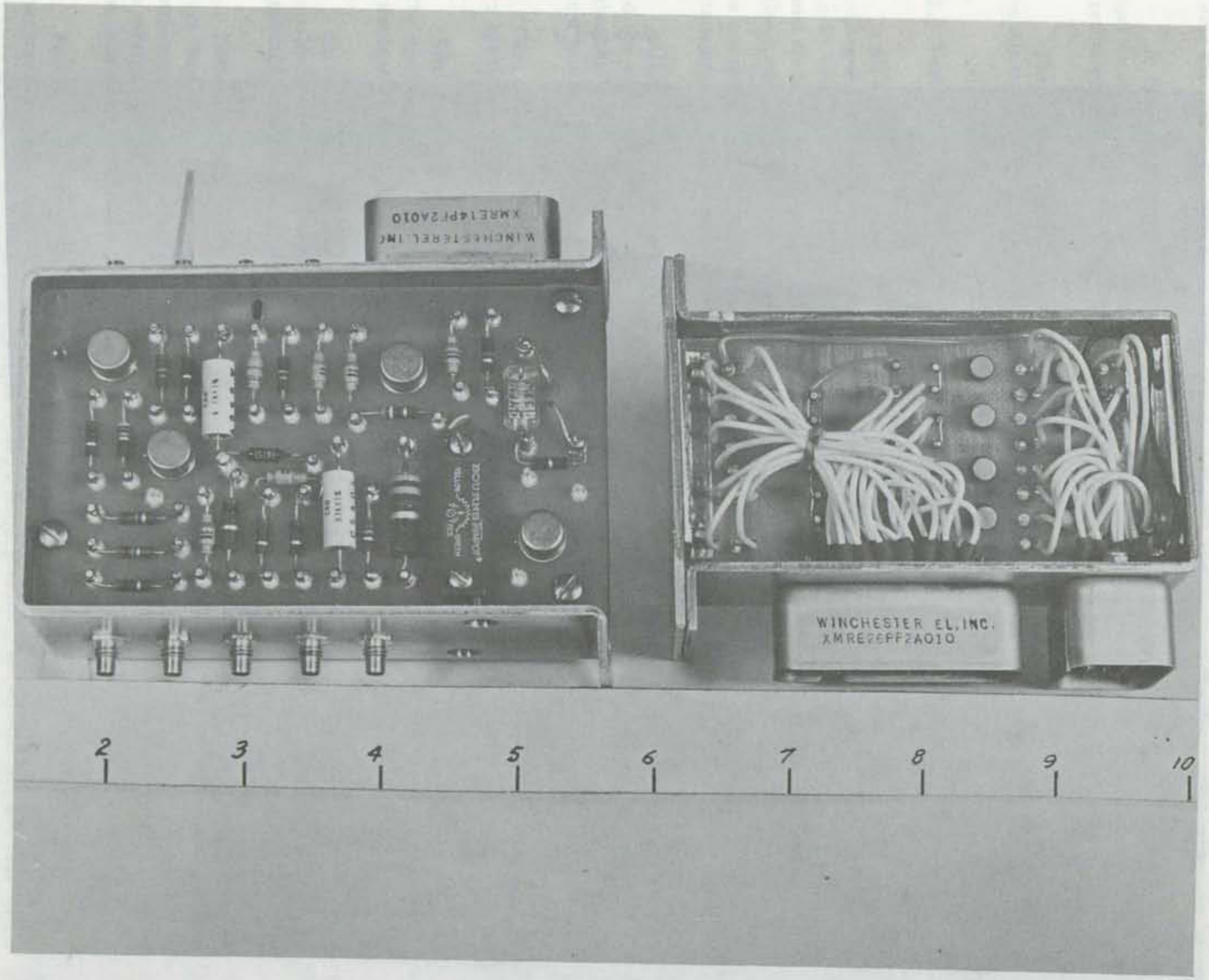

Video Adder and Temperature and Voltage Monitor Boxes.

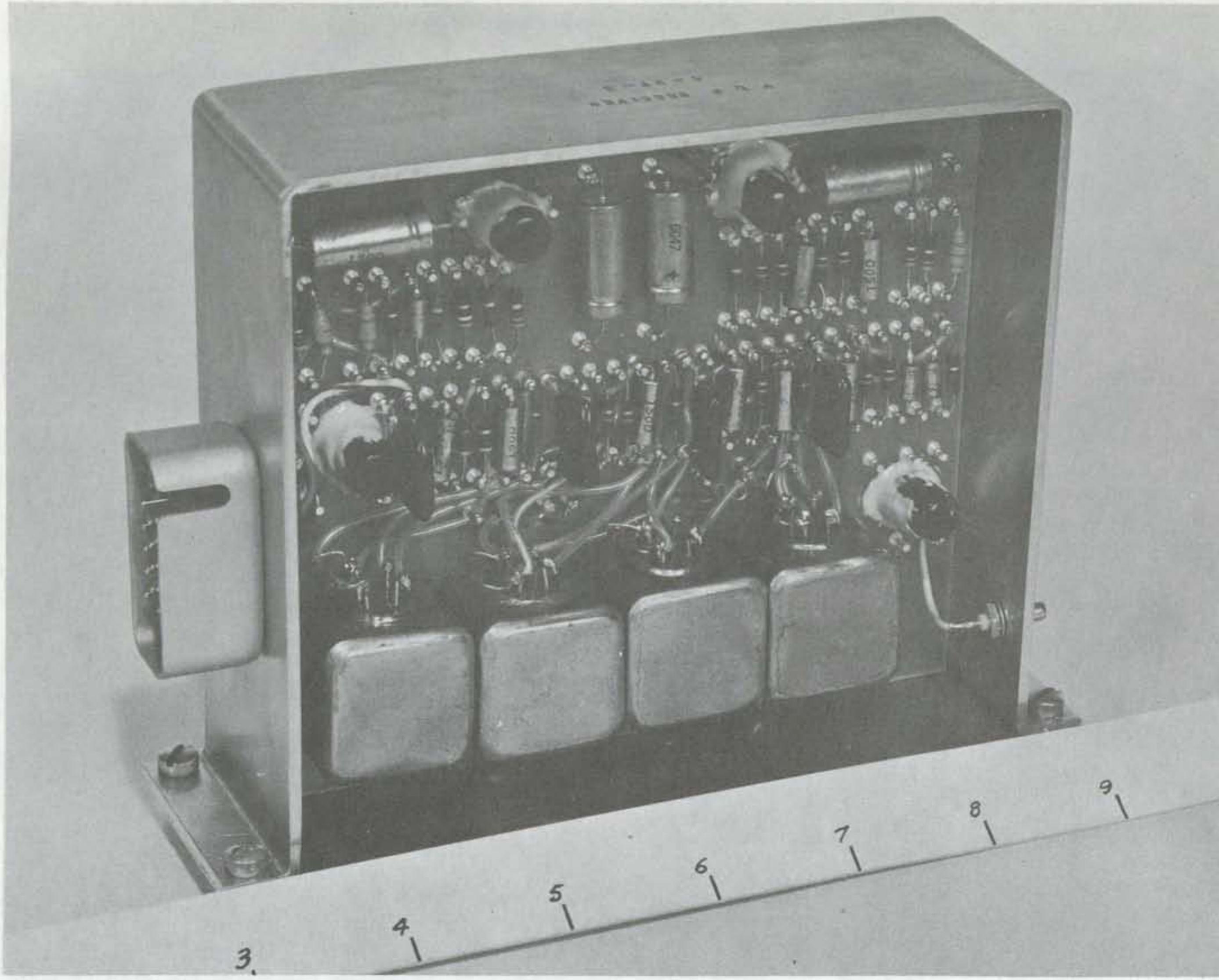

VLF Receiver.

The boards or platforms were mounted in aluminum boxes and then wired to the appropriate connectors. Following completion of system tests all boxes were potted in polyurethane foam (10 lb/cu ft density) which was post cured for a period of five hours to prevent shrinkage. To prevent the pins of connectors on potted units from being held rigid by the potting material, the pins were either fitted with rubber sleeves or else the rear of the whole connector assembly was encapsulated with Silastic 502 before the box was potted.

In the spacecraft wiring harness, wires and connector pins were, with few exceptions, doubled throughout the dc system [24]. Except for the wires to the thermistors and antenna motor, all leads were of stranded teflon-covered 22 SWG wire.

The photographs on pages 69 to 72 illustrate various constructional features of the electronic systems in Alouette I.

8.5 Testing

All diodes were tested to verify that leakage currents, forward voltage drops, and reverse breakdown voltages were within specification. Similarly, emitter-base and collector-base leakage currents, and breakdown voltages, were checked for all transistors. A Tektronix curve tracer was used to display transistor and diode characteristics and measure breakdown voltages, forward diode voltages, transistor current gain (h_{FE}), and transistor saturation voltages. Considerable care was needed in the testing of semiconductors to ensure that measurement procedures were safe, and that test equipment did not generate damaging transients or have dangerous failure modes.

All solid tantalum capacitors were measured for power factor and capacitance at two frequencies: 60 cps and, depending on capacitance, at a frequency between 2 kc/s and 10 kc/s. Units which showed abnormally large changes in power factor or capacitance with frequency were rejected. The object of the test was to pick out capacitors in which the tantalum pentoxide film was poorly formed or had pin holes.

Wet tantalum capacitors were given high reliability processing by the manufacturer and for this reason no special tests were carried out at DRTE. All other capacitors were only tested for capacitance value.

Resistors were only tested for resistance value. All inductors were tested for inductance and Q values. The hermetically sealed relays were tested for sensitivity and reliable latching. Finally, a thorough visual examination was carried out on all components.

No radiation tests were carried out at DRTE on any components used in the spacecraft; however, considerable background information suggested that all components would operate satisfactorily in the expected radiation environment.

Following construction, all electronics boxes were bench tested by their design engineer. The boxes were then transferred to a temperature-test group whose responsibility was to document and evaluate performance over a temperature range of $-50°$ to $+75°C$. The designer of the box was not normally permitted to take part in these tests. In the exceptional cases, where his assistance was required, he reported to the temperature-test engineer.

Following completion of temperature tests, the boxes were installed, unpotted, in their respective spacecraft. Since three satellites were involved, a prototype and two flight payloads, the bench and temperature testing phase of the program represented a major planning, documentation, and test effort. As it turned out, there were very few failures during bench and temperature testing so that hardly any time was required for repair and reworking of electronics boxes.

System testing of each spacecraft was carried out in a screened room, and it was this phase of the test program that caused by far the most trouble. Numerous electrical modifications were required to suppress conducted and radiated interference between boxes and subsystems. Ideally, all interference problems should have been rectified in the prototype spacecraft. In practice, there was not enough time to fully test this payload and many changes were required subsequently in both flight payloads. Modifications, to improve spacecraft performance, continued to within one week of launch, and in a number of cases involved changes in fully qualified flight boxes.

Most of the serious interference problems were due to spurious signals that leaked into the sounder receiver. Because the sweep-frequency receiver had a threshold sensitivity of -115 dbm from 1 Mc/s to 11.5 Mc/s, it proved extremely susceptible to conducted interference via power supply rails, and input leads, such as via the local-oscillator line to the sweep-frequency oscillator. Mixers, oscillators, fast pulse generators (e.g., the 33 $m\mu sec$ 1 Mc/s pulses in the frequency calibrator), telemetry transmitters, converters, and gating circuits generated such a wide range of harmonics and sum and difference frequencies that there was essentially no interference-free band within the frequency range of the receiver. Many of the interfering signals could not be reduced to receiver noise level[21]. Fortunately, most of this interference is masked, in orbit, by the background cosmic-noise level. The interference levels have proved stable and have not resulted in any deterioration in the performance of the spacecraft.

The levels and frequencies of interfering signals were similar in all three spacecraft. Approximately four months was required for system tests, and over half this time was spent on calibration measurements and on interference tests on the sounder receiver.

Vibration and thermal-vacuum testing of the complete spacecraft followed system tests. Apart from a broken wire in the sounder matching network of the prototype spacecraft no failures were recorded in any electronic box during vibration tests. In the thermal-vacuum tests the payload deck temperatures varied from 0° to +50°C. Since all electronics units had previously been tested from -50° to +75°C very few problems were encountered. One failure occurred during thermal-vacuum testing of the flight spacecraft, and was due to 'channeling' caused by water vapour in a power zener. No failures were observed in the back-up flight spacecraft. However, a wirewound current-sensing resistor (for one of the standby batteries) failed for no apparent reason when this spacecraft was returned to Ottawa. There were no failures in the prototype spacecraft during thermal-vacuum testing.

The connecting wires to a 10-cell 13.5-volt 1-amp-hour Mercury battery were cut, a few days before launch, to eliminate an undesirable, and previously unobserved spurious switching problem in the command system. This battery had been added to prevent the power-supply relay to the tracking beacon opening, and the transmitter switching off, during the launching of the spacecraft.

After the thermal-vacuum and vibration tests, and before shipment to the range, the prototype and flight spacecraft were tested as ground sounders. Due to interference from local stations and a rudimentary sounder antenna the quality of the ionograms was poor. Sufficient information was, however, obtained to suggest that the sounder system was operating as planned.

8.6 Ground Support Equipment

During the course of the Topside-Sounder Program a wide variety of equipment was utilized for testing the Alouette satellites and much of it had to be designed and constructed at DRTE. Umbilical equipment for monitoring spacecraft operation and for supplying power to the satellite played a vital role in the preparations leading to the launching of Alouette I. This equipment included external power supplies, battery chargers for blockhouse and laboratory use, suitcase testers for monitoring the state of the spacecraft, and sensing, control, display, and protective systems. The conditions under which the umbilical equipment operated were many and varied. In the early phases of spacecraft system testing, emphasis was on detailed hardwire monitoring functions and the supplying of external power to the satellite electronics and batteries. At the range the emphasis was on remote control of the satellite, from a distance of 11 miles, with frequent cross-checks on telemetered data by means of hardwire measurements. These operations were complicated by the presence of the gantry, the installation of the shroud, and the fact that the battery chargers had to be installed in a blockhouse over five hundred yards from the gantry and spacecraft. To reduce the possibility that failures in ground support equipment might damage the spacecraft, exceptional care was required in the design of much of this equipment, hence comprehensive protective circuitry was incorporated in all ground-support instrumentation. For example, all battery chargers had silicon-controlled rectifier 'clamps' which shorted any charging line to ground as soon as the voltage on this line exceeded a predetermined level.

In addition to the umbilical equipment, fixed and mobile command control equipment was required involving the design and construction of 25 mW and 35 W AM VHF command transmitters together with tone encoders.

The design and construction of the ground-support equipment represented a significant fraction of the overall electrical effort on the Alouette I program.

9. IN-FLIGHT PERFORMANCE

9.1 Introduction

Alouette I was launched with the tracking beacon, NRC particle experiments, and the PM telemetry system 'ON', and the automatic turn-off circuit inhibited. Following launch, the automatic turn-off function was restored by means of a separation micro-switch, that closed when the spacecraft separated from the vehicle. Therefore, engineering data was transmitted continuously from launch until ten minutes after separation, a period of approximately 57 minutes.

Analysis of telemetry signals received from the spacecraft throughout the first six minutes of the vehicle's flight, and during the first pass over Alaska, indicated that the spacecraft functioned normally during the launch phase and that the sounder antennae extended as expected following separation of Alouette I from the vehicle. Although arrangements had been made to station a tracking ship in the Indian Ocean, to monitor the extension of the sounder antennae and other engineering parameters, no usable data was obtained because of equipment and operator problems aboard the ship. Instead, the Johannesburg STADAN Station, although operating at near maximum telemetry range, verified separation and received usable PM signals for the first two minutes of antenna extension.

The first 'in-orbit' signals from Alouette I, with its sounder antennae fully extended, were received, therefore, at the College, Alaska, STADAN station. A DRTE engineer at this station verified that the command, telemetry, and power subsystems were operating as expected. Satisfactory operation of the sounder, cosmic noise, and particle experiments was subsequently verified following the first pass over Ottawa. Satisfactory operation of the VLF receiver was established several weeks later when this experiment was finally turned on. All systems have functioned essentially as planned, and, except for a particle counter, there has been no observable deterioration in the performance of any of the experiments.

At the time of writing, two electrical failures have been observed in Alouette I. The first has been the expected and unavoidable wear-out—after one year—of the junction particle detector. The second failure has been the loss of five channels in a commutator when the deck temperature is below $+17^{\circ}C$. Since four of these channels are carried by a second commutator, only one channel—the magnetometer—is, in fact, lost. The malfunction is probably due to radiation damage in a transistor.

Radiation damage to the solar cells reduced battery charging currents to 57 per cent of their launch values at the end of three years. This has now limited the operating time of the spacecraft to four hours per day, for a maximum shadowed orbit, but has not affected the performance of any of the experiments.

The only other degradation has been a possible small loss in charging efficiency in one of the standby batteries.

After the satellite had been launched it was found that the RF carrier of the beacon transmitter interfered with the scintillation counter. Since the PM transmitter can also be used for tracking, the problem was eliminated by turning the beacon transmitter off as soon as the orbit was well established.

An unexpected spurious turn-on pulse was detected in the command system. The effect is a subtle one and results in the closure of a separate turn-on relay to converter No. 4 when the spacecraft is commanded on. Operationally, the effect is unimportant.

Alouette I is controlled from DRTE, and world-wide operating schedules are issued each week. These take into account the state of the satellite batteries, the requirements of the experimenters, and the availability of STADAN stations. Essential engineering parameters such as battery and converter output voltages, automatic turn-off time, temperatures, solar charging currents, and modes of operation are read-out at Ottawa each day.

9.2 Solar Cells

Calculated and observed decay curves of total solar charging current vs time since launch were shown in Figure 40 (page 50). The observed values in this figure were obtained by measuring the current in each active battery with converters 1, 2 and 3 switched off and converter 4 turned on. Therefore, solar charging currents were measured directly for converter 1, 2 and 3 subsystems, and indirectly for converter 4 subsystem, i.e., allowance had to be made for the varying load current drawn by converter 4. All four solar supplies have degraded at the same rate, hence the percentage reduction in total solar charging current can also be derived from Figure 41 (page 50) which illustrates the decay in solar charging current to the converter 3 battery. Although the error in measuring solar charging current is less than ± 5%, the accurate determination of the percentage degradation in solar cell output currents proved surprisingly difficult. For example, variations in the Albedo (earth's reflected light), can produce significant changes in solar current. Furthermore, the solar currents decayed rapidly during the first few days in orbit and, because of the short time interval involved and the fact that only a few stations were initially commanding the satellite on, not enough readings were obtained to average reliably through the Albedo-induced fluctuations. Therefore, it was not possible to determine unambiguously the initial values of solar charging currents. For the converter 3 sybsystem, the measured solar currents and the predicted shape of the radiation damage curve suggested that a figure of 500 mA should be assigned to the initial charging current, i.e., at orbit injection. The calculated value of this current was 540 mA (see Appendix II), assuming an Albedo of 35 mW/sq. cm. and taking into account cell efficiency and area, and losses due to shingling, filtering, angle of incidence, mismatch, etc.

In addition to radiation damage and Albedo considerations, it appears, from Alouette I data, that degradation analyses must also take into account changes in solar charging current due to normal and unexpected variations in solar cell temperatures. Because there have been large long-term changes in the orientation of the spacecraft, and because the spin rate has been steadily decreasing and is now essentially zero, the solar cell temperatures have probably fluctuated in a fairly complex fashion. Since cell temperatures are not monitored, the thermal behaviour of the solar cells can only be estimated. Assuming no change in solar cell a/e ratio, the effect of zero spin is to increase average cell temperatures, for a given spacecraft orientation, thus further reducing solar charging currents.

Finally, in comparing calculated and observed decay curves in Figure 40 it should be noted that the calculated radiation damage curve (a) is based on an equivalent 1 Mev electron flux of 2.5×10^{12} electrons/ cm^2-day. No allowance has been made for the fact that the average electron flux from the artificial radiation belt has decayed exponentially, with a time constant of approximately 7 months at the height and inclination of the Alouette I orbit. The proton flux level, for Alouette I, has been relatively constant at 5 x 10^7 protons/cm^2-day for proton energies greater than 15 Mev[25]. Extrapolating to 8 Mev (the proton cut-off energy for the solar cell cover glasses) gives a flux of approximately 10^8 protons/cm^2-day. Using the approximation that, for damage calculations, one proton is roughly equivalent to 10^3 electrons, we find that the proton flux is equivalent to 10^{11} 1 Mev electrons/cm^2-day. Assuming a decay time constant of 210 days for the electron flux in the artificial radiation belt, this flux decayed in 1.8 years by a factor of twenty-five, to the background proton level of 10^{11} equivalent electrons/cm^2-day. Therefore we would expect the calculated worst-case degradation curve in Figure 40 to give pessimistic values after 6-12 months, and this explains why, in Figure 40, the observed degradation curve departs from the calculated curve (a), one year after launch.

After one year, solar charging currents, to all converter batteries, were down to approximately 62 per cent of their launch values. At the end of the second and third years these currents were down to 60 and 57 per cent of their launch values, respectively. From a comparison between predicted and measured values in Figure 40, it appears that, for the first year in orbit, most of the solar cell degradation in Alouette I can be attributed to radiation damage. The increased scattering of points with time in Figure 41 is probably due to temperature effects associated with spin decay and changing orientation of the spacecraft.

9.3 Batteries

With one exception, the performance of all batteries has been nominal since launch. After two years, the voltage of one of the standby batteries (No. 5) showed a ten per cent reduction below normal levels when powering converter No. 3, the heaviest load in the spacecraft. Since the battery voltage recovered when the number of operating hours per day was reduced, it is likely that there has been a deterioration in its charging efficiency. To allow for battery inefficiency, the charge in ampere hours delivered to each battery is adjusted, from the ground, to be fifteen per cent greater than the discharge in ampere hours removed by its load. The use of a constant value of 1.15 for the battery inefficiency factor is an approximation, since this factor is variable and increases with increasing temperature and decreasing charging current. For charging currents less than 150-200 mA the inefficiency factor may be greater than 1.15 at +25°C and almost certainly exceeds 1.15 at +40°C. It is possible that radiation damage to the solar cells in Alouette I will eventually reduce charging currents to such low levels that battery efficiency will be seriously effected. If this occurs, corrective measures can be taken since it is possible, on command, to connect any or all of the solar charging rails to either of the two standby batteries as shown in Figure 39 (page 48). A standby battery would then power more than one converter but would be charged at a higher current level, thus increasing battery efficiency. In the limit, all the solar cells can be used to charge one of the standby batteries which, in turn, would then power all the converters.

In practice, the operating time of the satellite has, to date, been determined by the power consumption of converter 3. Table 12 gives the calculated and scheduled operating hours per day since launch for this subsystem, using a battery inefficiency factor of 1.15, a converter input current of 850 mA, and observed values of solar charging current.

For a maximum sun orbit the operating time T, in hours per day, is given by

$$24\, I_{CH} = F\, T\, (I_L - I_{CH}) + T\, I_{CH}$$

hence

$$T = \frac{24\, I_{CH}}{F\, I_L + (1 - F)\, I_{CH}}$$

where I_{CH} = solar charging current

I_L = converter input current

and F the battery inefficiency factor

$$= \frac{\text{amp-hours of charge}}{\text{amp-hours of discharge}}$$

TABLE 12

Calculated and Scheduled Hours of Operation per day since Launch for Converter 3 Subsystem

Time from Launch	Charging Current (mA)	Maximum Shadowed Orbit Hours		Maximum Sun Orbit Hours	
		Calculated	Actual	Calculated	Actual
0	500	8.6	-	13.3	-
1 week	430	7.4	7.0	11.3	-
3 months	348	5.9	5.0	9.0	-
6 months	329	5.6	5.0	8.5	7.0
9 months	319	5.4	4.5	8.2	-
1 year	310	5.2	4.4	8.0	6.8
2 years	300	5.1	4.3	7.7	6.5
3 years	285	4.8	4.0	7.3	6.0

For a minimum, i.e., 67 per cent, sun orbit the daily operating time T is given by

$$16\, I_{CH} = 0.67\, T\, [F\, (I_L - I_{CH}) + I_{CH}] + 0.33\, T \cdot [F] \cdot [I_L]$$

hence

$$T = \frac{16\, I_{CH}}{[F \cdot I_L + 0.67\, I_{CH}\, (1\text{-}F)]}$$

In deriving T for a minimum sun orbit it is assumed that the satellite is turned-on for 0.33 T hours in darkness and 0.67 T hours in sunlight.

Referring to Table 12, it was not possible to exceed 7 hours of operating time per day because of limited ground station coverage. One week after launch the satellite was in a 73-75 per cent sun orbit, hence, no observed data is available for either the maximum or minimum shadowed orbit performance. Also, at three and nine months after launch, the satellite was in a minimum sun orbit so that no observations are available for the maximum sun condition.

In Table 12 it can be seen that the calculated T is always greater than the actual T. One reason for this discrepancy was the use of a load current of 900 mA for converter No. 3 instead of the 850 mA level used for the calculated T values in Table 12. This was done for conservative operation, and specifically, to cover the possibility of the spare FM telemetry transmitter being accidentally switched in. With this transmitter connected, the current drain at the input to converter No. 3 is 1 amp. Table 12 shows that the scheduled daily operating hours for Alouette I have been typically 16% lower than the maximum calculated values. Operationally this has probably been a sound procedure. The observed T values in Table 12 are scheduled figures and do not include subsequent deletions by the STADAN network for priority, equipment, or other reasons.

During the first year in orbit the standby batteries were used only occasionally to power converters. Subsequently, these batteries have been rotated regularly around the four converter positions in the spacecraft.

Laboratory experience with Alouette I-type NiCd batteries suggests that their reliability is degraded by extended periods of 'standby' operation. It is perhaps significant that the only signs of battery deterioration in Alouette I are in a battery that has been on standby for an extended period since launch.

The variation in output voltage of batteries 1 - 4 over a one-month interval is shown in Figure 45. Battery No. 3 supplies the heaviest load, hence it has a lower and more variable output voltage.

The variation in dc-dc converter output voltages since launch is shown in Figure 46. It can be seen that long-term drifts in system voltages have so far been small and that converter output voltages have rarely varied more than ± 5%.

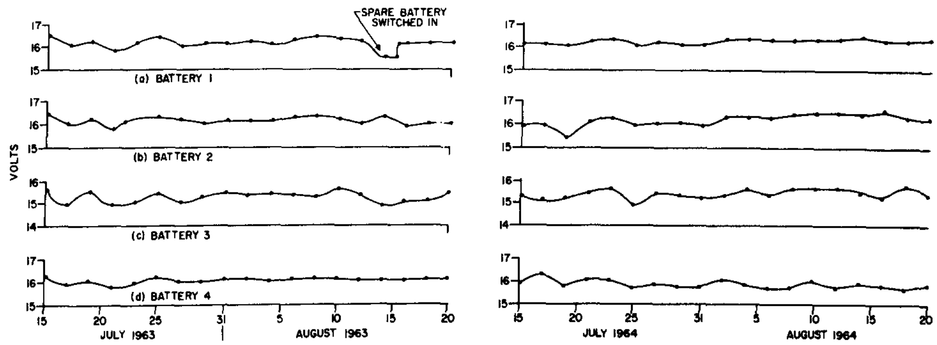

Fig. 45. In-Flight Battery Voltages.

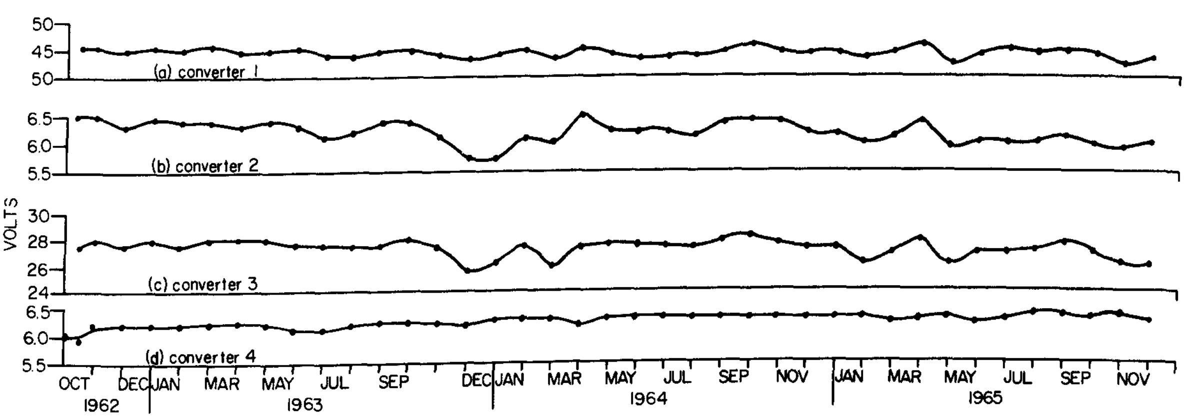

Fig. 46. Typical In-Flight dc-dc Converter Output Voltages.

9.4 Temperatures

All temperatures have been nominal since launch. Payload deck temperatures reach a minimum of + 5°C during 66 per cent sun orbits and a maximum of + 35°C during 100 per cent sun orbits. During a single 66 per cent sun orbit deck temperatures vary ± 1°C with a thermal time constant of approximately 12 hours. Maximum and minimum battery temperatures have been + 40°C and + 5°C, respectively, and there has been negligible drift in these limiting values since launch. Although the electronics can operate from - 50°C to + 75°C the batteries must be kept within the temperature range - 10°C to + 50°C, for reliable long-term operation.

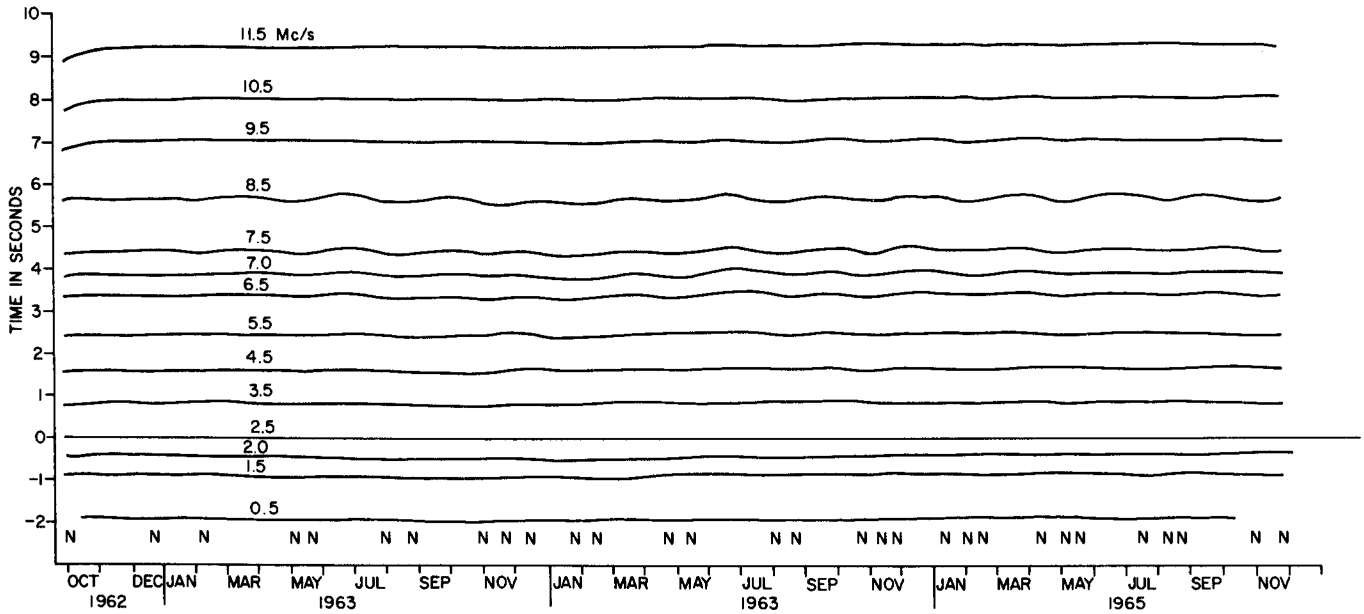

Fig. 47. In-Flight Frequency Stability and Linearity of the Sweep-Frequency Oscillator.

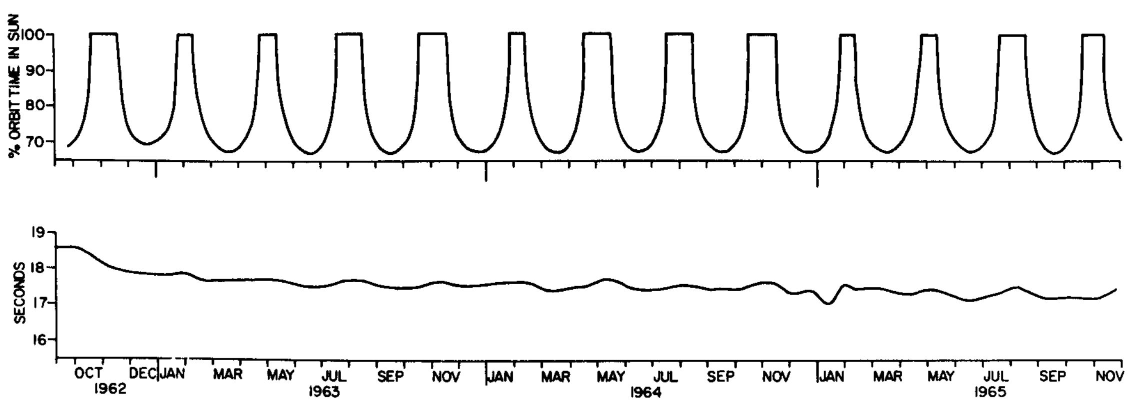

Fig. 48. In-Flight Frame Period Stability of the Sweep-Frequency Oscillator.

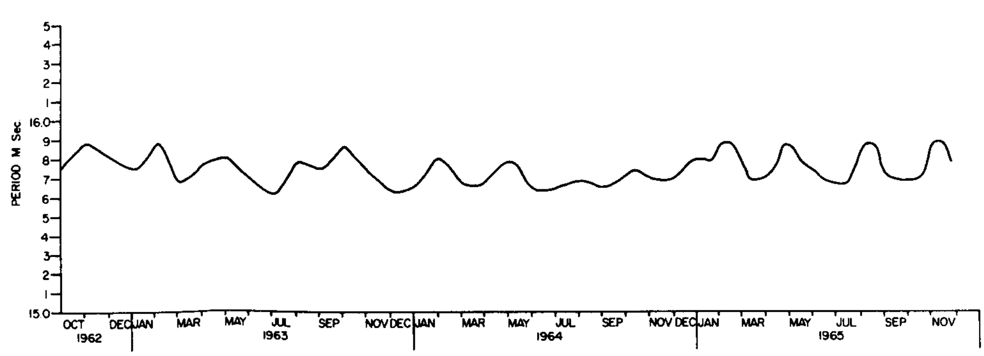

Fig. 49. Variation of Sounder Line Period Since Launch.

9.5 Ionospheric Sounder

Of the subsystems, the ionospheric sounder has the highest probability of failure because of its complexity, limited redundancy, and the relatively high component stress levels in the T-R switch, transmitter output circuits, and antenna matching network. At the output terminals of the sounder transmitter, the peak-peak RF voltage can, for certain frequencies and load conditions, be as high as 1000, and in the antenna matching network, Q multiplication effects can result in peak RF voltages that reach 70% of capacitor breakdown ratings. Although thermal-vacuum tests, and in-flight performance, indicated that there were no corona problems, in retrospect, this hazard was possibly underestimated, and more time should have been allowed for outgassing in orbit before turning on the sounder. The dc motor, used to drive out the sounder antennae, was probably the least reliable component in the sounder system. This motor was an unsealed permanent magnet type with 'sea-level' brushes, and was not given any high reliability processing by the manufacturer. It performed satisfactorily, in flight, but due to telemetry problems in a tracking ship it was not possible to verify whether motor currents or extension rates were normal beyond the first two minutes of extension of the sounder antennae.

Before launch there was some anxiety that, with the sounder antennae extended, the transmitter would oscillate at certain frequencies in the sounding band, due to direct feedback from the antennae or via circulating currents induced in the shell and deck of the spacecraft. It also seemed possible that the feedback might be enhanced at or below the plasma frequencies of the medium. Transmitter instability, due to antenna feedback, was frequently observed during early ground sounding tests, when a development model Alouette sounder was connected to a delta antenna. Because it was difficult to simulate freespace conditions on the ground it was not possible to verify, prior to launch, that the oscillation hazard had been eliminated from the flight spacecraft. In-flight results have since shown that there are no observable instabilities anywhere in the Alouette I sounding band.

Variations in sounder sweep rate, and in sweep duration, have been negligible since launch and are illustrated in Figure 47. The ordinate scale is in seconds, and time $t = 0$ corresponds to the time of occurrence of the 2.5 Mc/s frequency marker. Frequency identification is by means of crystal-controlled markers generated in the spacecraft by the frequency calibrator. The periodic loss of the 0.5 Mc/s frequency marker is due to changing deck temperatures and the resultant drift in the starting frequency of the sweep-frequency oscillator. The variation in the time of occurrence of the 7.0 Mc/s identification marker is due to a temperature dependent zener voltage in a sweep linearizing circuit and has nothing to do with the frequency stability of the crystal calibrator. Accuracy of the frequency markers was $\pm .1$ kc/s at launch, and from the relatively constant separation between the 1.5, 2.0 and 2.5 Mc/s markers in Figure 47 it is almost certain that there has been no serious drift in either of the two crystal oscillators in the frequency calibrator. The accuracy of the frequency calibrator can also be checked from the ground by transmitting a high frequency signal to the satellite at, for example, 10 Mc/s, and then detecting this signal in the sounder receiver. Measurement error would be less than $\pm$ 20 kc/s, and since the main marker grid is derived from the harmonics of a 1 Mc/s crystal oscillator the percentage error would be the same for all frequency markers, and equal to $\pm$ 0.2%.

Figure 48 illustrates the variation in the frame period of the sweep-frequency oscillator since launch, and Figure 49 shows the variation in sounder line period during the first three years in orbit. The periods are slightly temperature dependent and fluctuate in value as spacecraft deck temperatures vary from +5 to +35°C, due to precession of the plane of the orbit and resulting changes in orbital per cent sunlight.

Approximately 1.2×10^6 ionograms have been telemetered to the ground, and of these about 60% are good to excellent in quality. The poor quality of the remaining ionograms is largely due to interfering signals from high-frequency transmitters on the ground, causing intermodulation products in the front end of the sounder receiver and reducing its sensitivity. The effect has seriously degraded night-time ionograms over much of North America and has virtually eliminated ionograms, *day* and *night*, over large areas of Europe. In less populated regions, such as the Falkland Islands and Singapore, the interference is negligible at all times.

Figure 50 shows a poor quality ionogram obtained at night over Canada. The AGC voltage of the sounder receiver is locked at its maximum value, which reduces the receiver gain to a minimum over the entire frequency sweep. A good quality ionogram in daytime, obtained at Antofagasta, Chile, is shown in Figure 51. The sounder receiver AGC voltage shows a smooth variation with frequency, indicating cosmic noise as the dominant noise background. Note the relative absence of spurious responses in the receiver AGC trace. As an indication of the magnitude of the intermodulation problem, a ground station with an antenna gain of 20 db, and a transmitter power of 100 kw at 5 Mc/s, will generate, at a range of 1000 miles, a signal of 150 mV across the 300 Ω input impedance of the Alouette I sounder receiver. This interfering signal level is 104 db above the threshold sensitivity of the receiver. Since there are large numbers of transmitters with effective radiated powers of ~ 10 megawatts it is perhaps not surprising that severe intermodulation effects have been observed from time to time in the sounder receiver.

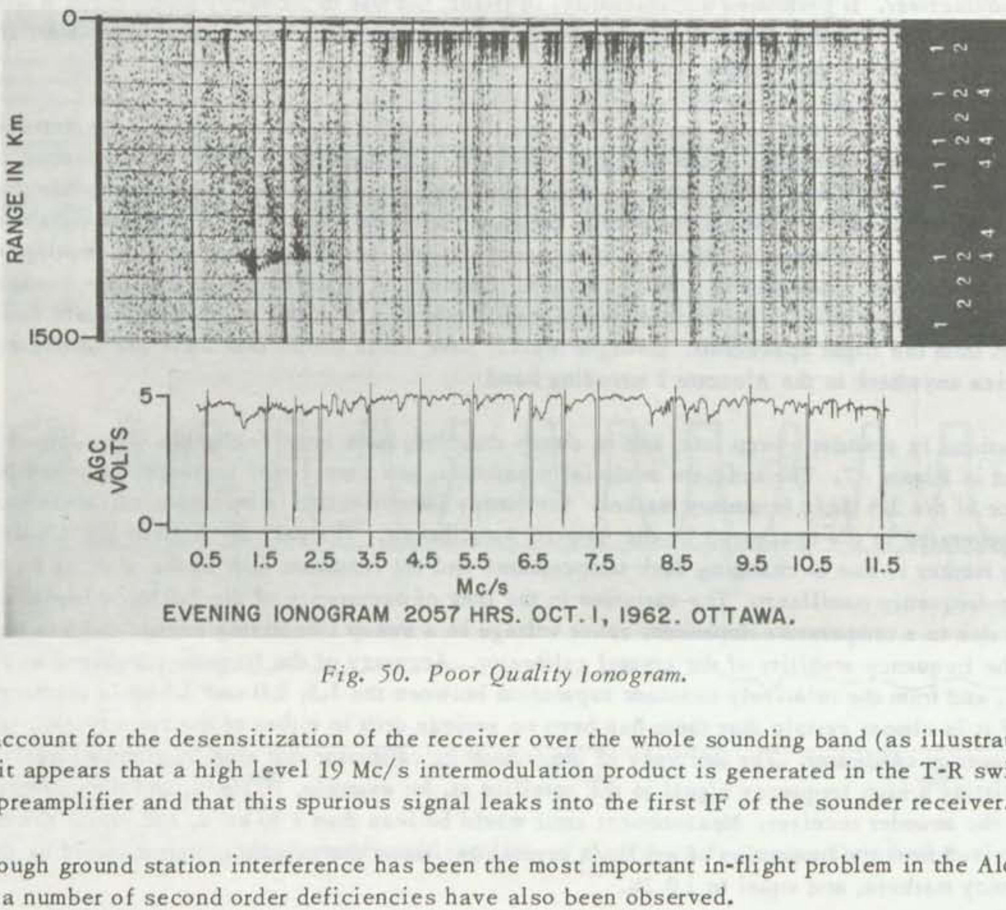

Fig. 50. Poor Quality Ionogram.

To account for the desensitization of the receiver over the whole sounding band (as illustrated in Fig. 50) it appears that a high level 19 Mc/s intermodulation product is generated in the T-R switch and/or receiver preamplifier and that this spurious signal leaks into the first IF of the sounder receiver.

Although ground station interference has been the most important in-flight problem in the Alouette I sounder, a number of second order deficiencies have also been observed.

The 100 μs zero range pulse from the sounder should, ideally, produce a trace of constant width across each ionogram. In practice, the sounder receiver generates a spurious output following each transmission period and for frequencies below 1.5 Mc/s this 'splash' or spurious echo can persist for up to 600 μs after the end of the transmitter pulse. The effect is illustrated in Figure 51 where the zero range trace is up to 300 μs wide below 1.5 Mc/s. In Figure 50 there is negligible widening of the zero range trace because of the reduced gain of the sounder receiver. The origins of transmitter splash are many and complex, and were not fully understood until after Alouette I was launched. Two main mechanisms, however, appear to be operating. The first and most important is due to RF leak through, and around, the T-R switch during the transmission interval. The leak signal is large enough to overload the first mixer in the sounder receiver and, because of finite leak from the gated sweep-frequency oscillator, a large 19 Mc/s signal is produced at the output of the mixer. This high-amplitude pulsed leak signal from the mixer causes the 19 Mc/s IF

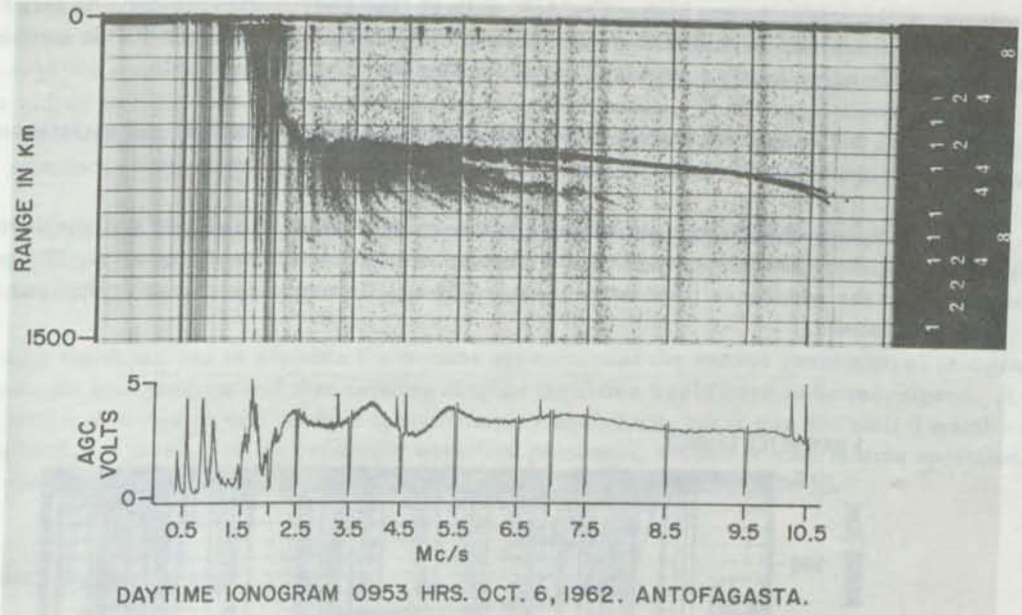

Fig. 51. Good Ionogram.

crystal filter to ring, and the resulting damped oscillation typically takes several hundred microseconds to decay to receiver noise level. The second major source of transmitter 'splash' is magnetostrictive noise generated in the ferrite core of the output transformer in the sounder transmitter. This noise is significant below 1.5 Mc/s; it is generated during the transmission interval, and decays with a time constant that depends on the mechanical loading and magnetostrictive properties of the transformer core. The effect of magnetostrictive noise and crystal filter ringing is, therefore, to produce a spurious pulse that can last for several hundred microseconds at the output of the sounder receiver. The most serious consequence of transmitter 'splash' is to obscure, over most of the sounding range, the amplitude of the zero range pulse as well as the 100 μs telemetry zero level between the end of the transmit pulse and the initiation of receiver turn-on. Loss of these amplitude levels means that accurate absolute measurements of echo signal strength are virtually impossible.

Several months after Alouette I was launched, an experiment was carried out involving direct transmissions from the ground to the sounder receiver in the spacecraft. The results of this experiment, and observations on spurious plasma resonances, strongly suggest that the image rejection of the sounder receiver is only - 15 to - 20 db. Since there are no records of the image response of this receiver ever being measured it is possible that its image rejection was low when Alouette I was launched. Tests on the back-up flight spacecraft receiver gave an image rejection of - 70 db, thus indicating that the basic receiver design was sound; and that the flight unit may have been launched with a defective IF crystal filter.

The poor image response hypothesis was subsequently used to explain the deterioration in signal-to-noise ratio observed on many Alouette I ionograms at and beyond foF2. The evidence appeared conclusive until the in-flight performance of Alouette II showed that loss of signal-to-noise ratio in the region of foF2 is probably not an image problem, but instead is due to an increase in deviative absorption as the virtual range starts to increase rapidly.

The AGC voltage of the sounder receiver is not clamped when the receiver is gated off for 400 μs during each line period. If the received noise level is high, the AGC voltage will decay significantly during this 400 μs interval and when the receiver is gated on again, its sensitivity, and therefore its noise output voltage, will initially be too high. The AGC voltage, therefore, increases until its original voltage level is restored, hence the increased noise in the first 200 km of range in Figure 50. In most ionograms, however, the cosmic noise level is not high enough for this effect to be observable.

Loss of signal due to antenna pattern fading has not been a serious problem and satisfactory sounder operation has been maintained in spite of a reduction in spin rate to 0.1 rpm.

In all other respects the sounder performance has been normal. If we exclude a slight drift in SFO starting frequency, there has been no observable deterioration in any of the electronics. The stability of the performance of the sounder is illustrated in Figure 52 which compares ionograms taken one day and 3 1/2 years after launch.

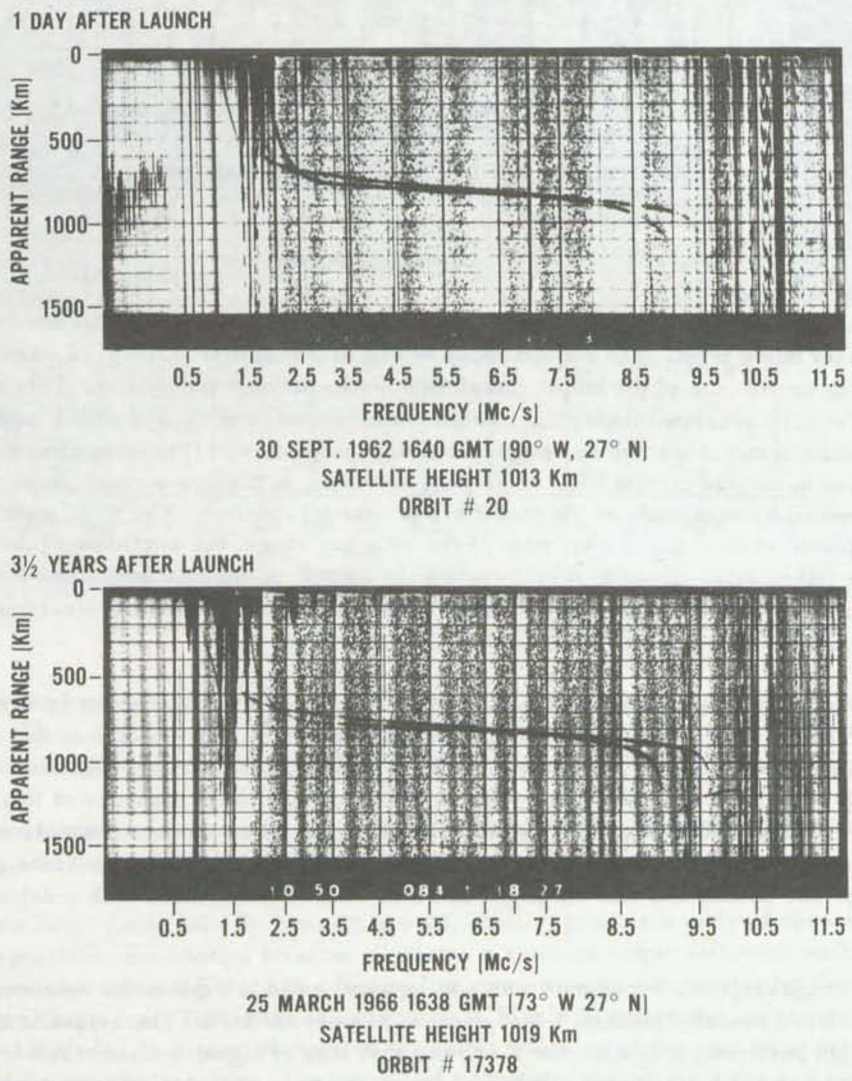

Fig. 52. Comparison of Ionograms Taken One Day and 3 1/2 Years After Launch.

As a general comment it should be noted that, as a pulse ranging system, the sounder performs very well indeed, but as a pulse-amplitude measuring instrument its performance is not so impressive. This is partly because the receiver has to cover such a wide range of background noise and echo signal strengths (hence the use of an AGC loop and logarithmic amplification), and partly because of poor amplitude calibration on the video format. If the echo amplitude has to be measured absolutely, as against being measured relatively, accurate aspect sensing is also required and this was not provided in Alouette I.

Finally, there has been the problem of mass-producing suitably coded, high quality ionograms, from magnetic tapes contaminated with telemetry noise, sounder interference, tape drop-outs, ground station noise, spurious responses, varying recording levels, etc.

Following the launching of Alouette I it became apparent that the routine generation of ionograms was a particularly difficult problem and that existing display facilities would have to be redesigned. A crash effort was initiated to design and produce special display equipment, but it was not until 9 months after launch that ionogram production, by relatively unskilled personnel, became a truly routine operation at DRTE. A view of part of the DRTE Data Processing Centre is shown in Figure 53.

9.6 Redundant Equipment

The T-R switch and sounder preamplifier, and the FM, PM, and sounder transmitters were duplicated for redundancy. Back-up units are tested regularly, all are in good working order, and since none of the primary units have failed there has, so far, been no need for the redundant electronics.

9.7 Secondary Experiments

9.7.1 Particle Experiments

The NRC particle experiments were turned on at launch and although the high voltage rails at 1100 volts, 700 volts and 500 volts must have produced arcing, there has been no observable damage due to corona effects. Apart from the expected deterioration and loss of a junction particle detector, all the particle electronics have functioned normally since launch. Analysis of directional particle data became increasingly difficult as the satellite spin rate decayed, and when the spin and tumbling rates became comparable, in March 1964, data from the four directional counters became almost impossible to interpret. This was because the orientation of the aircraft with respect to the earth's magnetic field could no longer be deduced from the single axis magnetometer.

9.7.2 VLF Experiment

The VLF receiver has functioned satisfactorily since launch and has provided good spectrograms; however, because the receiver AGC voltage is not monitored, absolute amplitude levels cannot be obtained. Converter interference is negligible in darkness, but when the spacecraft is in sunlight, the interference level increases and is amplitude modulated at the spin rate of the satellite. The amplitude-modulated converter interference is large enough to actuate the receiver AGC, with the result that VLF signals are observed to fade at the spacecraft spin rate. The VLF spectrogram in Figure 54 illustrates the abrupt increase in the amplitude of the first, second, and third harmonics of the 2.4 kc/s converter signals, as the satellite transits from darkness into sunlight (at $t = 2$ seconds). Fading of converter interference, due to spacecraft spin, occurs between $t = 11$ seconds and $t = 17$ seconds. Note the increase in receiver gain and the reappearance of VLF signals during this latter time interval.

Before launch, it was thought that the VLF and sounder experiments could not be operated simultaneously because of excessive mutual interference. In practice, although interference levels are relatively high, valuable information is often obtained when both these experiments are on. Interference on the

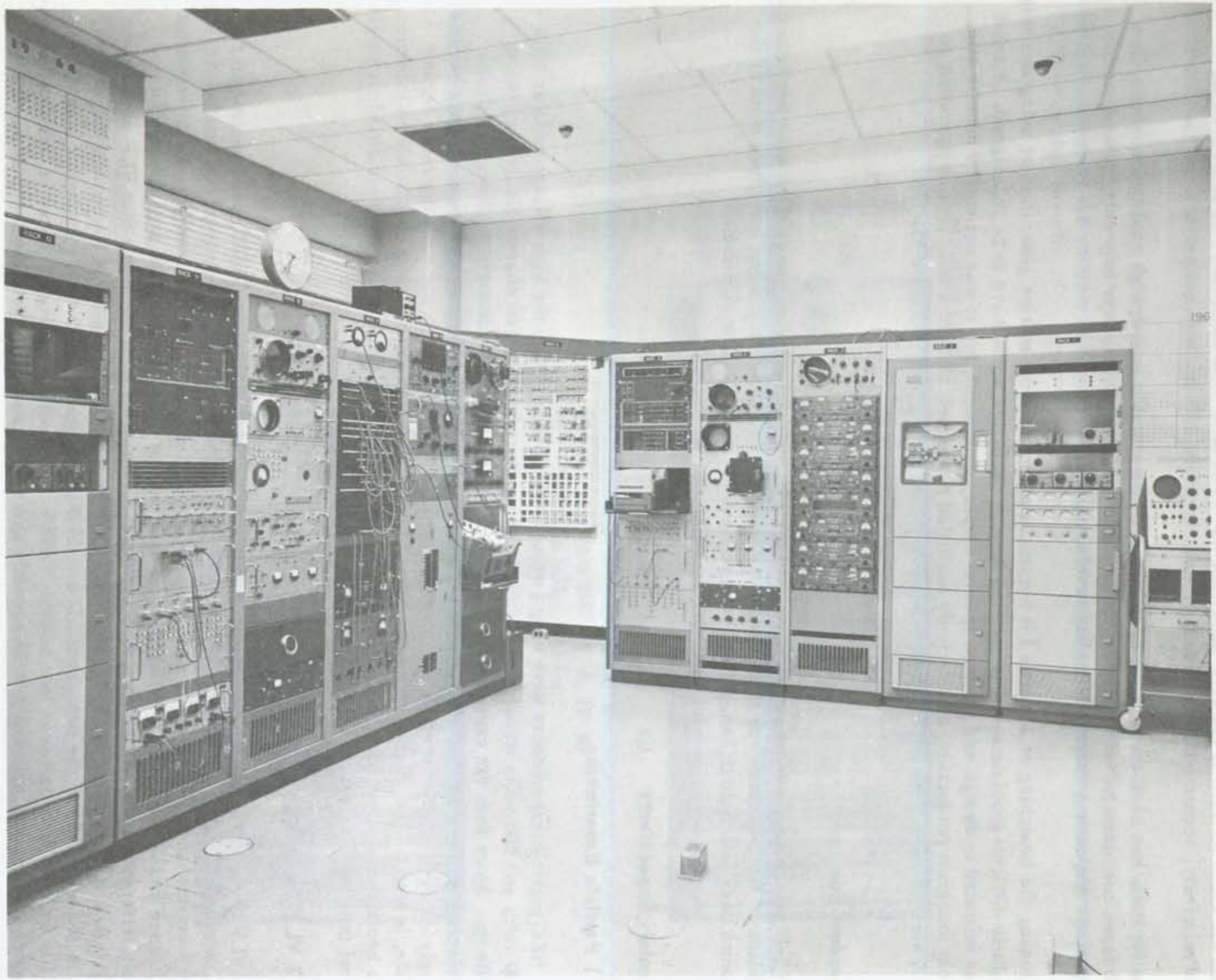

Fig. 53. DRTE Data Processing Centre for Alouette I.

ionograms is due mainly to switching transients from the sounder transmitter that enter the front end of the VLF receiver, every line period, to produce a damped oscillatory transient at the receiver output terminals that lasts for several milliseconds. Interference from the sounder into the VLF experiment is less severe. Harmonics of the 62 cps sounder video signal appear in the VLF spectrograms but the interference is less serious than expected and is usually negligible above 1.5 kc/s.

9.7.3 Cosmic Noise Experiment

Although signal-to-noise ratios have been satisfactory since launch, the data format could have been improved. Only a zero-volt reference level was provided for the 14.5 kc/s subcarrier oscillator channel, hence amplitude calibration must be carried out on the ground. This means that the linearity and modulation sensitivity of the subcarrier oscillator in the spacecraft must be known. Since there is a redundant 14.5 kc/s subcarrier, and since full scale deviations are occasionally observed, due to high frequency signals received from the ground, it can be stated with considerable confidence that sounder receiver AGC, and therefore cosmic noise voltages, are known to within ± 2%.

9.8 Telemetry

At a range of 1000 miles the average received signal strength for the 2 watt FM telemetry link is -94 dbm, approximately 7 db above the level required for full limiting in the FM telemetry receivers. With polarization diversity, telemetry noise is negligible to within a few degrees of the horizon, i.e., out to slant ranges of approximately 2500 miles. The performance of the 1/4 watt PM link is not so good, average received signal levels at 1000 miles are - 104 dbm, and drop-outs due to polarization fading occupy 3 - 10 per cent of a typical pass. If, however, an 'Electrac'-type combined tracking-filter and diversity combiner is used these drop-outs are virtually eliminated. Received signal levels from the tracking beacon are excellent and average - 105 dbm at a slant range of 1000 miles.

Since launch there has been no measurable reduction in average received signal levels. Frequency drifts are as follows:

2 watt Tx	<	1000 cps
1/4 watt Tx	<	500 cps
50 mw Beacon Tx	<	100 cps.

Telemetry transmissions now total 5820 hours, and the demodulated signals have been recorded on approximately 8200 miles of 0.5" wide, 1.5 mil thick, magnetic tape. Signal-to-noise margins on the FM link are such that an operator with a 7 - 8 db Yagi antenna and a simple receiver can easily obtain usable ionograms.

9.9 Command System

Approximately 39,200 commands have been transmitted and, neglecting station malfunctions, approximately one per week has failed to turn the payload on. No troubles have been experienced at maximum design range and the satellite has been commanded successfully as low as two degrees above the horizon.

All command functions have operated normally and, with one exception, have continued to provide full control of the satellite. For several days during low per cent sun orbits it has been found that the satellite cannot be commanded off when both the telemetry transmitters are operating. This command desensitizing is because cross-modulation products from the telemetry transmitters appear at the input to the command receivers. Operationally, this has caused no significant problems since command control is regained immediately following automatic turn-off. If, however, the automatic turn-off circuit fails, when the command receivers are desensitized, it is possible that all battery packs could become discharged, in which case

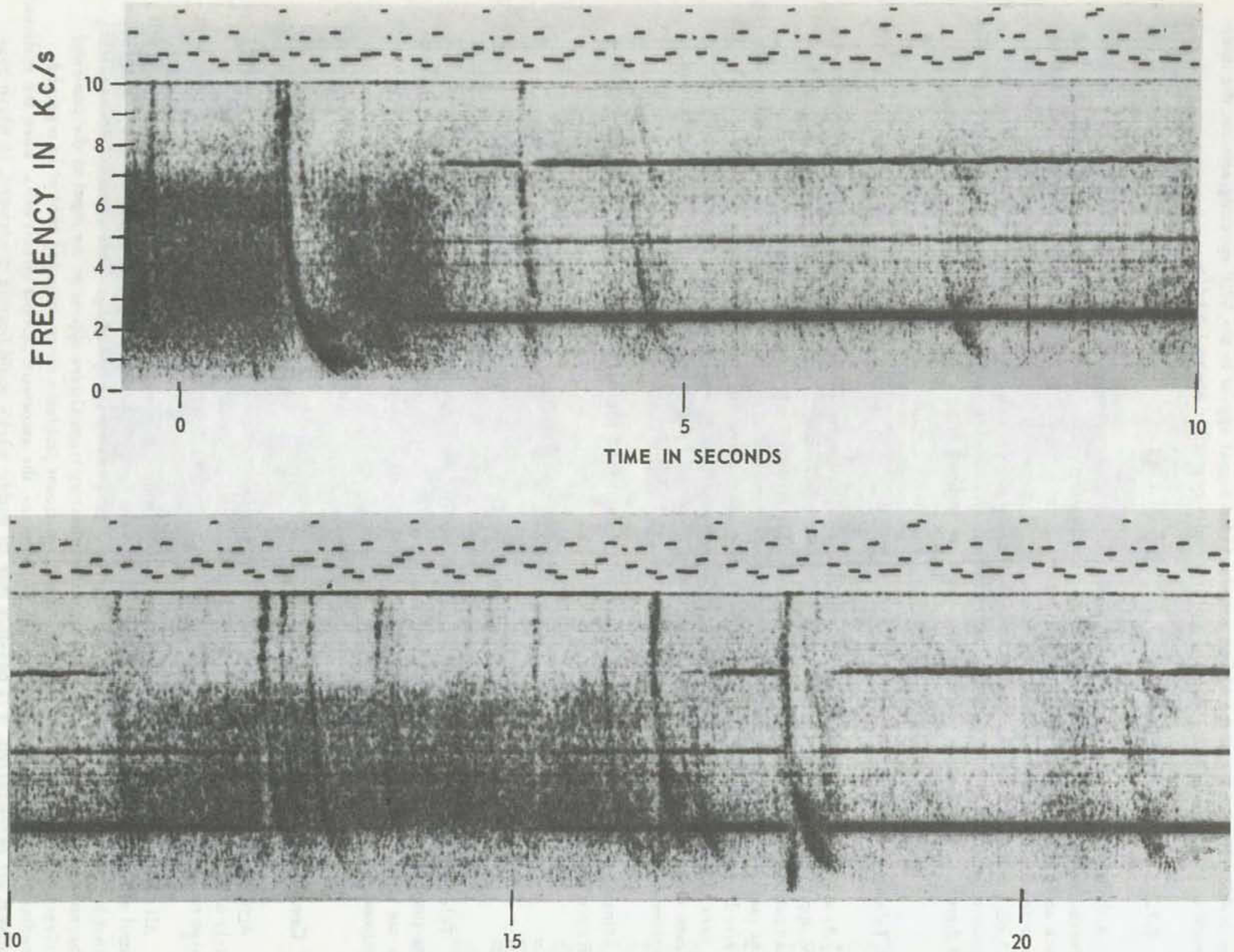

Fig. 54. Alouette I VLF Spectrogram Taken with the Ionospheric Sounder Switched Off.

command control would be permanently lost and the life of the payload ended. The turn-off time of this critical circuit is monitored daily at Ottawa, and a graph showing the variation of this parameter since launch is given in Figure 55. The oscillatory characteristic in the curve is due to temperature changes caused by variations in the orbital per cent sunlight.

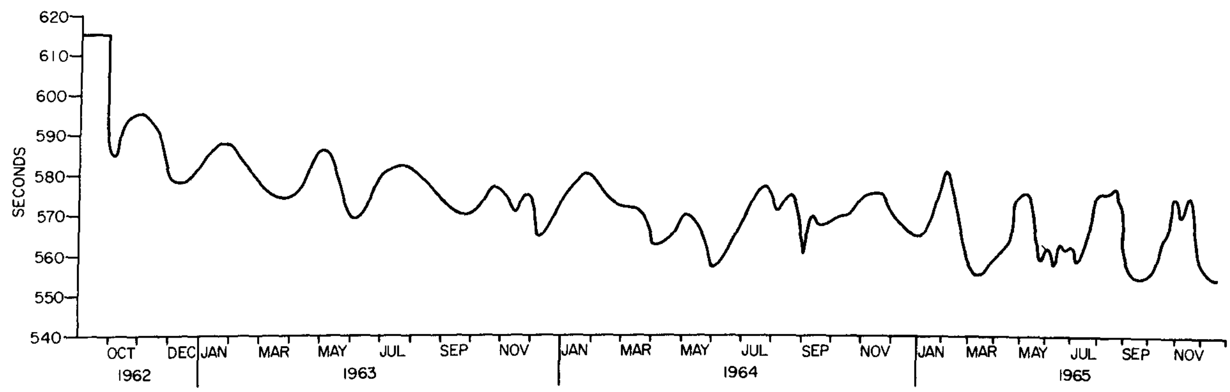

Fig. 55. Variation in Automatic Turn-off Time Since Launch.

9.10 Ground Stations

Initially, three telemetry and command ground stations were established in Canada for Alouette I. The stations were designed, installed, and operated by DRTE personnel and were located at Ottawa, Ontario, Resolute Bay, North West Territories, and Prince Albert, Saskatchewan. Eleven months after launch, the Prince Albert Station was closed down because of overlap in coverage with the East Grand Forks STADAN Station. An external view of the Ottawa Ground Station, including the steerable array of horizontally and vertically polarized Yagis is shown in Figure 56. The central Yagi of this antenna has a gain of 12 db and is connected to a 500 watt command transmitter. The remaining 8 Yagis provide a gain of 19 db, and are used for telemetry. The antenna is controlled by a potentiometer program unit which is preset prior to each pass, and which steps the antenna at intervals of half a second in time. In practice there have been tracking problems on near overhead passes due to the coarseness of these programmed steps. An interior view of the Ottawa ground station is given in Figure 57.

For routine operations, the satellite is only turned on if its maximum elevation angle, during a pass, is greater than 15°. With this restriction, the Ottawa and Resolute Bay stations can handle three and nine passes respectively, every twenty-four hours. The large number of passes seen per day from Resolute Bay is because the station is within the Arctic Circle, and Alouette I is in a near-polar orbit. The Resolute Bay telemetry antenna has no radome, and is identical with that used at Ottawa. Special precautions and maintenance procedures are, however, required to ensure reliable operation at low temperatures.

9.11 Predicted Life of Alouette I

The solar cell system is now degrading very slowly, it is unlikely to be seriously effected by random failures in cells and series diodes, and it may therefore operate indefinitely at a usable power level.

The electronics could last indefinitely in the sense that there is no observable degradation to indicate a definite end-point to the life of spacecraft. Random failures in certain parts of the system could, however, terminate operation at any time, and although it is impossible to predict when these will occur, serious failures are probably inevitable within the next few years.

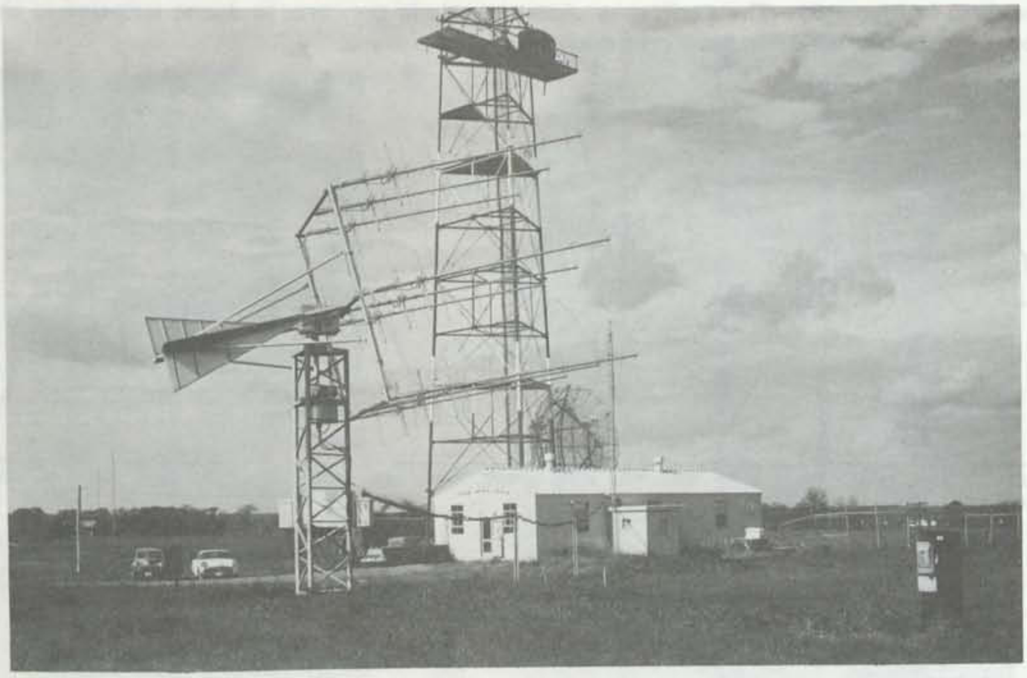

Fig. 56. External View of the Alouette I Ottawa Ground Station.

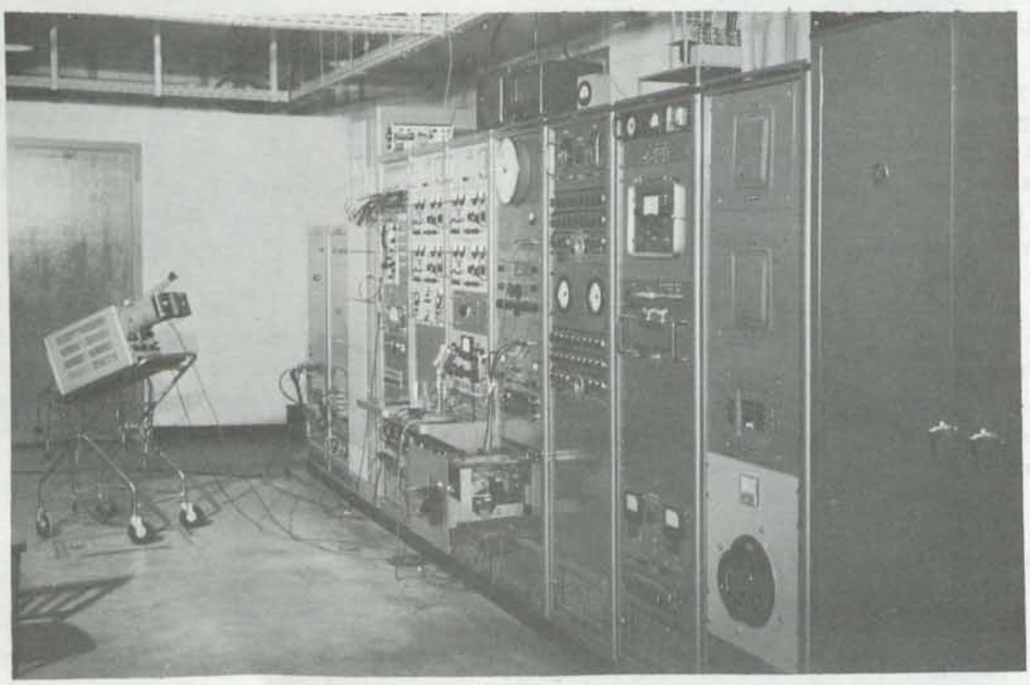

Fig. 57. Internal View of the Ottawa Telemetry and Command Station.

Leakage via the hermetic seals in the batteries may set an upper limit of ten years to the operating life of the spacecraft.

10. ACKNOWLEDGEMENTS

The Alouette project was part of a co-operative ionospheric space program between the United States and Canada. The Canadian Defence Research Telecommunications Establishment was responsible for the design and construction of the satellite and its instrumentation, for the installation and operation of three ground stations, and for data processing. The National Research Council of Canada designed and constructed the instrumentation for the high-energy particles experiments. The National Aeronautics and Space Administration provided the launch vehicle, launch facilities, and a world-wide network of ground stations. The Radio and Space Research Station, Slough, England, operates three ground stations and is co-operating in data analysis.

The author would like to acknowledge the assistance of Mr. P.A. Field and the members of the Space Electronics Section, DRTE, during the preparation of this report.

11. REFERENCES

1. Franklin, C.A., Bibby, R.J., Sturrock, R.F., and D.F. Page. *Electronic and System Design of the Canadian Ionospheric Satellite.* IEEE Convention Record **Vol. II**, part 5, 1963.

2. Franklin, C.A., Bibby, R.J., and R.F. Sturrock. *Telemetry and Command System for the Canadian Ionospheric Satellite.* Proc. of the International Telemetering Conference, IEE Savoy Place, London, 1963.

3. Molozzi, A.R. *Instrumentation of the Ionospheric Sounder Contained in Satellite 1962 Beta Alpha (Alouette).* Proc. of the Fourth International Space Science Symposium, Space Research **IV**, Warsaw, Poland, June, 1963.

4. Ferguson, E.E., and R.G. Green. *A Minimum Telemetry Receiving System for the Alouette Topside Sounder Satellite.* NBS Technical Note No. 222, October, 1964.

5. Coll, D.C., and J.R. Storey. *Ionospheric Sounding Using Coded Pulse Signals.* Radio Science, Jour. of Research, NBS/USNC-URSI, **Vol. 68D**, No. 10, October, 1964.

6. Gross, S.H. *Basic Laws of Ionospheric Propagation for Topside Sounding* IRE Transactions on Antennas and Propagation **AP-9**, No. 6, pp. 578-579, November, 1961.

7. Molozzi, A.R., Franklin, C.A., and J.P.I. Tyas. *Cosmic Noise Measurements from 1960 η 1 at 3.8 Mc/s.* Nature, **Vol. 190**, No. 4776, May 13, 1961.

8. Chapman, J.H., and A.R. Molozzi. *Interpretation of Cosmic Noise Measurements at 3.8 Mc/s from Satellite 1960 η 1.* Nature, **Vol. 191**, No. 4787, July 29, 1961.

9. *World Wide Radio Noise Levels in the Frequency Band 10 kc/s to 100 Mc/s.* NBS Circular No. 557, August 25, 1955.

10. Warren, H.R., and J. Mar. *Structural and Thermal Design of the Topside Sounder Satellite.* Canadian Aeronautics and Space Jour., **Vol. 8**, No. 7, September, 1962.

11. Richardson, J.R., and A.R. Molozzi. *A Broad Band HF Antenna System for Use in a Satellite Ionospheric Sounder.* Convention Record of Fifth Symposium on Global Communications, Chicago, May, 1961.

12. Secord, A.H., and W.V. Tilston. *Fano Technique Solves Matching Problems for Satellite Sounding Antennas.* Canadian Electronics Engineering, **Vol. 6**, No. 12, December, 1962.

13. Richardson, J.R. *The Antenna Systems for the Satellite S-27 and the Rocket J613.* Sinclair Radio Labs., Inc., December, 1962.

14. Franklin, C.A. *A 100 Watt Wide Band Amplifier for the 1 to 12 Mc/s Frequency Range.* International Solid State Circuits Conference Digest, 1962. Available through IEEE, New York.

15. Franklin, C.A. *TR Switches.* Canadian Patent No. 844/358. Filed February 8, 1962. Granted August 10, 1965.

16. Hartz, T.R. *A Study of Interference in the Alouette Topside Sounder Records.* DRTE Report No. 1123, October, 1963.

17. McDiarmid, I.B., Budzinski, E.E., Burrows, J.R., and M.D. Wilson. *Some Average Properties of the Outer Radiation Zone at 1000 KM.* Canadian Jour. of Physics, **Vol. 41**, pp. 2064-79, 1963.

18. Boag, J.C., Saunders, J., and J.M. Stewart. *A 2 Watt 136 Mc/s FM Crystal-Controlled Transmitter.* International Solid State Circuits Conference Digest, 1963.

19. Bibby, R.J., and D.F. Page. *Interaction between Telemetry and Beacon Transmitters and the Command Receiver in the Topside Sounder Satellite.* Preliminary Report, DRTE 0204-01-3 (E), July, 1962.

20. Franklin, C.A. *Short Circuit Protection for DC-DC Converter.* Canadian Patent Application No. 844/859. Filed March 14, 1962.

21. Booth, G.H. *Characteristics of the Alouette Satellite 1962 Beta Alpha One.* DRTE Report No. 1111, June, 1963.

22. Kowalik, H. *S-27-4 (Alouette) Satellite System Test and Calibration.* DRTE Report No. 1133, May, 1964.

23. Kowalik, H. *S-27 (Alouette) Satellite System Configuration and Wiring.* DRTE Report No. 1124, September, 1963.

24. Mackie, G.H.C. *Construction Techniques and Inspection Procedures for the S-27 Alouette Satellite Payload.* DRTE Report No. 1119, July, 1963.

APPENDIX I

WEIGHT DISTRIBUTION IN ALOUETTE I

Figure 58 illustrates the location of equipment in Alouette I [23]. The weights of individual electronics boxes, batteries, solar cells, antennas, structure, etc., are given in Table 13.

TABLE 13 – Alouette I Weight Distribution

			Weight (lbs.)
1. Deck I Electronic Units			
Sounder Antenna Matching Network		3.54	
Commutator I (with magnetometer probe bracket)		3.62	
Commutator II (with 22 kc/s SCO)		3.62	
Power Amplifier (Sounder Transmitter) 1A		4.17	
Power Amplifier 1B		4.18	
Transmit-Receive Switch and Preamplifier		1.66	
Transmitter Mixer		1.68	
Sweep Calibrator		1.92	
Sounder Receiver		2.84	
Timing Generator		0.77	
dc-dc Converter I		2.53	
dc-dc Converter II		3.15	
Temperature Measuring Unit II and Converter Input Voltage Monitor		0.42	
Video Adder		0.58	
Relay R-7-1		0.68	
Relay R-7-2		0.23	
Magnetometer Buffer Amplifier		0.27	
Battery Current Monitor		0.98	
Sweep Frequency Oscillator		5.00	
Magnetometer		0.24	
Current Sensor and Surge Suppressor (6)		2.37	44.45
2. Shell I Harness			14.70
3. Deck II Electronic Units			
National Research Council Particle Experiments		12.00	
2-Watt Telemetry Transmitter Mount and Heat Sink		1.18	
2-Watt Telemetry Transmitters (2)		1.94	
Command Receivers and Decoders		7.25	
¼-Watt Telemetry Transmitters (2)		3.87	
Automatic Turn-Off Unit		0.99	
Battery Switching Unit		2.02	
dc-dc Converter III		2.77	
dc-dc Converter IV		2.89	
Temperature Measuring Unit I		0.26	
Relay Unit R-10		0.34	
Relay Unit R-11		0.39	
Relay Units R-13, R-14		0.44	
Relay Unit 8		0.30	
Very-Low-Frequency Receiver		1.35	
Beacon Transmitter		0.55	38.54
4. Shell II Harness		10.4	
5. Center Structure (including beacon antenna mount)		31.5	
Sounder antennas, motor, and gear train		45.0	
6. Batteries (including wiring and bolts)		75.55	
7. Shells I and II		24.8	
8. Radiation Hoods I and II		6.62	
9. Solar Cells with Panels (large units)	12.69		
(small units)	6.87	19.56	311.12
Added balance weights, telemetry and beacon antennas, various screws and fasteners, etc.		9.55	
FINAL WEIGHT of the SPACECRAFT after BALANCE			320.7 lbs.

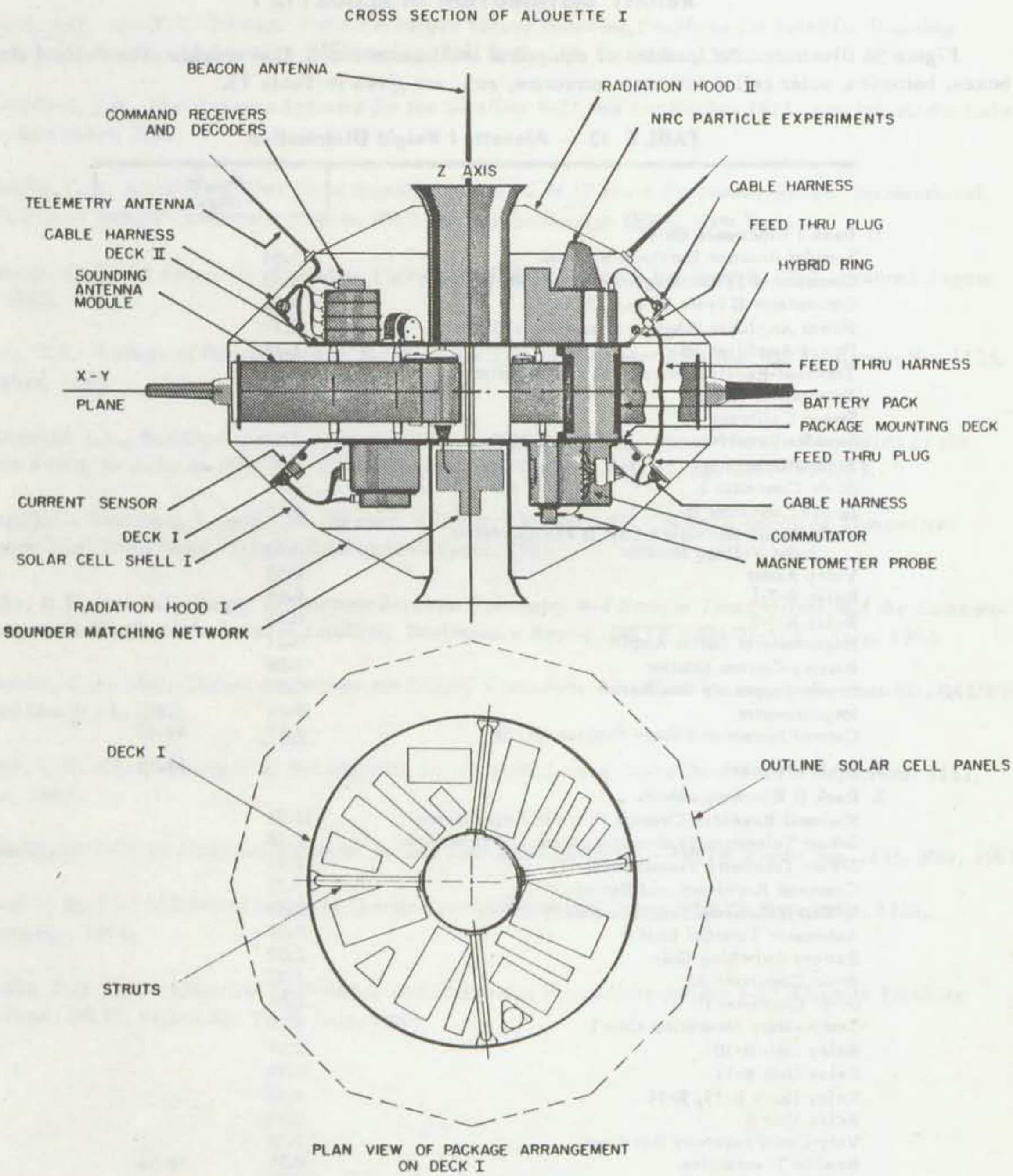

Fig. 58. Location of Equipment in Alouette I.

The way in which the weight was distributed among the subsystems and cable harness is detailed in in Table 14.

TABLE 14

Subsystem	Weight (lbs.)	Percentage of Total S/C Weight
Structure	61	19
Power (including solar cell mounting panels)	112	35
Telemetry and command	23	7
Experiments (including sounder antennas)	103	32
Cable harness	22	7
TOTAL	321	100

APPENDIX II

SOLAR POWER CALCULATIONS

The calculation of solar power output in a satellite must take into account the large efficiency losses which can occur when implementing a practical system. For Alouette I, these losses reduced the maximum theoretical output by 44% at +25°C, as shown in the following:

Number of cells	= 6480
Area of each cell	= 2 sq. cm.
Total cell area	= 12960 sq. cm.
Aspect ratio	= 4.15 ± 5%
Therefore, the total projected solar cell area	= 3120 ± 160 sq. cm.

Although the gridded solar cells have outside dimensions of 2 cm x 1 cm, the active area of each cell is only 1.8 sq. cm.

Hence, the active projected solar cell area = 2810 ± 140 sq. cm.

Solar constant	= 140 mW/sq. cm.
Average Albedo	= 35 mW/sq. cm.
and the total solar energy input	= 175 mW/sq. cm.
Nominal cell efficiency	= 8.5% at 25°C.

If there were no other losses the solar power output would be

$$2810 \times 175 \times 10^{-3} \times 8.5 \times 10^{-2} \text{ watts} \pm 5\% = 41.8 \pm 2.1 \text{ watts.}$$

In practice, there were the following additional losses:

(i) A 0.8 volt drop across the silicon diode in series with each solar cell string. A 0.6 volt drop across the battery, wiring harness, and current sensing resistances, due to the solar charging current. Therefore, for a 15.6 volt battery the output voltage from each solar cell string is 17.0 volts, and the power loss due to the above voltage drops is 8%.

(ii) Angle of incidence losses due to reflection of light from solar cells. At angles of incidence greater than 75-80° very little solar energy is absorbed by the cells. This effectively reduces the solar energy flux by approximately 15%.

(iii) Filtering losses in the optically coated cover glasses effectively reduced solar energy flux by 6%.

(iv) Shingling losses due to series connection of cells of varying efficiency. Efficiency of each string tends to be the efficiency of the worst cell in the string. Average power loss due to this effect was estimated at 6%.

(v) Mismatch losses. Because of the reduction in solar charging current with time (mainly because of radiation effects), and the V-I characteristics of the cells, the solar supply was initially mismatched to the battery-load system to provide maximum average long term power output. Cell voltage for maximum power output at +25°C was 430 mv, whereas the design value for the initial solar cell voltage in Alouette I was only 380 mv when charging a 15.6 volt battery. Taking into account the cell V-I characteristics, this represents an initial efficiency loss of approximately 10%.

(vi) Shadowing losses due to the sounder antennas. Laboratory measurements indicated a maximum power loss of 10% for the spin axis of the spacecraft perpendicular to the ecliptic. An average loss of 5% was allowed for shadowing.

Taking the above losses into account the final power output is calculated as follows:

Maximum theoretical power output	= 41.8 watts
Shadowing losses	= 5%
Filtering losses	= 6%
Angle of incidence losses	= 15%
TOTAL	= 26%
Power output	= 30.9 watts
Mismatch losses	= 10%
Shingling losses	= 6%
TOTAL	= 16%
Power output	= 26.0 watts
Diode losses	= 4.7%
i^2R losses	= 3.5%
TOTAL	= 8.2%

Therefore, the calculated power output of the Alouette I solar supply = 23.9 watts

Observed initial power output in Alouette I = 23.3 watts.

Calculated initial charging currents for the four converter subsystems, assuming a nominal battery voltage of 15.6 v, are given in the following table:

Converter Subsystem	Number of Solar Cell Strings	Calculated Charging Current (mA)	Observed Charging Current (mA)
1	34	362	350
2	28	298	290
3	48	511	500
4	34	362	350

The solar cell and battery voltages both have negative temperature coefficients, so that although the power output typically drops 0.5% for a matched supply, the charging currents to the batteries remain essentially independent of temperature. For the charging currents to be constant, however, the battery temperatures must closely follow the solar cell temperatures and must not go outside the range -10°C to +50°C. Initially, this condition was approximately true in Alouette I, but due to the effects of despin and changes in orientation of the spacecraft, illuminated solar cell temperatures have, for increasing periods of time, probably been 30-35°C above design values. Since there has been no corresponding increase in battery temperatures, solar charging currents, for the above conditions, must, in fact, have decreased with increasing temperature.

In practice, the solar cell charging current was found to be a more convenient design parameter than solar power output, and nearly all specifications and calculations for the solar supply were in terms of this current, rather than of the more fundamental quantity of power.

DEFENCE RESEARCH BOARD

DEPARTMENT OF NATIONAL DEFENCE
CANADA

DEFENCE RESEARCH TELECOMMUNICATIONS ESTABLISHMENT

ALOUETTE I: THE FIRST THREE YEARS IN ORBIT

PART III – MECHANICAL DESIGN AND ENVIRONMENT

by

JOHN MAR

DRTE REPORT NO. 1159-3

PCC No. D48-02-04-01

Submitted September 1965
Published April 1967
OTTAWA

66-375

TABLE OF CONTENTS

PART III

Page

ALOUETTE I: THE FIRST THREE YEARS IN ORBIT

PART III – MECHANICAL DESIGN AND ENVIRONMENT

by

John Mar

ABSTRACT

This part of the report is concerned with the mechanics and spacecraft environment aspects of the Alouette I satellite project. The design criteria and their implementations, together with the performance of the spacecraft's structural, extendible antennae, payload packaging, thermal, dynamics, and ground handling systems are discussed. A section describing the satellite's environmental test program is included.

1. INTRODUCTION

Following the September 29th, 1962, Thor-Agena-B launching of Alouette I from the Pacific Missile Range in California, as part of a long term international program for studying the ionized constituents of the upper atmosphere, the precise orbital parameters of the spacecraft, as measured on October 29th were as follows:

Period	105.409 minutes
Inclination	80.463 degrees (prograde)
Right Accession of Ascending Node	143.939 degrees
Argument of Perigee	183.829 degrees
Mean Anomaly	87.890 degrees
Perigee	993.80 km
Apogee	1033.23 km
Rotation of line of Apsides	2.566 degrees per day
Nodal Regression	0.984 degrees per day.

The spacecraft is equipped for four experiments. The primary one was designed to measure the world-wide electron density distributions, above the ionospheric F-layer, to near-orbital height for a period of one year. The experiment employs an echo-ranging technique carried out by means of a swept-frequency pulsed transmitting and receiving system. The frequency range is from 1 to 12.0 Mc/s, which necessitates a physically large antenna system. In conjunction with the primary experiment, measurements are made of cosmic and solar noise levels between 0.4 and 12.0 Mc/s. A third experiment utilizes a series of particle detectors to measure energetic electron and ion flux densities. The last experiment is a very-low-frequency (VLF) receiver operating over the range from 400 cps to 10 kc/s.

For a scientific satellite, the spacecraft is relatively large and has a diameter of 42 inches, a height of 34 inches, and a weight of 320 lbs. An approximately spherical shape (Fig. 1) was chosen to simplify passive temperature control and to ensure fairly constant solar cell charging current over all possible orientations of the payload relative to the sun. 6480 solar cells, mounted on panels attached to the outer surface of the satellite, provide an average power of 12 watts during a 66% sun orbit (Figs. 1 and 2).

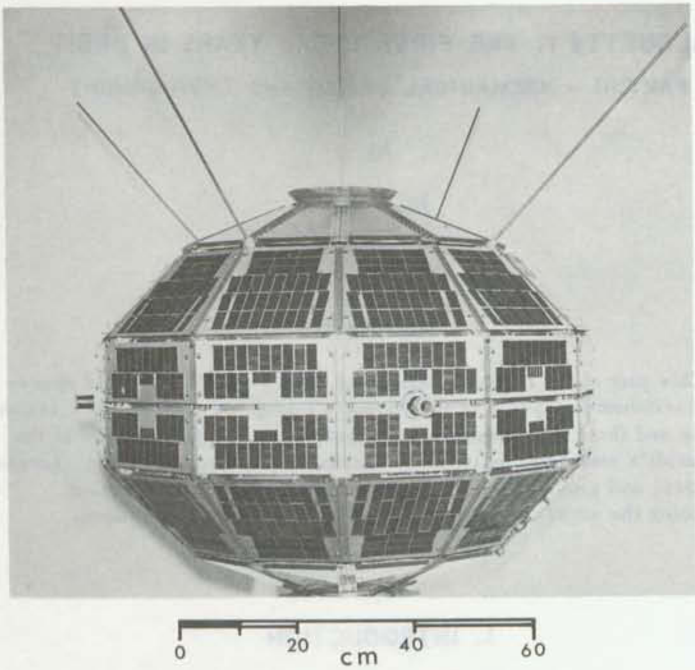

Fig. 1. Alouette I Spacecraft.

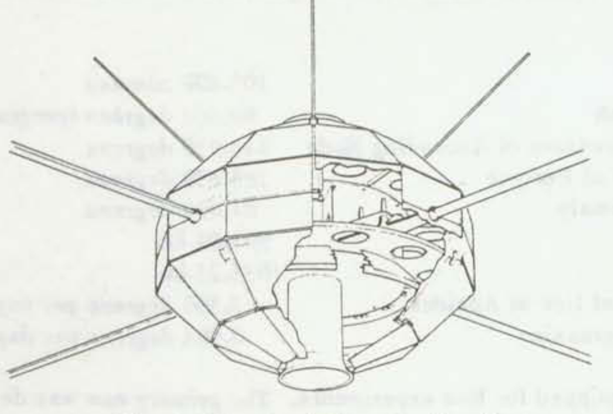

Fig. 2. Sketch of Alouette Structure.

All satellite systems, including the sounder, were transistorized to increase reliability and to meet limitations on weight, size, and power consumption.

The mechanical design problems were primarily in three areas. First, it was essential that the spacecraft be able to cope with the space environment. Secondly, it had to survive the severe stresses in the launch phase. Thirdly, special structures were required to perform the intended experiments. The environmental and launch problems are related directly to structural design, physical shape, temperature control and to studies involving the dynamic characteristics of the spacecraft. The structure had to combine ease of access to electrical circuits with the ruggedness required for the launch phase. Moreover, the spacecraft's shape and temperature control facilities are related in that a constant aspect ratio of the solar cell area with respect to the sun was required, while temperatures had to be held within narrow limits. The dynamics of the spacecraft were concerned with such matters as spin lifetime, orbit lifetime, attitude stability, and the special problems associated with the long sounder antenna poles.

The extendible metallic sections used for sounder antennas represented a unique and major contribution to the field of space hardware. These sections are stored in the form of stressed flat ribbons on a drum inside the spacecraft, and then extended after launch to form tubes 75 feet and 37.5 feet long. The device was invented in Canada, developed by a Canadian firm and is now in wide use.

The satellite itself is a non-rigid structure, and as such has displayed many interesting dynamic anomalies in orbit, some of which are discussed in this report.

For details of 'history and organization' and 'scientific results after two years in operation', the reader is referred to references 1 and 2 in the bibliography at the end of this part of the report. Since a very broad scope of reference material was used in carrying out the phase of the project described herein, no attempt is made to list the large number of sources of information. Only those references directly related to the project are listed under the bibliography of Part III.

2. STRUCTURAL SYSTEM DESIGN

One of the major tasks in the design of Alouette I was to achieve a minimum weight to accommodate its high-density payload package. Thus, the final structural and packaging configuration of Alouette I was evolved from considerations of basically three environmental phases in which the spacecraft must operate reliably. These are pre-launch, launch, and long-term operation in space. How these conditions determined the structural system design is best illustrated by the following discussion of these three environmental requirements.

2.1 Pre-Launch Environment

The pre-launch environment involves general ground handling operations, mechanical assembly and disassembly of the spacecraft, repeated removal of payload packages for testing and modification, accessibility for purposes of final adjustments to electronic boxes, ground atmospheric conditions such as high humidity and dust, and storage facilities.

To meet the requirement for accessibility, packages are mounted on two circular decks (Fig. 3) connected by a central thrust (load) bearing tube. Access to each deck is accomplished by removal of the radiation shields. In addition, the entire outer shell, on which the solar cell panels and main electronic system cabling harness are fastened, may be removed in two halves by taking out screws located around the periphery of the equatorial band. Removal of the outer shell exposes the central structure (Fig. 4) and permits access to the NiCd battery packs and the sounder antenna units.

Corrosion resistance and machinability were two of the factors that determined the selection of space stable materials. Consequently, stainless steel in fasteners and aluminum in the structure were chosen.

For the outer surface finish, apart from that of the glass covered solar cells, anodized aluminum and polished aluminum were selected. These finishes were selected not only because of their usefulness in passive temperature control, but also because of their relative insensitiveness to surface deterioration (e.g., to tarnish, chipping, etc.) under normal ground handling and storage. Moreover, a clean surface finish could be maintained easily by swabbing with an alcohol solution.

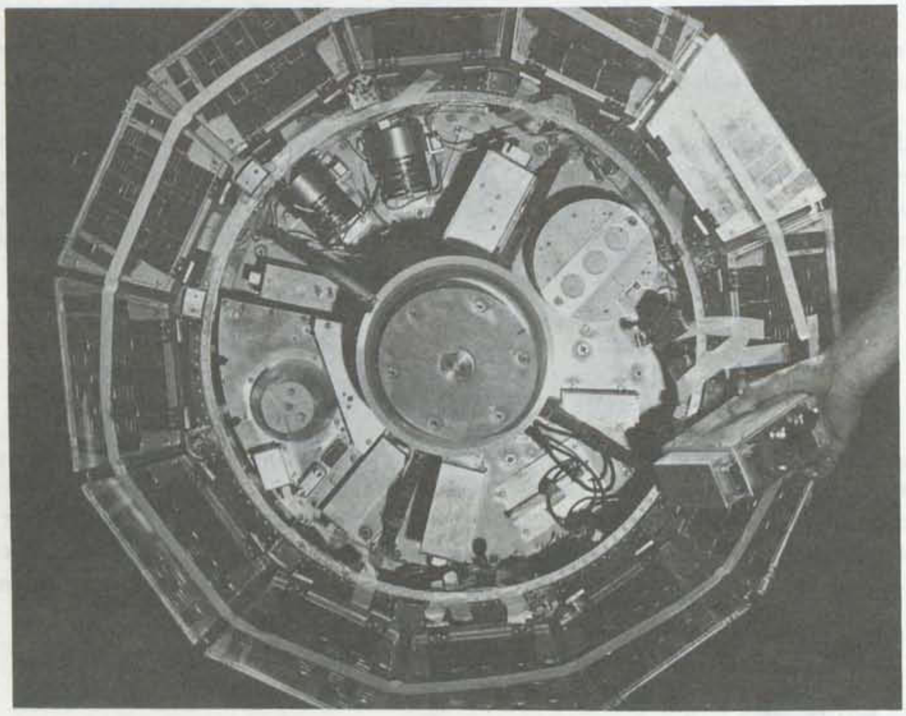

Fig. 3. Spacecraft with Radiation Covers Removed Showing Access to Instrument Deck.

2.2 Launch Environment

The launch environment is associated with the flight characteristics of the launching rocket. Typically, these characteristics are high steady acceleration, structurally transmitted severe vibrations, high acoustic noise, and rapidly decreasing ambient pressure. The requirement of minimum weight combined with the need to withstand intense vibration was one of the difficult problems encountered in the design of Alouette I.

In arriving at the final design, extensive structural testing was carried out on a full scale 'dynamic' model. During first vibration tests, a major resonance frequency at 21 cps was discovered. This led subsequently to failure of the main thrust tube hold-down screws. Because this resonance was a result of a non-linear cross coupling between thrust tube and outer shell structure, and was not predicted in the normal design analysis, additional dynamic response studies and static load deflection tests of the structure had to be carried out to extract fundamental modes to a higher degree of accuracy.

A modification in the form of additional braces was carried out to stiffen the structure. This increased the first resonance frequency to 29 cps, which resulted in amplitudes much lower than that at 21 cps. At this new frequency, the structure met test specifications.

Final design stressing to 50% of ultimate stress was used as a safety factor.

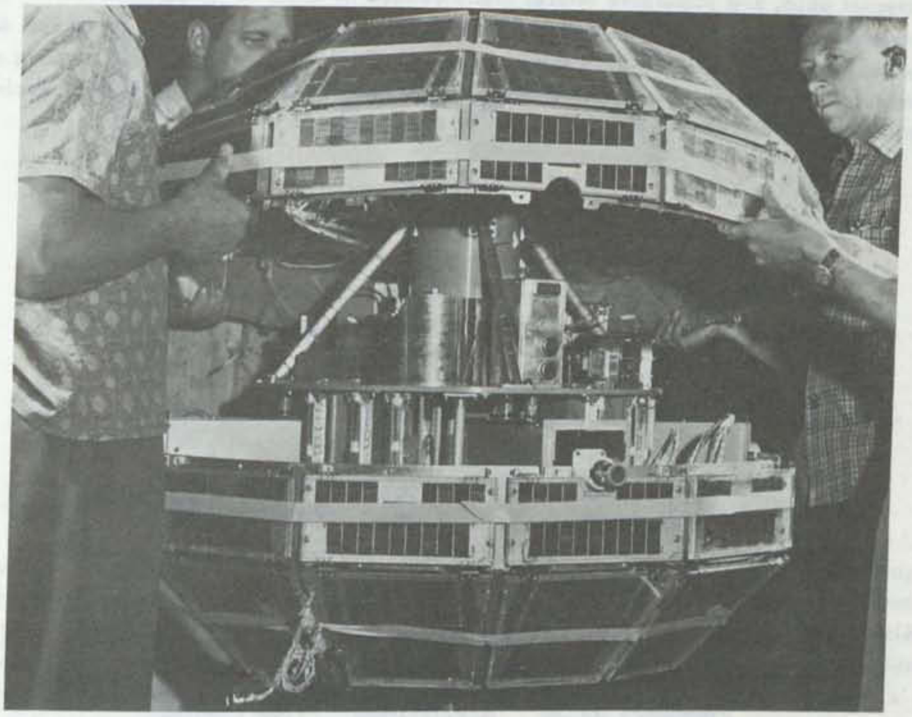

Fig. 4. Central Structure Showing Location of Batteries and Sounding Antennas.

2.2.1 Steady Acceleration

To simulate effects of acceleration forces during rocket-powered flight and stage-separation phases, and of the spin-up of the satellite prior to orbit injection, the Alouette I structure was subjected to the tests shown in Table 1. The levels shown are representative of measurements obtained from previous flights on Thor-Agena rockets.

TABLE 1

Acceleration and Spin Tests

Acceleration	
Longitudinal	12.6 g at spacecraft's center of gravity for 10 min
Lateral	2.4 g
Spin	
240 rpm following dynamic balance	

2.2.2 Vibration

Mechanical vibrations in the launching rocket are caused by motor combustion, LOX turbo-pump cavitation, ground-reflected acoustic noise from the nozzle, aerodynamic boundary-layer pressure fluctuations on the external skin, and impulsive lateral loads caused by wind shear during ascent. These vibrations are transmitted structurally to the spacecraft thrust-tube interface. To check the design, the spacecraft was subjected to a total of 27.3 minutes of sinusoidal vibration (i.e., 9.1 minutes along each axis), and 24 minutes of random vibration (8 minutes along each axis). These vibration levels are shown in Table 2, and represent 3σ (about 98%) reliability of that expected in flight.

TABLE 2

Vibration Test Levels for Alouette Prototype

A. Sinusoidal Vibration

Frequency Range (cps)	Vector Acceleration (g)	
	Thrust Axis	Lateral Axis
5 - 250	± 3.0	± 2.3
250 - 400	± 4.5	± 3.0
400 - 3000	± 7.5	± 7.5

Sweep Rate: 1 octave/min.

B. Sinusoidal Vibration Simulating Effects of Booster LOX Turbo-pump Cavitation - Applied in Thrust Direction Only

Frequency Range (cps)	Acceleration (g)	Time Duration (sec)
16 - 22	± 4.0	13
38 - 48	± 3.2	6

C. Random Vibration

Frequency Band (cps)	Power Spectral Density (g^2/cps)	Approx. Equivalent Acceleration (g rms)
20 - 2000	0.045	9.5

Applied along each of 3 axes for 8 min. (Total time, 24 minutes)

2.2.3 Acoustic Noise

As a result of direct reflection from the ground, the acoustic noise from the rocket engines had its greatest effect on Alouette I at lift-off. The estimated overall sound pressure level inside the shroud (nose cone) was 138 db ($2(10^{-4})$ dynes/cm^2 db reference) and that outside was approximately 150 db. Since the induced frequency is high and therefore implies a large number of stress cycles, fatigue stress checks of the thin-skinned structural members such as the aluminum spun skin, and solar cells, were carried out. The estimated sound spectrum level experienced by Alouette I within the shroud during launch is plotted in Figure 5.

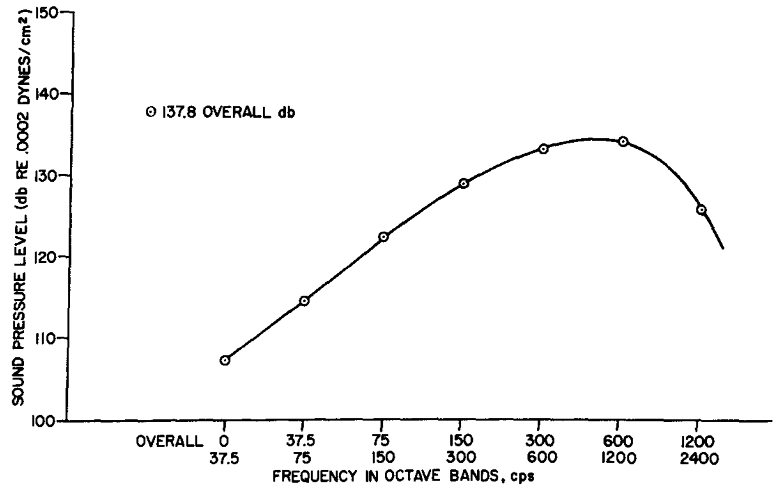

Fig. 5. Estimated Sound Spectrum Level Inside Agena B Shroud for Alouette I.

2.2.4 Rapidly Decreasing Pressure

Although the dominant design concern of rapidly decreasing pressure is the resulting corona effect on the electrical system, the effect of a rapid decrease in pressure on cellular structural members was also considered during the ambient pressure drop phase of the launch. In Alouette I, the cellular members consisted of aluminum hexcell honeycomb, and polyurethane epoxy foam, used for potting electronic circuit boards. Subsequent tests on samples in a vacuum chamber showed no ruptures or 'explosion' tendencies in these materials.

2.3 Long Term Space Environment

Once in orbit, the structure is essentially in a state of 'free fall', in a vacuum, and is subjected to bombardment by solar particles and photons, and by meteoroids.

2.3.1 Vacuum

Because the high vacuum condition encountered by Alouette I corresponds to pressures of approximately 10^{-16} mm Hg, materials with high partial pressures were generally avoided in construction since these sublime readily in this degree of vacuum. Although this may not lead to catastrophic structural failures, contamination of exposed circuitry and temperature control optical surfaces by redeposition of escaping molecules can occur. This can lead to electrical short-circuits and upset of heat balance. Consequently, the use of magnesium alloys, zinc or cadmium plating and greases and oils was avoided. The Alouette I structure is entirely of aluminum, steel, and stainless steel.

Even though there are no specific requirements for high structural strength in orbit, it is of interest to note that the impact and fatigue strength of the aluminum members probably increase with time in high vacuum as a result of depletion of the outer metallic oxide layer by natural sublimation. Removal of the oxide layer from the metal surface effectively lessens the highly concentrated surface stressing caused by the 'wedging' action of oxides acting in surface grain boundary fissures.

Use of grease and oil was confined to the ball bearings in the sounding antenna mechanism. Since there was no requirement for these to operate in a long-term space environment, standard sealed ball bearings were used throughout.

2.3.2 Radiation

The space radiation environment important to spacecraft operation at a height of 1000 km had to be taken into account in the mechanical design of Alouette I. Briefly, there are four groups of particles that are considered significant. These are:

(a) *Cosmic Radiations* – These by far contain the most energetic particles (as high as 10^{10} Bev) and comprise about 85% protons, 14% alpha particles, and 1% of various heavier elements. The distribution of cosmic particles in space is basically isotropic and uniform.

(b) *Solar Flares* – In this case streams of protons with energies as high as 10Bev and electron energies of around 100Mev that are believed associated with sunspot and solar flare activities, comprise the particle contribution.

(c) *Solar Wind* – This is the continuous stream of protons and/or electrons that emanate from the sun during quiescent conditions. The density of solar wind particles is a function of distance from the sun, and obeys roughly an inverse square law. At great distances the sun may be considered as a point source. The energies observed near the earth are around 1Kev.

(d) *Trapped (Van Allen) Particles* – Proton and electron particles trapped in the earth's magnetic field form the well known Van Allen Belts. The energy spectrum of protons range up to 60 Mev while that of electrons reach as high as 600 Kev.

In addition to energetic particles, the ultraviolet and soft X-ray components in the sun's electromagnetic spectrum can disrupt many chemical bonds and thereby initiate chemical reactions. Particularly affected by this are the organic polymers. Metals, ceramics, and inorganic compounds are not as adversely affected.

In the case of Alouette I, the radiation environment did not affect the metallic structure. Non-metallics used in Alouette I were judiciously chosen on the basis of the best available data on stability of materials against molecular, structural, and optical changes under radiation effects. In Alouette I, the materials selected were teflon, micarta, polyurethane epoxy, aluminized mylar, unbonded glass fibre paper, commercial brown wrapping paper, epoxy-based FeO paint, and polyurethane-based TiO_2 paint.

Although materials selected were believed to be reasonably stable against deterioration in space, even teflon, the most commonly used non-metallic in space applications, will lose up to 73% of its tensile strength when subjected to large amounts of radiation.

2.3.3 Thermal Effects (Outer Shape of Alouette I)

Although the size of Alouette I was determined by the need to provide adequate room for housing the electron equipment and to shield the equipment against the direct solar electromagnetic spectrum, its approximately spherical shape was chosen primarily to satisfy temperature control requirements.

Since an earth satellite receives heat by electromagnetic radiation from the sun and the earth, and reflected sun radiation from the earth, a spherical object receives the same amount of radiant energy from each source regardless of satellite aspect; consequently, this eliminates local 'hot spots' and any need for attitude control.

The temperature of Alouette was controlled passively by a careful balancing of the heat received against the heat lost by re-radiation. This was achieved by treating the outer surface so that it has specifically determined emissivity characteristics.

2.3.4 Meteoroid Damage to Structure

Because damage from meteors is possible in a space environment, the specification of structural outer skin thickness required consideration of the degree of internal payload protection the skin would provide against meteoroids. The bulk of the potential meteoroid damage is in the form of surface 'sand-blasting'. An 0.129 inch effective thickness for the Alouette outer skin was estimated to be sufficient to ensure that the probability of one meteoroid puncture occurring in one year would be no greater than 15%. The amount of damage likely to result from collision with meteroids depends on the mass of the impacting meteoroid, the relative impact velocity, and the frequency of impact. The theoretical mean frequency of impact is based on the time-swept volume of the spacecraft through a meteoroid medium of flux density, ϕ. The peak distribution of meteoroid flux is located on the ecliptic plane, with the main flux travelling in a highly elliptical prograde orbit around the sun (same direction as the earth).

A best fit to the data yields the following relation for the rate at which all particles of mass greater than m grams strike a surface.

$$\phi = 10^{-12} m^{-1.11} \text{ particles/m}^2\text{/sec} \qquad \ldots\ldots (1)$$

From equation (1), it is evident that the mean impact frequency on an object with surface area, A, is simply ϕA particles/sec. Hence, for a total exposure time, t, the mean number of impacts on the object will be ϕAt. Then following a Poisson distribution, the probability of n meteor impacts will be

$$P(n) = \frac{(\phi At)^2 e^{-\phi At}}{n!} \qquad \ldots\ldots (2)$$

The penetration of approximately spherical particles into targets at hypervelocities is not well understood. While theories of penetration differ widely, there is general agreement that penetration depends on impact velocity and mass of the projectile. From available experimental data on aluminum striking aluminum and iron striking iron at normal incidence, penetration, p, is shown to be best correlated to the one-third power of momentum as follows:

$$\text{For aluminum, } p_{Al} = 1.09\,(mv)^{1/3} \text{ cm} \qquad \ldots\ldots (3)$$

$$\text{For iron, } p_{Fe} = 0.606\,(mv)^{1/3} \text{ cm} \qquad \ldots\ldots (4)$$

where p = penetration depth in cm,
m = mass of particle in gm,
v = velocity of particle in km/sec.

Meteoroid penetration into an aluminum or silicon surface should be closely defined by equation (3) since the specific gravity of meteors (stone) is very near that of 2.8 for aluminum. (Specific gravities of Al, Fe, stone, glass and silicon are about 2.7, 2.0, 2.8, 2.8 and 2.4, respectively.) Assuming this to be the case, the meteoroid flux rate that enables penetration to an effective depth p on an aluminum surface structure will be, from equations (1) and (3),

$$\phi_p = (10^{-12})(\bar{v})^{1.11} \left(\frac{p}{1.09}\right)^{-3.33} \qquad \ldots\ldots (5)$$

where $\bar{v}$ = mean meteorite velocity.

From radar measurement surveys, meteor velocities range from 11 to 72 km/sec, the average being about 30 km/sec. The dispersion of velocity is primarily due to the relative velocity with respect to the earth; i.e., to essentially whether the earth strikes a particle in a prograde or retrograde orbit.

Considering the accuracy of the initial data, the Alouette spacecraft may be approximated by a sphere 40 in. in diameter. The total skin thickness (solar cells and aluminum structural shell) is 0.052 in. Since the penetration equation is for normal impact only, a mean effective skin thickness may be defined for the sphere to account for impact incidences that are other than normal.

The normal unit vector, $\underline{n}$, of a reference elemental area on the surface of the sphere (Fig. 6) is equal to n ($\cos\phi \sin\theta$ i + $\cos\phi \cos\theta$ j + $\sin\phi$ k). Similarly, the velocity vector $\underline{V}$ of an impinging meteoroid may be set arbitrarily equal to V (0i + 1j + 0k) since there is spherical symmetry about the origin 0. The cosine of the incident angle β between the meteoroid velocity vector and the surface element considered is then

$$\cos\beta = \underline{n} \cdot \underline{V}$$

and the mean incidence is

$$\overline{\cos\beta} = \frac{1}{n^2} \int_{-\pi/2}^{+\pi/2} \int_{-\pi/2}^{+\pi/2} \cos\phi \cos\theta \, d\phi \, d\theta = 0.404 \qquad \ldots\ldots (6)$$

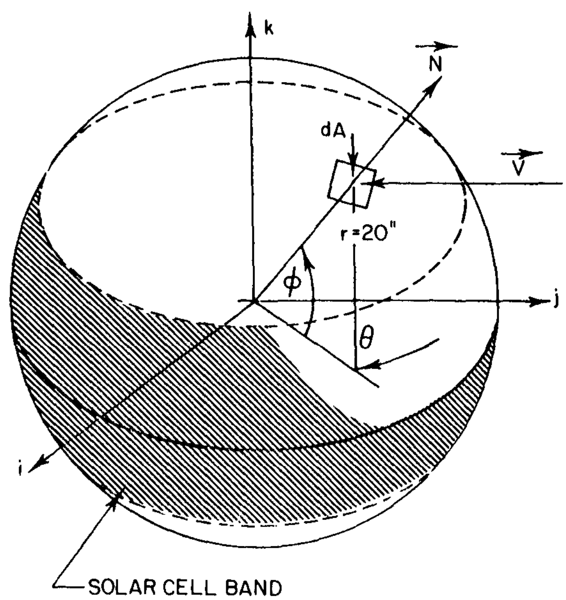

Fig. 6. Coordinate System of Alouette Equivalent Sphere.

The mean effective skin thickness for total penetration should be taken as 0.052/0.404 or 0.129 in. (0.327 cm). Using this thickness as p in equation (5), and taking a total surface area of 3.25 m^2, the probability for punctures, P(n), is plotted in Figure 7. From this figure it is evident that the probability of a puncture during the first twelve months of operation is small. In fact, the probability for no puncture, P(o), is 0.999 for the first month in orbit, and 0.88 for the first six months in orbit.

Of the curves shown in Figure 7 the plot for n = 0 is perhaps the only one that conveys the obvious fact that the chances of a meteoroid strike increase with time in orbit. The remaining curves for values of n greater than zero show the probability for discrete numbers of punctures to occur.

During one year of operation there is only a 15% chance that one meteoroid would penetrate to the inner payload. On the other hand, the exposed electrical components, such as solar cells, are more susceptible to penetration damage during a year's operation.

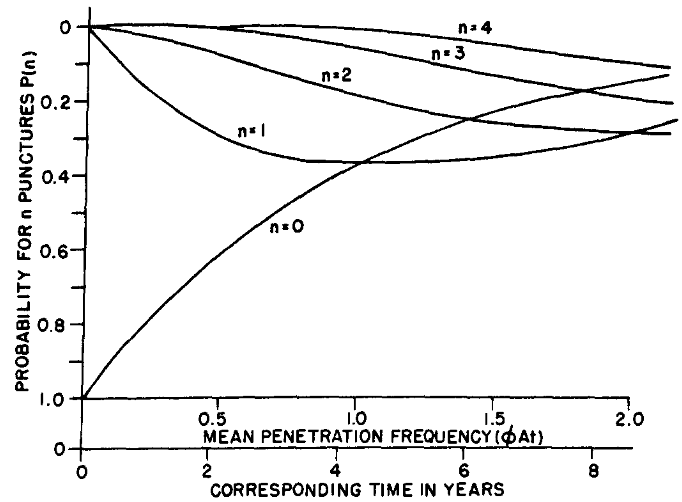

Fig. 7. Probability Functions of Alouette Shell Puncture.

Lacking the benefit of even a thin metallic shield, solar cells are not only likely to undergo a much higher rate of penetration, but glass covers would also suffer the sandblasting effect of non-penetrating micro-meteorite impingements. In due course this would change the optical properties of exposed surfaces. In the case of solar cells, this represents a degradation in efficiency, and in the case of thermal control surfaces, it causes a change in temperature equilibrium.

2.3.5 Free Fall Environment

Consideration of the state of 'free fall' did not directly affect the structural design. However, this did require a consideration of the dynamical behaviour of the free motions of bodies in orbit and its implications on spin stability.

3. ANTENNA ERECTION UNITS

Perhaps the most novel structural aspect of Alouette is the extendible antennas. The principle of operation of the antenna involves a tape of spring steel, that has been previously heat treated, and that is opened flat and wound on a drum for storage purposes, (Fig. 8). When this material is unwound from its storage drum by the drive belts shown, it curls into its natural tubular shape, with about 180° of overlap, to form a tube with considerable bending strength. This idea, conceived by Mr. G.J. Klein of the National Research Council in Ottawa, was developed by him first during World War II as an extendible mast; since the war it has been further developed by the Army Development Establishment.

3.1 Design and Test

In Alouette I, four of the antenna units form a crossed dipole, with a span of 150 ft. in one direction, and 75 ft. in the other. A view of the fully assembled antenna unit is shown in Figure 9. A clutch arrangement is provided on the top of the unit so that the drive to the belt system can be declutched when the pair of units that carry the shorter lengths of antenna tube reach full extension; this permits the other pair of tubes to unwind to their full length. A safety interlock is provided to shut off power to the motors once all four antennas have been extended. In the event of failure of this, a mechanical stop is provided that prevents any over-riding of the drive drum. The weight of an antenna unit, including 75 ft. of tube material, is about 10 lb.

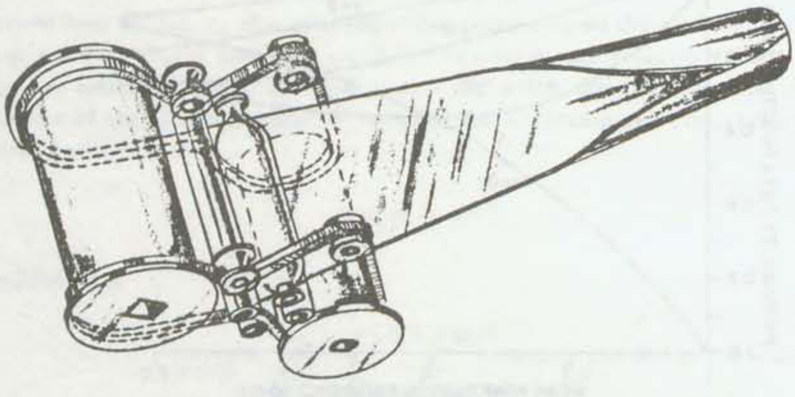

Fig. 8. Principle of Extendible Antenna.

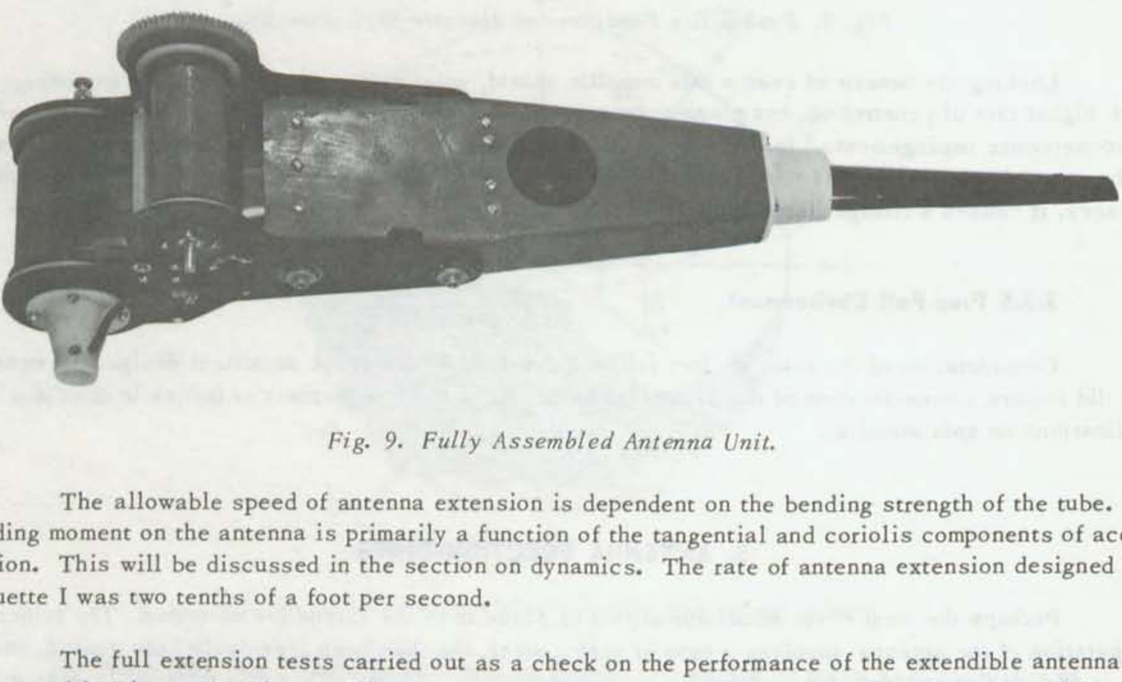

Fig. 9. Fully Assembled Antenna Unit.

The allowable speed of antenna extension is dependent on the bending strength of the tube. The bending moment on the antenna is primarily a function of the tangential and coriolis components of acceleration. This will be discussed in the section on dynamics. The rate of antenna extension designed for Alouette I was two tenths of a foot per second.

The full extension tests carried out as a check on the performance of the extendible antennas are illustrated in Figure 10. The satellite stands beneath a system of crossed tension wires, on which are hung a number of carriers, as shown at the left of Alouette. These carriers support the antennas at regular intervals as they extend outwards in four directions. Continuous recordings are made of extension rates, and drive motor current and voltage. One useful result of this test is that it determines the synchronism of extension of the four antennas and checks out the declutching operation at the completion of the extension.

3.2 Javelin Rocket Test

As the success of the satellite depended so much on the proper functioning of the long antennas, a check on antenna extension in the actual space environment was carried out in June, 1961. In the test a Javelin rocket with a pair of antenna units mounted in the nose cone was launched to satellite altitude. Because of the narrow confines of the nose cone it was necessary to arrange a mechanism by which the two antenna units could be folded down from an in-line position to a radial position. The mechanism for carrying this out is shown in Figure 11 and Figure 12 and shows the completed nose cone, on the full extension rig. Although some improvements were indicated, the Javelin test was considered successful and confirmed the practicability of the antenna design.

Fig. 10. Full Extension Test of Antenna System.

4. PAYLOAD PACKAGING

4.1 Package Design and Construction

The packaging design of the Alouette payload proved to be very reliable and more than adequately met all expectations. No structural failure of boxes occurred as a result of vibration testing, nor have any failures been indicated since launch into orbit.

Although the payload design does not represent the optimum in packaging and weight efficiency, it does reflect the considerable emphasis on flexibility and accessibility that went into the project. It was essential that the removal of any one circuit for test or repair would not seriously impede any work in progress on the remainder of the payload. Thus ease in removal and replacement of parts of the payload was a governing design criterion.

Extensive miniaturization of packages was unnecessary because full use was made of all available space within the structural shell. The size of the spacecraft envelope was established primarily by solar cell requirements rather than by packaging.

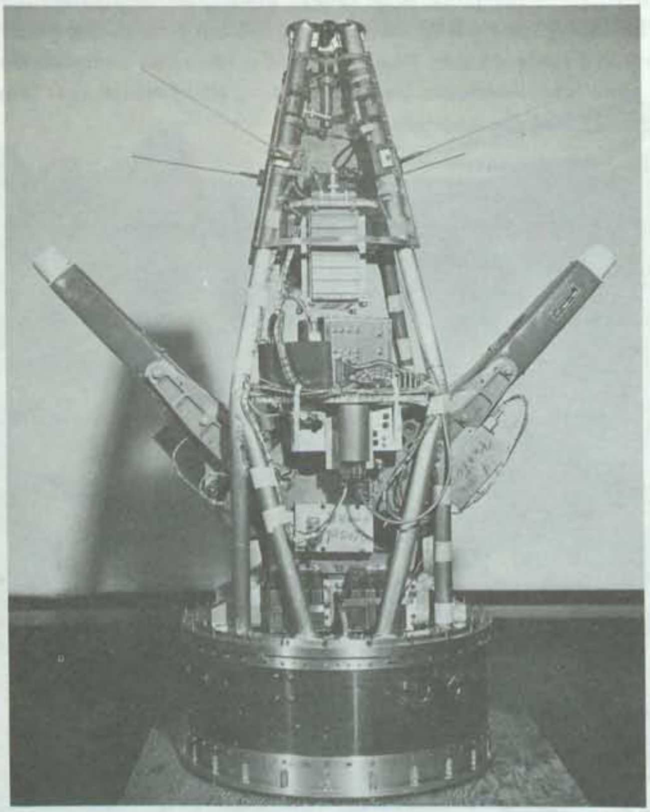

Fig. 11. Javelin Fold-Down Unit.

4.1.1 Structural and Dynamic Requirements

Because the satellite is spin stabilized, the layout of various packages in the system was determined by the need to establish a dynamic and static balance about the centre of gravity. To ensure spin stability, the spin axis is also the axis of greatest moment of inertia.

Finally, packages are located so that installation of fasteners such as captive nuts, tapped holes, Delron fasteners, etc., do not adversely affect the mechanical strength of the structure.

4.1.2 Package Configuration

Because the Alouette payload consists of many distinct circuits integrated into a single overall system, it was decided to design the system in separate units for ease of construction, sub-systems testing, replacement of defective units, and to speed production and assembly. This allowed simultaneous checking of more than one package, with minimum disruption.

Circuit components are mounted on both sides of 1/16 in. epoxy boards. The completed boards are installed in open-sided aluminum frames or boxes (Fig. 13). The open-sided frame construction permitted access to board components during assembly, as well as for the test phases that preceded final potting. The resulting package shape generally corresponded to the flat rectangular configuration of the circuit boards used. Box sizes were kept to a minimum by restricting the clearance for the components on each side of the board to one-eighth inch.

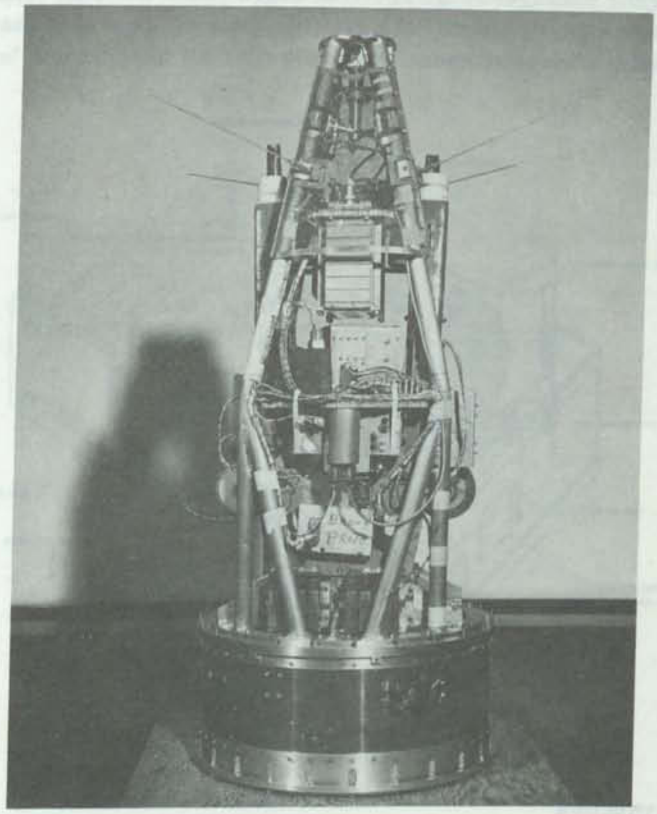

Fig. 12. Completed Javelin Payload.

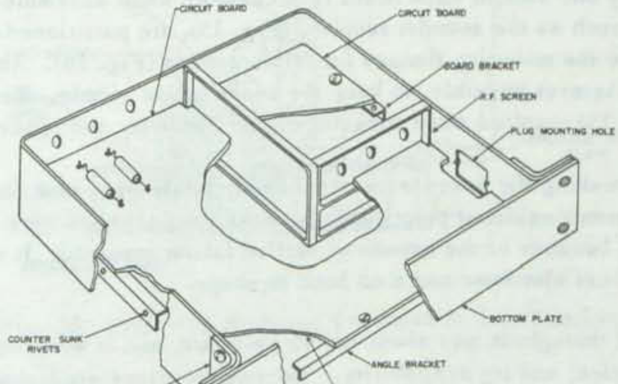

Fig. 13. U-Frame Package Construction.

Upon final completion of electrical and thermal vacuum tests of individual circuits, all boards were potted in their boxes with polyurethane foam to provide maximum rigidity and damping against vibration.

Those circuits that required electrical isolation were shielded by glueing 0.005 in. copper foil to the potting on the sides of the packages (Fig. 14). The edges of the foil were folded over the frame and secured with glue and narrow capping strips. The glue used to bond the foil to the frame was silver-filled epoxy, which provided good electrical contact.

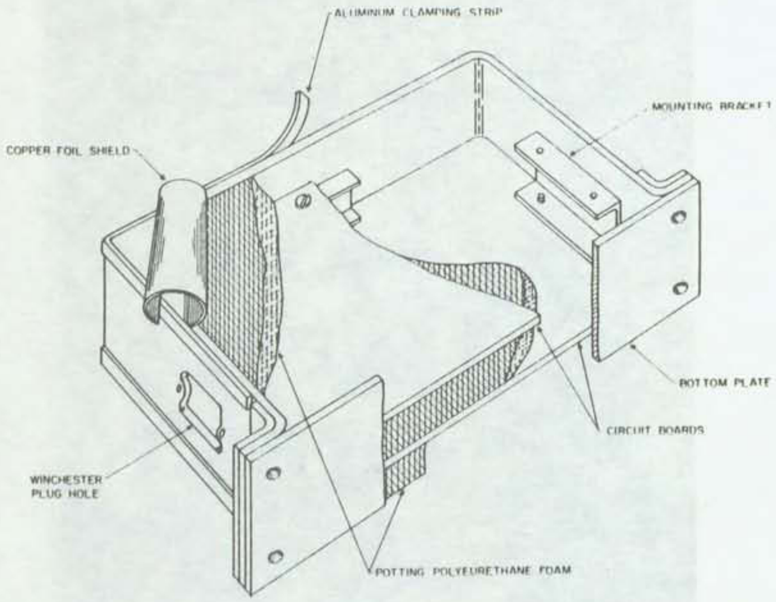

Fig. 14. Typical Shielded Box.

4.1.3 Box Construction

The boxes are made in the shape of an inverted 'U' with flanges that project outwards. In a few cases where boards have insufficient area to locate all of the components required in a circuit, two boards are mounted back-to-back and placed in a deep frame. Such back-to-back mounting of circuit boards is generally avoided since only one side of each board is accessible when assembled in the frame. Some special purpose packages, such as the sounder receiver (Fig. 15), are partitioned. On very tall and narrow boxes, brackets are added to the mounting flanges for reinforcement (Fig. 16). An attempt was made to use rectangular shaped boxes wherever possible, to keep the construction simple. Wedge shaped boxes like those for the receiver (Fig. 15) resulted when irregular circuit geometry and space made it necessary.

Three methods of making the boxes were considered: fabrication from sheet metal, milling, and casting. Casting was not considered practicable because the packages were not all the same size. Milling was not economical because of the amount of skilled labour involved. It was decided to fabricate the frames from 12 gauge sheet aluminum and then bend to shape.

The material used throughout was aluminum 3S half-hard, and it was chosen because of its light weight, good bending qualities, and its availability. Magnesium alloys are lighter than aluminum but were not used because their behaviour under high vacuum environment is questionable. Certain magnesium alloys have high vapour pressures and tend to sublime in a vacuum. The possibility that an alloy might sublime and redeposit on exposed circuitry could not be risked. Cadmium-plated screws were also avoided because of possible sublimation of the plating. Consequently, stainless-steel screws were used throughout.

4.1.4 Test of Box Design

To check the general design configuration and method of construction, a series of vibration tests were undertaken on typical boxes. Frames fitted with dummy circuit boards and components were used.

Some were potted and some were left unpotted so that the components could be observed. Test boxes were shaken to typical prototype vibration levels specified for the booster rocket. In addition, one tall, narrow, potted package was shaken to levels of over 20 g, through a frequency range of 5 to 3000 cps, in an attempt to precipitate mechanical destruction. No serious resonances or failures were observed.

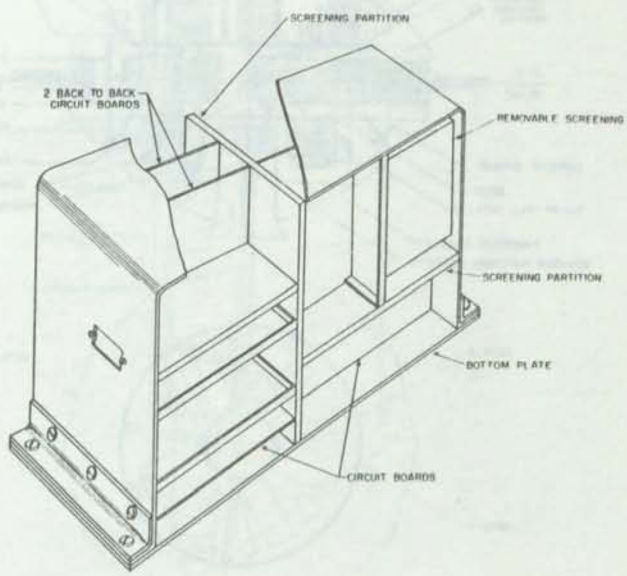

Fig. 15. Wedge Shaped Sounder Receiver Chassis.

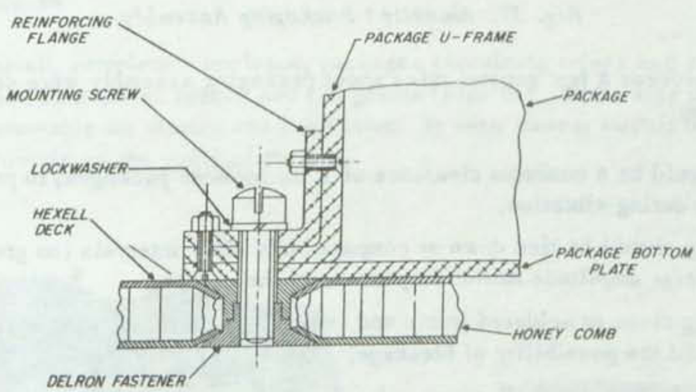

Fig. 16. Method of Mounting Packages to Satellite Deck.

4.1.5 Payload Assembly

In the Alouette satellite two decks made of hexcell sandwich structure were provided for mounting the electronic packages (Fig. 17). These were installed on the decks by means of Delron fasteners. A space was left between the decks for mounting the extendible antenna units and their associated drive-out mechanism.

Because of the large number of circuits and the limited deck space, packages were located by a more or less trial-and-error process to establish the best compromise between easy access, electronic compatibility, and balance.

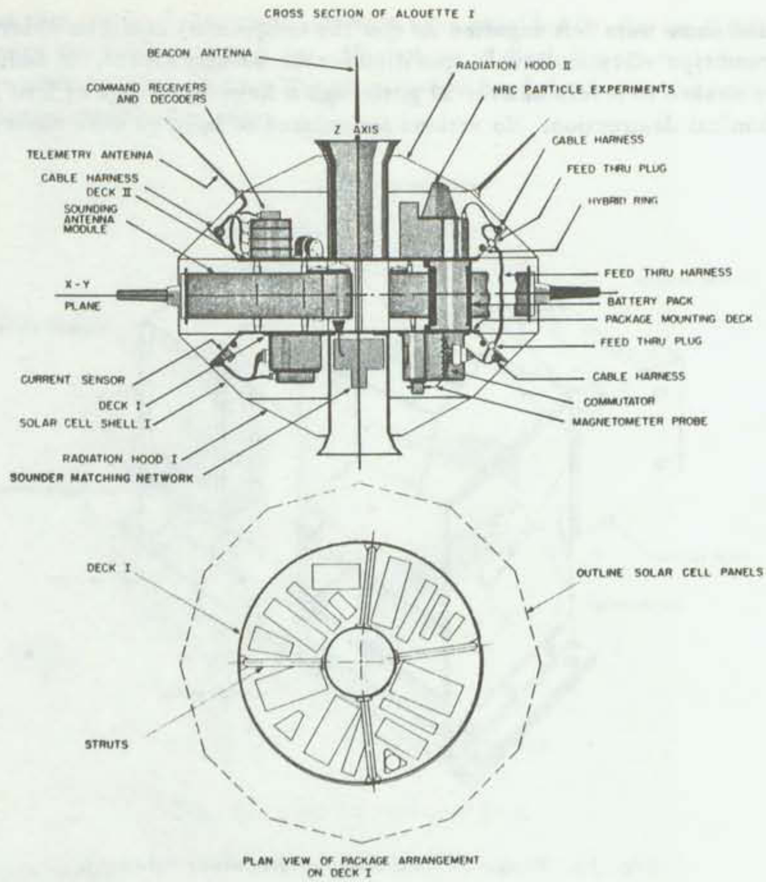

Fig. 17. Alouette I Packaging Assembly.

During this process a few general rules about packaging assembly were developed and found to be useful. These were:

(1) There should be a minimum clearance of ¼ in. between packages, to prevent contact between packages during vibration,

(2) All wiring should be tied down at comparatively short intervals (no greater than 6 in.) to prevent large amplitude motion in portions of the cables,

(3) All wiring close to soldered joints and connectors should be supported to minimize excessive flexing and the possibility of breakage,

(4) Some residual slack in all wires and cables is necessary to minimize tension caused by structural deformation under vibration.

4.2 Special Purpose Packages

4.2.1 Batteries

In the packaging of NiCd cells it was necessary to provide good heat conduction, support against cell bulging under internal gas pressure buildup, and isolation between individual cells. In addition, it was necessary to locate all batteries in the most temperature-stable position in the spacecraft.

These requirements were met by packaging the cells in machined aluminum castings (Fig. 18) and locating the castings in the centre section of the spacecraft between the sounding antennas (Fig. 17). This location provided the maximum temperature stability and also met balance and inertia requirements. The location of the castings also added to the strength and rigidity of the centre structure.

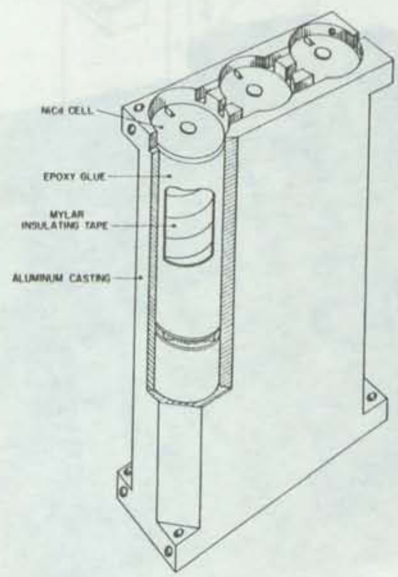

Fig. 18. Battery Pack.

4.2.2 Relay Boxes

Several very small, completely enclosed, packages containing relays and circuitry related to switching were fabricated from milled pieces and flat plates (Fig. 19). Where size permitted, the sides of the boxes were made removable for testing and inspection. In some cases, circuit boards were omitted by mounting components directly on the walls of the box.

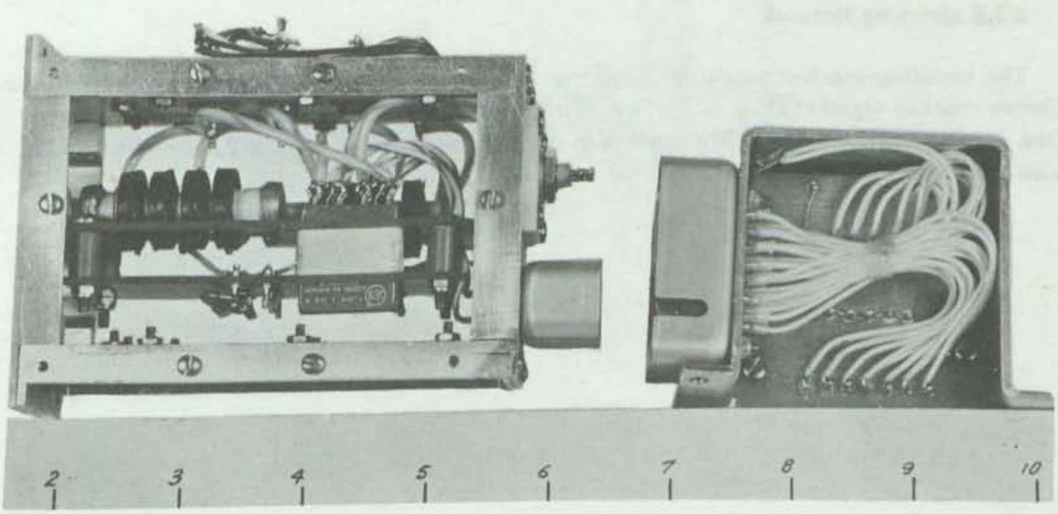

Fig. 19. Relay Box.

4.2.3 Commutators

The commutator circuitry was laid out on nine separate printed-circuit boards as these could not be packaged conveniently in the standard frame. They were potted individually in moulds and then strapped together by a removable framework (Fig. 20).

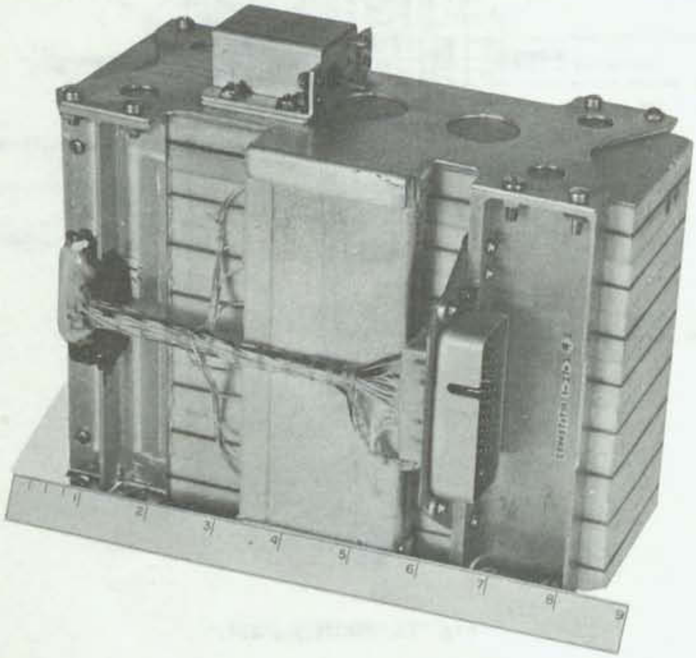

Fig. 20. Commutator Assembly.

4.2.4 Converters

Because the converters needed heavier shielding and required an arrangement for mounting large, heavy, toroidal transformers, these packages were built with an inward projecting flange and a side plate of heavier gauge to support the transformer (Fig. 21).

4.2.5 Matching Network

The sounding-antenna matching-network was made up of a group of RF coils mounted in individual milled boxes stacked together (Fig. 22). The entire cluster was potted into a single unit shaped to fit inside the spacecraft thrust tube. The insides of the individual boxes were not potted because of adverse effects on the electrical characteristics of the network.

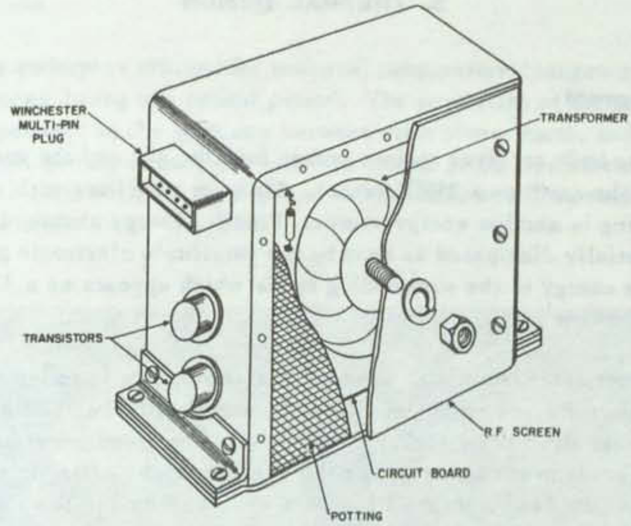

Fig. 21. DC to DC Converter.

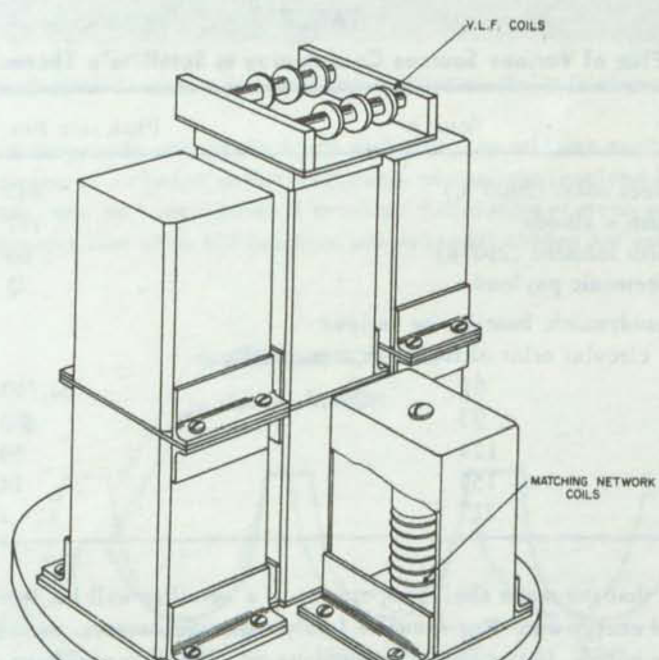

Fig. 22. Matching Network Package.

5. THERMAL DESIGN

5.1. The Thermal Environment

An earth-orbiting body receives radiant energy from the sun and the earth. The sun appears as a 6000°K heat source, and the earth as a 250°K source. Also, for satellites with altitudes below 200 statute miles, aerodynamic heating is another energy source. Finally, energy absorbed from the sun and stored in the battery system is partially dissipated as heat by the satellite's electronic payload. The orbiting vehicle, in turn, radiates energy to the surrounding space which appears as a 3.3°K sink, that is, for all practical purposes, at absolute zero.

Much of the direct solar radiation on the earth's atmosphere is reflected and scattered by the earth and its cloud cover. This reflected energy is called the earth's albedo. The albedo may represent from 27% to 54% of the direct received solar energy, depending on the cloud cover and, to a lesser extent, on the amount of snow and ice cover over northern and polar regions. Quite often, in thermal design problems, the albedo contribution is assumed constant at 40%, and also is assumed to have the same spectral distribution as solar radiation.

A relative comparison of flux rates of the various sources is given in Table 3.

TABLE 3
Heat Flux of Various Sources Contributing to Satellite's Thermal Energy

Source	Flux rate Btu/ft^2/hr
Direct solar (6000° K)	442
Earth's albedo	177
Earth infrared (250° K)	68
Electronic payload	Q
Aerodynamic heating for various circular orbit altitudes (h statute miles)	
62	62,700.
93	480.
124	59.
155	14.4
217	2.6

It is evident that the mean shell temperature of a satellite will be determined by the equilibrium between energy in and energy out. For Alouette I only radiative sources are important since the orbit altitude is 624 statute miles. Hence the instantaneous mean shell temperature may be obtained from

$$\frac{dT}{dt} = \frac{1}{mC}\left[\begin{matrix}\text{Direct} \\ \text{Solar}\end{matrix} + \begin{matrix}\text{Earth Reflected} \\ \text{Solar}\end{matrix} + \text{Earth} + Q - \begin{matrix}\text{Satellite} \\ \text{Re-radiation}\end{matrix}\right] \quad \ldots\ldots (7)$$

where mC is the outer shell heat capacity.

The radiation terms are defined by the well known Stefan Boltzmann's and Lambert's laws. Stefan Boltzmann's law concerns the energy absorbed and emitted by a body in terms of its optical properties and its absolute temperature. Lambert's law relates the source to the receiver system's geometry or, more specifically, to the view or shape factor.

5.2. Temperature Fluctuation

An earth Satellite undergoes orbital and seasonal temperature changes corresponding to the sun-to-shadow ratio it experiences during one orbital period. The proportion of the orbital path shielded from the sun by the earth is dependent on the geometry between orbit plane, earth, and sun (Fig. 23). The satellite receives a minimum amount of sunlight when its orbital plane lies on the earth-sun line, and a maximum amount when the orbital plane is most normal to the earth-sun line, such that the satellite receives full sunlight over its entire orbit.

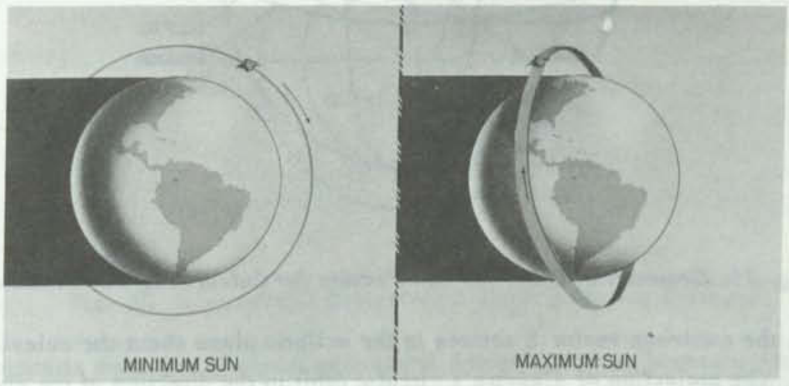

Fig. 23. Orbital Geometry for Maximum & Minimum Solar Illumination.

Since the satellite precesses around the earth with time, the relative earth, satellite, and sun geometry changes. This produces a change in the percentage of sunlight received by the satellite per orbit. This variation in 'per cent sun' constitutes a seasonal fluctuation of mean satellite temperature. Some typical curves for Alouette that show the per cent sun seasonal change for various launch hours are shown in Figure 24.

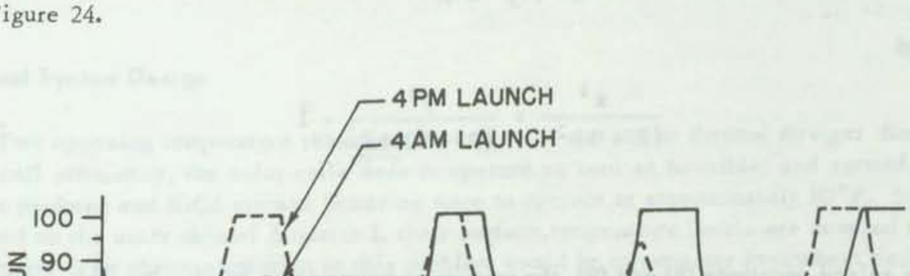

Fig. 24. Typical Per Cent Change for Two Launch Hours near Spring Equinox.

5.3 Calculation of Per Cent Sun

For Alouette I, the variation of per cent sun with time from launch was calculated by considering the earth orbit geometry shown in Figure 25, where I, J, K are earth-fixed coordinates axes, with I and J lying on the equatorial plane. The precession of the orbit plane around K is represented by rotation of its unit normal vector M around K with a velocity of 0.985°/day.

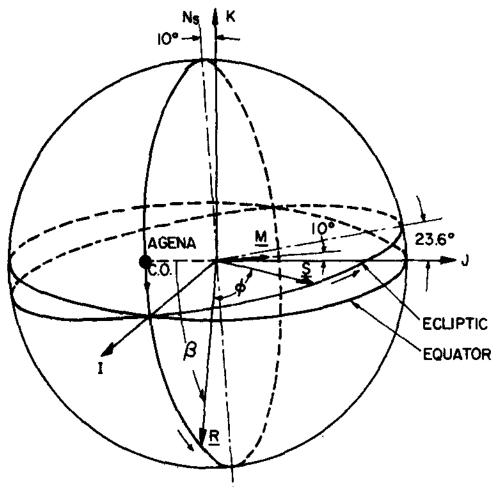

Fig. 25. Geometry of Orbit and Sun Vectors for Calculating Per Cent Sun.

Similarly, the earth-sun vector $\underline{S}$ rotates in the ecliptic plane about the celestial north, N_s, with a period of 1 year. The projection of Alouette's circular orbit in the direction of the sun (i.e., $\underline{S}$) is an ellipse with semi-major axis $R + L$ and semi-minor axis $(R + L)(\underline{M} \cdot \underline{S})$.

The terminator points are then obtained by calculating the interceptions between the projected orbit path ellipse and projected circular outline of the earth. Thus in terms of cartesian coordinates

$$x^2 + y^2 = R^2 \qquad \ldots\ldots (8)$$

for the earth and

$$\frac{x^2}{(R + h)^2} + \frac{y^2}{(R + h)\underline{M}\cdot\underline{S}} = 1 \qquad \ldots\ldots (9)$$

for the orbit.

Having solved equations (8) and (9), the terminator points (Fig. 26) T_1, T_2 define the chord of the shadowed arc and are used to determine the per cent of shadow per orbit simply by

$$\frac{1}{\pi} \sin^{-1} \frac{T_1T_2}{2(R+h)} (100\%) \qquad \ldots\ldots (10)$$

5.4 Vehicle Temperature Control

A selection of mean-shell-temperature levels is made possible by specifying the radiation absorption and emission characteristics and physical shape of the vehicle. More specifically, the solar absorptivity coefficient to infrared emissivity coefficient (a/e) ratio of the satellite surface finish mainly determines mean temperature.

Temperature control systems used in satellites may be either passive or active. Passive control systems employ surfaces with certain desirable optical characteristics. Usually, to obtain the desired optical finish, the satellite's outer skin is treated with ceramic flame sprays (Rokide), electro-plating, metallic oxide deposition or, more commonly, is just painted with specially prepared hard-baked epoxy or polyurethane-based pigmented enamels. The desired a/e ratio is obtained by selecting the proper proportion of high a/e (hot) and low a/e (cold) coatings for a given area.

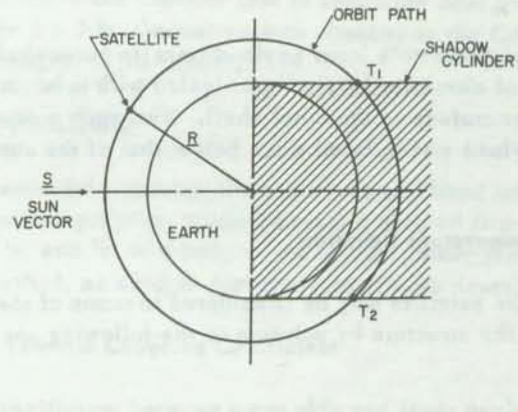

Fig. 26. Intercepts of Orbit Path & Earth's Shadow Cylinder.

Active systems make use of thermomechanical devices, such as bimetallic-strip activated vanes, or blinds, which vary the proportional exposure of high and low a/e surfaces. In addition, thermal switches are also used to provide conductive coupling between inner payload and outer shell.

Outer shell temperature ranges of less than 120°F are generally unattainable with passive designs. This spread can be reduced to about 40°F on well-designed active systems. Unfortunately, active systems lack the reliability afforded by the simplicity of passive designs. Alouette I was therefore designed with a passive system.

5.5 Thermal System Design

Two opposing temperature requirements had to be met in the thermal design: first, to gain maximum cell efficiency, the solar cells were to operate as cool as possible; and second, the inner instrument package and NiCd storage batteries were to operate at approximately 80°F. Since solar cells are mounted on the outer skin of Alouette I, their surface temperature levels are coupled to those of the inner package. The obvious solution to this problem would be to separate instrument package and solar cells by use of external extended 'paddles'. However, for reliability reasons, this was not desirable. Consequently, a compromise in cell and package temperature requirements was adopted.

From the solar cell point of view, the geometry adopted for Alouette I is more desirable than one that uses 'paddles', since the area of cells illuminated is nearly constant regardless of solar aspect. This feature enables an essentially constant power level in a randomly oriented satellite. The solar cell aspect ratio of Alouette I, defined as area of cells illuminated divided by total cell area, ranges between 1/3.8 to 1/4.2 over all possible orientations to the sun.

Since Alouette I was spin stabilized in orbit to avoid 'gravity capture' (where the long sounding antenna becomes earth pointing), temperature was conveniently averaged around the outer shell.

The desired passive control a/e was obtained by use of optically coated glass-covered solar cells on anodized aluminum (a/e = 0.95), and polished aluminum (a/e = 2.5).

5.6 Instrument Package Design

The Alouette I payload generates an average of ten watts of power which must be dissipated into space. For a 320 lb. satellite, this power dissipation is small, hence, a design which provides relatively poor radiative and conductive coupling between outer shell and inner payload is most effective in achieving the system requirements.

Radiative isolation of Alouette's inner payload from its outer shell was obtained by placing a radiation insulator consisting of aluminized mylar inter-leafed with unbonded glass paper (known as Kropschot blanket) on the inner surface of the outer shell. With such a design, the ambient temperature excursion around the inner payload was reduced much below that of the outer shell.

5.7. Generalized Satellite Temperature Equation

The temperature of the satellite may be considered in terms of the instantaneous heat balances associated with n regions of the structure by solution of the following set of n simultaneous differential equations.

$$\sum_{j,k=1}^{n} (C_{jk}(T_k - T_j) + r_{jk}(T_k^4 - T_j^4)) + D_j a_j S F_1 +$$

$$B_j a_j R S\, g(h,\phi)(\cos\theta) F_2 + E_j e_j \sigma T_j^4\, g(h,\theta) + Q_j -$$

$$A_j e_j \sigma T_j^4 - (mc)_j\, dT_j/dt = 0. \qquad \ldots\ldots (11)$$

where

j,k = reference regions
C = heat conduction coefficient
T = temperature
r = radiation coupling coefficient
D = area elements receiving solar radiation
B = area elements receiving albedo radiation
a = solar absorptivity coefficient
e = thermal emissivity coefficient
S = solar radiation constant
F_1 = 1, 0 step function for sunlight and shadow, respectively
F_2 = 1, 0 step function for albedo and albedo cut off at terminator point respectively
R = earth's albedo
g = transfer function of albedo and earth radiation to B
h = orbit altitude
ϕ = angle between satellite spin axis and orbit radius vector
θ = angle between sun vector and satellite orbit radius vector
T_e = earth's absolute temperature
mc = thermal capacity
Q = heat dissipated by inner payload
σ = Stefan - Boltzmann constant
t = time.

Before the solution for Alouette I could be carried out, the surface emissivities and thermal coupling coefficients had to be determined. As described in the following sections, these quantities must be determined experimentally.

5.8 Experimental Determination of Emissivity and Thermal Coupling

Spacecraft surface emissivity and the effective mean thermal coupling between inner payload and outer skin must be determined by experiment. For Alouette, tests of full-scale reference 'black' models in a vacuum chamber with carbon-arc solar simulators were used to establish emissivities, while the full-scale prototype structure was used in the chamber test to determine heat transfer coupling coefficients. All tests were carried out in the 6 x 7 ft. thermal-vacuum chamber at the Canadian Armament Research and Development Establishment (CARDE) at Valcartier, P.Q.

5.8.1 Measurement of Emissivity

The determination of emissivity through the use of standardized reference emissivity models, an original technique developed for this program, produced results of good first order accuracy. Without such a method, the determination of 'a' and 'e' of a body would involve rather precise measurements with optical pyrometric instruments. The method, as used in Alouette I design, is described in detail in Appendix I.

5.8.2 Measurement of Thermal Coupling Coefficient

The thermal coupling coefficient between outer skin and inner payload structure comprises two parts: a conduction and a radiation term. In general, it is almost impossible to determine how much each term contributes to the mean overall coefficient. As a result, a mean overall coupling coefficient, C, assumed a function of $T_1 - T_2$, was used for Alouette I. Thus, the first two terms of (11) may be written

$$C_{jk}(T_k - T_j) + r_{jk}(T_k^4 - T_j^4) \approx C(T_k - T_j) \qquad \ldots\ldots (12)$$

For Alouette I, C was measured experimentally in an evacuated test chamber by producing a temperature change on the outer shell of the prototype spacecraft with carbon arc lamps. For this test, no internal heat dissipation was used. The form of the two-node heat transfer equations was obtained by curve fitting to the experimental results. An illustration of the fitted result over the experimental is shown in Figure 27.

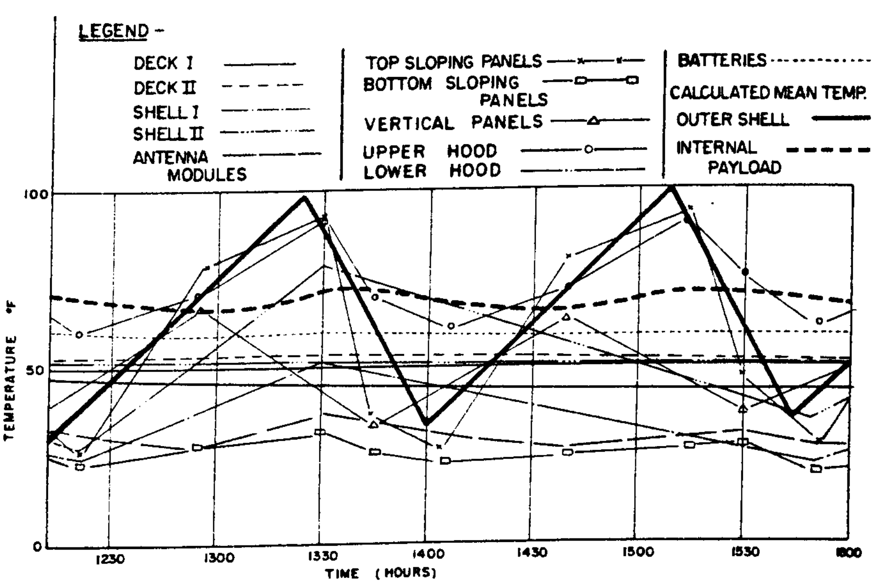

Fig. 27. Minimum Sun Thermal Simulation in Chamber.

The numerical value of C was found to be 13.3 Btu/°F. In addition, the assumption that C is a function of T_1-T_2 appeared a reasonable one to make for Alouette I. The fitted results shown in Figure 27 correspond to a mean test chamber wall temperature of -35°F. Using thermal capacities of 10 and 32 Btu/°F, respectively, for outer shell (including solar cell panels) and inner payload and structure, the temperatures of the outer shell, T_1, and of the inner mass, T_2, may be deduced as follows:

For the outer shell:

$$\frac{dT_1}{dt} = \frac{1}{(mc)_1} \left[C(T_1 - T_2) + \begin{matrix}\text{arc}\\\text{lamp}\end{matrix} + \begin{matrix}\text{chamber}\\\text{wall}\end{matrix} - \begin{matrix}\text{satellite}\\\text{radiation}\end{matrix} \right] \quad \ldots\ldots (13)$$

The known quantities are :

$(mc)_1 = 10$ Btu/°F,

T_1, T_2 = temperatures measured in the test,

Energy received by spacecraft from arc lamps:

$aA_pS = 1620$ Btu/hr,

Energy received by spacecraft from chamber wall:

$eA_T(V)\sigma T_w^{\,4} = 753$ Btu/hr,

where $a = 0.523$ absorptivity
- $e = 0.475$ emissivity
- $S = 442$ Btu/ft^2/hr. lamp output equivalent to one sun
- $A_p = 7$ ft^2 projected area of spacecraft to lamp
- $A_T = 28$ ft^2 total spacecraft surface area
- $V = 1$, view factor between spacecraft and chamber walls
- $T_w = 425$°R test chamber wall temperature
- $\sigma = 1.74\,(10^{-9})$ Btu/ft^2°R^4 hr Stefan-Boltzmann's constant.

For inner mass:

$$\frac{dT_2}{dt} = \frac{1}{(mc)_2} \quad C(T_1 - T_2) + Q \quad \ldots\ldots (14)$$

where $(mc)_2 = 32$ Btu/°F.

These result in the equations

$$\frac{dT_1}{dt} = 1.33\,(T_1 - T_2) + 162F_1 + 75.3 - 2.3(10^{-9})\,T_1^{\,4} \quad \ldots\ldots (15)$$

$$\frac{dT_2}{dt} = 0.416\,(T_1 - T_2) + Q \quad \ldots\ldots (16)$$

where T_1 = mean outer shell temperature
- T_2 = mean inner payload temperature
- F_1 = 1, 0 step function for sun and no sun respectively
- t = time
- Q = electronic equipment heat dissipation (set equal to zero for the test)

which describes the thermal behaviour of Alouette I in the thermal-vacuum chamber at CARDE.

With the coupling coefficient, C, determined, the solution of the orbit temperature equations now becomes possible.

5.9 Prediction of Temperature in Orbit

The average internal payload and external skin temperatures may be obtained by considering the system as a simple two-node problem; i.e., when $n = 2$ in equation (11) of the previous sections. This assumes a lumped internal package insulated from the outer shell, in the same fashion as in the vacuum test chamber case.

By assuming the spacecraft's configuration to be approximately spherical, and by using a mean albedo view factor, and then consequently applying the albedo contribution in step form, the following orbit temperature equations result from equations (11) and (12), where area elements D and B in (11) are now taken as one-quarter and one-half of the total surface area of Alouette, approximated as a sphere of radius 'r'.

$$(mc)_1 \frac{dT_1}{dt} = C(T_1 - T_2) + \pi r^2 aSF_1 + 2\pi r^2 g(h,\phi) \cos\theta \, aSF_2R$$

$$+ 2\pi r^2 e\sigma T_e^4 g(h,\phi) - 4\pi r^2 e\sigma T_1^4 \qquad \ldots\ldots (17)$$

$$(mc)_2 \frac{dT_2}{dt} = C(T_1 - T_2) + Q \qquad \ldots\ldots (18)$$

where πr^2 = 7 ft^2 projected cross sectional area of spacecraft,
a, e = absorptivity and emissivity,
S = 442 $Btu/ft^2/hr$ solar constant,
F_1 = 1, 0 sun, shadow step function as defined previously,
F_2 = 1, 0 albedo cut-off step function as defined previously,
$g(h,\phi)$ = satellite earth geometry factor in terms of altitude h and angle ϕ of line-of-sight vector between spacecraft and unit normal of reference surface area alement on earth,
R = 0.24 to 0.54 reflectivity factor of earth's surface that produces albedo,
θ = $\cos^{-1} \underline{P}\cdot\underline{M}$ angle between satellite radius vector $\underline{P}$ and sun vector $\underline{M}$ referred to earth centered coordinates,
T_e = 451°R earth black-body temperature in space,
Q = 10 watts average, 30 watts peak, electronic payload dissipation.

In carrying out the spacecraft design, limiting temperature cases were of primary interest. These corresponded to 100 per cent sun orbit and maximum earth shadowed, or 66 per cent sun orbit plus suitable combinations of power off, power on, high and low albedo. Intermediate cases, such as 80 per cent sun, were also checked out to ensure that the maximum heating condition did, in fact, correspond to the case of 100 per cent sun. It is noted that for high polar orbits, such as that of Alouette I, the albedo contribution is a minimum for a 100 per cent sun orbit.

5.9.1 Solution for 100 Per Cent Sun

Solution of the equations (17), (18) for the 100 per cent sun case is immediately evident, since this represents the steady state solution.

Thus for the outer shell:

$$C(T_1 - T_2) = \text{ 30 watts for 102.4 Btu/hr (coupled term),}$$
$$\pi r^2 aSF = \text{ 1620 Btu/hr (direct solar),}$$
$$2\pi r^2 e\sigma T_e^4 g(h,\phi) = \text{ 212 Btu/hr (earth radiation).}$$

About one-half of the total satellite surface area views the earth, thus $2\pi r^2$ is used for the earth radiation term. Also, it may be shown that $g(h,\phi)$ may be approximated by $(1 - \sqrt{2y})$, (ref. 6) where $y = h/r_o$

$$h = 625 \text{ sm orbit altitude}$$
$$r_o = 3995 \text{ sm mean earth radius}$$
$$2\pi r^2 Rg(h,\phi)\cos\bar{\theta}\, aS = 109 \text{ Btu/hr (albedo)}$$

and where

$$\cos\bar{\theta} = \overline{\underline{P}\cdot\underline{M}} \cong \frac{1}{2\pi}\int_0^{2\pi}\theta(\xi)\,d\xi = 0.153 \quad , \quad \theta(\xi) = \underline{P}(\xi)\cdot\underline{M}$$

The physical significance of the $\cos\bar{\theta}$ evaluation for both 100 per cent and 66 per cent suns is evident from Figure 28.

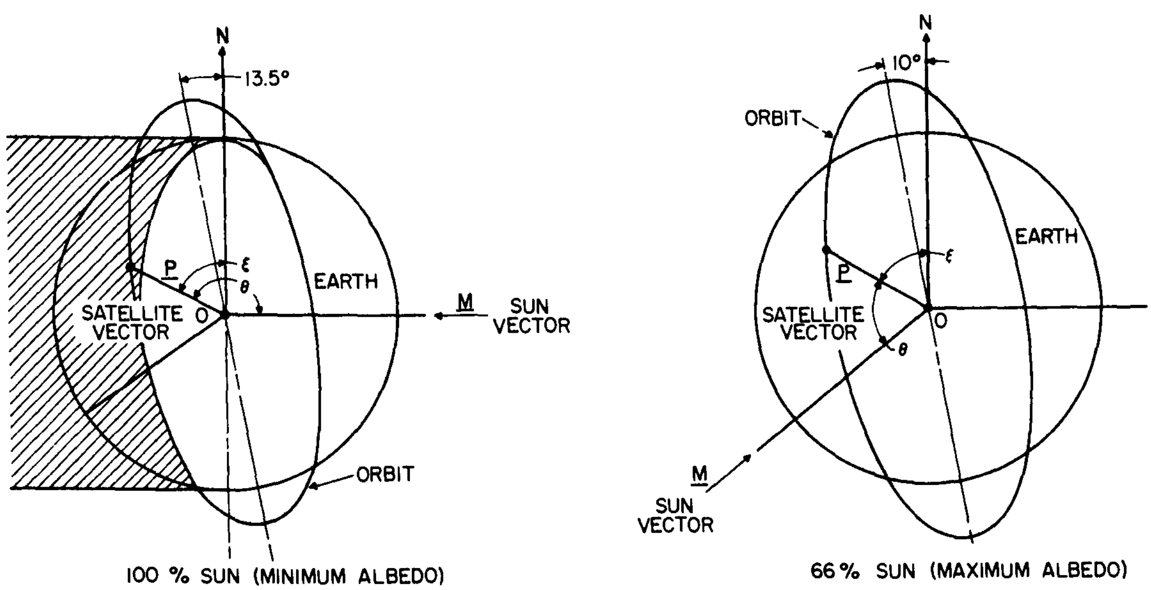

Fig. 28. Geometry of Satellite and Sun Vectors for Minimum and Maximum Albedo.

The albedo factor, R, was assigned a value of 0.5 for this maximum heating case.

With all the quantities thus known, the solution of equation (17), gives $T_1 = 545°R$ (85°F).

The inner payload temperature is from equation (18),

$$T_2 = 92.7°F.$$

5.9.2 Solution for 66 Per Cent or Minimum Sun

The albedo environment used for minimum sun is R = 0.36. In addition, $\theta(\xi)$ may for all practical purposes be approximated by $\cos\theta$ over the limits $-\frac{\pi}{2} \leq \theta \leq +\frac{\pi}{2}$ (See Fig. 28). The amount of albedo radiation that the satellite receives beyond the limits of $+\frac{\pi}{2}$ and $-\frac{\pi}{2}$ is insignificant. Consequently, $\cos\overline{\theta}$ may be evaluated as

$$\cos\overline{\theta} = \frac{1}{\pi}\int_{-\frac{\pi}{2}}^{+\frac{\pi}{2}} \cos\theta \, d\theta = \frac{2}{\pi} \qquad \ldots\ldots (19)$$

This results in an albedo of 324 Btu/hr, nearly three times greater than that of the 100 per cent sun case.

The step functions F_1, F_2 may be established in terms of time by simply considering the orbit earth-shadow geometry. As an illustration, $F_1 = 1$ for 1.15 hr and 0 for 0.60 hr during an orbital period of 1.75 hr.

Substituting numerical values into equations (17) and (18) and assuming no power generation (minimum temperature case) for $F_1 = F_2 = 1$ (Sun and Albedo), then

$$\frac{dT_1}{dt} = 1.33\,(T_1 - T_2) + 216 - 2.3(10^{-9})T_1^{\,4} \qquad \ldots\ldots (20)$$

$$\frac{dT_2}{dt} = 0.416\,(T_1 - T_2). \qquad \ldots\ldots (21)$$

For $F_1 = 1$, $F_2 = 0$ (Sun only),

$$\frac{dT_1}{dt} = 1.33\,(T_1 - T_2) + 183 - 2.3(10^{-9})T_1^{\,4} \qquad \ldots\ldots (22)$$

$\frac{dT_2}{dt}$ as in Equation (21).

For $F_1 = F_2 = 0$ (shadow)

$$\frac{dT_1}{dt} = 1.33\,(T_1 - T_2) + 21.2 - 2.3(10^{-9})T_1^{\,4} \qquad \ldots\ldots (23)$$

$\frac{dT_2}{dt}$ as in Equation (21).

These equations were solved by numerical integration and are shown in Figure 29(a). A comparison of the calculated results with those observed in orbit, Figure 29(b), shows good agreement in average temperature levels. Internal power dissipation, as the computations and observed data indicate, makes very little difference to the temperature limits exacted by the environment.

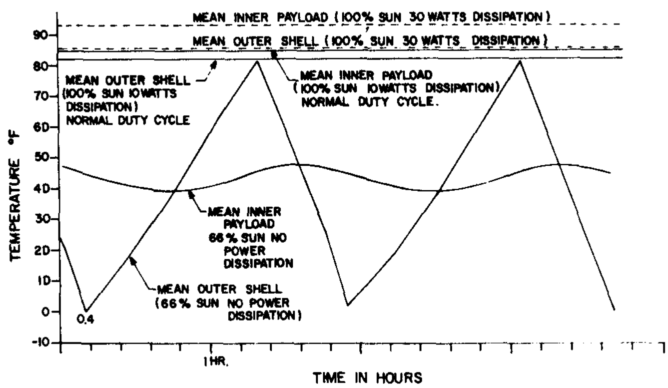

Fig. 29(a). S-27 Spacecraft Maximum and Minimum Predicted Temperatures in Space.

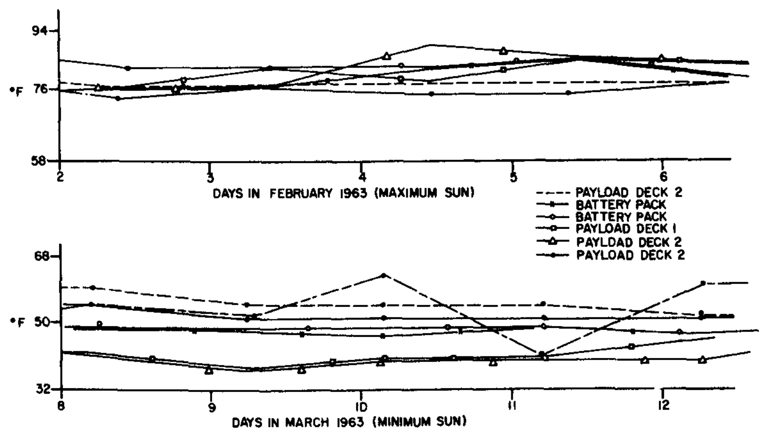

Fig. 29(b). Typical Recorded Orbit Temperatures of Alouette I.

6. THERMAL DISTORTION OF SOUNDING ANTENNAS

One inch diameter, 0.005 inch wall thickness, sounding antenna tubes of Alouette I are believed to distort in orbit as a result of differential heating. The manner in which such a distortion might occur is illustrated in Figure 30. To estimate the amount of distortion, the following analysis was performed and the results were then compared with thermal-vacuum test data on a sample of tubing.

6.1 Tube Temperature Equation

Consider the reference element of antenna tube, with associated geometric designation shown in Figure 31. The energy in and energy out of a control volume (Fig. 32) in the tube element is as follows :

For IN –

$aS(\delta\gamma\, R\, \delta L) \cos\beta \cos\gamma\, F$	solar radiation
$e(\delta\gamma\, R\, \delta L)\, Q_R$	internal radiation
$-Kb\,\delta L \left.\dfrac{\delta T}{R\,\delta\gamma}\right\rvert_{\gamma}$	circumferential conduction
$-Kb\,\delta\gamma R \left.\dfrac{\delta T}{\delta L}\right\rvert_{L}$	longitudinal conduction

For OUT

$2e(\delta\gamma\, R\, \delta L)\sigma\, T^4$	radiation from inner and outer surface
$-Kb\,\delta L \left.\dfrac{\delta T}{R\delta\gamma}\right\rvert_{\gamma + \delta\gamma}$	circumferential conduction
$-Kb\,\delta\gamma R \left.\dfrac{\delta T}{\delta L}\right\rvert_{L + \delta L}$	longitudinal conduction

The excess of energy in over the energy out is the amount stored in the control volume:

$$\rho\, c\, \delta\gamma\, \delta L\, \frac{\delta T}{\delta t}$$

Since the Energy In – Energy Out = Energy Stored, then dividing through by $\delta\gamma\,\delta L$ and taking the limit $\delta\gamma$, δL, $\delta t \to 0$, gives the tube temperature equation

$$\rho\, c\, \frac{\partial T}{\partial t} = \left(\frac{Kb}{R^2}\ \frac{\partial^2 T}{\partial \gamma 2} + R^2\ \frac{\partial^2 T}{\partial L^2}\right) + aS \cos\beta \cos\gamma F + eQ_R - 2e\sigma\, T^4 \qquad \ldots\ldots (24)$$

where
- S = solar constant
- ρ = mass density per unit length
- c = specific heat of antenna material
- k = thermal conductivity coefficient
- b = tube wall thickness
- R = tube radius
- T = temperature
- L = tube length
- γ,β = angles as defined in Figure 31
- a = absorptivity coefficient
- e = emissivity coefficient
- σ = Stefan-Boltzmann constant
- Q_R = internal radiation coupling function
- t = time
- F = 1,0 step function for sun and no sun respectively.

The internal radiation coupling function, Q_R, may be evaluated by considering the flux exchange between two reference area elements, dA and dA_1, as shown in Figure 33. For a solid angle $d\omega$, in the direction $\underline{r}$ joining dA_1 and dA, the energy flux radiated from dA_1 is:

$$e\sigma T_1^{\,4} \cos\phi_1\ \frac{d\omega_1}{\pi}$$

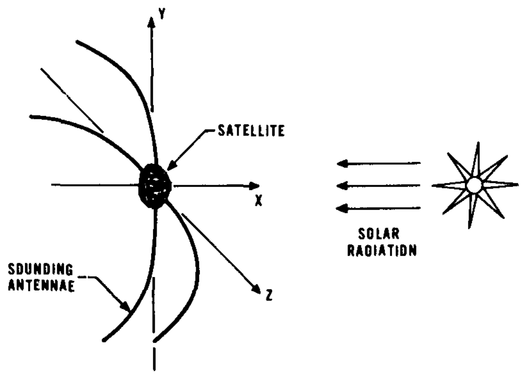

Fig. 30. Sketch of Antenna Distortion in Orbit.

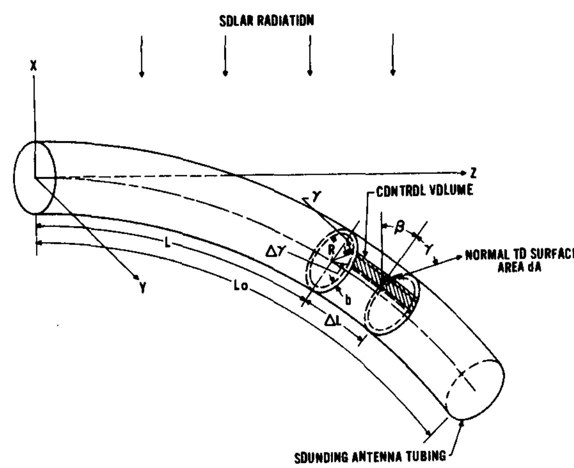

Fig. 31. Geometry of Antenna Distortion.

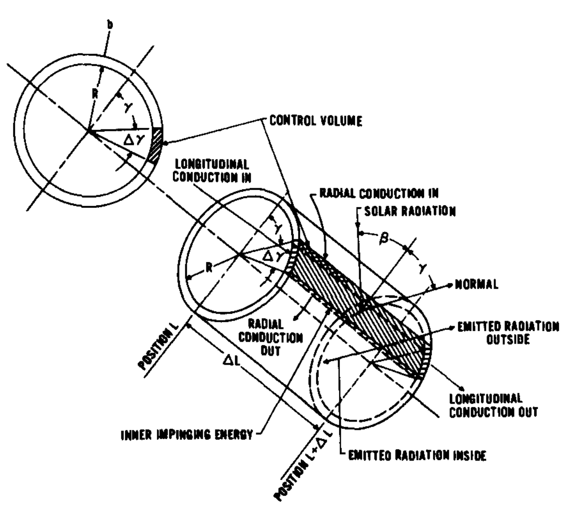

Fig. 32. Energy Balance of Control Volume of Tube.

with a solid angle $\frac{\cos\phi}{\underline{r}^2}\,dA$ subtended by dA.

The flux received by dA from dA_1 is then

$$dq = e\sigma T_1^{\,4}\;\frac{\cos\phi_1 \cos\phi}{\pi \underline{r}^2}\;dA_1\,dA, \qquad \ldots\ldots(25)$$

in which case,

$$dQ_R = \frac{dq}{dA} = e\sigma T_1^{\,4}\;\frac{\cos\phi_1 \cos\phi}{\pi \underline{r}^2}\;dA_1 \qquad \ldots\ldots(26)$$

and

$$Q_R = \int_{A_1} e\sigma T_1^{\,4}\;\frac{\cos\phi_1 \cos\phi}{\pi \underline{r}^2}\;dA_1 \cong e\sigma T_m^{\,4} \qquad \ldots\ldots(27)$$

where T_m is the mean antenna temperature.

The detailed solution of the integral is shown in Appendix II.

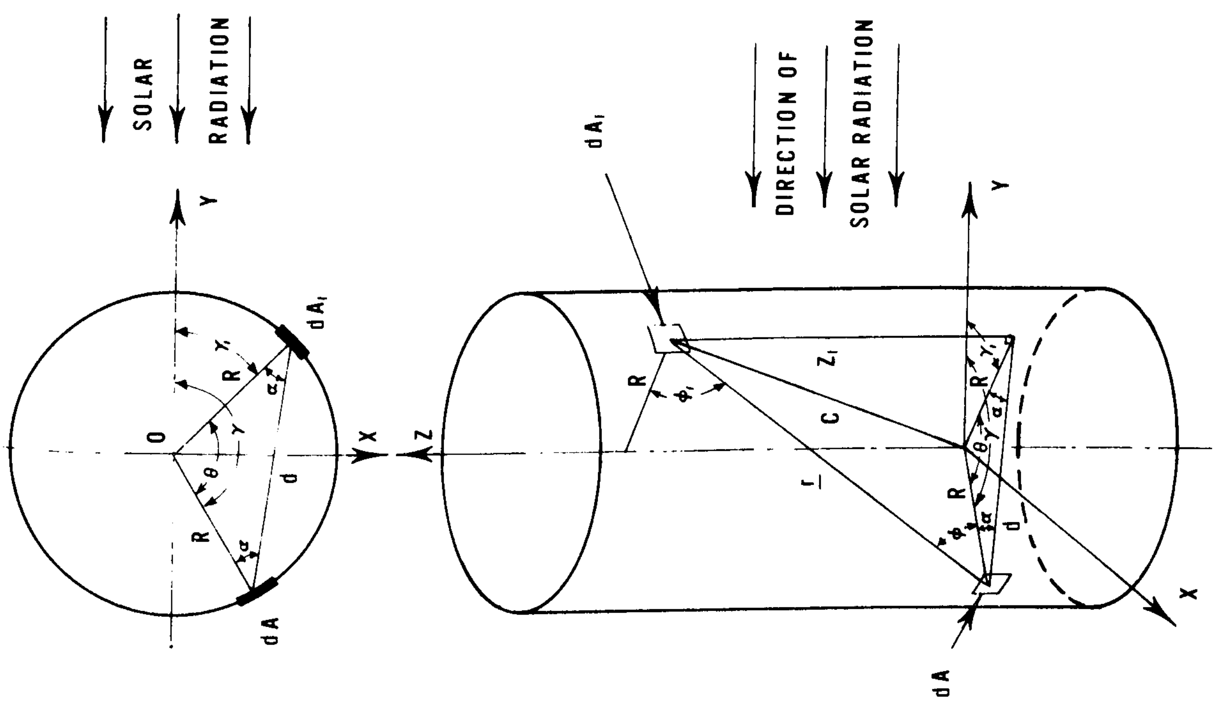

Fig. 33. Flux Exchange Inside Antenna Tube.

6.2 Tube Temperature Distribution

Before a solution of the general temperature equation was attempted, a few simple laboratory experiments were undertaken to assess the importance of certain parameters. A time response test carried out in air, using a row of flood lamps to heat an 8 ft. sample of steel antenna, showed that full thermal deflection was achieved in approximately 10 seconds.

The magnitude of thermal deflection can become large if the spin period of the spacecraft is longer than the antenna thermal response time. Since the spin period of Alouette I at orbit injection was about 43 seconds, antenna deflection was calculated for the steady-state case. (Since the writing of this report, a transient solution of this equation has become of interest because of considerations of spin decay interaction with the solar field.)

It was further established by test and sample numerical calculations that the longitudinal conduction term is small compared with the circumferential term, and hence may be neglected.

A solution of equation (24) for the case $\frac{\partial T}{\partial t} = 0$, $\frac{\partial^2 T}{\partial L^2} = 0$, with boundary conditions $\left.\frac{\partial T}{\partial \gamma}\right|_{\gamma=0} = \left.\frac{\partial T}{\partial \gamma}\right|_{\gamma=\pi} = 0$, and the assumption of a circumferential temperature distribution

$$T_1 = T_m + T_o \cos \gamma \qquad \ldots\ldots (28)$$

where T_o = maximum amplitude of temperature excursion, produces the result shown in Figure 34.

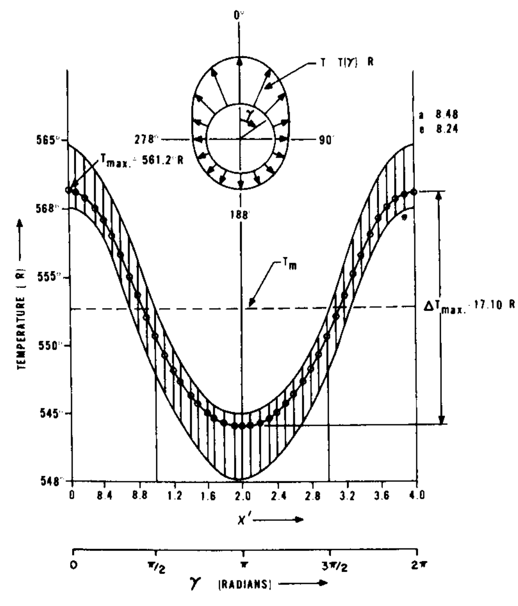

Fig. 34. Calculated Circumferential Temperature Distribution Around Tube.

The corresponding temperature distribution around a tube segment, as measured in a solar simulation test in a vacuum chamber for three positions of the seam, is shown in Figure 35. This shows reasonable agreement with calculation.

Finally, the difference in thermal expansion between extreme fibres of the tube results in the antenna deflection curve shown in Figure 36. As the length becomes large, the antenna asymptotically approaches the solar radiation vector.

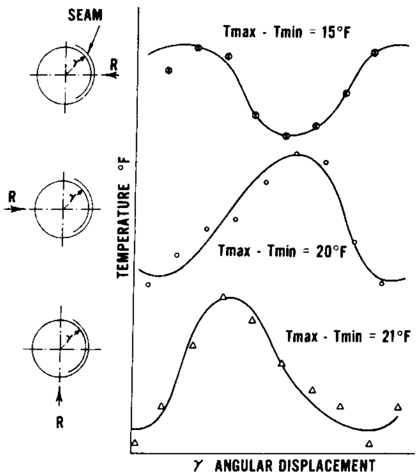

Fig. 35. Measured Circumferential Temperature Distribution Around Tube.

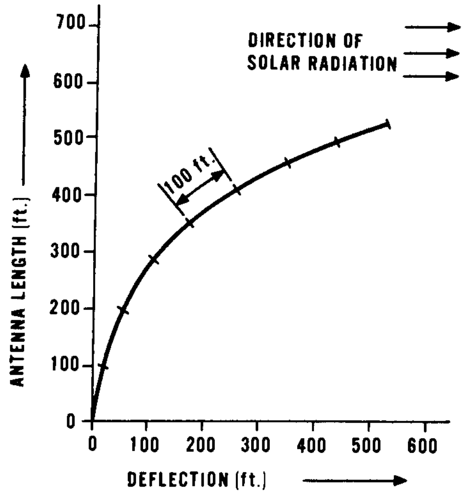

Fig. 36. Calculated Antenna Deflection.

7. ASCENT HEATING AND SPECIFICATION OF LAUNCH TIME

The selection of a suitable time to launch Alouette I was based primarily on thermal restraints. Launch times between 2:30 and 4:00 in the morning were to be avoided, since sunrise light conditions would saturate the Agena B pitch-down attitude-control horizon sensors.

For reasons of reliability, a time which would produce 70 to 80 per cent sunlight, and increasing sun orbit, was specified. This was to ensure against initial gross failure in case the thermal design failed to maintain desired temperatures at 100 per cent and minimum sun conditions. On the other hand, a relatively high and increasing per cent sun orbit was necessary to provide sufficient power to allow a maximum number of soundings to be taken at the outset, before any major failure of electronic systems might occur.

The desire to avoid overheating solar cell panels exposed to the direct sun during the shedding of the shroud in the ascent trajectory also governed the final choice of launch time. Since the satellite is not spinning during this phase of flight, solar heating is not equalized around its shell. Consequently, cell panels that face the sun become too hot unless the trajectory traverses the earth's shadow cylinder. The launch sequence and corresponding 90 nm altitude trajectory used for Alouette I are shown in Figures 37 and 38. From these, it may be seen that the aerodynamic shroud is ejected (Fig. 38) at about 260 sec after lift off at which time the altitude is about 86 nm. (The method of shroud separation is shown in Figure 39.) The exposed spacecraft and Agena B then coasts for approximately 48 minutes to orbit injection altitude and Agena second burn, and subsequent spin-up of the satellite.

The thermal environment to which Alouette I is exposed during this phase is shown in Figure 40. As in the previous section on heat transfer, the radiation terms are functions of the orbit and vehicle attitude geometry.

7.1 Time of Launch

To maintain solar cell temperatures below 200°F, it was necessary to avoid direct solar illumination for part of the ascent trajectory. Consequently a launch time, between 11:30 p.m. and 1:30 a.m. PST, which places the spacecraft initially in the earth's shadow prior to emergence into sunlight, was chosen (Fig. 41).

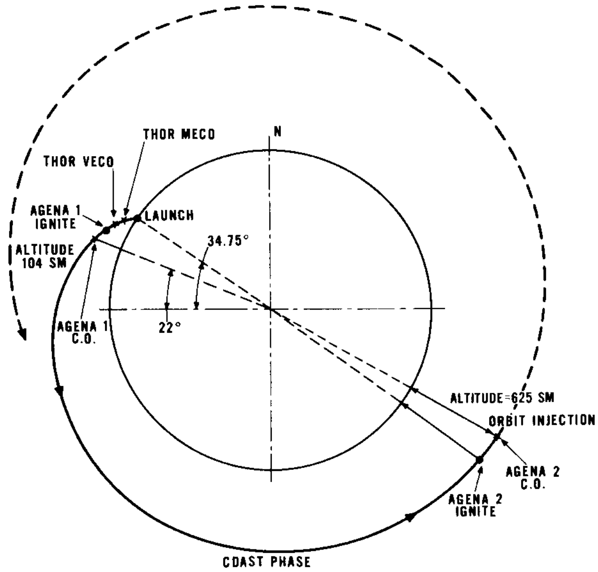

	LATITUDE	LONGITUDE	TIME (SEC.)
LIFT OFF	34 .75°N	120.62°	D
THOR MECO	33.76°N	120.47°	147.65
THDR VECO	33.52°N	120.41°	156.65
AGENA 1 IGNITE	32.6B°N	120.32°	107.57
AGENA 1 C.O.	22.76°N	118.78	419.9B

Fig. 37. Launch Sequence.

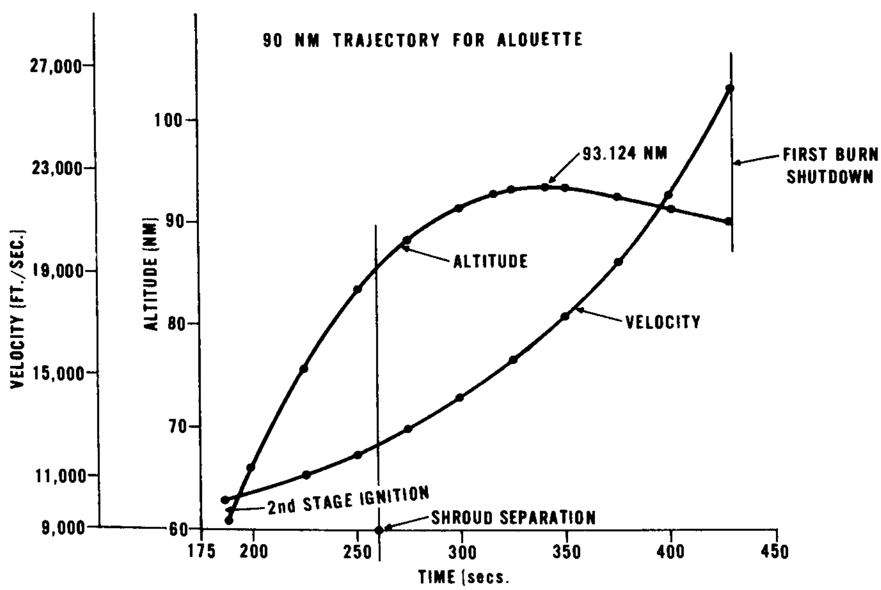

Fig. 38. Alouette I Launch Trajectory.

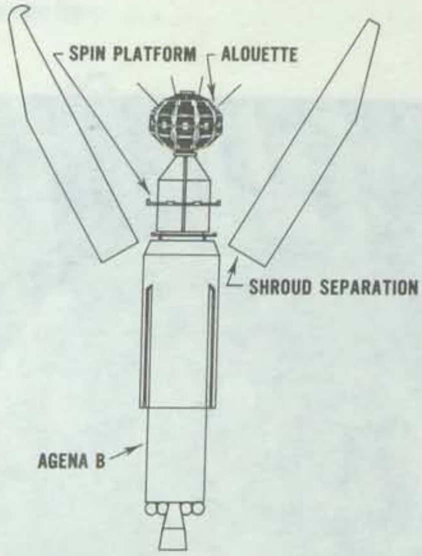

Fig. 39. Ejection of Agena B Shroud.

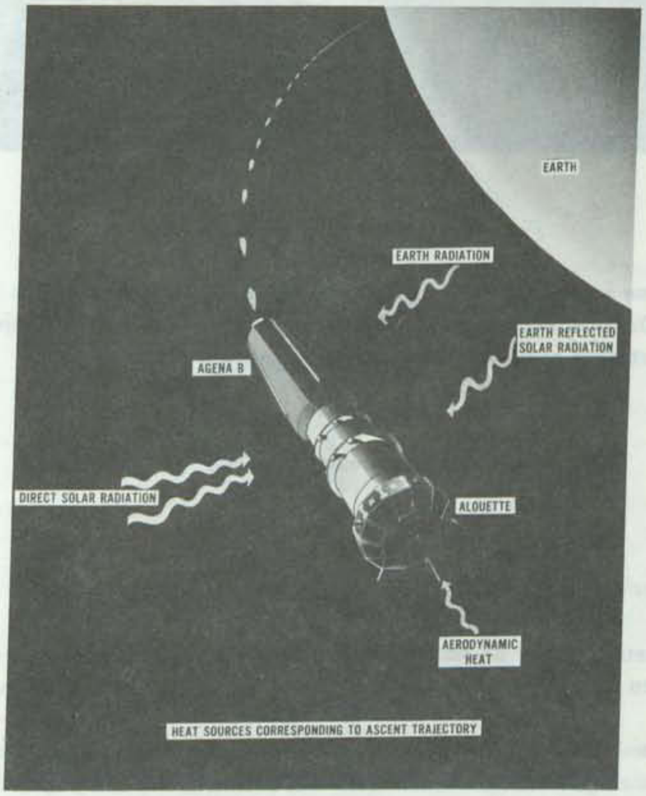

Fig. 40. Ascent Heat Sources.

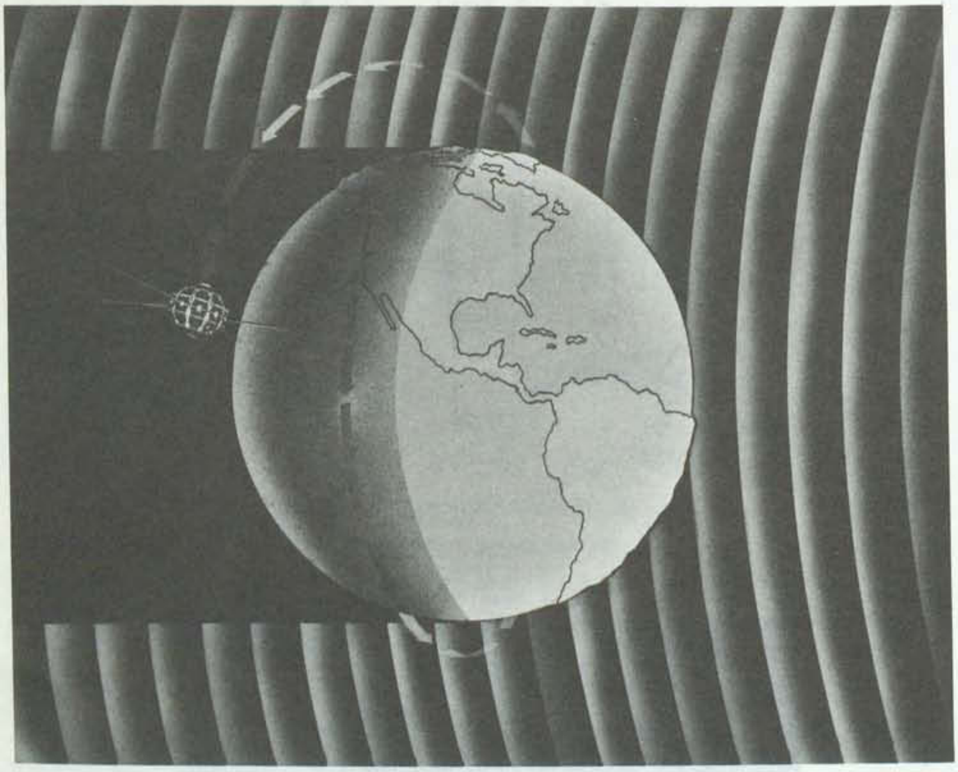

Fig. 41. Launch into Earth Shadow.

The length of time in shadowed flight was calculated by considering the sub-orbital elements starting with Agena 1 C.O. (first burn cut-off) altitude as perigee (140 nm) and injection altitude as apogee (625 nm). The pertinent geometry is shown in Figure 42, where

$\underline{M}$ = orbit unit normal vector

$\underline{R}$ = spacecraft position vector

$\underline{S}$ = sun vector

$\phi = \cos^{-1} \underline{R} \cdot \underline{S}$

β = orbit angle measured from Agena 1 C.O.

From this geometry, it may be shown that the altitude, y, of the earth's shadow cylinder in the plane of the orbit is given by

$$y = \frac{R_o (1 - \sin \phi)}{\sin \phi} \qquad \ldots\ldots (29)$$

where R_o = 3960 statute miles mean earth radius.

Neglecting the small effect of nodal regression of the orbit plane, as well as the motion of $\underline{S}$, the altitude, h, of the spacecraft is

$$h = \frac{a (1 - e^2)}{1 + e \operatorname{Cos} \beta} - R_o \qquad \ldots\ldots (30)$$

with corresponding flight time, t, given by:

$$t = \sqrt{\frac{a^3}{GM}}\ (E - e \text{ Sin } E) \qquad \ldots\ldots (31)$$

where $e = \frac{r_{max} - r_{min}}{r_{max} + r_{min}} = 0.0603$ orbit eccentricity

r_{max} = 4585 statute miles radius vector at apogee

r_{min} = 4064 statute miles radius vector at perigee

a = semi major axis

G = universal gravitational constant

M = mass of the earth

$$E = \sin^{-1} \frac{(\sqrt{1 - e^2} \sin \beta}{1 + e \cos \beta}$$

It may be seen from the foregoing that the flight time required for altitude h to equal shadow cylinder height y is dependent on the launch time or starting value of ϕ.

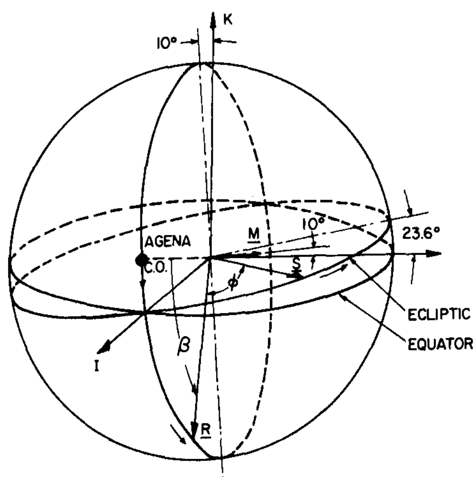

Fig. 42. Geometry Used for Calculating Length of Time in Shadowed Flight.

7.2 Aerodynamic Heating

Since the launch trajectory was into the earth's shadow, the initial dominant spacecraft heating source was due to rarefied gas or free molecular flow impact. At a nominal altitude of around 100 statute miles, the typical value of mass velocity, Ux, is 27,000 fps.

For free molecule flow, a conservative estimate of temperature based on a solar cell panel in 'flat plate' steady flow ($\theta = 90°$) may be obtained from the following for a diatomic gas:

$$\alpha (E_t + nkT_i) - \frac{5}{2} \alpha nkT_w - e\sigma T_w^4 = 0 \qquad \ldots\ldots (32)$$

In the above equation, E_t is the total molecular kinetic energy which strikes the cell panel per unit area, and per unit time. Thus

$$E_t = \frac{m}{2} N \int_{-\infty}^{\infty} \int_{-\infty}^{\infty} \int_{0}^{\infty} \underline{V}^2 V_x f'(V_x, V_y, V_z)\, dV_x\, dV_y\, dV_z \qquad \ldots\ldots (33)$$

where V_x, V_y, V_z = x, y, z, components of total molecular velocities
(i.e., $V = U + T$ where U = mass velocity
T = thermal velocity)

$\underline{V}$ = total molecular velocity vector

$f'(V_x, V_y, V_z)$ = Maxwell's velocity distribution function for total velocities = $e^{-\beta^2 (T_x^2 + T_y^2 + T_z^2)}$,

where m = mass of one molecule,
N = no. of molecules per unit volume.

Carrying out the integration produces

$$E_t = \left[nm \frac{U^2}{2} + \frac{1}{2\beta^2} \left\{ 1 + \frac{1 + 3/2\sqrt{\pi}\beta U_x [1 + \mathrm{erf}(\beta U_x)]_e \beta^2 U_x^2}{1 + \sqrt{\pi}\beta U_x [1 + \mathrm{erf}(\beta U_x)]_e \beta^2 U_x^2} \right\} \right] \qquad \ldots\ldots (34)$$

where $\beta = \frac{1}{Vm}$ Reciprocal of most probable molecular speed V_m, and

$$V_m = \sqrt{\frac{2gR_1T}{M}} \qquad \ldots\ldots (35)$$

where R_1 = universal gas constant (1544 ft-lb mole°R)

T = absolute temperature (°R)

g = gravitational acceleration

M = molecular weight (lb/lb mole)

$$\mathrm{erf}(\beta U_x) = \frac{2}{\sqrt{\pi}} \int_0^{\beta U_x} e^{-x^2} dx \qquad \ldots\ldots (36)$$

$$n = N \left\{ \frac{e^{-\beta^2 U_x^2}}{2\sqrt{\pi}\beta} + \frac{U_x}{2} [1 + \mathrm{erf}(\beta U_x)] \right\} \qquad \ldots\ldots (37)$$

which gives the total number of molecules striking the panels per square ft., per second.

The term nkT_i accounts for the thermal energy of incident molecules at temperature T_i, while $5/2\, nkT_w$ accounts for the energy of the molecules at the wall temperature T_w; $e\sigma T_w^4$ is the usual radiation loss term, and k is Boltzmann's constant.

Further, the accommodation coefficient, a, is assumed to be unity. This assumes that molecules adjust themselves to the cell panel temperature during the time they are in contact.

For the case in point:

$$U_x = 27{,}000 \text{ fps}$$
$$e = 0.596 \text{ emissivity}$$
$$T_i = 1385°R$$
$$V_m = 2182 \text{ fps}$$
$$m = 3.28(10^{-27}) \text{ slugs/molecule}$$
$$n = 2.59(10^{-19}) \text{ molecules/ft}^2 \text{ sec}$$
$$k = 5.66(10^{-24}) \text{ ft lb/°R molecule}$$
$$E_t = 31.5 \text{ ft-lb/ft}^2 \text{ sec}$$
$$nkT_i = 0.203 \text{ ft-lb/ft}^2 \text{ sec}$$
$$\frac{5}{2} nkT_w = 3.66(10^{-4}) T_w \text{ ft-lb/ft}^2 \text{ sec}$$
$$e\sigma T_w^4 = 2.23(10^{-10}) T_w^4 \ .$$

The solution of the equation for T_w results in $T_w = 615°R$, or 155° F, which is the temperature rise of the forward Alouette I solar cell panel as a result of free molecule flow heating.

A confirmation of the calculated ascent temperature was not possible because the spacecraft was beyond ground telemetry station range. Operation of the satellite in orbit indicated no permanent damage to any part of the system because of high temperatures.

8. ALOUETTE I DYNAMICS

8.1 Forces on Sounding Antennas during Extension

At the instant of antenna extension, Alouette I was supposed to be rotating about its spin axis at a design speed of 165 rpm. To calculate the maximum stresses in the antenna tube during extension, the equation of motion of the antenna tube had to be considered.

Reference is made to an element of antenna, dr, as shown in Figure 43. The vector $\underline{r}$ of the antenna may be treated in terms of the classical rate of change of a vector in a rotating frame. Hence $\underline{r}$ is referred to a set of space fixed coordinate axes S, and if S' is defined as a set of moving axes (body fixed) with unit vectors $\underline{i}$, $\underline{j}$, $\underline{k}$, and with angular velocity ω with respect to S, then:

$$\underline{r} = r_1 \underline{i} + r_2 \underline{j} + r_3 \underline{k}$$

and

$$\frac{d\underline{r}}{dt} = \frac{\partial \underline{r}}{\partial t} + \underline{\omega} \times \underline{r} = \underline{v} \text{ (velocity)} \qquad \ldots\ldots (38)$$

where

$$\frac{\partial \underline{r}}{\partial t} = \frac{\partial r_1}{\partial t} \underline{i} + \frac{\partial r_2}{\partial t} \underline{j} + \frac{\partial r_3}{\partial t} \underline{k}$$

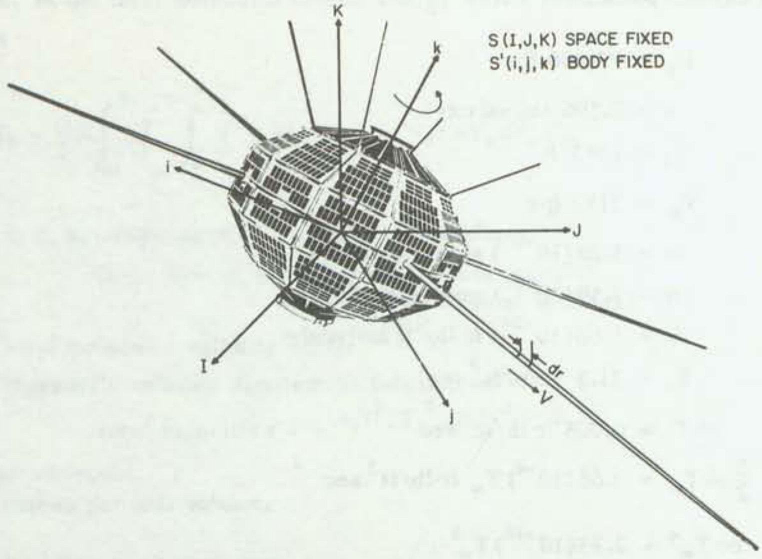

Fig. 43. Reference Axes Used for Alouette I Antenna Extension.

The acceleration of the system is obtained directly by differentiating the velocity vector $\underline{v}$. Thus:

$$\frac{d\underline{v}}{dt} = \underline{a} = \frac{\partial \underline{v}}{\partial t} + \underline{\omega} \times \underline{v} \qquad \ldots\ldots (39)$$

and

$$\frac{\partial \underline{v}}{\partial t} = \frac{\partial^2 \underline{r}}{\partial t^2} + \underline{\omega} \times \frac{\partial \underline{r}}{\partial t} + \underline{r} \times \frac{\partial \underline{\omega}}{\partial t}$$

$$\underline{\omega} \times \underline{v} = \underline{\omega} \times \frac{\partial \underline{r}}{\partial t} + \underline{\omega} \times (\underline{\omega} \times \underline{r}) .$$

Therefore

$$\underline{a} = \frac{\partial^2 \underline{r}}{\partial t^2} + 2(\underline{\omega} \times \frac{\partial \underline{r}}{\partial t}) + \underline{r} \times \frac{\partial \underline{\omega}}{\partial t} + \underline{\omega} \times (\underline{\omega} \times \underline{r}) \qquad \ldots\ldots (40)$$

where

$\frac{\partial^2 \underline{r}}{\partial t^2}$ = acceleration due to non-uniform antenna extension (assumed to be negligible)

$2(\underline{\omega} \times \frac{\partial \underline{r}}{\partial t})$ = coriolis acceleration

$\underline{r} \times \frac{\partial \underline{\omega}}{\partial t}$ = tangential acceleration

$\underline{\omega} \times (\underline{\omega} \times \underline{r})$ = centrifugal acceleration

$\frac{\partial \underline{r}}{\partial t}$ = rate of antenna extension.

Applying the component accelerations on the antenna element in the directions indicated by the foregoing vector terms (e.g., coriolis component is normal to $\underline{\omega}$ and $\frac{\partial r}{\partial t}$) as shown in Figure 44, gives the following load distribution P(r) along the antenna, neglecting centrifugal effects.

$$P(r) = -(2v\omega + r\dot{\omega})\rho \, dr \text{ ....in scalar form} \qquad \ldots\ldots (41)$$

where

$$v = \frac{\partial r}{\partial t}$$

ρ = mass per unit length.

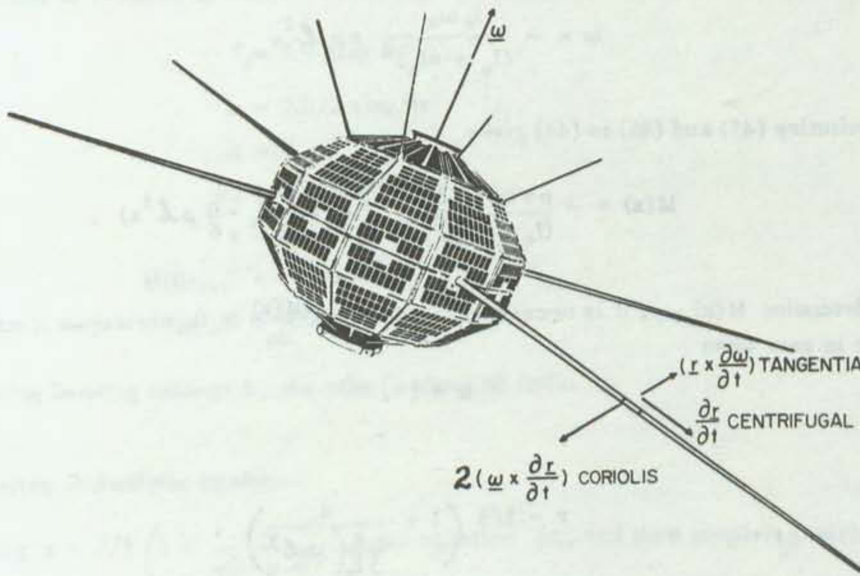

Fig. 44. Accelerations on Antenna Element.

8.2 Maximum Bending Moment on Antennas

From structural theory, the shear distribution S(r) for a beam of length ℓ is:

$$S(r) = \int_o^r p(r)dr = -\rho[2v\omega(\ell - r) + (1/2)\dot{\omega}(\ell^2 - r^2)], \qquad \ldots\ldots (42)$$

and the bending moment M(r) is:

$$M(r) = \int_o^r S(r)dr = -\rho(\ell - r)^2[v\omega + (1/6)\dot{\omega}(2\ell + r)] \qquad \ldots\ldots (43)$$

Putting $x = r/\ell$, where $0 \le x \le 1$

$$M(x) = -\rho\ell^2(1-x)^2\{[v\omega + 1/6\,\dot{\omega}\ell(2+x)]\} \; . \qquad \ldots\ldots (44)$$

From the law of the conservation of angular momentum,

$$\omega = \frac{I_o \omega_o}{I_o + nI_a} \qquad \ldots\ldots (45)$$

where I_o = initial moment of inertia about spin axis

ω_o = initial spin rate

n = number of antenna tubes

$I_a = 1/3\,\rho\,\ell^3$ moment of inertia of antenna about spin axis at any time 't'.

Also

$$\dot{\omega} = -\frac{I_o \omega_o}{(I_o + nI_a)^2}\, n\rho\ell^2 v \quad . \qquad \ldots\ldots (46)$$

Substituting (45) and (46) in (44) gives

$$M(x) = -\frac{\rho v \omega_o I_o \ell^2}{(I_o + \frac{n}{3}\rho\ell^3)^2}\,(\ell - x)^2\,(I_o - \frac{n}{6}\rho\ell^3 x) \quad . \qquad \ldots\ldots (47)$$

To determine $M(x)_{max}$, it is necessary to examine $\frac{dM(x)}{dx} = 0$, whereupon it may be shown that the derivative is zero when

$$x = 1 \;, \qquad \ldots\ldots (48)$$

and when

$$x = 1/3\left(1 + \frac{4}{\frac{n}{3I_o}\rho\ell^3}\right) . \qquad \ldots\ldots (49)$$

The minimum bending moment occurs at $x = 1$, at the tip where bending is zero. Hence the maximum is given by (49), in which x, for practical values (positive) of $\frac{n}{3I_o}\rho\ell^3$, is always greater than 1/3. The condition for a maximum to occur is: (Ref. 7)

$$\frac{1}{3}\left(1 + \frac{4}{\frac{n}{3I_o}\rho\ell^3}\right) < 1$$

or

$$\frac{n}{3I_o}\rho\ell^3 > 2$$

$$nI_a > 2I_o \quad . \qquad \ldots\ldots (50)$$

When, during extension, the antenna length out is such that equation (50) is not yet satisfied, no analytic maximum exists and the maximum bending occurs at the root (or at $x = 0$), since $M(x)$ increases monotonically from the zero value at the tip. The maximum bending must be calculated for both the cases of

$$x = 0$$

and

$$x = \frac{1}{3}\left(1 + \frac{4}{\frac{n}{3I_o}\rho\ell^3}\right) .$$

8.2.1 Maximum Bending at the Root

Substituting $x = 0$ in equation (44) produces

$$M(0)_{max} = -0.582\, v\, \omega_o\, \rho^{1/3} \left(\frac{I_o}{n}\right)^{2/3} \quad \ldots\ldots (51)$$

The corresponding length at which the bending moment occurs is:

$$\ell = \left(\frac{3\, I_o}{2\rho\, n}\right)^{1/3} \quad \ldots\ldots (52)$$

For the case of Alouette I, with the following numerical values,

$$I_o = 7.9 \text{ slug ft}^2$$

$$\rho = 0.072 \text{ slug/ft}$$

$$n = 4$$

$$\omega_o = 17.3 \text{ r/sec}$$

$$v = 0.2 \text{ ft/sec}$$

one obtains

$$M(0)_{max} = -15.82 \text{ in-lb,}$$

$$\text{at } \ell = 3.46 \text{ ft.}$$

The buckling bending moment for the tube is about 60 in-lb.

8.2.2 Bending at Analytic Maximum

Substituting $x = 1/3 \left(1 + \dfrac{4}{\frac{n}{3 I_o} \rho \ell^3}\right)$ into equation (44), and then simplying, yields

$$M(x)_{max} = 0.038\, v\, \omega_o\, \rho^{1/3}\, \frac{I_o}{n}^{2/3} = 1.03 \text{ in-lb} \quad \ldots\ldots (53)$$

and the corresponding length at which the bending moment occurs is

$$\left(76\, \frac{I_o}{\rho n}\right)^{1/3} = 12.8 \text{ ft.}$$

8.3 Satellite Spin Behaviour

The abnormally rapid spin decay of Alouette I has been a subject of continuing study during the course of the program. The well known mechanisms, such as interaction with the earth's geomagnetic field, neutral particle, and charged particle drag, were insufficient to explain the spin decay of Alouette I. As a result, the study of non-rigid bodies in orbit, including such mechanisms as large structural flexures and energy dissipation modes, was pursued.

The satellite was initially spun up to 165 rpm prior to separation, but as shown in Figure 45, it actually separated at 120 rpm due to a malfunction of the booster spin-up hardware. Upon separation, micro-switches located in the satellite's thrust-tube were closed to energize the sounding antenna drive-out electric motor. The spin rate decreased to 1.4 rpm at completion of antenna extension. The observed spin decay since that time is shown in Figure 46.

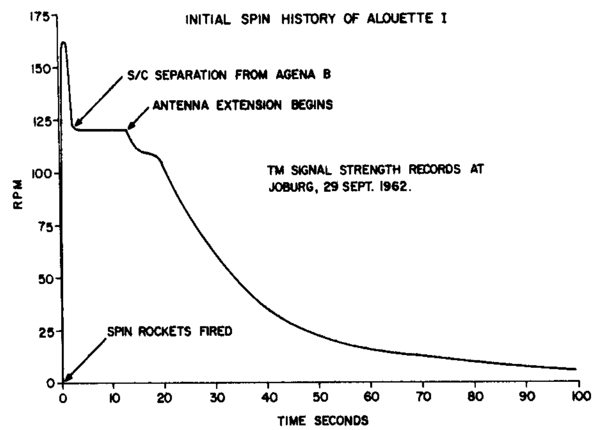

Fig. 45. Initial Spin History of Alouette I.

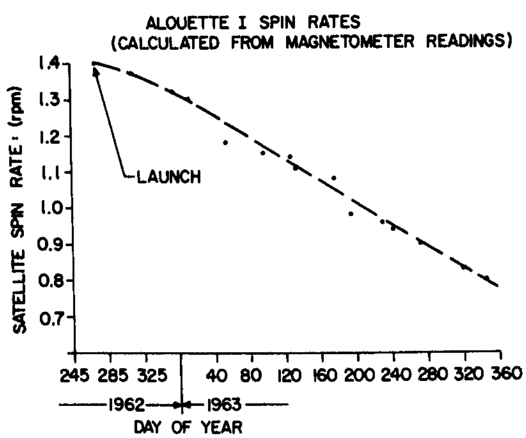

Fig. 46. Observed Spin Decay of Alouette I.

8.3.1 Spin Interaction with Geomagnetic Field

Spin damping contributions from neutral and charged particle drag were found to be negligible. However, geomagnetic interaction that causes eddy current and magnetic hysteresis losses for a rigid rotating body does contribute and was calculated.

The spacecraft is a conducting shell rotating in the earth's magnetic field. The manner in which currents are induced in the shell to cause I^2R losses may be visualized by considering a differential ring element on the spacecraft as shown in Figure 47.

For an orbit inclination of 80°, the average horizontal and vertical components of the earth's field at the surface of the earth is given by:

$$\overline{H_h} = 0.304\left(\frac{180}{80^\circ \pi}\right)\int_0^{80^\circ} \cos\phi \, d\phi = 0.214 \text{ gauss} \qquad \ldots\ldots (54)$$

$$\overline{H}_v = 0.304 \left(\frac{360}{80^\circ \pi}\right) \int_0^{80^\circ} \sin\phi \, d\phi = 0.360 \text{ gauss} \qquad \ldots\ldots(55)$$

where ϕ is given by equation (70)
The resultant is

$$\overline{H}_o = \sqrt{\overline{H}_h^{\,2} + \overline{H}_v^{\,2}} = 0.419 \text{ gauss.}$$

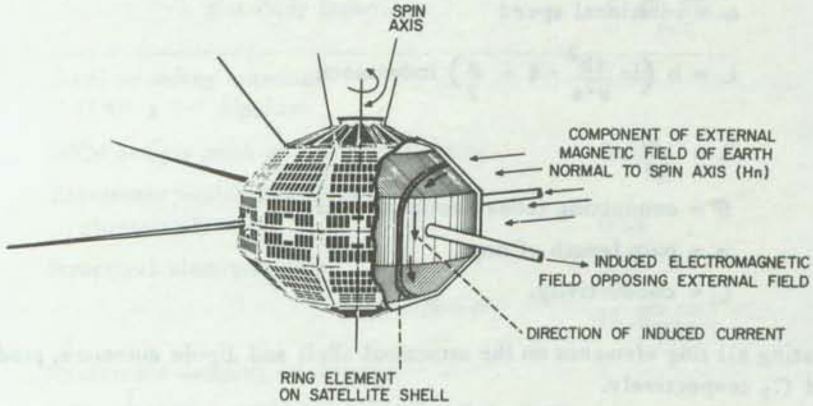

Fig. 47. Generation of Eddy Current Losses in Alouette Structure.

The corresponding mean total magnetic field at Alouette I altitude is calculated in terms of orbit eccentricity 'e' and altitude 'a', in earth radii.

Thus $$\overline{H} = \overline{H}_o \left[\frac{(1-e^2)^{3/2}}{a^3}\right] = 0.270 \text{ gauss} \qquad \ldots\ldots(56)$$

Before the induced current in the ring element can be calculated the component of $\overline{H}$ normal to the spin axis is required.

$$\overline{H}_n = \overline{H}\sqrt{\frac{(\overline{H}_v/\overline{H}_h)^2\,\overline{\sin}^2\alpha + \overline{\sin}^2\theta}{1+(\overline{H}_v/\overline{H}_h)^2}} = 0.183 \text{ gauss} \qquad \ldots\ldots(57)$$

$$\overline{\cos}\,\theta = \frac{2}{\pi}\int_0^{\frac{\pi}{2}} \frac{\cos M dM}{\sqrt{1+\cot^2 i \sec^2(180-\omega+M)}} = 0.626 \qquad \ldots\ldots(58)$$

where

α = angle between $\overline{H}_v$ and spin axis

θ = angle between $\overline{H}_h$ and spin axis

$\overline{\sin}\,\alpha = 2/\pi$ for a circular orbit

M = mean anomaly of orbit

i = orbit inclination (80°).

With the evaluation of $\overline{H}_n$, the resulting torque on the ring element on the spacecraft shell may be computed:

$$\Delta C = \frac{A^2 \mu^2 \overline{H}_n^2 \omega}{2(L^2 \omega^2 + R^2)} \left(R + \sqrt{L^2 \omega^2 + R^2}\right) \text{ dynes} \qquad \ldots\ldots (59)$$

where

A = enclosed area

μ = effective magnetic permeability

ω = rotational speed

$L = b\left(\ln \frac{4b^2}{\pi^2 a} - 4 + \frac{\mu}{2}\right)$ inductance

$R = \frac{b}{\zeta s}$

S = conducting cross sectional area

b = path length of ring

ζ = conductivity.

Integrating all ring elements on the structural shell and dipole antennas, produces eddy damping torques C_1 and C_2 respectively.

$$C_1 = \zeta \mu^2 \overline{H}_n^2 \omega h^4 K \left[\frac{\pi}{4}\left(\frac{3}{k} + 1 + \frac{K}{2}\right) - \left(1 + \frac{1}{2 - 2K}\right) - \frac{3 - 4K}{2K(1 - K)\sqrt{K^2 - 1}} \ln\left(K + K^2 - 1\right) \right] \Delta r = 8.5\, \omega \text{ dyne-cm} \qquad \ldots\ldots (60)$$

for the structural shell

where

$K = \frac{2r}{h}$

r = radius of shell

h = height of cylindrical shell

$$C_1 = \int_0^h \tfrac{1}{4}\, \zeta\, \overline{H}_n^2\, \pi \mu^2 \omega r^3 \, dr dh = 1.52\, \omega \text{ dyne-cm for antennas} \qquad \ldots\ldots (61)$$

The total eddy damping of Alouette I is summarized in Table 4.

The ferromagnetic materials in the spacecraft are subjected to a hysteresis loss as a result of reversals in direction of magnetization. The bulk of the ferromagnetic material in Alouette I is contained in the steel sounding antennas. A toroid of antenna material was measured in the laboratory under a field of 0.2 gauss and found to have a hysteresis loss per unit volume of

$$\oint HdB = 0.0164 \text{ ergs/cycle/cm}^3$$

For the total volume of antenna material in Alouette I, the hysteresis loss, E_h, amounts to 11.6 ergs/cycle.

Equating rate of change of angular momentum to eddy current torque and hysteresis torque results in:

$$-I\frac{d\omega}{dt} = 11\,\omega + 1.84$$

TABLE 4

Net Eddy Damping

Net Eddy Damping	$\frac{c}{\omega}\ \frac{gm\ cm^2}{sec}$
Steel sounding antennas (150' x 75' dipoles)	1.52
NiCd battery pack & aluminum holders	0.32
Electronic payload packaging aluminum boxes	0.65
Structural aluminum skin	8.50
Net ≅	11 $\frac{gm\ cm^2}{sec}$
Hysteresis damping on dipoles for $\oint$ HdB = 0.0164 ergs/cm^3 at 0.2 gauss	
Hysteresis loss E_h = 11.6 ergs/cycle	

the solution of which yields

$$\omega = \frac{1}{11}\left[(11\,\omega_o + 1.84)\, e^{-\frac{11t}{I}} - 1.84\right] \qquad \ldots\ldots (62)$$

A plot of this spin equation is compared with the observed results in Figure 48.

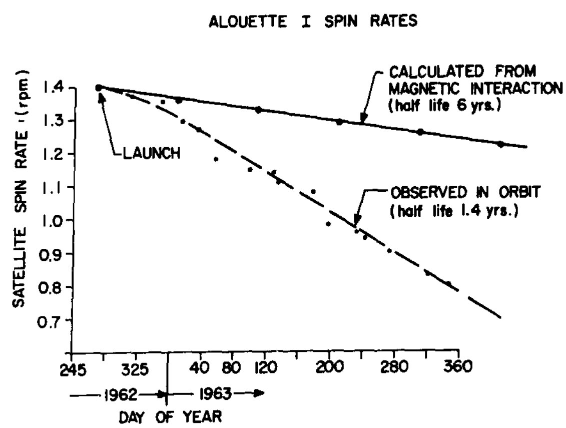

Fig. 48 Comparison of Observed and Calculated Spin Rates – Alouette I.

The discrepancy between the observed spin and that accounted for by magnetic interaction is believed to be associated with the non-rigid characteristic of the long antennas. At the time of this writing, it is believed that losses are caused by interaction between effects of thermal distortion of the structure and the radiation pressure field. Other possible effects, such as interaction of the flexible spacecraft with the plasma (magnetosphere), and neutral particle drag are still under study.

8.4 Alouette I Spin Axis Motion

The motion of the spin vector of Alouette I may be defined by Euler's equation

$$\text{Torque} = \frac{\partial H}{\partial t} + \underline{\omega} \times \underline{h}$$

where $\underline{h}$ = angular momentum vector of the spacecraft

$\underline{\omega}$ = angular velocity of spacecraft axes to inertial axes

$$\frac{\partial h}{\partial t} = \frac{\partial h_1}{\partial t}\underline{i} + \frac{\partial h_2}{\partial t}\underline{j} + \frac{\partial h_3}{\partial t}\underline{k}$$

Specification of torques caused by gravitational gradient, magnetic, and eddy current damping is obtained by first considering the spacecraft dynamic parameters as shown in Figure 49. It is noted that the x, y, z axes correspond to the long antenna, short antenna, and spin axis respectively.

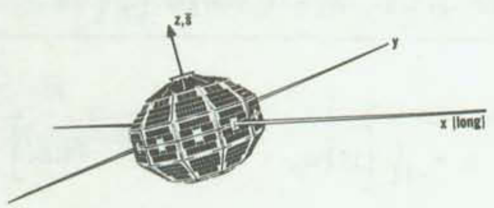

HEIGHT	34 in.
DIAMETER	41 in.
WEIGHT	319.2 lb.
LENGTH OF LONG ANTENNAS	150 ft.
LENGTH OF SHORT ANTENNAS	75 ft.
Ix	77.3 SLUG ft.²
Iy	568.9 SLUG ft.²
Iz	640.6 SLUG ft.²

Iz : Iy : Ix = 8.3 : 7.45 : 1

ALOUETTE I PARAMETERS

Fig. 49. Alouette I Inertial Parameters.

Defining orbit parameters as in Figure 50, where

$\underline{\Omega}$ = orbit angular rotation vector

i = orbit inclination

and letting $\underline{S}$ be the satellite spin vector, gives the corresponding gravity torque as:

$$\underline{T_g} = \frac{6\pi^2}{T_n^2}\left(I_z - \frac{I_y + I_x}{2}\right)(\underline{S} \cdot \underline{\Omega})(\underline{S} \times \underline{\Omega}) \qquad \ldots\ldots (63)$$

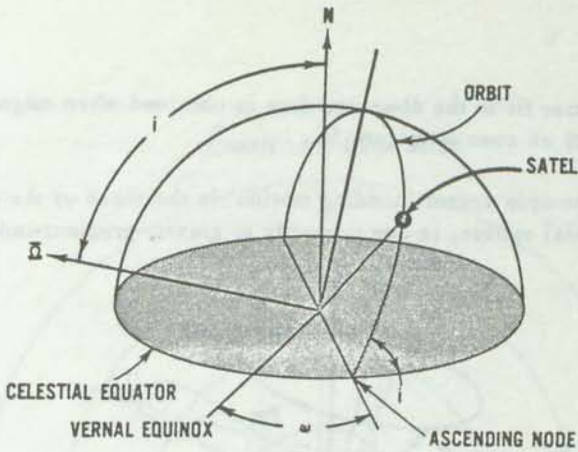

Fig. 50. Alouette I Orbit Parameters.

This torque produces a precessional motion of the spin vector $\underline{S}$ which is proportional to $\underline{S} \times \underline{T_g}$.

$$\underline{P_g} \propto \underline{S} \times \underline{T_g} = (\underline{S} \cdot \underline{\Omega}) \left[\underline{S}(\underline{S} \cdot \underline{\Omega}) - (\underline{S} \cdot \underline{S})\underline{\Omega}\right] \qquad \ldots\ldots (64)$$

A pictorial representation of this motion is shown in Figure 51.

If the satellite possesses a permanent magnetic moment $\underline{M}$ (usually between 200 to 500 dyne-cm/oersted for average spacecraft), then a magnetic torque $\underline{T}_m$ exists:

$\underline{T}_m = \underline{M} \times \underline{H}$ where $\underline{H}$ is the field strength.

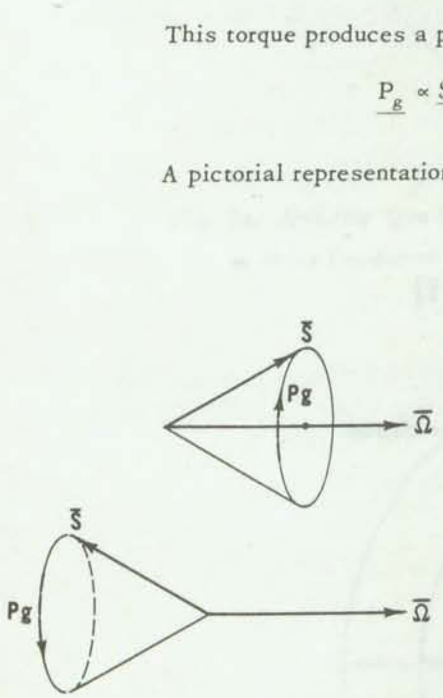

Fig. 51. Precessional Motion of Spin Vector.

This torque produces another component of spin vector precession:

$$\underline{P}_m \propto \underline{S} X (\underline{S} \times \underline{H}) = \underline{S}(\underline{S} \cdot \underline{H}) - (\underline{S} \cdot \underline{S})\,\underline{H} \qquad \ldots\ldots (65)$$

Similarly, the eddy current damping torque

$$\underline{T}_e = p\underline{H}X(\underline{H} \times \underline{S}) = p\left[\underline{H}(\underline{H} \cdot \underline{S}) - (\underline{H} \cdot \underline{H})\,\underline{S}\right] \qquad \ldots\ldots (66)$$

results in an eddy precession proportional to

$$\underline{S} \times \underline{H}\,(\underline{H} \cdot \underline{S})$$

The resulting spin vector precessional motion due to magnetic and eddy current torque is shown in Figure 52.

Adding the effects of gravity, magnetic, and eddy current torques results in a motion shown schematically in Figure 53.

The plot of spin vector motion on the celestial sphere, starting from day 0 (at launch) on through to day 400, is shown in Figures 54 and 55. The dotted line shown in Figure 54 is that calculated using gravitational torque only. A better fit to the observed data is obtained when magnetic and eddy current torques are included with gravity as seen in Figure 56.

It would appear that the spin vector 'nodding motion' in the plane of the orbit, resulting in a five pointed 'star' plot on the celestial sphere, is due primarily to gravity-gradient-induced torque on the spacecraft.

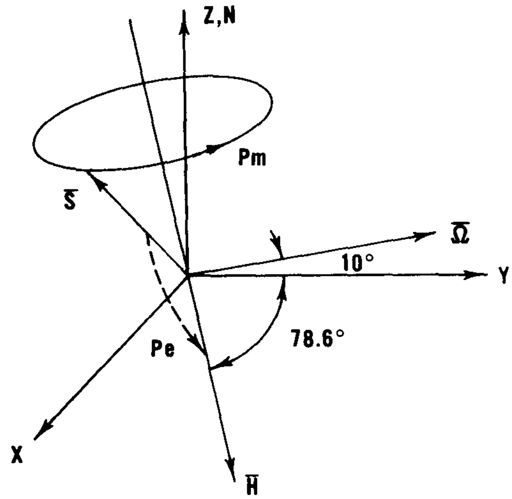

MAGNETIC TORQUE

$$T_m = \bar{M} \times \bar{H} = M\,(\bar{S} \times \bar{H})$$

PRECESSION

$$P_m \propto \bar{S} \times (\bar{S} \times \bar{H}) = \bar{S}\,(\bar{S} \cdot \bar{H}) - (\bar{S} \cdot \bar{S})\,\bar{H}$$

EDDY CURRENT TORQUE

$$\bar{T}_e = p, \bar{H} \times (\bar{H} \times \bar{S}) = p, \left[\bar{H}\,(\bar{H} \cdot \bar{S}) - (\bar{H} \cdot \bar{H})\,\bar{S}\right]$$

PRECESSION

$$P_e \propto \bar{S} \times \bar{H}\,(\bar{H} \cdot \bar{S})$$

Fig. 52. Pictorial Representation of Spin Vector Motion.

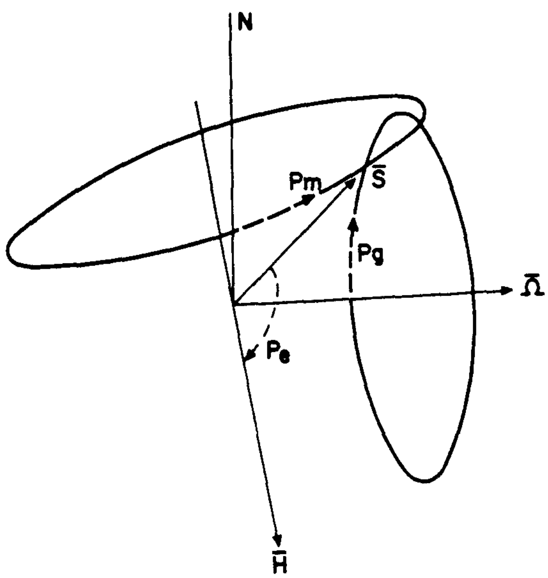

RESULTANT PRECESSION FOR GRAVITY, MAGNETIC AND EDDY CURRENT TORQUES

Fig. 53. Resultant Spin Vector Motion.

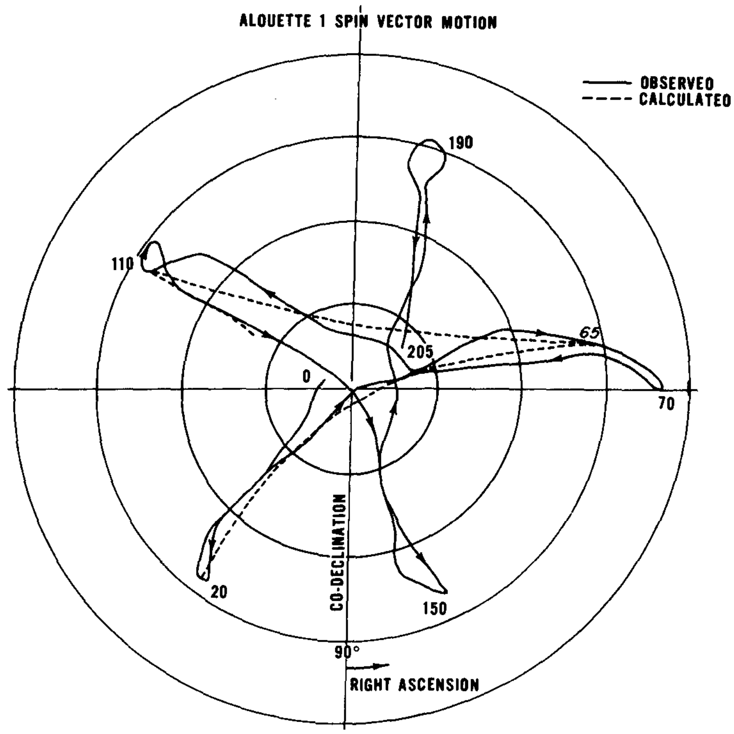

Fig. 54. Alouette Spin Vector Motion Projected on Celestial Sphere for First 205 Days in Orbit Compared with Calculated Values, using Gravitational Torque Only.

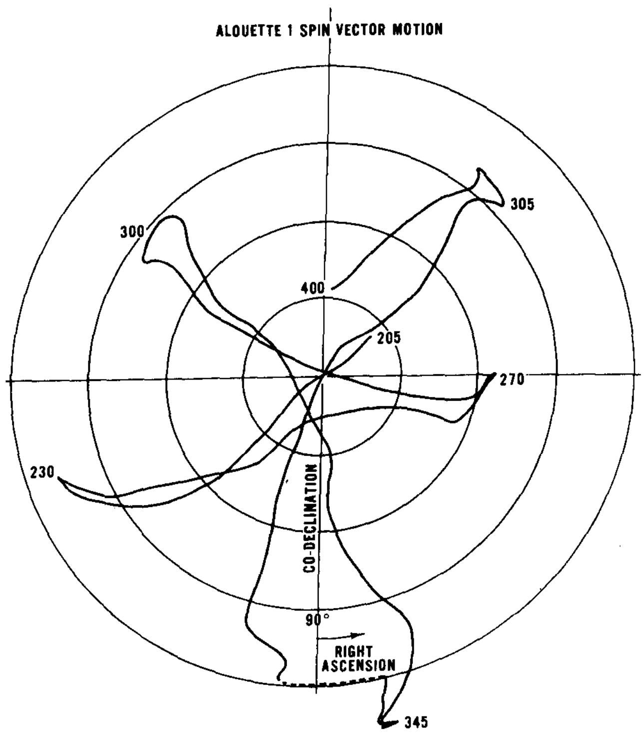

Fig. 55. Spin Vector Motion to 400 Days in Orbit.

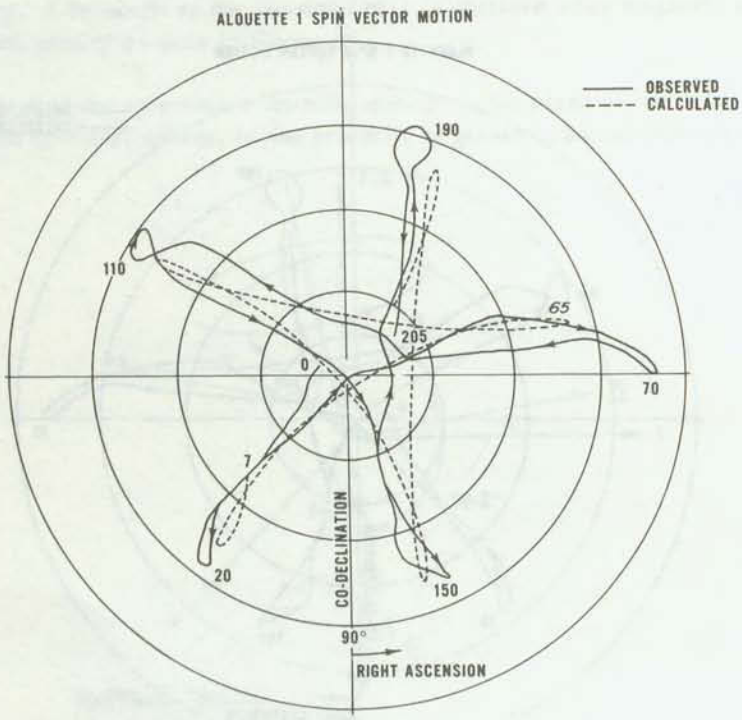

Fig. 56. Comparison of Observed Spin Vector Motion with Calculated Values, using Gravity and Magnetic Torques.

8.5 Effects of Thermal Distortion

As mentioned under the section dealing with spin decay, it is believed that thermal distortion of the long antennas produces loss of spin. Thermal distortion, as envisaged in Figure 30, also affects the stressing of the structure as shown in Figure 57.

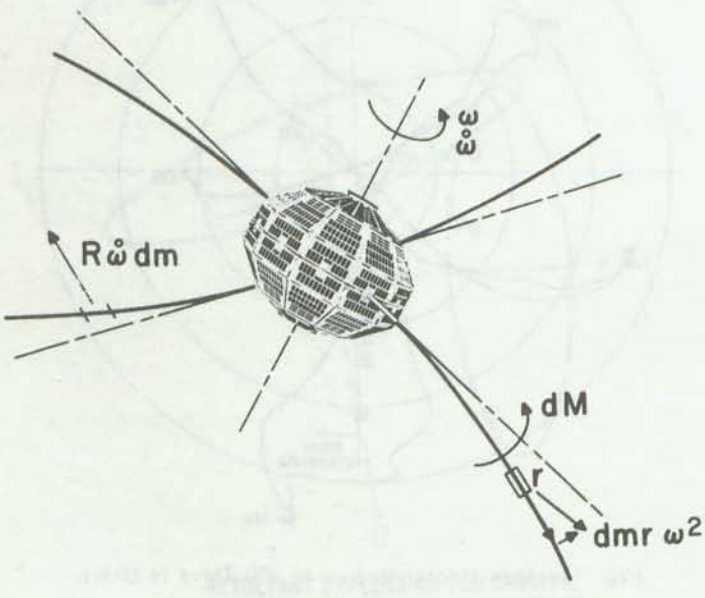

Fig. 57. Antenna Bending Resulting from Thermal Distortion.

The thermal bending of antennas causes an effective foreshortening of the body with respect to its spin axis. This induces a change in spin rate and consequently a tangential acceleration of the antennas. At the same time, the centrifugal acceleration tends to bend the distorted antennas back to their straight form. The implications of these actions are being studied from the standpoint of thermal-elastic phenomena and associated spin-to-orbit-coupled energy dissipation.

Foreshortening, or change in moment of inertia, also affects the gravitational-gradient-induced torque. Referring to Figure 58, the gravitational potential may be written as:

$$U = \frac{K}{2\underline{R}^3}(I_3 - I_1)(1 - \cos^2\theta), \qquad \ldots\ldots (67)$$

where $K = 3GM$

G = universal gravitational constant

M = mass of the earth

$\underline{R}$ = geocentric radius

θ = angle of spin vector to local horizontal.

From the foregoing, the gravitational torque may be obtained:

$$\frac{\partial U}{\partial \theta} = T_g = -\frac{3K}{R^3}(I_3 - I_1)\sin 2\theta \qquad \ldots\ldots (68)$$

Calculations indicate that only a maximum of 3% change in inertias results from thermal bending in Alouette I.

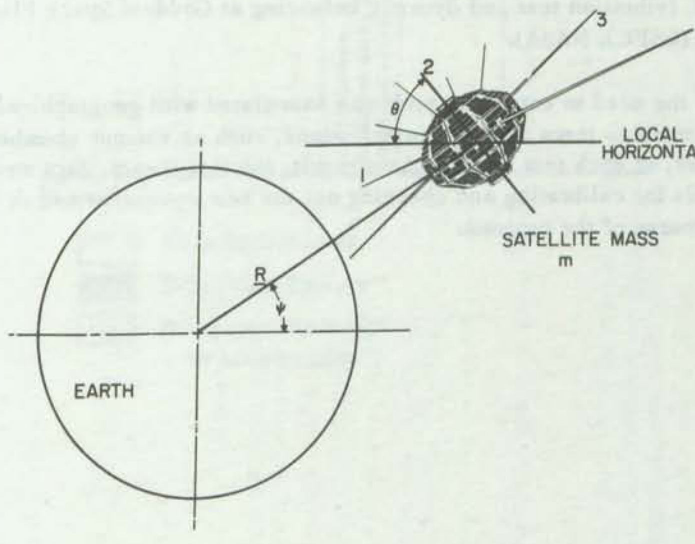

Fig. 58. Coordinate System for Gravitational Potential.

9. SPACECRAFT ENVIRONMENTAL TEST PROGRAM

During the design of the spacecraft it was subjected to vibration, centrifuge, spin, and thermal-vacuum tests to simulate the flight environment. The testing was divided into two categories: prototype design qualification tests, and flight acceptance tests. The former specified that 'g' levels during vibration and centrifuge tests be 1.5 times higher than those to be expected in actual flight, and that the duration of thermal-vacuum tests be of not less than ten days. The latter required only a 1.25 times increase in g's over flight and also only five days duration in thermal vacuum.

A total of four satellite models were constructed. These consisted of a structural or 'dynamic' model (used exclusively for mechanical structural, heat conduction, and booster vehicle integration tests), a prototype (complete with live systems) and two flight quality spacecraft. The tests performed and the results obtained from each of the satellite models are summarized in Tables 5 to 8. The Tables indicate that Alouette I was generally of a very successful design.

9.1 Test Facilities

The environmental test activity represented a major task in the Alouette program. Since the project staff had no access to a completely equipped test facility at the time, Alouette testing had to be carried out in four different geographic locations. These locations, and their relevant services, were as follows:

Ottawa, Ont. (subsystems temperature test at the Defence Research Telecommunications Establishment (DRTE)).

Valcartier, Que. (thermal-vacuum at CARDE).

Toronto, Ont. (spin and centrifuge tests at DeHavilland Aircraft).

Greenbelt, Md. (vibration test and dynamic balancing at Goddard Space Flight Center, (GSFC), NASA).

In addition to the need to cope with problems associated with geographically dispersed test sites, Alouette I was first to undergo tests on major installations, such as vacuum chamber, solar simulator, centrifuge, and vibrators, at each test locale. As a result, the test theory, data measurement and recording techniques, and methods for calibrating and checking out the new equipment had to be specified and developed during the course of the program.

TABLE 5

Structural Model Test

Item	Structural Model		
	July 12-17 1961	July 17-20 1962	July 1961 to July 1962
Weight, cg			
Balance		□	
Spin			
Vibration	■		
Ground compatibility			
Hot T.V.			
Cold T.V.			
Thermal design			
Centrifuge			
Antenna extension			
Pedestal tests DAC			□
Range operations			
Remedial action	D		
Remarks	Screws between thrust tube-instrument decks failed, 8 struts placed to support decks.		

Key:

□ Test Satisfactory

■ Subsystem Failure

D Subsystem Redesign or Modification

TABLE 6
Prototype Tests

Item	1961					1962 PROTOTYPE							
	Oct 30 Nov 10	Dec 4-6	Dec 8	Dec 8-13	Dec 14-19	Jan	Feb 1-3	Feb 5-24	Feb24 Mar 1	Mar 9	Apr 9-10	Aug 10	Aug 22 Sept 30
Weight, CG			○										
Balance				○									
Spin				○									
Vibration					●							○	
Ground Compatibility		○											
Hot T.V.	⦶							○					
Cold T.V.	⦶								○				
Thermal Design	○												
Centrifuge							○						
Antenna Extension						●				●	○		
Pedestal Tests DAC													
Range Operations													○
Remedial Action	(D)				(R)	(D)				(D)			
Remarks	Command receivers desensitized as a result of spurious output of Hughes 2-watt telemetry Xmtr. Changed to RCA Xmtr. Abbreviated T.V. Test.				Broken wire in one antenna matching network. Was not potted. Flight units will be potted.	Jammed at 35 ft. Nylon idler gear. Put stainless steel bushing on instead of aluminum.				Binding caused by idler gear, spring, nylon sleeve. Partly caused by T.V. Clearance increased.			

Key: ○ Test Satisfactory ⦶ Special Problem (R) Subsystem Repaired

● Subsystem Failure (D) Subsystem Redesign or Modification

TABLE 7

Flight 1 Test

Item	FLIGHT 1					1962				
	May 11-15	May 15-17	May 18	May 29 June 5	July 3-10	July 5	Aug 11	Aug 13-14	Aug 17 Sept 30	Sept 29
Weight, C.G.	○							○		
Balance	○		○					○		
Spin			○							
Vibration		○					○			
Hot T.V.				○	○					
Solar Simulation				○	○					
Cold T.V.				●	○					
Antenna Extension						○				
Range Operations									⦶	
Launch										○
Remedial Action				Ⓡ					Ⓓ	
Remarks	Weight = 320.6 lbs.; Residual Unbalance: Static 11.5 oz-in. Dynamic 210 oz-in^2. C.G. = 16.91" from interface.		Wt. = 320.6 lbs.; Residual Unbalance: Static 2.1 oz-in. Dynamic 88 oz-in^2.	1N2979B Motorola Zener Diode which functioned as over voltage control in Converter II failed. (2) Flight Transmitters not available. Used old Type.	(Components) Converter II and two RCA 2-watt transmitters qualified in chamber with Flight II.			Wt. = 322.4 lbs.; Residual Unbalance: Static 3.52 oz-in. Dynamic 173 oz-in^2.	3 resistors added to Converter #3 to ensure starting at low voltage because of increased radiation. Two 300 ma fuzes removed from NRC exp. Glass cover on one solar cell came off during cleaning.	

Key: ○ Test Satisfactory; ⦶ Special Problem; Ⓡ Subsystem Repaired; ● Subsystem Failure; Ⓓ Subsystem Redesign or Modification

TABLE 8

Flight 2 Test

Item	FLIGHT 2 May 23-26	May 28-29	July 3-10	July	1962 Aug 16	Aug 17-18	Aug 22 Sept 30
Weight, CG	◯					◯	
Balance	◯					◯	
Spin	◯						
Vibration		◯			◯		
Hot T.V.			◯				
Solar Simulation			◯				
Cold T.V.			(|)				
Antenna Extension					◯		
Range Operations							(|)
Launch							
Remedial Action							(D)
Remarks	Wt. = 320.6 lbs.; Residual Unbalance Static 11.2 oz-in, Dynamic 126 oz-in^2. CG = 16.95" from interface.		Video Adder output revealed series of spikes which continued after T.V. tests. Only with both telemetry transmitters on.			Wt. = 322.4 lbs.; Residual Unbalance: Static 4.8 oz-in., Dynamic 73 oz-in^2.	3 resistors added to Converter #3 to ensure starting at low voltage because of increased radiation. Two 300 milli-amp fuzes removed from NRC exp.

Key: ◯ Test Satisfactory (|) Special Problem (D) Subsystem Redesign or Modification

● Subsystem Failure (R) Subsystem Repaired

9.2 Spacecraft Checkout Procedures

Before and after every major test operation, the spacecraft was given a thorough overall systems check. This procedure, known as 'Major Spacecraft Checkout', is described in Appendix III. Similarly, a 'Minor Checkout Procedure' is described in Appendix IV. Both checkout procedures were specified by DRTE and were based on experience gained during design, construction, and operation of the satellite.

9.3 Centrifuge, Spin, and Antenna Extension Tests

Centrifuge testing of the prototype spacecraft was undertaken on a motor-generator-controlled rotating-beam centrifuge (Fig. 59) with a nominal radius of swing at the spacecraft's center of gravity of 42 in. The spacecraft was mounted in both horizontal and upright positions for longitudinal and lateral testing, respectively. The test levels used corresponded to stresses of 1.5 times those expected in flight and were as follows:

Longitudinal: 12.6 g at spacecraft center of gravity for 10 min.

Lateral: 2.4 g at spacecraft center of gravity for 10 min.

No failures were detected in the spacecraft system during centrifuge tests.

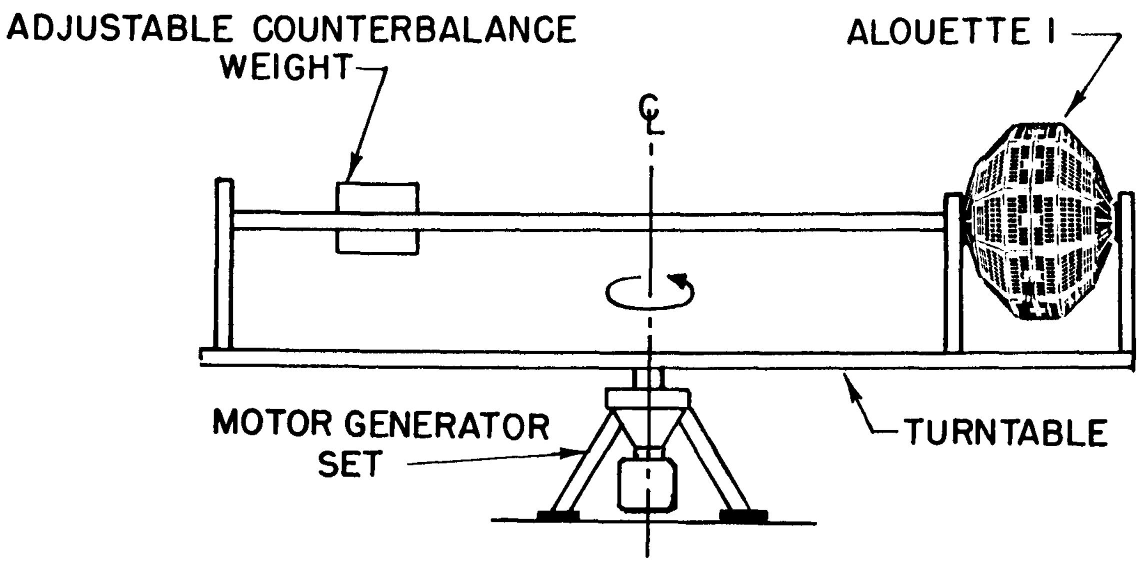

Fig. 59. Alouette I Centrifuge.

Spin testing with antenna extension was undertaken by mounting the spacecraft on the centrifuge, with the rotating beam removed. The antennas were extended remotely, via command telemetry, to the various lengths, at each speed range as follows:

To approx.	6 ft.	at	60 rpm
"	6 "	"	120 rpm
"	8 "	"	160 rpm.

The maximum length of tube extended in this test was governed by the limiting windage load on the tube. No failures resulted from this particular test and it was concluded that the design of the sounding antenna system was such that they could function under a simulated dynamic load.

A 'full out' extension test under static conditions (no spin) was made possible by supporting each antenna tube on a series of trolleys suspended from a system of cables. During this test, the spacecraft experienced difficulty because of a battery short-circuit in the antenna-drive battery pack, and a bearing seizure on a gear in the antenna-drive train. The short-circuiting was caused by imperfect insulation of cells from their aluminum holders and was quickly rectified. Gear seizure was caused by dirt particles that were imbedded into the bore of a nylon gear. This caused the gear to score and seize onto its aluminum shaft. This difficulty was overcome by installing stainless steel bushings around the aluminum shafts; this prevented the nylon from running on the softer aluminum.

Following repairs to the units, 'full out' extensions of antennas were carried out successfully a number of times.

9.4 Spacecraft Vibration Tests

Details of the test specifications, which originated from GSFC, were shown earlier in Table 2. The structural behaviour was discussed in the section under structural design. A typical accelerometer plot, showing response at various parts of the spacecraft for a typical test input, is shown in Figure 60.

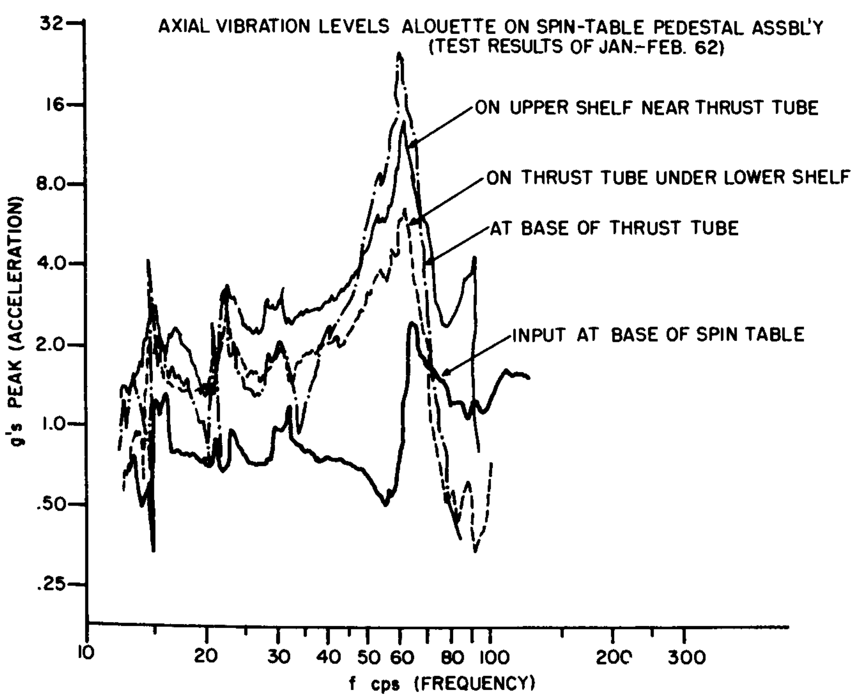

Fig. 60. Typical Vibration Test Input and Response.

During the latter stage of the Alouette program, A LOX (liquid oxygen) turbopump cavitation-induced resonance was discovered in the booster vehicle. This caused a rather significant increase in g's in the 16-22 and 38-48 cps range in the thrust direction. Consequently, the prototype and flight spacecraft were required to undergo a retest (Fig. 61) at GSFC about four months before launch. Both spacecraft survived the additional test, but only with a minimum safety margin.

9.5 Thermal-Vacuum Tests

Thermal-vacuum testing was carried out on both prototype and flight spacecraft to simulate the thermal and vacuum conditions which prevail on a body in orbit. The chamber (Fig. 62) used for the tests did not reproduce space conditions but sufficed only in providing a radiation heat transfer environment, and a vacuum that allows volatile materials to ' out gas'. The capability of the CARDE chamber as compared with space conditions is shown in Table 9.

TABLE 9

	Test Chamber at CARDE	Space Environment
Pressure	10^{-5} mm Hg	10^{-16} mm Hg
Background temperature	-35° F	-460° F
Electromagnetic Spectrum	Carbon arc	Sun

During the test procedures Alouette I was placed in the chamber on a remotely controlled 'turntable' that rotated to simulate the satellite's expected spin rate in orbit. The satellite system was then operated in the various modes and duty cycles anticipated in flight.

Test progress of the spacecraft was monitored directly through its umbilical cord. Temperature measurements at various locations on the spacecraft were taken using thermistors and these were fed through the chamber wall to a digital-voltmeter multiplexing recorder.

Details of the thermal-vacuum tests carried out on both prototype and flight spacecraft are described in Appendix V.

10. DESIGN OF GROUND HANDLING EQUIPMENT

10.1 Introduction

Special handling equipment was required for lifting and manipulating Alouette I. The outer shell of the spacecraft is covered with panels of solar cells which are very fragile to handle. The only external load bearing members that could be handled safely were the thrust tube flanges. The lower thrust tube flange is clamped to the rocket booster for launching. Consequently, the thrust tubes bear the entire transfer of load to the spacecraft.

The following describes the equipment and procedure used for handling the spacecraft.

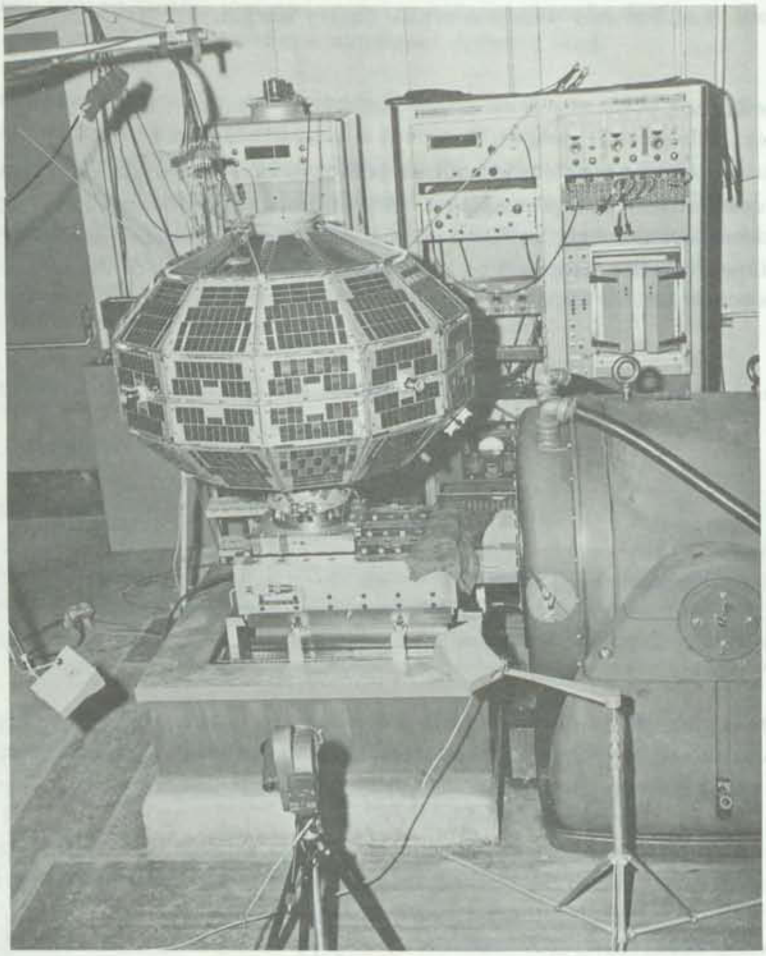

Fig. 61. Alouette I Flight Vibration Test.

10.2 Handling Dolly

To facilitate work on the spacecraft during assembly and testing, a special handling dolly (Fig. 63) was designed. This provided a secure platform on which to attach the spacecraft and also allowed

(i) easy access to all parts of the spacecraft,

(ii) easy removal of parts from the spacecraft, and

(iii) mobility in lab areas, with protection against collision with equipment, furniture, doorways, etc.

In using this equipment, the spacecraft is secured to the dolly by means of Marman clamps (Fig. 64) which fasten the thrust tube flanges to the dolly trunnions (a similar clamp is used to secure the spacecraft to the rocket). The trunnions are mounted in bearings on the ends of two support arms which form a yoke. This permits the spacecraft to be rotated about its thrust axis in the yoke, thereby providing easy access to all sides. The spacecraft is clamped in the yoke by locking the rotating trunnions. In addition, the entire yoke and spacecraft combination can be rotated on its bearing-mounted pivot. This feature permits the spacecraft to be tilted or inverted to facilitate access to either the upper or lower payload deck.

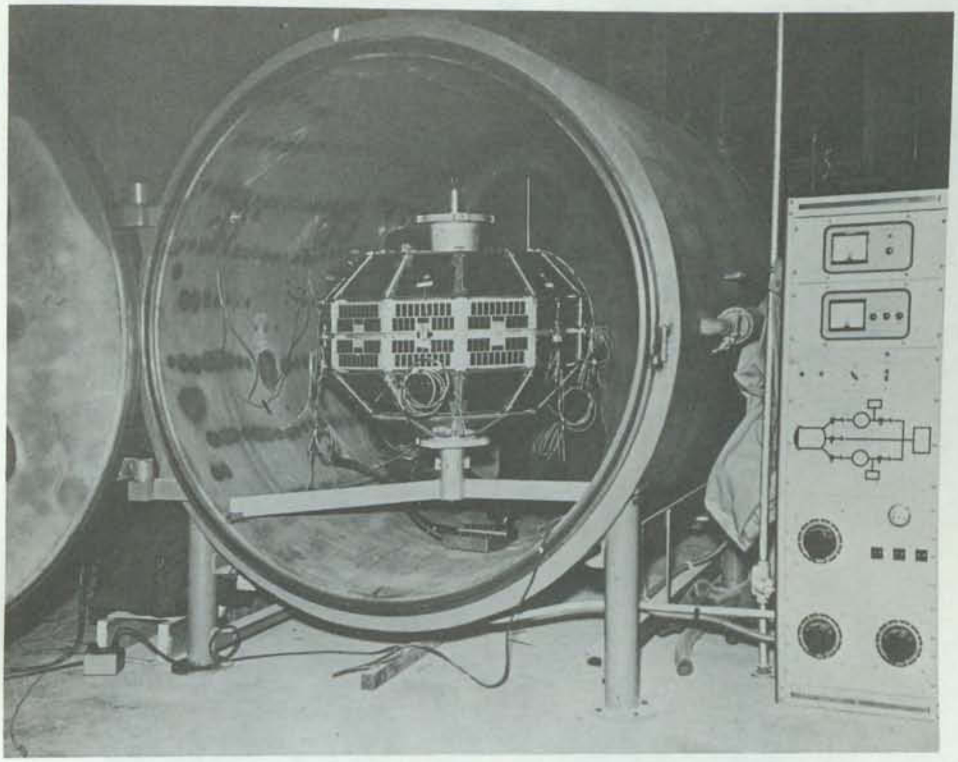

Fig. 62. Vacuum Test Chamber at CARDE.

To permit disassembly and removal of the outer shell structure, either arm of the yoke may be disassembled from the hub (Fig. 65). Consequently, each arm of the yoke is designed to support the spacecraft's weight independently, in any position.

Casters provide mobility to the dolly. The spacecraft is protected during transport on the dolly by a circular bumper ring with a diameter that exceeds that of the spacecraft. This prevents the spacecraft from contacting walls, furniture, and door jambs during transport. The spacecraft is also protected against sharp jarring when it is being transported over rough surfaces, door sills, etc., by the spring action of the dolly arms.

10.3 Shipping Cannister

Since the completed Alouette models had to undergo many shipments by truck and aircraft between laboratory and test sites before final shipment to the Pacific Missile Range for launching, the shipping containers had to protect the spacecraft against handling and shipping shock loads, humidity, dust, and collision with other objects.

A Pratt and Whitney, Wasp Aero-Engine shipping cannister, met the requirements. Besides being the right size and shape (Fig. 66), this cannister may be sealed against dust and humidity and only minor modifications were required to adapt it to satellite use. The spacecraft is horizontally mounted by clamping trunnions to each thrust tube. The trunnions are then secured to shock-mounted pillow blocks in the cannister. The cannisters are strong, reasonable in weight (1000 lbs.), and easily handled with a fork lift or hoist.

Fig. 63 Handling Dolly.

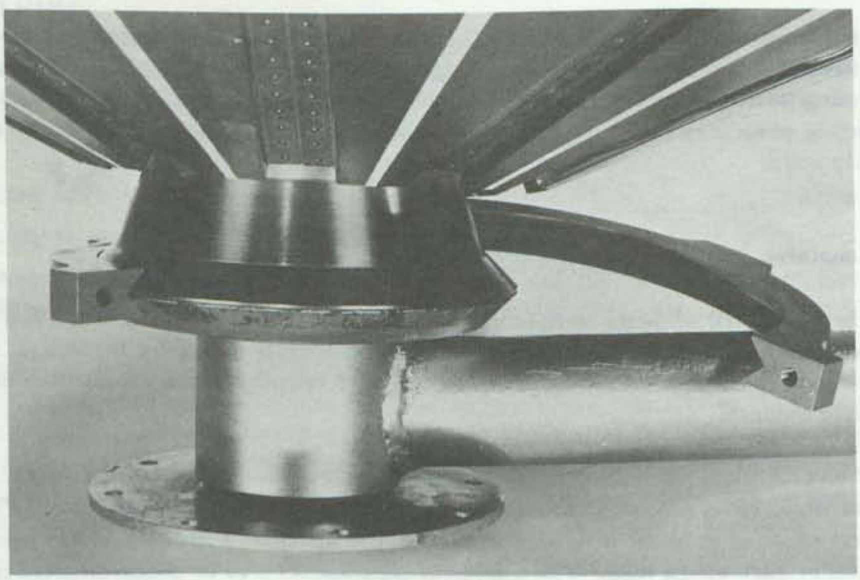

Fig. 64. Marman Clamp Holding Spacecraft to Dolly Trunnion.

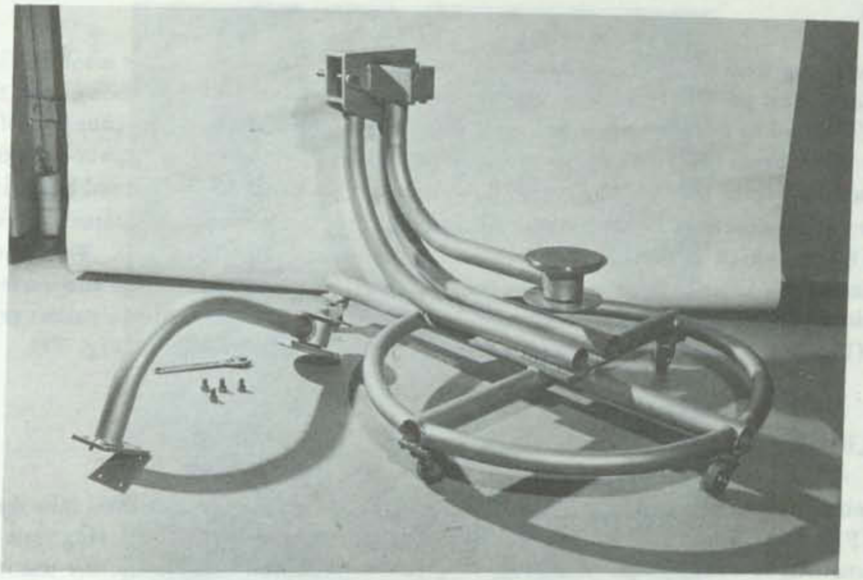

Fig. 65. *Handling Dolly with One Arm Removed.*

Fig. 66. *Satellite Shipping Cannister.*

10.4 Lifting Jig

In transferring from shipping cannister to handling dolly, the spacecraft must be lifted from the cannister in a horizontal position and then rotated to a vertical position for lowering onto the dolly. A lifting jig was designed to accomplish this lifting and rotating operation. This consists of an I-beam bent into a C-shape. This beam (Fig. 67) spans and fastens to the two ends of the spacecraft thrust-tube trunnions. A toothed sector made by fastening a rack to the backside of the curved beam is mounted on this beam. The entire assembly is then rotated by a hand cranked pinion conveniently located on the movable lifting block, which is constrained to run on the I-beam flange (Fig. 68). When the spacecraft is in vertical position, the lifting block is locked by a pin so that the spacecraft is suspended directly from the upper trunnion. The lower portion of the I-beam has been made detachable to permit removal of the lower trunnion (Fig. 69) when securing the spacecraft to the dolly support arm (Fig. 70).

10.5 General Lifting and Carrying

For general vertical lifting by a hoist, crane, etc., an eyebolt is threaded into the end of a thrust-tube trunnion (Fig. 71). For lifting in horizontal position, long turn-buckles hanging from a spreader bar (Fig. 72) are attached to eyebolts threaded into the Marman clamps which fasten the trunnions to the thrust tubes. The turnbuckles provide adjustment of horizontal attitude when horizontal mating operations (i.e., attaching to balance machines, etc.) are undertaken.

Fig. 67. Alouette Lifting Jig.

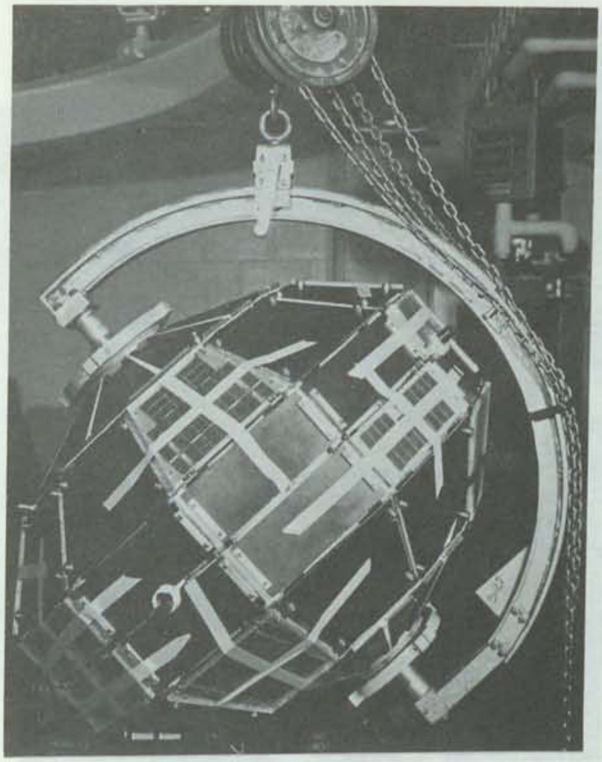

Fig. 68. Movable Lifting Block on Lifting Jig.

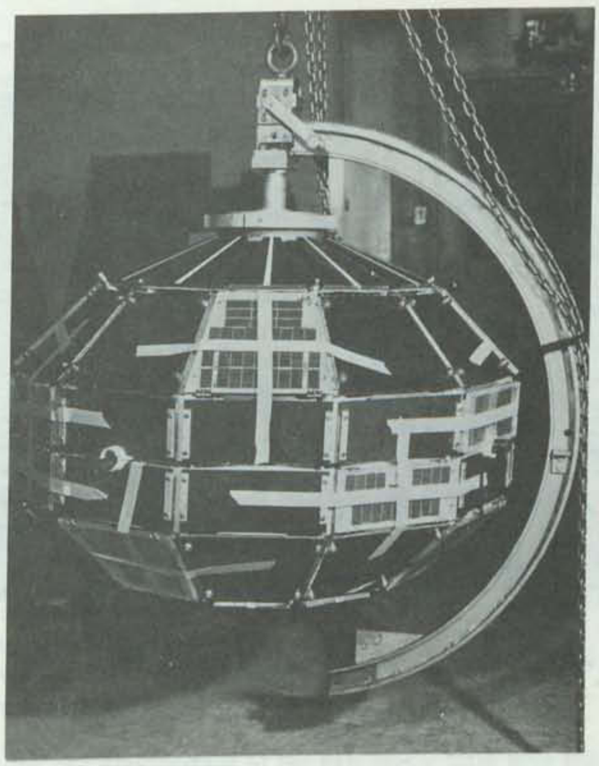

Fig. 69. Lifting Jig with Lower Portion Removed.

Fig. 70. Lowering of Spacecraft to Handling Dolly.

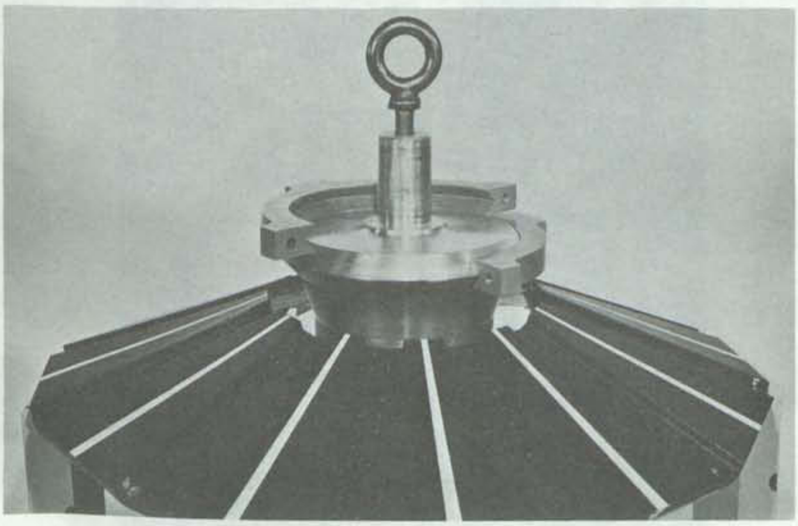

Fig. 71. Lifting Trunnion Eye Bolt.

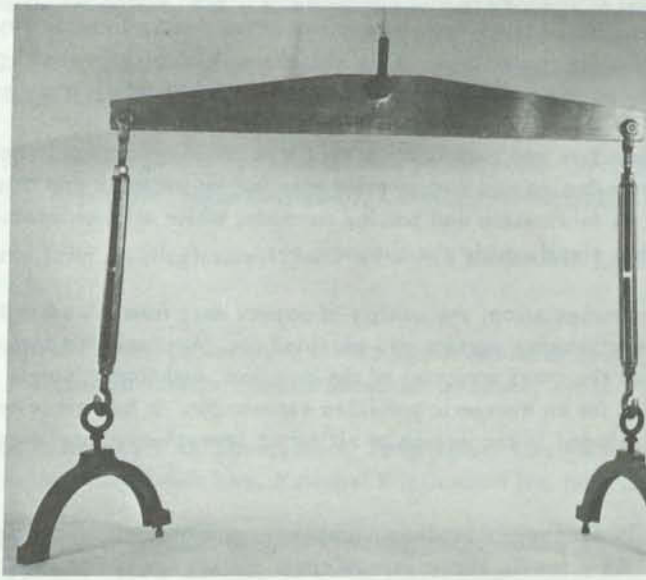

Fig. 72. Spreader Bar with Turnbuckles.

11. CONCLUSIONS

In general, the thermal and mechanical system of Alouette I functioned successfully through launch and has continued to do so for the past three years of its operating life. There has been no detectable degradation in the design temperature levels with time in orbit. This would indicate that the passive control system used in Alouette I is relatively insensitive to micrometeoroid erosion and ultraviolet radiation effects, and consequently might be construed to be a reliable method for use on other satellites with similar requirements.

The spin life of Alouette I met requirements for a one year period of operation without difficulty, but has decayed much faster than originally predicted and is, at the time of this writing, showing little detectable spin. It is suspected that the motion now observed might represent a transition from spin stabilized motion to that of gravity capture which ultimately results in the long sounding antenna pointing earthward. If and when this occurs, the null in the dipole radiation pattern will point into the ionosphere with a resulting loss of sounding data.

Despite the undesirable consequences of loss of spin to the sounding and energetic particles experiments, the behaviour of Alouette I has uncovered a new area for study in spacecraft dynamics. This is associated with the behaviour of semi-rigid and fully non-rigid bodies in orbit. To the writer's knowledge, Alouette I is the first satellite to be placed into orbit which has non-rigid characteristics in its motion. The long metal antennas of Alouette I interact with the sun's electromagnetic field, and with the earth's gravitational and geomagnetic fields. This results in significant geometric distortions of the body. This must be accounted for in understanding its motion in orbit. Because of this a study of dynamics of non-rigid orbiting bodies has been undertaken by DRTE.

Since the adoption and development of the extendible mast idea for Alouette I has proved highly successful, a wide-scale application of this principle has resulted. Extendible masts of this type have now been widely used in American satellites and manned space capsules in the form of antennas, booms for retractable probes, and gravity gradient rods.

Although the structural configuration of Alouette I has proved successful, the main cause of vibration problems has been attributed to the cross-coupling of the overly-flexible payload package deck structure with the main load bearing thrust tube. This situation could be improved by designing the payload package to mount directly on the main load bearing member (thrust tube).

Although the electronic box and packaging design withstood severe environmental tests and launch conditions extremely well, their design and construction was far too complex and time consuming. This points to a need to simplify box fabrication and potting methods, while still maintaining a high level of reliability, and thus decreasing significantly the time and cost.

On the subject of instrumentation, the quality of aspect data from Alouette I has left much to be desired, since no proper aspect sensing system was provided for. Approximate aspect was obtained from the temperature distribution on the outer structure of the satellite, and from a single axis magnetometer which happened to be included for an energetic particles experiment. It has since been recommended that aspect sensing systems be included in the design of all future ionospheric satellites that use long antennas.

Due to lack of readily accessible environmental test equipment and facilities, procedures and test gear were often improvised. As a result, these improvisions did not always produce the desired accuracies, hence a close examination to improve the degree of accuracy of test data and the degree of simulation of flight conditions should be made.

Because test facilities were widely dispersed, testing procedures involved many man hours and much money. Moreover, the satellite was subjected to abnormal risk of damage in transit. It is concluded, therefore, that a centralized test facility (thermal-vacuum chamber, solar simulation lamps, a 10,000 lb-force electrodynamic vibrator) should be established at the place of spacecraft design and construction.

12. ACKNOWLEDGEMENTS

The author gratefully acknowledges the close association and support of the Goddard Space Flight Center of the U.S. National Aeronautics and Space Administration, as well as the Special Products and Applied Research Division of DeHavilland Aircraft Company of Canada - the mechanical contractors on the Alouette I project.

Acknowledgement is also due to the fellow members of the Space Technology team of the Defence Research Telecommunications Establishment, in the performance of the work described in this report. Special thanks are accorded to Mr. C.D. Florida, Mr. P.A. Field and Dr. I.R. Paghis of DRTE's staff for their critical review of this manuscript.

13. BIBLIOGRAPHY

1. Chapman, J.H. *Topside Sounding of the Ionosphere.* Proceedings of American Astronautical Society Symposium on Scientific Satellites, **Vol. 12**, Advances in the Astronautical Sciences, December 1962.

2. *Alouette I: The First Three Years in Orbit, Part I – Ionospheric Studies, Part II – Electrical Design and Performance.* DRTE Report No. 1159, 1966.

3. Livingston, W.A., Jr. *Outer-Space Environment Models for Use with Space Vehicle Simulators.* Technical Documentary Report No. **MRL-TDR-62-80**, Cornell Aeronautical Labs., May 1962.

4. Goetzel, Claus G., and John B. Singletary. *Space Materials Handbook.* Lockheed Missiles and Space Company, January 1962.

5. Allen, J.M. *Environmental Factors Influencing Metals Applications in Space Vehicles.* DMIC Report 142, Defense Metals Information Center, Batelle Memorial Institute, 1961.

6. Buwalda, E.P., Hibbs, A.R., and T.O. Thostesseu. *Temperature Control in the Explorer Satellites and Pioneer Space Probes.* Jet Propulsion Lab. External Publication No. 647, Cal Tech, May 7, 1959.

7. Stonell, A. *Extensible Rigid Antennas.* **DHC-SP-TN.150**, DeHavilland Aircraft of Canada Ltd., Downsview, Ontario, 1961.

8. Franklin, C.A., Bibby, R.J., Sturrock, R.F., and D.F. Page. *Electronic and System Design of the Canadian Ionospheric Satellite.* IEEE Convention Record, **Vol. 11**, Part 5, 1963.

9. *Environmental Test Specification and Test Plan for S-27 Topside Sounder.* Goddard Space Flight Center, Test and Evaluation Division, December 6, 1961.

10. *The Environmental Test Program and System Evaluation of the Canadian S-27 (Topside Sounder) Spacecraft.* Goddard Space Flight Center, Test and Evaluation Division, April 30, 1963.

11. Phillips, G.G., Mar, J., and P. Jacques. *Payload Packaging Design—Alouette Satellite.* DRTE Report No. 1116, June 1963.

12. Mar, John. *Meteoroid Impact on the Topside Sounder Satellite.* Canadian Astronautics and Space Journal, **Vol. 8**, No. 9, November 1962.

13. Warren, H.R., and J. Mar. *Structural and Thermal Design of the Topside Sounder Satellite.* Canadian Aeronautics and Space Journal, **Vol. 8**, No. 7, September 1962.

APPENDIX I

DETERMINATION OF EMISSIVITY

A body in space can transmit or receive heat energy only by electro-magnetic radiation. In the immediate problem, it is expedient to consider a very simple ideal case of a perfect black body enclosed by a heat sink which presents an area to the black body that is much greater than the area of the black body itself. This case is extended to a solar cell panel within the vacuum chamber.

A perfect black body absorbs and emits all radiation completely over the entire electromagnetic spectrum. The total energy emitted by a perfect black body is proportional to its absolute temperature to the fourth power and may be expressed by Stefan-Boltzmann's total radiation law as follows:

$$Q_{emitted} = \sigma AT^4 \qquad \ldots\ldots (1)$$

where

σ = Stefan-Boltzmann's natural constant

A = Total surface area of the body

T = Absolute temperature of the body.

Similarly, the total energy the perfect black body receives from its surrounding sink is

$$Q_{received} = \sigma AT_s^4 \qquad \ldots\ldots (2)$$

where

T_s = Absolute temperature of the sink.

For any given wavelength point of reference, a practical, non-perfect, black body absorbs and emits total radiation in proportion to that of a perfect black body, but never as well. The degree of absorption and emittance is wavelength (temperature) dependent, and is referred to as absorptivity 'a' when energy is being received, and emissivity 'e' when energy is being emitted. The absorptivity is dependent on the wavelength (temperature) of the radiating sources from which energy is being received, and the emissivity is dependent on the wavelength (temperature) of the body itself which is radiating energy out.

Consequently, the following may be written for any general body, such as a cell panel within the vacuum chamber:

$$Q_{emitted} = e\sigma AT^4 \qquad \ldots\ldots (3)$$

$$Q_{received} = a\sigma AT_w^4 \qquad \ldots\ldots (4)$$

In this case,

T = Absolute temperature of the panel

T_w = Absolute mean temperature of the chamber walls

A = Total surface area of the cell panel.

Consider a cell panel with its entire area, except the active face for which the 'a' and 'e' is to be determined, coated with a reference paint, suspended by thermocouple wires in a vacuum chamber, and under steady illumination from a carbon-arc solar-simulation source. Assuming that the heat loss by conduction through the thermocouple wires is negligible, the following heat balance condition may be written for steady-state conditions.

The energy received by the panel is

$$a_{sun}\,(Ap)S \quad + \quad \overline{a}_{wall}\,(A)\,\sigma\,T_w^{\,4}$$

$$\underset{(\text{sun})}{\text{arc lamps}} \quad + \quad \underset{(\text{sink})}{\text{chamber walls}}$$

where

a_{sun} = absorptivity of cell panel to the solar (arc lamp) wavelength

A_p = projected area of panel exposed to illumination from the arc lamp

S = energy density of the arc lamps at panel (i.e., watts/cm^2, etc.)

$\overline{a}_{wall}$ = mean absorptivity of entire cell panel to the chamber wall wavelength (a mean value is defined here since the front face of panel is different from the backside).

A = total area of cell panel (since all surface area of cell panel 'sees' the chamber wall)

T_w = absolute mean temperature of chamber wall (sink).

Energy radiated out to the sink by the panel:

$$\overline{e}\,(A)\,\sigma\,T^4$$

where

$\overline{e}$ = mean emissivity of entire cell panel at panel temperature

T = steady-state absolute temperature of cell panel.

Hence, for steady-state conditions

$$a_{sun}\,(Ap)S + a_{wall}\,(A)\,\sigma\,T_w^{\,4} = \overline{e}\,(A)\,\sigma\,T^4 \qquad \ldots\ldots (5)$$

From the above, Ap, A, T_w, and T are measurable quantities.

Next, consider a model panel suspended in the chamber under illumination similar to that described above. The model panel must be a close full-scale replica of the actual cell panel. This serves to maintain the same 'look' aspect to the chamber wall. In the present case, the model panel is cut from a sheet of aluminum plate and painted over with a black epoxy-based FeO paint for which the 'a' and 'e' are known. For this, the steady-state energy balance equation is:

$$a_{sun_R}\,(Ap)_R S + a_{wall_R}\,(A)_R\,\sigma\,T_w^{\,4} = e_R(A)_R\,\sigma\,T_R^{\,4} \qquad \ldots\ldots (6)$$

where the subscript R denotes (reference) model quantities. It will be noted that S is held constant (lamp setting fixed) from actual cell panel to reference model case. In addition, it is convenient to maintain T_w the same for the two cases. As before $(Ap)_R$, A_R, T_w and T_R are known quantities.

It is convenient to simplify (5) and (6) by introducing the approximation that for temperatures that correspond to wavelengths greater than 4μ, the emissivity (or absorptivity) for most common materials becomes very nearly equal. Since T_w and T are both in the long wavelength region, it is legitimate to set $a_{wall} \simeq e$ (or $a_{wall} \simeq e_R$ for reference panel). The error introduced by this approximation is within the accuracy of the experimentally measured quantities. Introducing these approximations into (5) and (6) and rearranging:

$$a_{sun}(Ap)S = \bar{e}(A)\sigma(T^4 - T_w^4) \qquad \ldots\ldots (7)$$

$$a_{sun_R}(Ap)_R\, S = e_R(A)\sigma(T_R^4 - T_w^4) \qquad \ldots\ldots (8)$$

If the frontal shape of the reference model is made exactly the same as the cell panel, i.e., $(Ap) = (Ap)_R$, we obtain the 'a' of the solar cell panel face from (7) and (8).

$$a_{sun} = a = \frac{(a_{sun_R})}{e_R}\, \frac{\bar{e}\,(A)}{e_R}\, \frac{(T^4 - T_w^4)}{T_R^4 - T_w^4} \qquad \ldots\ldots (9)$$

For the black paint of the reference model,

$$\frac{(a_{sun_R})}{e_R} \cong 1.$$

It remains to determine the quantity $\bar{e}$, from which 'e' is obtained.

The quantity $\bar{e}$ is obtained from the cooling curve of the cell panel in the chamber. If the chamber wall temperature T_w is less than the panel temperature T at the instant the carbon arc lamp is shut off (i.e., S becomes zero), the panel will start to lose energy to the chamber walls. Further, it is noted that the thermal mass of the chamber is much greater than that of the cell panel, so for all practical purposes T_w remains constant.

The time rate-of-change of the panel temperature is determined by the rate-of-change of energy of the panel divided by its thermal mass.
Thus:

$$\frac{dT(t)}{dt} = \frac{1}{mc}\left(\underbrace{\bar{e}\,(A)\sigma T_w^4}_{\substack{\text{energy}\\ \text{received from}\\ \text{chamber wall}}} - \underbrace{\bar{e}(A)\sigma T(t)^4}_{\substack{\text{energy radiating to}\\ \text{chamber wall from}\\ \text{panel during cooling}}}\right) \qquad \ldots\ldots (10)$$

Here T(t) is the panel temperature at any given time, and mc is the panel mass multiplied by its heat capacity. Rearranging (10), we obtain:

$$\bar{e} = \frac{mc\left(\frac{dT(t)}{dt}\right)}{\sigma A\,(T_w^4 - T(t)^4)} \qquad \ldots\ldots (11)$$

With $\bar{e}$ determined from the cooling curve, 'a' may be obtained from (9).

In a similar fashion, e_R may be determined by applying (11) to the reference panel cooling curve.

In the final determination of 'e', the following is immediately evident:

$$\bar{e}(A) = e_R\,(A - Ap) + e\,(Ap) \qquad \ldots\ldots (12)$$

where (A - Ap), or total cell panel area less frontal face area, is the area painted with the reference paint and for which e_R has been determined. Since both 'a' and 'e' of the solar cell panel varies slightly with temperature, an average must be taken over the cooling curve. The resulting values of 'a' and 'e' found for the solar cell panels were 0.564 and 0.596 respectively.

Utilizing the technique outlined above, the mean Alouette solar absorptivity 'a' and infrared emissivity 'e' were determined as 0.523 and 0.475, respectively.

APPENDIX II

DERIVATION OF INTERNAL RADIATION COUPLING OF ANTENNA

Referring to Figure 33 and equation (27) in the text, the computation of Q_R may be obtained as follows:

$$Q_R = \int_{A_1} e\sigma T_1 \frac{\cos\phi_1 \cos\phi}{\pi r^2} dA_1 \quad \ldots\ldots (1)$$

It is evident from Figure 33 that

$$dA_1 = R d\gamma_1 \, dZ_1,$$

and also it may be shown from symmetry that

$$\phi_1 = \phi$$

Following, it is required to express $\cos\phi$ and the distance r in cylindrical coordinates. Thus

$$e^2 = R^2 + Z_1^2 \quad \ldots\ldots (2)$$

$$e^2 = r^2 + R^2 - 2rR\cos\phi \quad \ldots\ldots (3)$$

Therefore

$$r^2 - 2rR\cos\phi - Z_1^2 = 0.$$

Whereupon

$$r = R\cos\phi \pm \sqrt{R^2\cos^2\phi + Z_1^2}$$

$$= R\cos\phi + \sqrt{R^2\cos^2\phi + Z_1^2} \quad \ldots\ldots (4)$$

for $r \neq 0$.

A second expression of r may also be obtained:

$$r^2 = Z_1^2 + d^2 \quad \ldots\ldots (5)$$

where

$$d = 2R\cos\alpha \quad \ldots\ldots (6)$$

$$\alpha = \frac{\pi - \theta}{2}$$

As evident from the triangle $dA \, dA_1 \, 0$,

$$\cos\alpha = \cos\left(\frac{\pi - \theta}{2}\right) = \sin\frac{\theta}{2} = \pm\sqrt{\frac{1 - \cos\theta}{2}}$$

But

$$\theta = (\gamma - \gamma_1)\cdot$$

Therefore

$$\cos\,\alpha = \pm\sqrt{\tfrac{1}{2} - \tfrac{1}{2}\cos\gamma\cos\gamma_1 - \tfrac{1}{2}\sin\gamma\sin\gamma_1} \qquad \ldots\ldots (7)$$

From (5),

$$d^2 = 4R^2\cos^2\alpha$$

$$= 2R^2\,(1 - \cos\gamma\cos\gamma_1 - \sin\gamma\sin\gamma_1) \qquad \ldots\ldots (8)$$

Substituting (8) in (5) results in

$$r^2 = Z_1^{\,2} + 2R^2\,(1 - \cos\gamma\cos\gamma_1 - \sin\gamma\sin\gamma_1) \qquad \ldots\ldots (9)$$

Eliminating r^2 between (4) and (9) and simplifying yields:

$$\cos^2\phi = \frac{R^2(1 - \cos\gamma\cos\gamma_1 - \sin\gamma\sin\gamma_1)^2}{Z_1^{\,2} + 2R\,(1 - \cos\gamma\cos\gamma_1 - \sin\gamma\sin\gamma_1)} \qquad \ldots\ldots (10)$$

From (9) and (10), the integrand of (1) becomes:

$$\frac{\cos\phi_1\cos\phi}{r^2} = \frac{\cos^2\phi}{r^2} = \frac{R^2(1 - \cos\gamma\cos\gamma_1 - \sin\gamma\sin\gamma_1)^2}{\left[Z_1^{\,2} + 2R\,(1 - \cos\gamma\cos\gamma_1 - \sin\gamma\sin\gamma_1)\right]^2} \qquad \ldots\ldots (11)$$

Equation (1) may now be integrated, first with respect to Z_1, between the limits $-\infty$ and $+\infty$, since T_1 is some unknown function of γ_1.
Thus

$$Q_R = \int_0^{2\pi} \frac{e\sigma}{\pi}\,T_1^{\,4}\,R^3(1 - \cos\gamma\cos\gamma_1 - \sin\gamma\sin\gamma_1)^2$$

$$\left\{\int_{-\infty}^{+\infty} \frac{dZ_1}{\left[Z_1^{\,2} + 2R(1 - \cos\gamma\cos\gamma_1 - \sin\gamma\sin\gamma_1)\right]^2}\right\} d\gamma_1 \qquad \ldots\ldots (12)$$

which, after integration, gives

$$Q_R = \int_0^{2\pi} \frac{e\sigma T_1^{\,4}}{4\sqrt{2}}\sqrt{1 - \cos\gamma\cos\gamma_1 - \sin\gamma\sin\gamma_1}\;\;d\gamma_1 \qquad \ldots\ldots (13)$$

An approximate solution of (13) may be obtained by assuming a cosine temperature distribution around the tube.

$$T_1 = T_m + T_A\cos\gamma_1 \qquad \ldots\ldots (14)$$

where T_m = mean antenna temperature

T_A = amplitude of temperature distribution.

Substituting (14) into (13) results in

$$Q_R = \frac{e\sigma}{4\sqrt{2}}\left(T_m^{\,4}\int_0^{2\pi}\sqrt{1 - \cos\gamma\cos\gamma_1 - \sin\gamma\sin\gamma_1}\;\;d\gamma_1\right.$$

$$+ 4T_m^3 \; T_A \int_0^{2\pi} \cos \gamma_1 \sqrt{1 - \cos \gamma \cos \gamma_1 - \sin \gamma \sin \gamma_1} \quad d\gamma_1$$

$$+ 6T_m^2 \; T_A^2 \int_0^{2\pi} \cos^2 \gamma_1 \sqrt{1 - \cos \gamma \cos \gamma_1 - \sin \gamma \sin \gamma_1} \quad d\gamma_1$$

$$+ 4T_m \; T_A^2 \int_0^{2\pi} \cos^3 \gamma_1 \sqrt{1 - \cos \gamma \cos \gamma_1 - \sin \gamma \sin \gamma_1} \quad d\gamma_1$$

$$+ T_A^4 \int_0^{2\pi} \cos^4 \gamma_1 \sqrt{1 - \cos \gamma \cos \gamma_1 - \sin \gamma \sin \gamma_1} \quad d\gamma_1 \Big) \qquad \ldots\ldots(15)$$

Integration of (15) was performed graphically and the numerical values, Q_R minimum (for $\gamma = 0$), and Q_R maximum (for $\gamma = \pi$), were found equal to within $\pm$ 3.5%. Therefore, for all practical purposes,

$$Q_R = e\sigma T_m^4 \; . \qquad \ldots\ldots(16)$$

APPENDIX III

MAJOR SPACECRAFT CHECKOUT PROCEDURES

Visual Examination

(a) Place spacecraft on DRTE handling dolly, beacon side down.

(b) Visually inspect solar cells, panels, and cell wiring.

(c) Inspect sounding antenna initial position, and end plugs.

(d) Remove radiation shield (canopy).

(e) Inspect all accessible fasteners holding down components for tightness.

(f) Check matching network fasteners in thrust tube.

(g) Inspect security of thermal insulation.

(h) Inspect all wiring, connectors, cable clips, etc.

(i) Check screws in thrust tube braces.

(j) Check screws between hexcell deck and spun shell.

(k) Check solar panel hold-down screws.

(l) Check screws holding thrust tube to central spider.

(m) Inspect all accessible screws holding down sounding antennas.

(n) Invert spacecraft on DRTE handling dolly, and remove beacon antenna mounting plate in thrust tube.

(o) Repeat checks (e) through (l).

(p) Replace beacon antenna mounting plate and whip, and telemetry antennas (if removed).

Electrical Systems Check

(a) Check for solar cell shorts to ground.

(b) Set up battery switching circuit.

(c) Using external power, check converter input currents.

(d) Attach oscilloscopes to video output (spare) and cosmic noise output. Check overall system and check commutator output. Check telemetry transmitter outputs. (Note: Flight model video will be checked via telemetry outputs.)

(e) Install flight plugs and repeat (d) while checking battery currents.

Sounding Antenna Check

(a) Buffering the antenna motor battery, command 'ON' antenna extension. Extend antennas five to six feet and monitor motor current and analogue potentiometers. (Note: Antenna clutches should be engaged at this point of the test, and no further clutch engagement shall be attempted prior to antenna extension.)

(b) Declutch all antennas.

(c) Manually rewind antennas.

(d) Clutch all antennas.

Spacecraft Turnoff

(a) Command all converters OFF.

(b) Command battery switches OPEN.

(c) Remove flight plugs (N.B.).

(d) Remove umbilical cable.

APPENDIX IV

MINOR SPACECRAFT CHECKOUT PROCEDURES

A less thorough checkout procedure, used during the course of a major test operation and termed 'Minor Spacecraft Checkout', is as follows:

Visual Examination

(a) Visually inspect all external structure and solar cells.

(b) Remove beacon antenna and beacon mounting plate.

(c) Remove radiation shield.

(d) Visually check all fasteners, insulation, component packages, wiring, connectors, cable brackets, etc.

(e) Check packages for loose potting, shielding, cracks in box frames, etc.

(f) Manually spot check component package fasteners. If any are found loose, go over all accessible screws on entire spacecraft.

(g) Check thrust-tube hold-down screws.

(h) Check fasteners on thrust tube braces.

(i) Fasten lifting trunnion with 3/4 inch eye-bolt on thrust tube. Lift spacecraft clear of shaker table (vibration test program) with crane.

(j) Repeat steps (c) and (h).

(k) Replace spacecraft on shaker table and secure.

Antenna Check

(a) Install flight plugs and umbilical cable.

(b) Command 'ON' antenna extension. Extend to about five feet.

(c) Declutch antenna.

(d) Manually rewind antennas.

(e) Clutch antennas.

(f) Command spacecraft off.

(g) Remove flight plugs and umbilical cable.

(h) Reset spacecraft on shaker (for vibration test program).

Electrical System Check

(a) Command a general turn-on.

(b) Examine sounder operation via telemetry receiver.

(c) Examine commutator data via telemetry receiver.

(d) Command all systems off.

APPENDIX V

PROTOTYPE AND FLIGHT THERMAL VACUUM TESTS

1. PROTOTYPE SPACECRAFT ACCEPTANCE TEST

1.1 Temperature Test (Air in Chamber)

While non-operative, the payload was subjected to a test chamber temperature of -30°C for six hours, followed by a temperature of +60°C for six hours. The chamber temperature was then lowered to -10°C and the temperature of the spacecraft stabilized. The spacecraft was then turned on and its performance checked. The chamber temperature was then raised to +50°C and the temperature of the spacecraft stabilized. The spacecraft was again turned on and its performance checked.

1.2 High Temperature Test (Vacuum)

(i) The chamber was evacuated to a pressure of $1(10^{-4})$ mm Hg or less with the spacecraft remaining at around room temperature (75° F). Starting from pump-down, the 1/4 watt telemetry transmitter and the beacon were operated for a duration of 1/2 hour.

(ii) The wall heaters of the chamber and the arc lamps were adjusted and used to maintain a spacecraft steady-state temperature of +50°C. (The spacecraft was under rotation on its stand for all tests.)

(iii) Under the conditions of (ii) the spacecraft was operated on a duty cycle typical of that in orbit: namely 30 minutes on, and 75 minutes off. This procedure was continued for a minimum of seven days. During this test, an external charging source for the batteries was substituted for solar cells as a power source.

1.3 Low Temperature Test (Vacuum)

(i) The chamber was maintained at a pressure of $1(10^{-4})$ mm Hg or less.

(ii) The walls of the chamber were refrigerated to obtain a spacecraft steady-state temperature of -10°C.

(iii) At the conditions of (ii) the spacecraft was operated on its duty cycle (i.e., 30 minutes on, 75 minutes off) continuously for a period of two days, provided the chamber was not opened after the high temperature test under para 1.2 above. If the chamber was opened, the test had to last five days from the time stable conditions were re-established. As in 1.2 (iii), an external source was used to charge batteries.

2. FLIGHT SPACECRAFT ACCEPTANCE TEST

2.1 High Temperature Test (Vacuum)

(i) The chamber pressure was evacuated to $1(10^{-4})$ mm Hg or less. During evacuation, the 1/4 watt telemetry transmitter and the beacon were operated for a duration of 20 minutes.

(ii) The wall heaters of the chamber and arc lamps were used to obtain a spacecraft steady-state temperature of $+40°C$.

(iii) When the conditions of (ii) were reached, the spacecraft was operated on its duty cycle (as before) continuously for a period of two days. An external battery charging source was substituted for solar cells.

(iv) On completion of (iii) the chamber walls were refrigerated to their lowest attainable temperature while still at $1(10^{-4})$ mm Hg pressure (or less). The spacecraft was then subjected to continuous arc lamp illumination while the spacecraft payload was operated on its duty cycle with the batteries placed under charge from the solar cells. The test was terminated after steady-state temperature was reached, and the temperatures had been recorded.

2.2 Low Temperature Test (Vacuum)

(i) Continuing from 2.1 above, the chamber walls were adjusted to obtain a spacecraft steady-state temperature of $0°C$.

(ii) When the condition of (i) was reached, the spacecraft was operated on its duty cycle (as before) continuously for a period of one day. External battery charging was used. If the chamber was opened after test 2.1 (iv) the period of operation was continued for at least three days after stable conditions were re-established.

3. FREQUENCY OF TEMPERATURE READINGS

Temperature readings were taken before and after each spacecraft payload turn on.

Temperature readings were taken at least every 20 minutes during transient heating in item 2.1 (iv), Appendix V. Frequency of readings were gradually decreased to one every hour as steady-state temperatures were approached.

In all tests, temperatures had to be recorded with sufficient frequency to permit control of environmental temperatures of spacecraft and chamber. In addition, maximum and minimum temperatures reached in all tests were recorded.

DUE DATE

JUL 1 8 1997			
SEP - 9 1998			
	201-6503		Printed in USA